Force sensor manufactured with laser-based powder bed fusion

Additiv gefertigter Kraftsensor basierend auf pulverbettbasiertem Laserstrahlschmelzen
Zur Erlangung des akademischen Grades Doktor-Ingenieur (Dr.-Ing.)
Genehmigte Dissertation von Romol Chadda aus Kabul
Tag der Einreichung: 28.03.2023, Tag der Prüfung: 11.08.2023

1. Gutachten: Prof. Dr. mont. Mario Kupnik
2. Gutachten: Prof. Dr.-Ing. Matthias Weigold
Darmstadt, Technische Universität Darmstadt

TECHNISCHE
UNIVERSITÄT
DARMSTADT

Electrical Engineering and
Information Technology
Department

Measurement and Sensor
Technology Group

Force sensor manufactured with laser-based powder bed fusion
Additiv gefertigter Kraftsensor basierend auf pulverbettbasiertem Laserstrahlschmelzen

Accepted doctoral thesis by Romol Chadda

Date of submission: 28.03.2023
Date of thesis defense: 11.08.2023

Darmstadt, Technische Universität Darmstadt

Bitte zitieren Sie dieses Dokument als:
URN: urn:nbn:de:tuda-tuprints-246200
URL: http://tuprints.ulb.tu-darmstadt.de/24620
Jahr der Veröffentlichung auf TUprints: 2023

Erklärungen laut Promotionsordnung

§ 8 Abs. 1 lit. c PromO

Ich versichere hiermit, dass die elektronische Version meiner Dissertation mit der schriftlichen Version übereinstimmt.

§ 8 Abs. 1 lit. d PromO

Ich versichere hiermit, dass zu einem vorherigen Zeitpunkt noch keine Promotion versucht wurde. In diesem Fall sind nähere Angaben über Zeitpunkt, Hochschule, Dissertationsthema und Ergebnis dieses Versuchs mitzuteilen.

§ 9 Abs. 1 PromO

Ich versichere hiermit, dass die vorliegende Dissertation selbstständig und nur unter Verwendung der angegebenen Quellen verfasst wurde.

§ 9 Abs. 2 PromO

Die Arbeit hat bisher noch nicht zu Prüfungszwecken gedient.

Darmstadt, 28.03.2023

R. Chadda

Acknowledgment

First of all, I would like to thank my supervisor Prof. Dr. mont. Mario Kupnik for giving me the opportunity to conduct research in the field I have been enthusiastic about for a long time. His trust in me and the very valuable discussions were essential aspects that made this work possible. I am very grateful that you made this PhD journey possible, which not only gave me the opportunity to fulfill myself, but also to continue to grow as a researcher and a person.

I would like to thank Prof. Dr.-Ing. Matthias Weigold for his valuable input in our regular discussions within our collaborative project AddKraft and for reviewing this thesis. Furthermore, I would like to thank Martin Link and Holger Merschroth, who supported me in fabricating the sensors for this work and sharing their know-how regarding additive manufacturing in our regular discussions.

Additionally, I would also like to thank Prof. Dr.-Ing. Roland Werthschützky for always being available for me and discussing about my work.

I would like to thank my colleagues at the measurement and sensor technology group for always being supportive to me. It was a lot of fun working together with you. A big thanks go to Felix Herbst for rendering some of the images and to Bastian Latsch, Jan Helge Dörsam and Alexander Altmann for their support even shortly before submitting this work. Special thanks goes to Omar Ben Dali for being a great colleague and even more a great friend, who supported me unconditionally.

A big thanks go to all my supervised bachelor's and master's students, who have supported my research and this thesis with their work. Special thanks go to Tim Engel and Esan Sundaralingam, who have been working for a long time with me and assisted me in various experiments.

I would like to thank the Deutsche Forschungsgemeinschaft (DFG) for funding this research within the project AddKraft under grant 418628981.

Furthermore, I would like to thank my family and my friends for their support and encouragement through all these challenging years during my PhD journey.

Last but not least, I would like to express a big thank to my spouse Soni, who has been always there for me and believing in me. Your backing and support have been a major reason for me being able to reach my goal.

Abstract

Structural health monitoring (SHM) and condition monitoring are gaining in importance due to the increasing digitalization in several fields such as industry automation, energy and aerospace industry as well as in plant construction. The main objective is to monitor the condition of a system or plant in order to facilitate predictive maintenance and prevent failures on one hand and to increase the productivity on the other hand. This requires high-quality data within relevant locations of the plant, which inevitably leads to the integration of sensors into existing structures to provide in-situ measurements. In this context, force sensors are of great importance, as they allow the detection of load peaks. However, since commercially available force sensors are designed as closed systems, it is not always possible to integrate them into existing structures, or only with high effort. Therefore, force sensors with a high degree of individualization in terms of geometry and measuring range are necessary. These requirements can be met with additive manufacturing processes such as laser-based powder bed fusion (LPBF), since they allow manufacturing of almost any geometry combined with their characteristic layer-by-layer build-up that enables the integration of a sensor at a specific layer. However, there is no systematic approach up to now for the realization of LPBF-manufactured force sensors based on strain gauges, which are the gold standard as sensing elements in conventional force sensors.

In this thesis, a disruptive manufacturing approach is presented that breaks and re-arranges the well-known state of the art assembly sequence of force sensors, and, thus, enables a systematic integration of strain gauges into LPBF-manufactured parts. This approach is based on a published patent application and involves inserting a steel plate applied with strain gauges, which serves as a measuring element carrier, into an LPBF-manufactured part during a process interruption. The LPBF-manufactured force sensors (80 mm x 25.5 mm x 14 mm) are investigated regarding two key aspects that significantly influence their performance, which are: the strain transfer from the LPBF-manufactured part to the inserted measuring element carrier and the behavior of the strain gauge in terms of linearity and sensitivity after integration in the rough manufacturing environment. Investigating the first aspect has shown that the LPBF-manufactured force sensors using the disruptive manufacturing approach are reproducible and feature linearity and hysteresis errors of $\pm\,0.1$ % and $\pm\,0.2$ %, respectively. The achieved results are very similar to a conventionally manufactured reference force sensor showing the competitive potential of the new approach. At this stage of investigation the strain gauges are not fully encapsulated. In addition, the temperature and creep behavior of the LPBF-manufactured force sensors are also investigated. A comparison of the sensitivity of the LPBF-manufactured force sensors with a FEA model shows excellent agreement, which provides a reliable prediction of strain transmission, allowing for a targeted design of such force sensors in advance. The comparison of the strain gauge behavior before and after being exposed to the LPBF-process shows an irreversible change of the base resistance by up to -0.15 %. This irreversible change results from the temperature load during the LPBF-process as well as a plastic deformation of the measuring element carrier and is larger the closer the location of the strain gauge to the scanned surface. However, this does not negatively affect the linearity and sensitivity of the LPBF-manufactured force sensor due to the chosen geometry of the force sensor and the location of the strain gauges, which undergo a maximum temperature of 145 °C.

However, a severe deformation of the measuring element carrier with a deflection of 0.5 mm in height

direction is present due to large temperature gradients during the LPBF-process in combination with the chosen geometry of the force sensor. The onset of this thermally induced deformation of the measuring element carrier is visible in measurements of the resistance of the strain gauge during the LPBF process. It shows that a tensile stress acts during establishing a material connection between the measuring element carrier and the LPBF-manufactured base body, which promotes the deformation. This thermally induced deformation is reduced by up to 67 % by adapting the geometry with respect to the height of the material connection as well as some parameters of the LPBF-process, such as scanning strategy and inter layer time.

Based on these findings, a geometry is developed for complete encapsulation of the strain gauges, which is not manufacturable by conventional subtractive or forming processes. The encapsulation increases the temperature experienced by the strain gauges, which reaches a maximum of 230 °C. It is shown that during the manufacturing time the strain gauges ar able to withstand these temperatures and maintain their characteristic values. The subsequent characterization of the LPBF-manufactured force sensor with complete encapsulated strain gauges shows linearity and hysteresis errors of ± 0.1 % and ± 0.2 %, respectively, which are in very good agreement with the LPBF-manufactured force sensors mentioned previously. Furthermore, the designed geometry offers possibilities for the realization of an overload protection as well as the adjustment of the measuring range.

In the last part of this thesis, LPBF manufactured-threads are investigated. Until now, the high surface roughness of LPBF-manufactured parts has prevented the fabrication of usable threads by means of LPBF, causing screws to break off during tightening. Therefore, the flank angle and the clearance of threads of the sizes M3 to M8 are adapted such that usable threads can be fabricated by means of LPBF. For this purpose, a torque test bench is used to insert screws in a defined manner into the LPBF-manufactured threads while measuring the tightening torque. It is found that LPBF-manufactured threads with an additional clearance of 60 µm for flank angles from 80° to 100° do not require any significant torque when tightening the screws. The possibility of manufacturing threads during fabricating the part using LPBF eliminates the need for subsequent processing steps, and, thus, significantly reduces the production time while increasing the cost-effectiveness.

This work proves that a defined integration of strain gauges into LPBF-manufactured parts is possible using the disruptive approach presented. Hence, custom additively manufactured parts can be fabricated that allow for in-situ measurements. In addition to the promising performance of the LPBF-manufactured force sensors introduced in this work, which is comparable with the conventionally manufactured force sensors, the design freedom allowed by the LPBF-pocess makes their integration in complex geometries a characteristic feature that can not be achieved otherwise. This work provide the basis for developing structurally integrated force sensors and shows the high potential for individualization.

Zusammenfassung

Struktur- und Zustandsüberwachung gewinnen durch die zunehmende Digitalisierung in den Bereichen Industrieautomatisierung, Energie- und Luftfahrtindustrie sowie im Anlagenbau immer mehr an Bedeutung. Das Ziel besteht dabei darin, den Zustand einer Anlage oder Systems zu überwachen, um einerseits eine vorausschauende Wartung zu ermöglichen und somit Fehlerfälle bzw. Ausfälle vorzubeugen und andererseits die Produktivität zu erhöhen. Voraussetzung hierzu ist die Bereitstellung aktueller Zustandsdaten an den kritischen Stellen des zu überwachenden Systems. Dies erfordert die Integration von Sensoren in eine bestehende Struktur, um sogenannte ïn-situ Messungenßu ermöglichen. In diesem Kontext spielen Kraftsensoren eine große Rolle, da diese die Erkennung von Lastspitzen ermöglichen. Da kommerziell erhältliche Kraftsensoren jedoch als Allzwecksensoren ausgelegt werden, ist deren Integration nicht immer oder nur erschwert in bestehende Strukturen möglich. Vielmehr sind Kraftsensoren mit einem hohen Grad an Individualisierbarkeit hinsichtlich Geometrie und Messbereich sowie vernachlässigbarer Rückwirkung auf das Bauteil erforderlich. Diese Eigenschaften lassen sich mit additiven Fertigungsverfahren, wie beispielsweise dem pulverbettbasierten Laserstrahlschmelzen (LPBF), realisieren, da sich einerseits nahezu jede Geometrie damit herstellen lässt und andererseits der typische Schichtauffbau die Intergration von Sensorik an beliebiger Stelle des Bauteils ermöglicht. Aktuell besteht allerdings kein systematischer Ansatz zur Realisierung von LPBF-gefertigten Kraftsensoren basierend auf Dehnungsmessstreifen (DMS), die bei konventionellen Kraftsensoren das Standard-Sensorelement darstellen.

Daher wird in dieser Arbeit ein neuartiger, disruptiver Fertigungsansatz vorgestellt, der die übliche Fertigungsreihenfolge von konventionellen Kraftsensoren aufbricht und neu anordnet und somit eine systematische Integration von DMS in LPBF-gefertigte Bauteile ermöglicht. Dieser Lösungsansatz wurde in einer eigenen bereits veröffentlichten Patentanmeldung fixiert. Dabei wird eine mit Dehnungsmessstreifen (DMS) applizierte Stahlplatte (Messelementträger), die als Verformungskörper dient, in dem LPBF-gefertigten Bauteil während der Unterbrechung des additiven Fertigungsprozesses eingesetzt. Mit den in LPBF-gefertigten Demonstratoren als Kraftsensoren werden die zwei wichtigsten Sensor-Qualitätskriterien, die Dehnungsübertragung vom LPBF-gefertigten Bauteil zum eingelegten Messelementträger und das geforderte statische Sensor-Übertragungsverhalten, welches die Empfindlichkeit und Linearität einschließt, unter realen Prozessbedingungen untersucht. Hierbei zeigt sich, dass die LPBF-gefertigten Sensoren (80 mm x 25.5 mm x 14 mm) nach disruptivem Herstellungsansatz reproduzierbar mit einem Linearitätsfehler von ± 0.1 % und einem Hysteresefehler von ± 0.2 % aufgebaut werden können. Diese Werte entsprechen den typischen Werten konventioneller Kraftsensoren. Außerdem werden das Temperatur- und Kriechverhalten der LPBF-gefertigten Kraftsensoren untersucht. Der Vergleich der Empfindlichkeit der LPBF-gefertigten Kraftsensoren mit einem FEM-Modell zeigt eine sehr gute Übereinstimmung, sodass eine zuverlässige Vorhersage der Dehnungsübertragung und damit eine gezielte Auslegung solcher Kraftsensoren im Vorfeld möglich ist. Der Vergleich des DMS-Verhaltens vor und nach Durchführung des LPBF-Prozesses liefert lediglich eine Abweichung des DMS-Grundwiderstandes von maximal 0.15 %. Diese Änderung resultiert aus der thermischen Belastung während des LPBF-Prozesses sowie einer plastischen Verformung des Messelementträgers und ist umso größer, je näher der DMS der belichteten Fläche ist. Dies wirkt sich aufgrund der gewählten Geometrie des Verformungskörpers und der Positionierung des DMS, die eine Temperatur von maximal 145 °C ausgesetzt sind, jedoch nicht negativ auf

die Linearität und Empfindlichkeit des LPBF-gefertigten Kraftsensors aus.

Nichtsdestotrotz ist eine starke Verformung des Messelementträgers mit einer Auslenkung von 0.5 mm in Höhenrichtung aufgrund auftretender großer Temperaturgradienten während des LPBF-Prozesses in Kombination mit der gewählten Geometrie des Verformungskörpers vorhanden. Der Beginn dieser Verformung des Messelementträgers ist bei Messungen des DMS-Widerstands während des LPBF-Prozesses ersichtlich und zeigt, dass zum Zeitpunkt der stoffschlüssigen Verbindung des Messelementträgers mit dem LPBF-gefertigten Bauteil eine Zugspannung wirkt und es somit zur Verformung des Messelementträgers kommt. Diese Verformung wird jedoch durch Anpassung der Geometrie hinsichtlich der Höhe der Materialanbindung sowie einiger Prozessparameter, wie beispielsweise die Belichtungsstrategie und Belichtungszeit, um bis zu 67 % reduziert.

Darauf aufbauend wird mit den optimierten Prozessparametern eine Geometrie für eine vollständige Verkapselung der DMS entwickelt, die mit konventionellen subtraktiven oder umformenden Verfahren nicht fertigbar ist. Durch die Verkapselung nimmt die von den DMS erfahrene Temperatur zu, die in diesem Fall bei maximal 230 °C liegt. Dabei zeigt sich, dass die DMS auch diesen Temperaturen standhalten und ihre Kennwerte beibehalten. Die anschließende Charakterisierung des LPBF-gefertigten Kraftsensors mit vollständig verkapselten DMS zeigt einen Linearitätsfehler von ± 0.1 % sowie einen Hysteresefehler von ± 0.2 %, die in sehr guter Übereinstimmung mit den restlichen in dieser Arbeit aufgebauten Kraftsensoren sind. Darüberhinaus bietet die Geometrie Möglichkeiten zur Realsierung eines Überlastschutzes sowie die Anpassung des Messbereichs.

Im letzten Teil der Arbeit werden zur Gewährleistung einer zweiseitigen Einbindung des Messelementes LPBF-gefertigte Gewinde untersucht. Aufgrund der Eigenschaft der hohen Oberflächenrauheit von LPBF-gefertigten Bauteilen, sind bisher keine nutzbaren Gewinde mittels LPBF herstellbar, sodass sogar Schrauben beim Anziehen abbrechen. Dazu werden in dieser Arbeit der Flankenwinkel und die Clearence von Gewinden der Größen M3 bis M8 so angepasst, dass sich nutzbare Gewinde mittels LPBF herstellen lassen. Hierfür wird ein vorhandener Drehmomentmessstand genutzt, um Schrauben definiert in die LPBF-gefertigten Gewinde einzubringen. Die Ergebnisse zeigen, dass LPBF-gefertigte Gewinde mit einer zusätzlichen Clearence von 60 µm für Flankenwinkel von 80° bis 100° kein nennenswertes Drehmoment beim Anziehen der Schrauben benötigen. Die Möglichkeit Gewinde direkt bei der Fertigung des Bauteils im LPBF-Verfahren mitzudrucken, erspart nachträgliche Bearbeitungsschritte und reduziert damit die Fertigungszeit sowie Produktionskosten eines LPBF-gefertigten Bauteils.

Insgesamt bestätigt die Arbeit, dass eine definierte Integration von DMS-Messelementen in LPBF-gefertigte Bauteile mit Hilfe des vorgestellten disruptiven Ansatz reproduzierbar möglich ist. Die mit LPBF gefertigten Kraftsensoren entsprechen in ihren Kennwerten denen konventionell gefertigter Kraftsensoren. Sie bilden daher einen Lösungsansatz für die Entwicklung von strukturintegrierten Kraftsensoren. Zusätzlich weisen diese neuartigen Kraftsensoren ein hohes Potential für individuelle Adaption in Konstruktionsbauteile auf.

List of Publications

2022

- O. Ben Dali, S. Zhukov, **R. Chadda**, A. Kasanski, H. von Seggern, X. Zhang, G. M. Sessler, and M. Kupnik, "Eco-Friendly High Sensitive Piezoelectrets for Force Myography," in *IEEE Sensors Journal*, vol. 23, no. 3, pp. 1943-1951, Feb. 2023, doi: 10.1109/JSEN.2022.3225723.
- **R. Chadda**, M. Link, T. Engel, C. Hartmann, O. Ben Dali, J. Probst, H. Merschroth, E. Abele, M. Weigold, and M. Kupnik, "Evaluation of Additively Manufactured Parts in Disruptive Manner as Deformation Elements for Structural Integrated Force Sensors," in *IEEE Sensors Journal*, vol. 22, no. 20, pp. 19249-19258, Oct. 2022, doi: 10.1109/JSEN.2022.3205172.
- F. Herbst, **R. Chadda**, C. Hartmann, J. Peters, D. Riehl, T. Gwosch, K. Hofmann, S. Matthiesen, and M. Kupnik, "Multi-axis Force Sensor for Sensor-integrating Bolts," in *Proc. IEEE Sensors*, pp. 1–4, 2022, doi: 10.1109/SENSORS52175.2022.9967220.
- S. Suppelt, **R. Chadda**, T. Büchner, N. Schäfer, R. Sader and M. Kupnik, "Measurement System for Human Lateral Mandibular Forces," in *Proc. IEEE Sensors*, pp. 1-4, 2022, doi: 10.1109/SENSORS52175.2022.9967072.

2021

- S. Suppelt, **R. Chadda**, N. Schäfer, R. Sader and M. Kupnik, "Sensor for Bilateral Human Bite Force Measurements," in *Proc. IEEE Sensors*, pp. 1-4, 2021, doi: 10.1109/SENSORS47087.2021.9639818.
- P. Mattfeldt, B. Latsch, J. Hielscher, S. Desch, N. Schäfer, **R. Chadda**, R. Werthschützky, A. Seyfarth, and M. Kupnik, "Machine learning for situation detection of an active knee-ankle-foot-orthosis," in *VDI Mechatroniktagung*, 2021.
- H. Krumb, D. Das, **R. Chadda**, and A. Mukhopadhyay, "CycleGAN for interpretable online EMT compensation," *International Journal of Computer Assisted Radiology and Surgery*, vol. 16, pp. 757–765, 2021, doi: 10.1007/s11548-021-02324-1.

2020

- **R. Chadda**, J. Probst, C. Hartmann, M. Link, M. Hessinger, E. Abele, M. Weigold, and M. Kupnik, "Disruptive force sensor based on laser-based powder-bed-fusion," in *Proc. IEEE Sensors*, pp. 1–4, 2020, doi: 10.1109/SENSORS47125.2020.9278934.
- M. Link, M. Weigold, J. Probst, **R. Chadda**, C. Hartmann, M. Hessinger, M. Kupnik, and E. Abele, "Investigation on structural integration of strain gauges using laser-based powder-bed-fusion (LPBF)," in *Proc. Production at the Leading Edge of Technology*, pp. 387–395, 2020, doi: 10.1007/978-3-662-62138-7_39 .

- J. Seiler, N. Schäfer, B. Latsch, **R. Chadda**, M. Hessinger, P. Beckerle, and M. Kupnik, “Wearable vibrotactile interface using phantom tactile sensation for human – robot interaction,” in *Proc. International Conference on Human Haptic Sensing and Touch Enabled Computer Applications - EuroHaptics 2020*, pp. 380–388, 2020, doi: 10.1007/978-3-030-58147-3_42.

- Y. Xue, X. Zhang, **R. Chadda**, G. M. Sessler, and M. Kupnik, “Ferroelectret-based flexible transducers A strategy for acoustic levitation and manipulation of particles,” *The Journal of the Acoustical Society of America*, vol. 147, no. 5, EL421–EL427, 2020, doi: 10.1121/10.0001274.

2019

- **R. Chadda**, S. Wismath, M. Hessinger, N. Schafer, A. Schlaefer, and M. Kupnik, “Needle tip force sensor for medical applications,” in *Proc. IEEE Sensors*, pp. 1-4, 2019, doi: 10.1109/SENSORS43011.2019.8956754.

- F. Greiner, **R. Chadda**, J. -E. Adolf, S. Beck and M. Kupnik, “Force sensor with increased local resolution for electronic Contact Normal Force measurement in electrical connectors,” in *Proc. IEEE Sensors*, pp. 1-4, 2019, doi: 10.1109/SENSORS43011.2019.8956630.

- O. Ben Dali, S. Zhukov, **R. Chadda**, P. Pondrom, X. Zhang, G. M. Sessler, H. von Seggern, and M. Kupnik, “Modeling of piezoelectric coupling coefficients of soft ferroelectrets for energy harvesting,” in *Proc. IEEE International Ultrasonics Symposium (IUS)*, pp. 2454-2457, 2019, doi: 10.1109/ULTSYM.2019.8925848.

- Y. Goergen, **R. Chadda**, R. Britz, D., Scholtes, N. Koev, P. Motzki, R. Werthschützky, M. Kupnik, and S. Seelecke, “Shape Memory Alloys in Continuum and Soft Robotic Applications,” in *Proc. ASME Conference on Smart Materials, Adaptive Structures and Intelligent Systems*, 2019, doi: 10.1115/SMASIS2019-5610.

- J. Fauser, **R. Chadda**, Y. Goergen, M. Hessinger, P. Motzki, I. Stenin, J. Kristin, T. Klenzner, J. Schipper, S. Seelecke, R. Werthschützky, M. Kupnik, and A. Mukhopadhyay, “Planning for Flexible Surgical Robots via Bézier Spline Translation,” in *IEEE Robotics and Automation Letters*, vol. 4, no. 4, pp. 3270-3277, 2019, doi: 10.1109/LRA.2019.2926221.

- Y. Goergen, **R. Chadda**, P. Motzki, N. Koev, R. Werthschützky, M. Kupnik, and S. Seelecke, “Entwicklung und Aufbau einer FGL-aktivierten Führungsdrahtspitze mit einstellbarer Steifigkeit und Krümmung,” in *4SMARTS - Symposium für Smarte Strukturen und Systeme*, 2019.

Abbreviations

ADC	Analog-to-Digital-Converter
AM	additive manufacturing
ASTM	American Society for Testing and Materials
BJT	Binder Jetting
CAD	computer-aided design
DED	Directed Energy Deposition
DfAM	design for additive manufacturing
DFG	German Research Foundation
DMD	Directed Metal Deposition
EBAM	Electron Beam Additive Manufacturing
EBM	Electron Beam Melting
FBG	Fiber Bragg Grating
FDM	Fused Deposition Modeling
FFF	fused filament fabrication
LPBF	Laser-based Powder Bed Fusion
MEX	Material Extrusion
MJT	Material Jetting
MUST	Measurement and Sensor Technology Group
PBF	Powder Bed Fusion
PCB	printed circuit boards
PLA	polylactic acid
PTW	Institute for Production Management, Technology and Machine Tools

RFID	radio frequency identification
SAS	sensor/actuator system
SDM	Shape Deposition Manufacturing
SHM	Structural Health Monitoring
SL	Sheet Lamination
SLM	Selective Laser Melting
SNR	Signal-to-noise ratio
TRL	technology readiness level
VT	Vat Polymerization

Contents

1 Introduction

Digitalization offers enormous potential for socially significant innovations and is omnipresent in the context of the trends *Industry 4.0* and *Internet of Things* (IoT) [1]. Here, the concept of fourth industrial revolution, known as Industry 4.0 [1], describes the revolution of traditional manufacturing processes towards intelligent manufacturing processes by using machines and devices that communicate with each others and additionally provide feedback to the user [2]–[4]. This communication is intended, on one hand, for adaptive adjustment and control of process chains [5] and, on the other hand, for monitoring the condition of the machines and the plant [6]. In particular, the latter aspect is of interest regarding Structural Health Monitoring (SHM), since it allows predicting the operational condition of the machinery [7]–[9]. This enables to detect fault cases in time, thus avoiding long periods of downtime [7]. Consequently, the reliability of machines can be increased. Therefore, this is a very promising approach for lifetime assessment and predictive maintenance of machines [7], [10], [11], providing cost savings compared to conventional periodic maintenance, where components are replaced too early [10], [12].

Based on the aforementioned benefits, SHM is increasingly required in several fields such as industry automation, energy and aerospace industry as well as civil engineering [9], [11], [13]–[15]. In order to realize SHM, process data of high quality needs to be acquired. That means, an integration of sensors into the machinery is inevitable for providing continuous feedback. Especially mechanical sensors, e.g. force and torque sensors, are of high interest for monitoring crucial parameters within a structure and detect overload cases that lead to physical damages [9], [16]–[19]. The conventional approach is based on attaching these sensors to easily accessible locations on the surface of the machinery [20]. In this case, measurements are usually taken at locations that are far away from the region of interest for process-relevant data acquisition [10], [20]–[22]. Furthermore, the measured data can be affected by environmental conditions [20]. Both result in poor and unreliable data [11], [21]. Therefore, an integration of sensors into existing process chains or structures is required, which allow reliable in-situ measurements providing data of high quality directly within the process or machinery [17], [21], [23], [24].

In order to provide such in-situ measurements, an integration of mechanical sensors within the loaded structure is required. However, a simplified integration of commercially available force and torque sensors is hampered due to complex structures that are generally present [25], [26]. In this context, a high degree of individualization and customization is required in terms of design geometry and size of these structural integrated mechanical sensors [18]. Here, metal-based additive manufacturing (AM) offers application-specific design options without the limitations of traditional manufacturing technologies [23], [27], [28]. The manufacturing of a part is typically done in a layer-by-layer build-up that allows easy access to the center of the fabricated part by interrupting the manufacturing process. This facilitates the integration of functional elements, such as sensors, within a fabricated part at a specific layer [25], [29], and, thus, provides the possibility to manufacture application-optimized and customizable structural integrated sensors.

This approach has been widely used in the state of the art by integrating different types of sensors such as optical fibers, thermocouples, PT100 elements or RFID tags. For monitoring mechanical loads and forces additively manufactured metallic components with integrated strain sensing elements are essential. Here, strain gauges offer a very promising solution as sensing elements, which are typically used in conventionally manufactured force sensors due to their linear behavior and ease of handling [30]. The main challenge when using strain gauges in combination with additively manufactured metallic parts, are the restrictions to ensure proper strain transmission. Therefore, the integration of strain gauges into additively manufactured metallic parts has been barely investigated so far. An approach that allows strain gauges to be integrated reliably into additively manufactured metallic parts would provide significant added value for structural integrated force sensors. Therefore, the goal of this thesis is the development of a manufacturing approach that bridges the aforementioned gap, and, thus, allows the integration of strain gauges within additively manufactured metallic parts.

1.1 State of the art of integrating sensors in additively manufactured parts

Based on the properties such as design freedom, light weight as well as design for functionality and part complexity, metal based AM-processes are arousing great interest in aerospace, oil and gas, automobile and medical applications [31]. The shared characteristic of all these application areas is the need of complex individualized components in small batches. These requirements are precisely met by metal based AM-processes, which enable economical production from batch size one [32] and customization without additional costs due to their tool-free and near-net-shape manufacturing properties [33]. This means that the geometric complexity of a component does not affect the cost per unit when using metal based AM-processes (Fig. 1.1). In contrast, conventional manufacturing processes have a maximum geometric complexity level of manufacturing a part, while a higher level of complexity is generally associated with higher costs [31], [34]. This attribute is referred to the term "complexity is free" in the context of metal based AM-processes [31], [35]–[38]. However, this only highlights the positive aspects of metal based AM-processes. In a comprehensive view, it becomes clear that actually one set of design constraints is traded for another [35]. In fact, not every component can be manufactured directly as it is. Rather, a re-design of the part needs to be done while employing the design for additive manufacturing (DfAM) guidelines that consider the limitations of metal based AM-processes such as

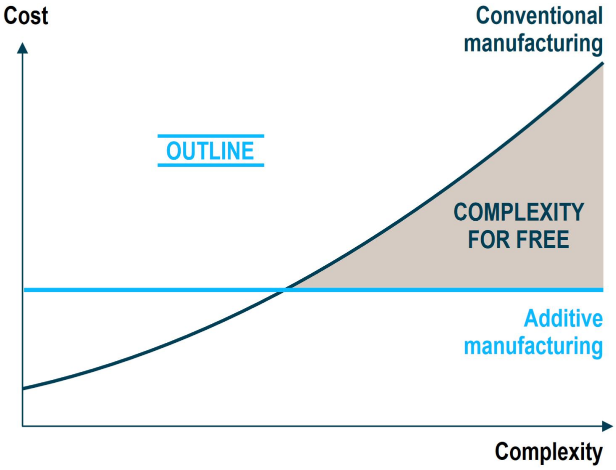

Figure 1.1: Cost vs. complexity between AM-processes and conventional manufacturing processes. The costs are almost independent of the complexity of a component when using AM-processes. In contrast, a higher complexity of a part is generally associated with higher costs when using conventional manufacturing processes. This graphic is taken from [31].

overhanging features, residual stresses, and thin walls [35], [39]–[41]. In addition, metal based AM-processes result in higher production costs regarding the part's level [33].

In order to compensate for these drawbacks and keep metal based AM-processes attractive, it is of great importance that functionality is added to additively manufactured parts such as lattice structures [42] or topology-optimized lightweight structures [29], [43]. This added functionality offers the potential to save costs when using the part during its remaining life cycle, which in turn counterbalances the higher manufacturing costs as well as the initial investment costs [33]. There are different ways to integrate functionality into metal based AM parts, which will be presented in the next section.

1.1.1 Integration of functionality in additively manufactured parts

Integration of functionality refers to the combination of different functionalities in one component, i.e., reduces the number of parts or the assembly effort, and, thus, typically results in a more complex geometry of the component [44]. In this context, metal based AM-processes are considered as a key technology for the realization of functionally integrated structures due to their application-specific design possibilities based on the layer-by-layer build-up principle [33], [45], [46]. The integration of functionality can be divided into the following three categories [33], [47], [48]:

Integration of functionality through design

The design of a component and its systematic modification enable the realization of new functions [38], [44]. An application for this is found in the injection molding process, where molten plastic is injected into a mold and adopts this shape when it has cooled down. Since the cooling time takes up 70 to $80\,\%$ of an entire cycle of production [49], a reduction of the cooling time leads to increased production efficiency. For this purpose, cooling channels are provided in conventional molds that feature a straight-line shape made by drilling [50]. The drawback of these conventional cooling channels is that they are unevenly distributed over the mold surface in complex-shaped injection molds, which results in an uneven cooling [49]. In order to overcome this drawback, conformal cooling channels exhibiting intricate layouts are used. These match the geometry of the mold cavities [Fig. 1.2(a)], and, thus, adjust the cooling conditions [50], [51]. However, these complex geometries are not manufacturable by conventional subtractive or forming processes in one part, but only made possible by metal based AM-processes.

Further areas of application that benefit from the high geometric design flexibility and high degree of customization offered by metal based AM-processes are the medical and dental industries [49]. They require highly complex parts that are individualized for each patient [33] such as a cranial implant that has to be perfectly tailored [Fig. 1.2(b)]. The third major sectors that also benefits from integration of functionality through design are the aerospace and automotive industry. The focus here lies on lightweight design such as implementing lattice structures [42], [52], which can lead to significant cost savings. This has become evident considering the cost of launching a SpaceX rocket, which was around $\$6078$ per kg in 2018 [53].

Integration of functionality through the process

The second method of integrating functionality into an additively manufactured part is through the manufacturing process itself, as this influences the material properties [33]. Here, properties of a part, such as the microstructure or composition, are locally tunable during manufacturing by varying process parameters such as the energy input for joining the layers [52], [54]. This can be utilized to realize specific material properties in defined directions of a part to tune the performance of the part.

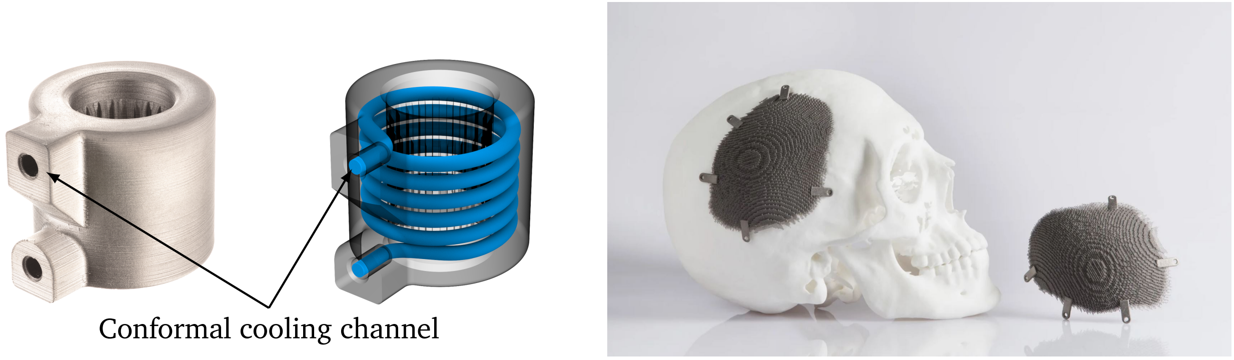

(a) (b)

Figure 1.2: Examples for integrating of functionality through design: (a) Mold with integrated conformal cooling channel that is manufactured using metal based AM-processes [image source: www.desktopmetal.com], (b) Tailored cranial implant made out of titanium [image source: www.eos.info/en].

Therefore, such parts are called functionally graded materials [55]. Application cases for this are found in orthopedics and implantology [54], [56]. In the case of total hip or knee arthroplasty, implants are used that are inherently stiff. This stiffness results in under-utilization of the surrounding host bone during loading, which leads to stress shielding or failure [54]. Here, it has been found that implants are more suitable as a press-fit system with a porous structure [Fig. 1.3(a)] [52], [54], [57]. This encourages the bone to grow into the implant, which has a positive effect on the healing process [56]. Furthermore, the porous structure reduces the mismatch in the mechanical properties between the bone and the implant [54]. Such parts with a specific porosity, i.e., optimized pore size and mechanical strength, are either not manufacturable with conventional manufacturing processes or only with great effort [54]. AM-processes offer elegant approaches for this purpose such as by varying the laser power in the case of the LPBF process [58] to influence the strut thickness of the pore structure [Fig. 1.3(b)].

Such porous structures are also in demand in the tooling sector, which enable a transport of fluids. This has been demonstrated in metal forming processes, where additively manufactured components

(a) (b)

Figure 1.3: Examples for integrating of functionality through the process: (a) Hip cup with integrated porous structure [image source: www.sme.org], (b) Adjusted porosity through laser power in case of Laser-based Powder Bed Fusion (LPBF) [image source: http://en.51shape.com].

with porous structures enable a uniform supply of lubricant [59]. In addition, additively manufactured components consisting of a combination of dense and porous sections for fuel cells were examined, where the porous part acted as a membrane [60].

Integration of functionality through integration of external components

The third method of integrating functionality into an additively manufactured part results from the characteristic layer-by-layer build-up, which enables the integration of external components such as sensors, actuators, electronics and further mechanical parts [25]. This opportunity was identified in the early development phase of the AM-processes for creating smart parts or smart electromechanical systems [61], [62]. The integration of sensors within additively manufactured parts enables monitoring during the use phase, when such smart parts are integrated into a system [33]. This allows the system to be operated at its optimum level on one hand, and to detect faults at an early stage as part of the SHM on the other hand. This type of integration of functionality was demonstrated through embedding piezo stack into an additively manufactured part [63]. Subsequently, this part was structurally integrated in a truss structure for active shunt damping (Fig. 1.4).

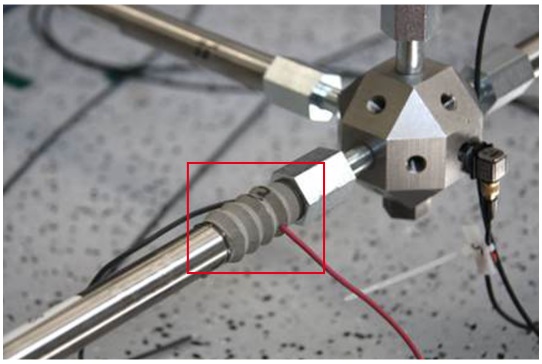

Figure 1.4: The additively manufactured active strut (outlined in red) with an integrated piezo stack is installed in a truss structure for active shunt damping [63].

In addition to the aforementioned components, this category of integration of functionality also includes the realization of hybrid structures. Here, a conventional component is considered as an external component on which another structure is built by means of the AM-processes [46]. Thus, multi-material components are manufacturable.

In conclusion, the described possibilities for the integration of functionality based on:

- design flexibility without additional costs for realizing complex geometries,
- producing ”single-part assemblies” that do not require assembly of several single parts and
- embedding of external components

highlight the tremendous potential of AM-processes. It is evident that AM-processes are currently not as suitable for mass production as conventional manufacturing processes (e.g. injection molding) with respect to cost and time aspects, but are of great interest when it comes to customized products in small series production [64]. Therefore, the motto for AM-processes is mass customization instead of mass production. In particular, the possibility of integrating external components, especially sensors, is a fundamental advantage of

AM-processes, which is seen as a core aspect in future applications of AM [25], [65] being fueled by the trends of Industry 4.0 and IoT. This has been recognized by many research groups resulting in the investigation of an increasing number of concepts for the integration of various sensors into additively manufactured metallic parts over the last almost 20 years. In this context, LPBF is predominantly used as AM-process, since it is currently the leading technology in the field of metal-based AM in both research and industry [66], [67] as it offers a high geometrical resolution, homogeneous process conditions and favorable mechanical properties [68]–[70]. Therefore, this work focuses on the LPBF-process. The basics of the LPBF-process are described in Sec. 2.6. In the following, several approaches are presented that deal with an integration of sensors within LPBF-manufactured parts.

1.1.2 LPBF-manufactured parts with integrated sensors

This section introduces various approaches for integrating sensors into additively manufactured metallic parts that have been investigated over the last 20 years. The focus lies primarily on LPBF-manufactured metallic parts. In order to integrate components, such as sensors and actuators, into an LPBF-manufactured part, a cavity has to be planned in it (Fig. 1.5). Once the cavity has been completely manufactured, the LPBF-process is interrupted and the metal powder in the cavity is removed. Afterwards, the sensor is inserted into the cavity and the LPBF-process is resumed to complete the part. Consequently, the integration of sensors requires an extension of the LPBF-process. This approach has been widely applied in the state of the art by integrating optical fibers [16], [71]–[75], thermocouples [28], [59], PT100 elements [70], radio frequency identification (RFID) tags [76], [77], hall effect sensors [33], eddy current sensors [10], [33] as well as piezoelectric sensors [69] into LPBF-manufactured parts.

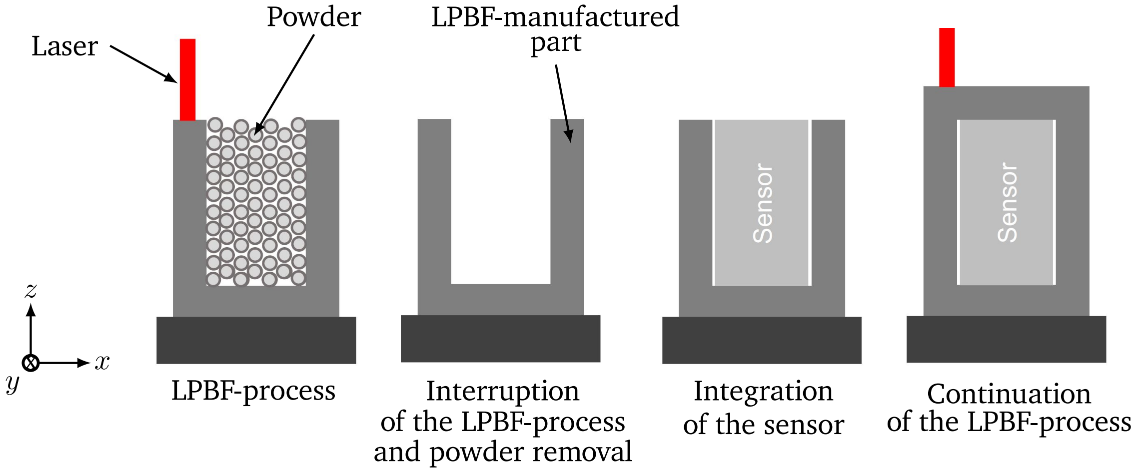

Figure 1.5: Integration of external components, such as sensors or actuators, in LPBF-manufactured parts by interrupting the LPBF-process. Here, z represents the build-up direction. This graphic is adapted from [46].

Fiber optic sensors

Fiber optic sensors have been investigated most extensively regarding their integration into additively manufactured parts. This is due to the beneficial properties of optical fibers such as small size (typically $125\,\mu\mathrm{m}$), immunity to electromagnetic interference and non-obtrusive embeddability [78]. Furthermore, they do not require electrical power at the point of measurement [33]. Thus, fiber optic sensors are considered for integration into additively manufactured parts to allow for monitoring critical parameters of materials and structures [79]. These optical fibers are available with a variety of sensor configurations. Among them, the Fiber Bragg Grating (FBG) is the most widely used ones [80]. A FBG is a periodic variation in the refractive index of the fiber core that acts like a wavelength-selective filter [79], [80]. In case of transmitting broadband light through the fiber core, light with a specific wavelength is reflected, which depends on the FBG [79]. Optical fibers with FBG's are well known for temperature and strain measurements [33], [78].

First experiments on the integration of optical fibers in additively manufactured metallic parts were conducted by Li in 2000 [20], [78], [79]. The Shape Deposition Manufacturing (SDM) process was used, which is a hybrid manufacturing process. First, metal powder is melted layer-by-layer using a laser beam and then reworked by milling [79]. Here, the fibers with an FBG were embedded in a nickel coating with a thickness up to 1.5 mm via electroplating and then integrated into an additively manufactured part made of steel using SDM. The integrated sensors enabled temperature and strain measurements with a nearly linear behavior. The work of Li has laid the foundation for the integration of external components into additively manufactured parts. This has inspired many researchers around the world to work on the integration of optical fibers as well as other sensors using different AM-processes.

The first works in the field of integration of optical fibers with an FBG in LPBF-manufactured parts focused on the optimization and further investigation of Li's approach. The focus was specifically on a reduction of the nickel coating as well as the investigation of the behavior of the optical fiber under cyclic temperature loading [73], [74], [81]. They achieved a reduction in thickness of the nickel coating resulting in metallic jacketed fibers with a diameter of 350 µm [71]. The subsequent integration of these metallic jacketed fibres with FBG into an Selective Laser Melting (SLM)-manufactured part that featured a U-shaped groove (Fig. 1.6) was performed in a manual SLM test setup. In this case, pre-tensioning the fiber during the continuation of the SLM-process was required to prevent movement of the fiber due to thermally induced deformation. The cross-section after completion of the embedding shows that a good bonding was made only in the upper part of the optical fiber (Fig. 1.6). The authors pointed out that process parameters significantly impact the bonding quality, thus their adjustment is required [71]. The results of temperature measurements showed that the embedded optical fibers with the FBG were suitable as temperature sensors. However, the measuring range of the temperature was limited to 450 °C, since above this temperature delamination effects occurred between the optical fiber and the coating surrounding it [71], [74]. This was due to the different coefficients of thermal expansion of the materials. Additional strain measurements, where the embedded optical fiber was loaded in a tensile test within the linear elastic region, showed a linear response of the FBG [71].

The research was continued in [13] to investigate the integration of optical fibers into SLM-manufactured parts for high-temperature applications with temperatures up to 1000 °C. Again, the manual SLM test setup was used as in the previous works. Here, a metallic jacketed optical fiber with Fabry-Perot sensors was integrated into a SLM-manufactured part that also featured a U-shaped groove (Fig. 1.6). Before the SLM-process was resumed, the optical fiber was fixed by vacuum brazing [13]. This filled the gaps below the optical fiber that were present in the previous works. The embedded optical fiber could therefore measure temperatures up to 1000 °C with an accuracy of ± 10 °C.

Temperature sensors

The integration of thermocouples and PT100 elements in the field of temperature sensors was investigated. Thermocouples are based on the Seebeck effect, which, in addition to the Peltier effect and the Thompson effect, utilizes the thermoelectric principle [82]. In contrast to the thermocouples, PT100 elements are based

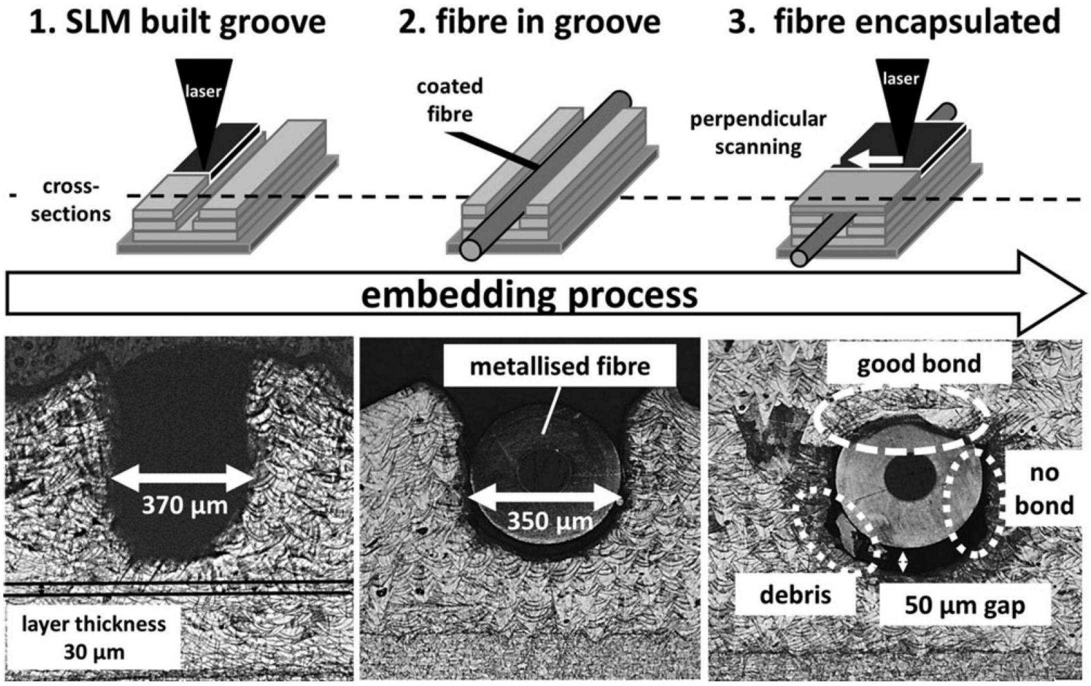

Figure 1.6: The metallic jacketed optical fibers are inserted to an U-shaped groove of an additively manufactured part that is fabricated with a manual SLM test setup. The encapsulation of the fiber is done by continuing SLM process [71].

on the thermoresistive principle [82]. A detailed explanation of the operating principles of both sensor elements is given in [82].

The feasibility of integrating commercially available thermocouples into LPBF-manufactured forming tools was demonstrated [28], [59]. In [59], a thermocouple was inserted into a cavity of the LPBF-manufactured forming tool out of tool steel (material no.: 1.2709) within a process interruption and welded to the surrounding part upon re-start of the LPBF-process. However, a systematic integration of the thermocouple was not the primary focus, hence the necessity of examining the cavity design. According to this method, thermocouples were integrated into a cavity of LPBF-manufactured molds out of tool steel (material no.: 1.2709) for injection molding in [28]. In this case, the thermocouples were positioned flush with the top layer. The result of both works is that the thermocouples survive the embedding process within the LPBF-manufactured parts and remain operational. Both works can be classified as a proof of concept, since no evaluation of the sensor performance with a reference sensor was performed.

The integration of PT100 elements into LPBF-manufactured parts made of stainless steel 316L (material no.: 1.4404) was investigated in [70]. Here, two different integration concepts were considered regarding the positioning of the PT100 element in the cavity. In the first concept, the provided cavity was not in the processing plane [Fig. 1.7(a)], thus completely concealing the PT100 element from the laser beam. The second concept consisted of a cavity that was covered by a 30 µm thick layer built by LPBF [Fig. 1.7(b)], thus providing potential for interactions between the laser and the PT100 element. Both concepts were successfully manufactured resulting in the Pt100 elements withstanding the integration process. For evaluation of the performance, the temperature of a heated surface was measured [Fig. 1.7(c)]. In this case, an additional PT100 element was used as a reference sensor. It was found that the PT100 element from the first concept showed a better performance than the PT100 element from the second concept in terms of both response time and accuracy. This is due to a possible damage of the PT100 element caused by the laser. This outcome shows that PT100 elements need to be integrated in cavities that are not in direct proximity to the laser. This issue was overcome in [83] by encapsulating a PT100 element in a casting compound, which is then integrated into an LPBF-manufactured part made out of AlSi10Mg alloy. The integration process was successful. However, the sensor exhibited a delayed response rate due to the isolation effect of the embedding.

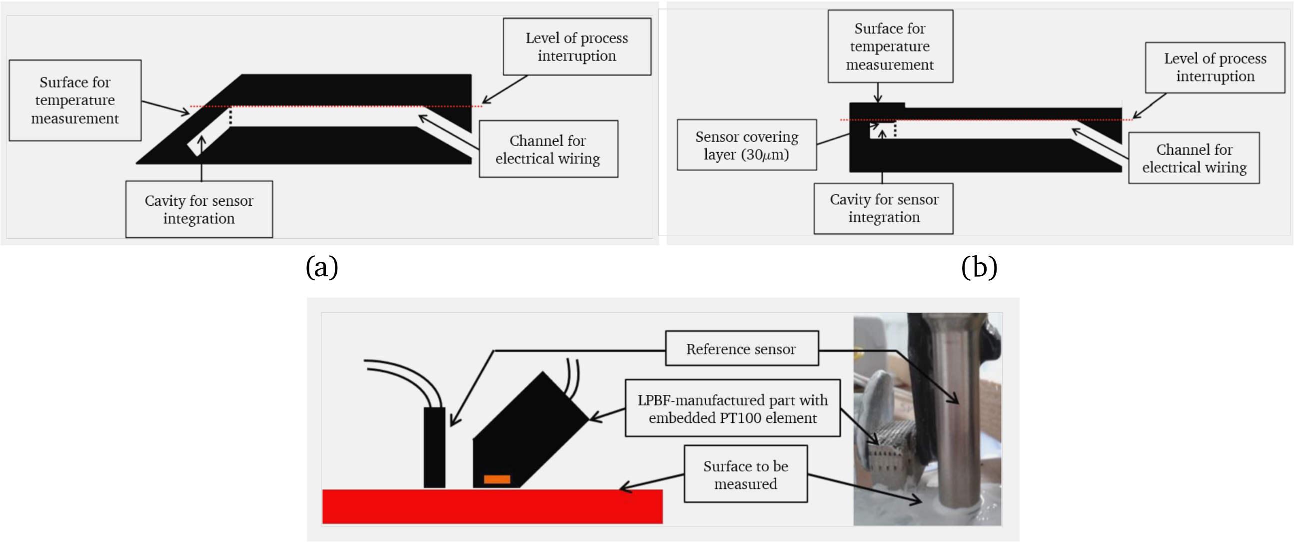

(a) (b)

(c)

Figure 1.7: PT100 elements were integrated into LPBF-manufactured parts that feature different cavities (a), (b) [70]. The performance of these embedded PT100 elements was determined by measuring the temperature of a heated surface while an additional PT100 element served as reference (c) [33].

RFID tags

RFID enables contactless exchange of data between a tag and a reading device via radio waves [76]. The tag contains stored data that can be read or overwritten by the reading device as soon as the tag is within the range of the transmission field of the reading device [84]. A distinction is made between active and passive tags, while active tags have an internal power supply such as batteries, passive tags do not require one [85]. In this case, the tag is supplied with energy through an electromagnetic field that is built by the reading device [85].

The integration of RFID tags into LPBF-manufactured parts has been investigated in several studies [76], [77], [86], with the aim of addressing applications in the areas of product identification and item management system for surgical instruments. In this context, fully embedding RFID tags into a metal part provides a major challenge, since a metallic environment has a negative impact on the transmission range [76], [86]. It was shown that RFID tags can withstand the harsh environmental conditions of the LPBF-process and can be fully embedded in stainless steel 17-4 PH (material no.: 1.4542) [77] and Inconel 718 (material no.: 2.4668) [76]. Furthermore, it was found that the wall thickness, the transmission frequency and the magnetic permeability of the material, into which the RFID tags are embedded, affect the reading distance [76]. Measurements showed that low-frequency RFID tags ($f = 125\,\mathrm{kHz}$) exhibit a read range of 7 mm even when encapsulated with metal with a wall thickness of $1.7\,\mathrm{mm}$. In contrast, the high frequency RFID tags ($f = 13.56\,\mathrm{MHz}$) could only be read when a slot was added in the LPBF-manufactured part. Thus, a readout of fully encapsulted high frequency RFID tags ($f = 13.56\,\mathrm{MHz}$) was not possible. Similar results were also found in [86]. Here, the low frequency RFID tags also performed best in terms of transmission out of a metal encapsulation. Additionally, it was found that a rectangular cavity is advantageous for integrating the RFID tags compared to a circular or polygonal cavity, as it allows for a larger read range [86].

Piezoelectric sensors

Piezoelectric sensors utilize the piezoelectric effect. This defines the interaction between the parameters of the electrical domain, such as polarization, electric field or surface charge, with the parameters of the mechanical domain, such as mechanical stresses and strains in solids [82]. This effect is reversible. On one hand, a mechanical force acting on a piezoelectric material causes a measurable surface charge. This is caused by the deformation of the piezoelectric material, which leads to a shift in charge within the crystal structure [82]. On the other hand, applying an electric field to a piezoelectric material leads to its deformation [82]. Therefore, piezoelectric materials can be employed as both sensors and actuators. A detailed explanation of piezoelectricity is given in [82], [87].

In [88], the integration of a piezo-ceramic (lead zirconate titanate (PZT)) in a Ti-6Al-4V part manufactured with Electron Beam Melting (EBM) was investigated. The method of interrupting the process and inserting the sensor element into a pre-designed cavity was also used here (called as “stop and go” process) [88]. The piezo-ceramic was placed in a ceramic housing, which served as protection for the piezo-ceramic [Fig. 1.8(a)]. This ceramic housing including the piezo-ceramic was then integrated into the EBM-manufactured part followed by the continuation of the EBM-process [Fig. 1.8(b)]. The temperature during the EBM-process was above $900\,^{\circ}\mathrm{C}$, which exceeded the Curie temperature of the piezo-ceramic of $350\,^{\circ}\mathrm{C}$. Therefore, a re-poling of the piezo-ceramic was necessary. The result of a compression test showed that the piezo-ceramic operated properly, which makes the presented method suitable for manufacturing smart parts [88]. Such an approach including the encapsulation of the sensor element is also applicable to the LPBF-process.

In the field of LPBF, the integration of a piezoelectric sensor/actuator system (SAS) in a femoral hip stem was investigated to enable an in vivo load monitoring of the implant [69]. The hip stem was manufactured from Ti-6Al-4V. The SAS was first sealed in a ceramic-metallic multi-layer structure that featured interface areas at both ends [Fig. 1.8(c)]. This sealed structure was then embedded in the LPBF-manufactured femoral hip stem during a process interruption. Subsequently, the LPBF-process was resumed and a proper connection between the interface areas of the sealed structure and the femoral hip stem was established. Besides the successful integration of the SAS, it was demonstrated that wireless power supply and data acquisition is possible.

Strain gauges

Strain gauges are one of the most fundamental sensing devices [30], and, thus, very widely used in transducers for measuring mechanical quantities [89]. The basics of strain gauges are described in Sec. 2.1. The integration of strain gauges in LPBF-manufactured metallic parts, or in additively manufactured metallic parts in general, has been investigated poorly in comparison to the previously described sensor principles [46]. The main challenge is to ensure a proper strain transmission from the LPBF-manufactured part to the strain gauge. Strain gauges also require preventive measures to protect them from the harsh process conditions, such as high process temperatures, thermally induced stresses or material splashes. However, coatings such as those used for opti-

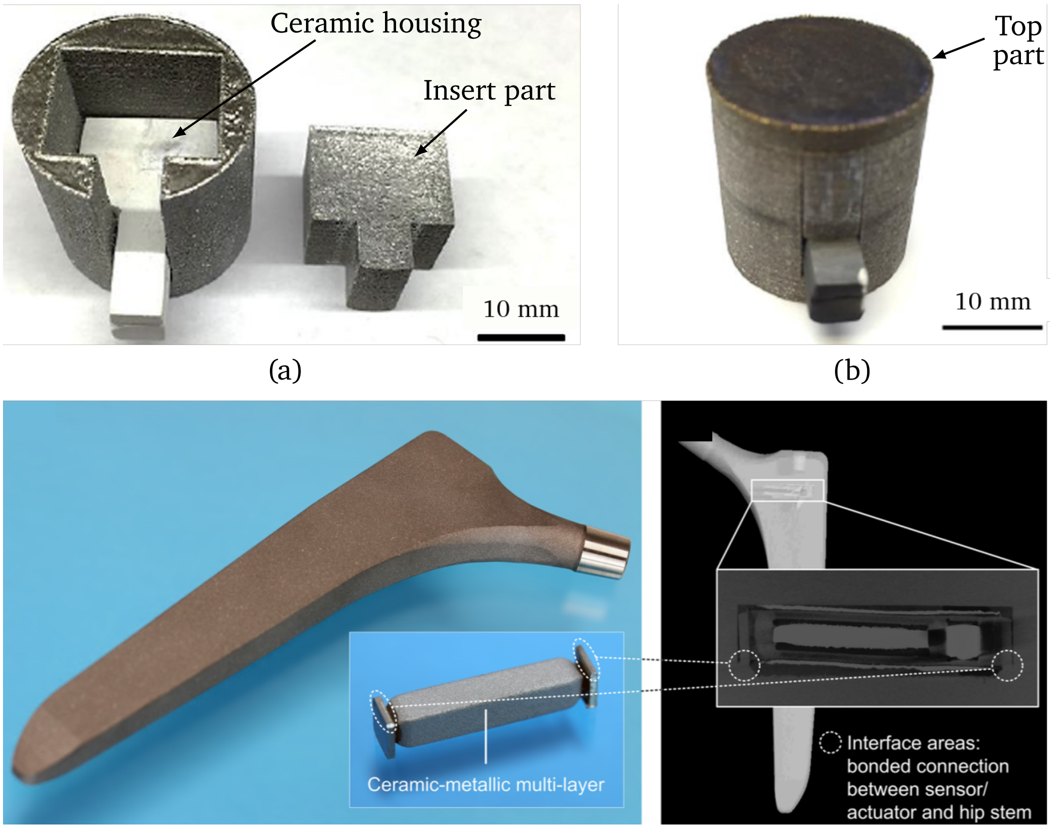

(a) (b)

(c)

Figure 1.8: The piezo-ceramic, which is encased in a ceramic housing, is integrated into the cavity of the EBM-manufactured part (a) [88]. Then, an insert part is placed into the cavity to avoid direct interaction of the electron beam with the ceramic housing and the piezo-ceramic (a). Encapsulation is achieved after continuing the EBM-process (b) [88]. The embedded sensor/actuator system in the LPBF-manufactured hip stem was sealed in a ceramic-metallic multilayer structure that featured regions for bonding it to the hip stem (c) [69].

cal fibers are not possible, as they would have a major impact on the transmission behavior of the strain gauges.

In [18], the mechanical characteristics of LPBF-manufactured parts for their use as spring elements for force sensing applications were investigated. For this purpose, the strain transmission behavior of LPBF-manufactured cantilevers (90 mm x 15 mm x 2 mm) made of steel (material no.: 1.4542) was investigated experimentally, since the strain transmission behavior determines the quality of a force sensor [90]. In order to benchmark the strain transmission behavior, and, thus, the performance of the LPBF-manufactured cantilevers, a comparison was made with a conventionally manufactured cantilever featuring the same size and material. Additionally, the dependency of the surface quality regarding different build directions (horizontal and vertical) was investigated [Fig. 1.9(a)]. The results showed that the horizontally built samples (x-y) exhibit a lower surface roughness than the vertical built samples (z). However, the residual stress of the horizontal built samples was significantly higher and led to a higher deflection compared to the vertical built samples [Fig. 1.9(b)]. The strain transmission behavior of the vertically built sample with an applied strain gauge, which was determined by loading the sample in a 4-point flexure test [Fig. 1.9(c)], showed a linear behavior. In fact, the linearity deviations of both the vertically built LPBF-sample and the conventionally manufactured reference sample were within ± $0.03\,\%$. At the same time, no significant hysteresis was found.

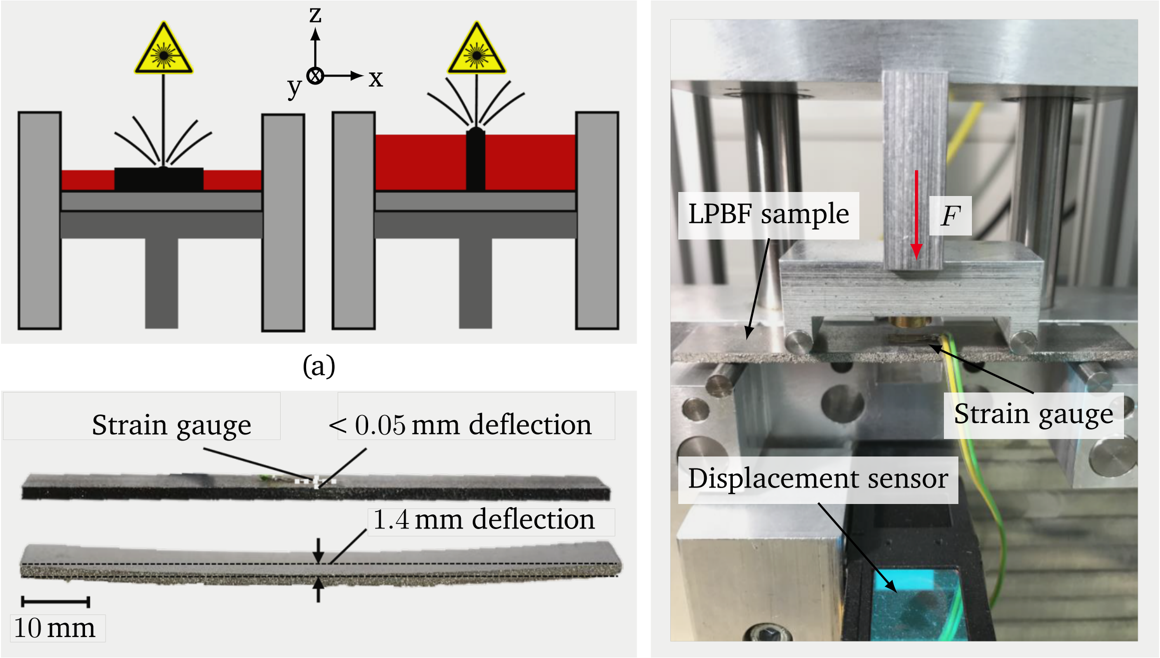

(a)

(b)

(c)

Figure 1.9: LPBF-manufactured samples with different built directions (a) [18]. The higher residual stress of the horizontally built sample than that of the vertically built sample lead to a larger deflection of the sample (b) [18]. The evaluation of the strain transmission behavior of the vertically built LPBF-manufactured sample was performed in a 4-point flexure test (c) [18].

The first known work that investigated the integration of strain gauges into LPBF-manufactured parts is from 2019 [28]. Here, an approach based on a designed cavity is presented, in which a high temperature weldable strain gauge (type: KHCD-5-200-G11 C2M, Kyowa, Tokio, JPN) can be integrated. These special and relatively expensive strain gauges are fixed on a small plate that can be spot welded to a component to be measured. The concept of integration is tested only with “dummies made of chromium-nickel steel” as stated in [28] and not the real strain gauges. However, a detailed description of the embedding procedure of this dummies is also not presented. Despite these issues, this work is linked to the statement of a successful embedding of strain gauges into LPBF-manufactured parts in subsequent literature.

Based on this work, the integration of weldable strain gauges (type: LS31 HT, HBK, Darmstadt, DE) into LPBF-manufactured tension rods made of AlSi10Mg (material no.: 3.2382) was also investigated in [91]. The tension rod exhibited a proper cavity for the integration of the weldable strain gauge. For bonding the metal plate (material no.: 1.4016) of the weldable strain gauge to the LPBF-manufactured tension rod, different configurations of welding seams were tested using the LPBF-process [Fig. 1.10(a)]. The tests showed that with a triple scanning, the weld seams with a length $l = 1.5\,\text{mm}$, a width $w = 0.8\,\text{mm}$ and a height $h = 0.8\,\text{mm}$ provided the strongest bond. A tensile test with five repetitions was conducted with the LPBF-manufactured tension rod to evaluate this concept and test the bonding strength between the strain gauge and the tension rod [91]. The tensile tests showed that the force is transmitted from the LPBF-manufactured tension rod to the integrated strain gauge. Although a linear behavior is present over a certain load range, there are also noticeable kinks that have not been explained, and, thus, need further investigations [Fig. 1.10(b)]. Moreover, deviations within the five test runs as well as a certain hysteresis are recognizable.

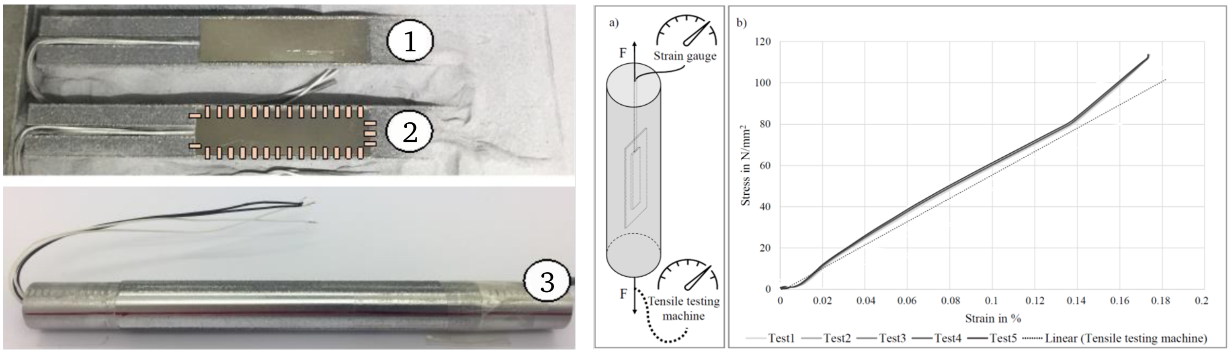

(a) (b)

Figure 1.10: The weldable strain gauge is inserted into a cavity of the LPBF-manufactured tension rod and bonded to it with welding seams that are created using the LPBF-process (a) [91]. Tensile tests show that a force transmission from the LPBF-manufactured tension rod to the integrated strain gauge is ensured, while some kinks are present in the data measured (b) [91].

1.1.3 Impact of the interruption of the LPBF-process

All of the approaches presented so far for integrating sensors into LPBF-manufactured parts require the extension of the LPBF-process in terms of interrupting the manufacturing process. During this interruption, the process chamber is opened, a sensor is inserted into a designed cavity, and the process is then resumed. This results in the LPBF-manufactured part being subjected to temperature fluctuations in addition to the influence of the missing inert gas atmosphere on the bonding locations or bonding layers [91]. Thus, there is a discontinuity in the fabrication of the LPBF-manufactured part that might affect the mechanical properties of it.

This was investigated with tensile specimens made from different materials [29], [91], [92]. In all works, multiple tensile specimens were built up horizontally and vertically, in which an interruption of the LPBF-process was conducted at medium height of the specimens. During this interruption of the LPBF-process, which lasted 40 [91] or 60 minutes [29] depending on the study, the process chamber was opened to allow the specimens to be in contact with ambient air. This corresponds to the procedure that occurs during the integration of sensors. In order to evaluate the mechanical properties, additional tensile specimens were manufactured without interrupting the LPBF-process that served as reference. The tensile tests of the specimens made of steel 316L (material no.: 1.4404) revealed that the interruption of the LPBF-process significantly influences the mechanical properties [29]. The ultimate tensile strength R_m of the horizontal and vertical built specimens with interruption of the LPBF-process were decreased by $11.5\,\%$ and $17.5\,\%$, respectively, in relation to the corresponding reference specimens without interruption. The same effect is recorded for the yield strength $R_{\mathrm{p}0.2}$ that showed a decrease of $13\,\%$ and $18.5\,\%$ for the horizontal and vertical built specimens, respectively. Further evaluations revealed that the locations of failure were distributed randomly, therefore not necessarily caused by the interruption of the LPBF-process itself. However, in some cases of the vertically built specimens, the location of failure was in direct vicinity of the location of the process interruption, but fractographic analysis showed bonding defects here. Consequently, even though the location of the failure is not directly negatively affected by the interruption of the LPBF-process itself, it does have a negative effect on the homogeneity of the powder layer when resuming the LPBF-process [29]. This in turn increases the probability of occurrence of lacks of fusion, which may cause a weak bonding [29]. These findings were also encountered in experiments with tensile specimens made of AlSi10Mg (material no.: 3.2382), which were also built horizontally and vertically including an interruption of the LPBF-process [92]. The tensile strength of the specimens with interruption of the LPBF-process decreased by 10 % compared to the reference specimen without interruption of the LPBF-process. The potential contributors to the reduced strength of specimens that are subjected to an interruption of the LPBF-process include oxidation on the surface of the manufactured part once the process chamber is opened as well as varying layer thicknesses in the bonding area [29], [91], [92].

1.1.4 Conclusion

The state of the art shows that AM-processes take a key role in manufacturing smart parts, which provide SHM and promote digitalization when used as structural integrated sensors. This is mainly based on the layer-by-layer build-up characteristic of the AM-processes. This characteristic offers not only the possibility to manufacture complex geometries but also to integrate a sensor, or more generally an external component, into the interior of a part during its manufacturing. In the field of research, the integration of various sensors, such as thermocouples, optical fibers with FBG and RFID tags has been demonstrated. In this context, the LPBF-process is considered as a promising technology for the integration of sensors into additively manufactured parts due to its homogeneous process conditions and the possibilities to realize a high geometric resolution as well as favorable mechanical properties. Moreover, the technical relevance of the LPBF-process for the industry, which is judged with a technology readiness level (TRL) of 6 to 7 according to [93], motivates the extensive research effort of integrating sensors into LPBF-manufactured parts.

The presented approaches for the integration of sensors into LPBF-manufactured parts show that a direct interaction of the laser beam and the integrated sensor should be avoided to prevent damaging the sensor. It was found that methods such as additional protective coatings or the integration of sensors in cavities that are not located directly in the processing plane provide a successful embedding of the sensors. Thus, the sensors maintain their functionalities. In this context, the integration of strain gauges has been investigated rather poorly compared to the other sensors despite the fact that additively manufactured metallic parts with integrated strain sensing elements are essential for monitoring mechanical loads. The main challenge is to ensure a proper strain transmission from the LPBF-manufactured part to the strain gauge. Thus, strain gauges can not simply be placed into a cavity of an LPBF-manufactured part. At the same time, a direct application of strain gauges in the cavity of an LPBF-manufactured part is a challenging task due to the powder environment. The approaches with integrated optical fibers with an FBG for strain sensing have the drawback of a required pre-stress of the optical fibers by means of a high effort [91], [94]. It is important to emphasize that the approaches presented regarding the integration of the optical fibers were implemented on a LPBF test setup that provides good accessibility, whereas in commercially available LPBF machines this is severly restricted [94]. Additionally, the nickel coating of the optical fiber, which serves as a protective layer against the harsh process conditions and enables a connection to the LPBF-manufactured part, is very labour-intensive [94]. Consequently, the development of a systematic approach that makes the integration of strain gauges into LPBF-manufactured parts feasible would provide significant added value. However, this systematic approach needs to include a method by which any type of strain gauge, i.e., not only limited to weldable strain gauges as in the state of the art, can be integrated into LPBF-manufactured parts. The benefits of this approach include the realization of complex geometries, a high degree of customizability and an increased reliability due to the encapsulation of the strain gauges, which provides significantly better protection against environmental influences (e.g. moisture). These features are particularly advantageous in areas such as medical technology as well as structural and system monitoring.

1.2 Disruptive manufacturing method

Conventional force sensors are generally based on measuring the strain of a specially designed deformation element, which deforms in response to the force applied to it. In most cases, the strain is measured using strain gauges, especially for static measurements. The deformation element is usually manufactured from a solid material by machining, which is in most cases steel or aluminum. Subsequently, a heat treatment is performed to relieve manufacturing-related material stresses. Finally, the strain gauges are manually applied to the deformation element, electrically contacted and then sealed with a silicone rubber or sealing compound. The conventional approach exhibits several drawbacks:

- There are restrictions in the design of the deformation element due to conventional manufacturing processes. Thus, manufacturing of deformation elements that feature complex geometries is either not possible or only possible with increased effort, which hampers the integration of the sensor into the force flow of certain applications. The same applies to the implementation of additional features in the deformation element such as a mechanical overload protection.
- Miniaturization is limited by tool paths during manufacturing of the deformation element as well as the required installation space for electrical contacting and encapsulation of the strain gauges.
- The geometry of the deformation element is decisive for the measuring range. At the same time, the manufacturing tolerances of the monolithic manufacturing affect the measurement uncertainty of the sensor negatively.
- The encapsulation with silicone rubber primarily serves to protect the strain gauges against moisture. In harsh environments such as industrial plants or challenging cleaning processes such as sterilization in medical technology, the long-term stability of the encapsulation is not guaranteed. Consequently, this type of encapsulation does not provide sufficient protection for the strain gauges in theses cases.

These drawbacks are circumvented using the LPBF-process, which allows manufacturing metallic deformation elements economically in small quantities that feature complex geometries. Currently, a systematic and reproducible approach for integrating strain gauges into LPBF-manufactured parts is lacking, which enables the development of structural integrated force sensors that offer a high degree of individualization. This is exactly the main objective of the project *Structural integration of force sensors by selective laser melting (AddKraft)*, which is funded by the German Research Foundation (DFG). This project is a collaboration between the Measurement and Sensor Technology Group (MUST) at Technical University of Darmstadt and the Institute for Production Management, Technology and Machine Tools (PTW) at Technical University of Darmstadt. A very promising approach to integrate strain gauges into LPBF-manufactured parts is based on a measuring element carrier onto which the strain gauges are applied. This measuring element carrier is a conventionally manufactured steel plate, which exhibits a low surface roughness. This allows implementing the commonly used method for integrating sensors into LPBF-manufactured parts from the state of the art (Fig. 1.5). First, a base body is manufactured by LPBF, which contains a suitable cavity for the measuring element carrier [Fig. 1.11(a)]. Once the cavity is manufactured, the LPBF-process is interrupted. During this interruption, the measuring element carrier with applied strain gauges is inserted upside down into the partially manufactured deformation element [Fig. 1.11(b)]. Subsequently, the LPBF-process is resumed to enable the embedding of the strain gauges as well as finalizing the design of the force sensor [Fig. 1.11(c)]. In this process, a material connection is made between the LPBF-manufactured base body and the inserted measuring element carrier by the LPBF-process. This enables a force flow from the LPBF-manufactured base body to the inserted measuring element carrier, which causes both to deform under an applied force. As a result, the strain of the measuring element carrier is measured by the strain gauge, and, thus, enables force sensing.

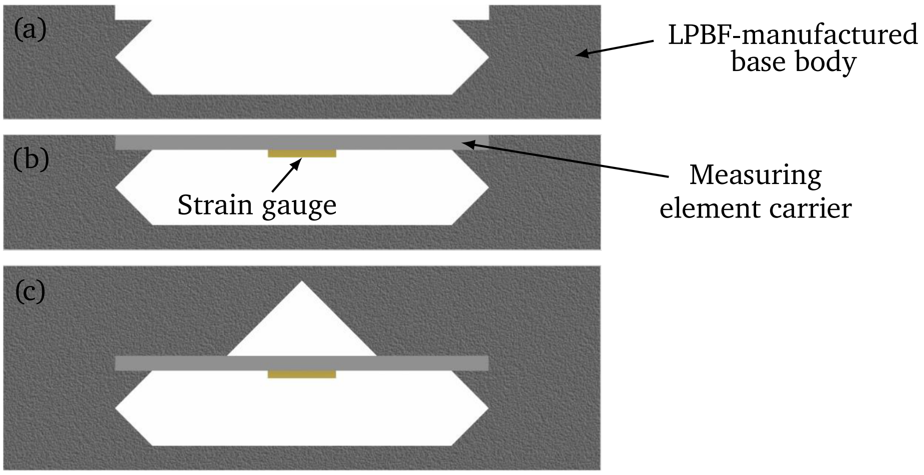

Figure 1.11: Disruptive approach to integrate strain gauges into LPBF-manufactured parts. First, a base body containing a suitable cavity is manufactured by LPBF (a). Then, the measuring element carrier with applied strain gauges is inserted to the cavity (b). Finally, a material connection is between the LPBF-manufactured base body and the inserted steel plate is made by the LPBF-process (c).

This method of integrating strain gauges into LPBF-manufactured parts through a measuring element carrier provides many advantages. Primarily, the measuring element carrier allows the strain gauges to be positioned away from the processing area. The material connection by LPBF is made with the measuring element carrier, thus the strain gauges are protected to some extent from the high energy input due to the laser radiation and the corresponding heat formation. In addition, the measuring element carrier facilitates the application of the strain gauges. In contrast to the conventional approach, in which strain gauges are applied sometimes on curved surfaces or in narrow installation spaces depending on the geometry of the deformation element, the flat measuring element carrier offers a defined surface without restrictions in terms of accessibility. The flat surface also provides the potential for an automated application of the strain gauge in the future. Furthermore, the surface roughness of the measuring element carrier is lower than that of LPBF-manufactured parts, which is typically in the range of 11 µm to 16 µm [46]. This allows reliable application of the strain gauges on a defined surface, which in turn ensures proper strain transmission to the strain gauges. Consequently, the uncertainty of measurement will be improved. Finally, favorable spring properties of the deformation element can be achieved by selecting a suitable material for the measuring element carrier.

This approach of integrating strain gauges into LPBF-manufactured parts breaks and re-arranges the well-known state of the art assembly sequence of force sensors (Fig. 1.12). Instead of manufacturing a deformation element monolithically (i.e., final design from solid material) and then applying strain gauges, only a part of the deformation element is manufactured first by LPBF. The strain gauges are then integrated into this part, and the final shape of the force sensor is achieved by continuing the LPBF-process. Therefore, this method, which is published as a patent application (DE 10 2020 124 707.9), is termed *disruptive manufacturing method* in this thesis.

1.3 Original work and contributions

Although this disruptive approach offers many benefits regarding the integration of strain gauges into LPBF-manufactured parts, however, further research effort is needed to resolve the following issues:

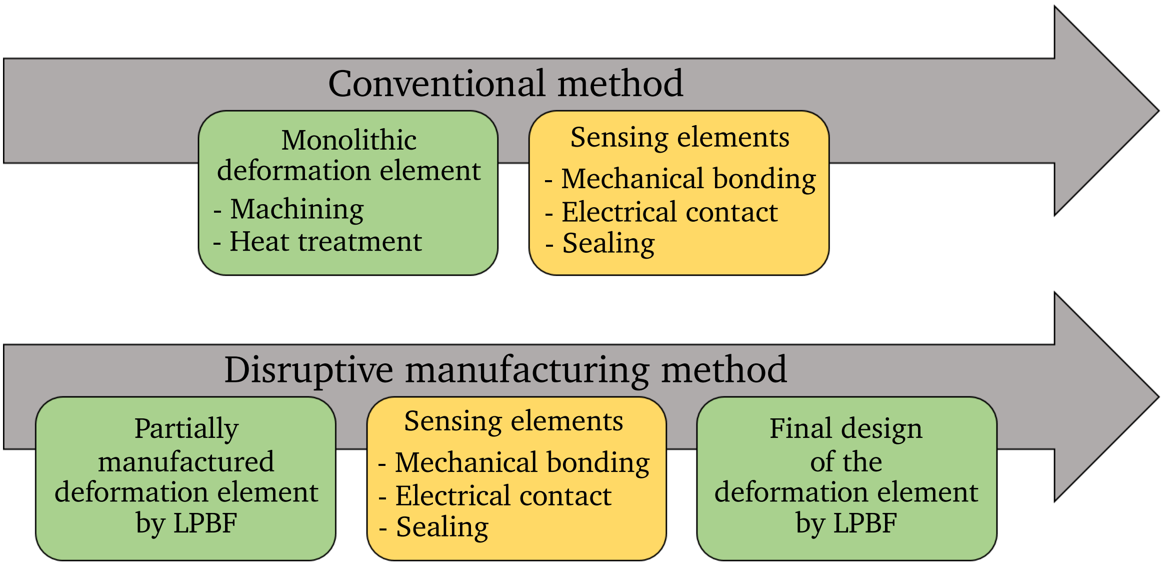

Figure 1.12: Comparison of the conventional and disruptive manufacturing method for the design of force sensors. The disruptive manufacturing method breaks and re-arranges the assembly sequence of force sensors known from the state of the art, since the final design of the deformation element (green boxes), or the force sensor, is done only after the integration of the sensor elements (yellow boxes).

- Is a damage-free integration of the measuring element carrier with sufficient process stability possible?
- Is it possible to ensure a reproducible strain transmission between the LPBF-manufactured base body and strain gauges that are applied to the inserted measuring element carrier?
- Is the performance of the LPBF-manufactured deformation elements with the inserted measuring element carrier equivalent to that of conventionally manufactured deformation elements regarding the strain transmission?
- Is a sufficiently accurate modeling of the structural mechanical behavior of the LPBF-manufactured deformation element possible despite the anisotropic character of LPBF-manufactured parts?
- Can the strain gauge withstand the LPBF-process, especially the arising temperatures?
- How does the LPBF-process and the resulting thermally induced stresses, which lead to a deformation of the measuring element carrier, influence the behavior of the strain gauge?
- Is it possible to control the thermally induced stresses in the deformation element caused by the LPBF-process?
- What is a suitable geometry of the LPBF-manufactured deformation element with integrated strain gauges, since the schematically shown geometry (Fig. 1.11) is too stiff, and, thus, allows less deformation of the measuring element carrier?

These unresolved issues need to be investigated and mastered in order to provide the means to manufacture customized structural integrated force sensors based on LPBF. In this context, these unresolved issues are divided between the two research groups within the collaborative project. The development of the overall process for the integration of the measuring element carrier in LPBF-manufactured parts is done in cooperation. The focus regarding the identification of suitable process parameters for realizing a high process stability lies with the PTW group, which is described in [46]. This includes the investigation of relevant LPBF-process as well as geometry parameters of the deformation element to reduce the thermally induced stresses, and, thus, the deformation of the measuring element carrier during the manufacturing process. Furthermore, recommendations for the reproducible and damage-free integration of the measuring element carrier into LPBF-manufactured part are derived by the PTW group. The remaining research gaps are adressed in this thesis.

Therefore, in the author's opinion, the main contributions carried out through this thesis are:

1. Investigation of the strain transmission.

   The strain transmission behavior of the deformation element determines significantly the quality of a force sensor. Therefore, it is necessary to investigate first if a proper strain transmission from the LPBF-manufactured part to the measuring element carrier is ensured. In this work, this is demonstrated using a widely employed deformation element geometry based on a bending beam that exhibits a S-shaped deformation under load. In particular, the material bonding between the LPBF-manufactured base body and the inserted measuring element carrier as well as the behavior of the LPBF-manufactured force sensor under static load are investigated and serve quality measures for the strain transmission. The results are published in [95], [96].

2. Comparison with a conventionally manufactured reference force sensor.

   In order to provide a basis for the development of structural integrated force sensors by LPBF, the performance of the LPBF-manufactured deformation elements has to be evaluated in comparison with a reference. This is done by comparing the LPBF-manufactured force sensors to a conventionally manufactured reference force sensor with same geometry in terms of characteristic parameters such as linearity, hysteresis and temperature behavior. It is shown that the LPBF-manufactured deformation elements are competitive with conventionally manufactured deformation elements. The results are published in [96].

3. Investigation of the behavior of the strain gauges before and after being exposed to the LPBF-process.

   In order to ensure linear behavior of the structural integrated force sensors fabricated according to the disruptive manufacturing method, the strain gauges have to withstand the harsh conditions of the LPBF-process. In this work, the behavior of strain gauges before and after being exposed to the LPBF-process is compared for the first time. It is shown that the strain gauges not only survive the LPBF-process but also maintain their linear transmission characteristics.

4. Measurements during the LPBF-process.

   It is shown that the approach through the measuring element carrier protects the strain gauges from the high energy input due to the laser radiation and the corresponding heat formation. This is done by measuring both the temperature and the resistance of strain gauges during fabrication of the deformation element within the LPBF-process. Furthermore, the measurement of the resistance of the strain gauges during the LPBF-process provides a possibility to detect the formation of thermally induced stresses and resulting deformations. This can be used in further applications to reduce thermally induced stresses.

5. Derivation of a deformation element geometry for complete encapsulation of strain gauges.

   The results of the previous investigations as well as the conclusions of the work from the PTW group [46] are combined to derive a deformation element geometry that enables complete encapsulation the strain gauges using the disruptive manufacturing method. In this context, a deformation element geometry is presented, which is built upon the bending beam approach with S-shaped deformation under load. This geometry can be considered as a black box with embedded strain gauges around which the desired design can be manufactured by LPBF for various use cases.

6. Application of the findings for LPBF-manufactured parts with multi-axial force measurement.

   The disruptive manufacturing method presented enables an integration of a measuring element carrier in the form of a steel plate into LPBF-manufactured parts. Based on the layer-by-layer build-up characteristic, a material connection is only made in the processing plane. However, a possibility for realizing a double-sided force-locked connection is provided by an LPBF-manufactured cavity with an integrated thread. Unfortunately, LPBF-manufactured threads are not usable without post-processing due to a high surface roughness. Therefore, an approach is presented to optimize these threads so that they can be used without post-processing. This allows the integration of geometrically more complex measuring element carriers with multiple strain gauges applied, and, thus, enables multi-axial force measurements.

7. Investigation of a 3D-printed strain gauge based on conductive filament.

   In this work, besides the known technologies for the realization of strain gauges, an additional technology is presented and investigated. This involves employing the Fused Deposition Modeling (FDM) process to fabricate a meander-shaped structure consisting of an electrically conductive filament onto an isolating substrate. It is demonstrated that such 3D-printed strain gauges can be used in a similar way to strain gauges for experimental stress analysis by gluing them onto a loaded structure.

1.4 Structure of this thesis

This thesis is divided into seven chapters and structured as follows. A motivation for the use of AM-processes for structural integrated force sensors is given, followed by the state of the art regarding the integration of sensors into LPBF-manufactured parts. Finally, the disruptive manufacturing method for integrating strain gauges into LPBF-manufactured parts is presented, from which the research gaps are derived.

In chapter 2, the fundamentals required for better understanding this work are introduced. First, the resistive sensing principle utilized by strain gauges is explained. Based on this, different technologies for the realization of strain gauges are presented with a brief overview of their respective benefits and drawbacks. Afterwards, the basics and characteristics of the LPBF-process are explained. This also address the design guidelines and restrictions when manufacturing with LPBF as well as the thermally induced stresses.

In chapter 3, the focus lies on the strain transmission from the LPBF-manufactured base body to the inserted measuring element carrier. Here, multiple LPBF-manufactured deformation elements are fabricated according to the disruptive approach, while the strain gauges are excluded first. This means that the strain gauges are applied only after completion of the LPBF-manufactured deformation elements. This ensures that the evaluation of strain transmission from the LPBF-manufactured base body to the inserted measuring element carrier is not affected by the influence of the LPBF-process on the strain gauges. Furthermore, characteristic values of the LPBF-manufactured force sensors are compared with those of a conventionally manufactured reference force sensor.

In chapter 4, the impact of the LPBF-process on the strain gauges is discussed. In this context, the impact of the LPBF-process on the base resistance and the sensitivity of the strain gauge as well as its behavior under load is examined. Based on this, the temperature profile and the deformation profile are measured with multiple applied thermocouples as well as strain gauges along the measuring element carrier. In particular, the measurement of the resistance of the strain gauge during the LPBF-process offers a deeper insight into the formation of thermally induced stresses, and, thus, the resulting deformation of the measuring element carrier. These serve as a measure of quality for optimization approaches to reduce the thermally induced deformation of the measuring element carrier.

In chapter 5, the findings from Chapters 3, 4 and 5 are combined to develop a geometry of the deformation element that allows complete encapsulation of the strain gauges. The encapsulation results in a stiffer structure of the deformation element. In particular, it lies parallel to the measuring element carrier regarding the force flow. However, the geometry of the deformation element, and in particular the measuring element carrier, is designed in such a way that an S-shaped deformation is achieved, when subjected to a force.

In chapter 6, LPBF-manufactured threads are investigated. In this context, thread parameters are identified that can be adapted to allow the manufacturing of threads that do not require any post-processing.

The last chapter covers the conclusion of this thesis and future work packages for further investigations.

2 Fundamentals

In this chapter, the fundamentals of strain gauges are discussed. In addition to the operating principle and the transmission behavior, different technologies for manufacturing strain gauges are presented. Finally, the basics of the LPBF-process are discussed.

2.1 Resistive strain sensing

The physical quantities force, torque and pressure are not measurable directly, but only through their effect on an object [82]. In this case, these quantities cause a mechanical strain, or more generally a mechanical stress, of the object by deforming it [82], [97]. Thus, such an object is called spring element. The resulting strain of the spring element can be measured with different sensing principles. These include [98], [99]:

- resistive strain sensing,
- capacitive strain sensing,
- optical strain sensing,
- piezoelectric strain sensing,
- inductive strain sensing.

In addition to these well-established strain sensing principles, three further principles exist, which, however, are used mainly in the field of research [98]. Among them are strain sensors based on the resonance principle, the magnetoelastic effect and textile fibers [98]. In this thesis, only the resistive strain sensing principle is discussed, since strain gauges are based on it. Furthermore, this principle is most widely used for strain sensing and predominant in the field of force sensing [99], [100]. The remaining principles are discussed in [98], [99], [101].

2.1.1 Basics and history

Resistive sensors are based on the correlation between the measured quantity and the slope of the electrical current-voltage characteristic that defines the electrical resistance R (Fig. 2.1). These sensors are used commonly to measure physical quantities such as temperature T, pressure p, force F, torque M, displacement ξ and angle φ [82], [97]. Thus, they belong to the group of electromechanical sensors and are the dominating measuring principle there [82], [97], [100].

In case of resistive strain sensors, the measured quantity corresponds to the strain ε that results from a spring element being subjected to physical quantities such as a force or torque. This strain is translated into a corresponding resistance R by means of a sensing element, which is in most cases a strain gauge [101]. The common measuring chain consists of converting this resulting resistance R into a voltage U, which is preprocessed in analog and then digitalized with an Analog-to-Digital-Converter (ADC) to provide a measured

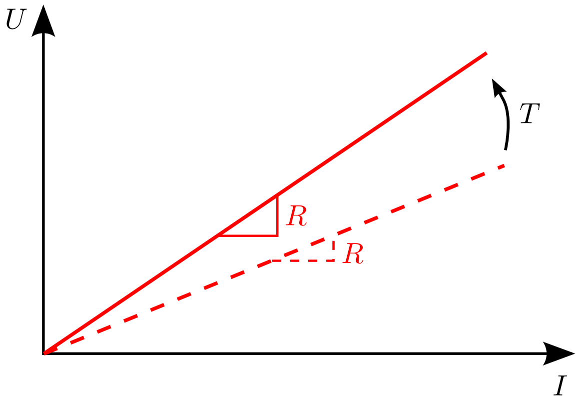

Figure 2.1: The physical quantity to be measured (e.g. a temperature T) leads to a change in the slope of the electrical current-voltage characteristic of resistive sensors.

output X (Fig. 2.2).

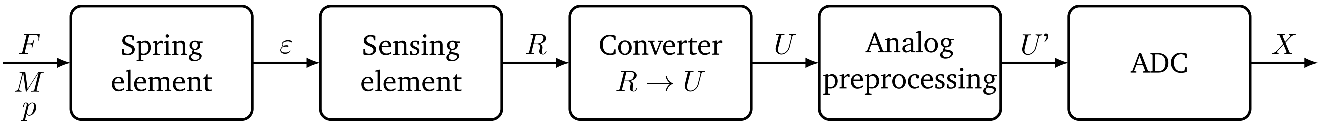

Figure 2.2: Measuring chain for the evaluation of resistive strain sensors. The sensing element is in most cases a strain gauge. This figure is adapted from [97].

A strain gauge is, in its simplest form, a piece of metal or a metal wire that changes its resistance when subjected to a mechanical load. This behavior was first discovered by Sir William Thomson (Lord Kelvin) in 1856, where he made two major findings [102]. First, he found that the electrical resistance of a metal wire changes proportionally by a value ΔR as a result of a change in length Δl caused by a tensile load. Second, he observed that different changes in resistance occur in geometrically identical wires made of different materials. His conclusions were that both the geometry of metal wires and their conductivity depending on the material would have to change, when being subjected to a mechanical load [97], [102]. Bridgman built on these findings by conducting systematic investigations of the resistance behavior of metals and alloys in different stress states from 1915 [103]–[106]. His investigations confirmed that mechanical loading of metals or alloys results in changes in geometry and material-dependent conductivity. In 1935, this effect was named *piezoresistance* by Cookson [107]. The term originated from the greek term *piezen*, which means to press [97], [108].

Based on these findings, efforts were made to utilize this phenomenon as a sensory effect. This was the birth of strain gauges, which took place during 1936 and 1938 [106]. During this period, Simmons and Ruge applied metal wires that were embedded a sticky carrier to various components to provide stress analysis [97], [106], [109], [110]. Subsequently, a huge number of investigations have been carried out by various researchers over the years, resulting in the development of strain gauges for a wide range of applications [106] with the well-known linear characteristic

$$\frac{\Delta R}{R_0} = k \cdot \frac{\Delta l}{l_0} = k \cdot \varepsilon, \tag{2.1}$$

where ΔR describes the change in resistance, R_0 describes the base resistance, k describes the gauge factor or sensitivity and ε describes the strain, which is defined by the change in length Δl referred to the l_0 initial length. A short time later, between the years 1948 and 1952, Jackson realized the possibility of manufacturing strain gauges based on a lithographically structured metal foil [89], [106], [111]. This idea originated with the emerging technique of printed circuit boards (PCB), in which a laminated copper foil was structured using photo-chemical etching techniques [111]. He used this method to produce the first metal foil strain gauges, as they are still commonly sold and used nowadays. In the following course, further properties were discovered, such as the cross-sensitivity, which leads to a nonlinearity of the resistance-strain behavior, or the temperature dependency of the sensitivity and the zero point [106].

2.1.2 Static transfer behavior

A mechanical load acting on a spring element on which a strain gauge is applied causes a strain which leads to a measurable change in the resistance ΔR of the strain gauge. In the following, the static transfer behavior of a strain gauge is examined in more detail to describe the occurring change in resistance that results from a mechanical load. Thereby, it can be shown that the change in resistance is based on two parts: a geometrical part, which occurs from the change in shape of the strain gauge, and a material specific part. For this purpose, a metal conductor piece, which is deformed by a tensile force (Fig. 2.3), serves as basis for determining the change in resistance.

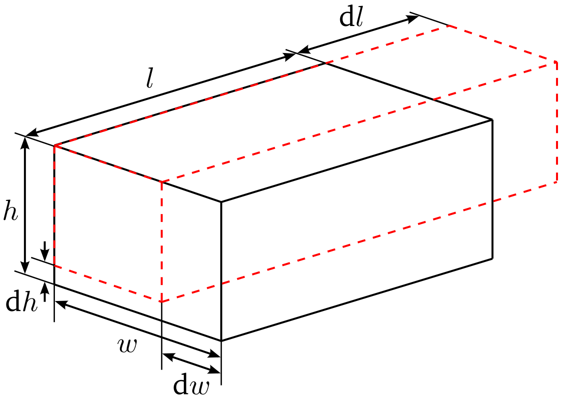

Figure 2.3: Mechanical loading of a metal conductor piece when subjected to tensile force leads to an increase in length l and, at the same time, to a decrease in both width w and height h (dashed in red) [82].

The electrical resistance R of this metal conductor piece (Fig. 2.3) in its initial state is [82], [89]

$$R = \rho \cdot \frac{l}{A} = \rho \cdot \frac{l}{w \cdot h}, \tag{2.2}$$

where ρ denotes the resistivity, l denotes the length and A denotes the cross section, which is determined by the width w and height h. When a tensile force is applied to the piece of conductor, an elongation occurs at the same time as the cross section is reduced (Fig. 2.3). Consequently, the resistance changes. Therefore, for sensory purposes, only the change against the initial state is of interest [97]. This change in resistance (Eq. 2.3) is determined through formation of the total differential and normalization to the initial state assuming a constant and gradient-free strain [82], [89], [98].

$$\frac{\mathrm{d}R}{R} = \left(\frac{\partial R}{\partial \rho} \cdot \mathrm{d}\rho + \frac{\partial R}{\partial l} \cdot \mathrm{d}l + \frac{\partial R}{\partial w} \cdot \mathrm{d}w + \frac{\partial R}{\partial h} \cdot \mathrm{d}h\right) \cdot \frac{w \cdot h}{\rho \cdot l} \tag{2.3}$$

$$= \underbrace{\frac{\mathrm{d}\rho}{\rho}}_{\substack{\text{material}\\ \text{specific}}} + \underbrace{\frac{\mathrm{d}l}{l} - \frac{\mathrm{d}w}{w} - \frac{\mathrm{d}h}{h}}_{\text{geometrical}}. \tag{2.4}$$

From equation 2.4, it can be seen that the relative change in resistance consists of a material-specific component and a geometric component. By introducing the strain $\varepsilon = \mathrm{d}l/l$ and the transverse contraction ν, which is the ratio between transverse strain and longitudinal strain or, in other words, the change of the transverse area to the change of the length, the sensitivity k (gauge factor) is determined for a uniaxial loading case [82], [89]

$$\frac{\mathrm{d}R}{R} = \frac{\mathrm{d}l}{l} \cdot \left(1 - \frac{\mathrm{d}w/w}{\mathrm{d}l/l} - \frac{\mathrm{d}h/h}{\mathrm{d}l/l} + \frac{\mathrm{d}\rho/\rho}{\mathrm{d}l/l}\right) \tag{2.5}$$

$$= \varepsilon \cdot \left(1 + 2\nu + \frac{\mathrm{d}\rho}{\varepsilon\rho}\right) = \varepsilon \cdot k. \tag{2.6}$$

In equation 2.6, the following relationships are taken into consideration using the transverse contraction [82]

$$\mathrm{d}w = -w \cdot \nu \cdot \varepsilon \quad \text{and} \quad \mathrm{d}h = -h \cdot \nu \cdot \varepsilon. \tag{2.7}$$

The resistivity ρ of a volume V is defined as [112]

$$\frac{1}{\rho} = \frac{N \cdot \gamma \cdot e \cdot \mu}{V}, \tag{2.8}$$

where N denotes the amount of atoms, γ denotes the amount of free charge carriers per atom, e denotes the charge and μ denotes the mobility of the charge carriers. Using equation 2.8 and the definition of the gauge factor k from equation 2.6, yields [112]

$$k = (1 + 2\nu) + \frac{1}{\varepsilon} \cdot \left(-\frac{\mathrm{d}(\gamma \cdot \mu)}{\gamma \cdot \mu} + \varepsilon \cdot (1 - 2\nu)\right). \tag{2.9}$$

The evaluation of equation 2.9 results in a strain-dependent gauge factor $k(\varepsilon)$, and, thus, a strain dependent sensitivity

$$k(\varepsilon) = \underbrace{2}_{\text{geometrical}} \underbrace{-\frac{\mathrm{d}(\gamma \cdot \mu)}{\varepsilon \cdot \gamma \cdot \mu}}_{\substack{\text{material}\\ \text{specific}}}. \tag{2.10}$$

Equation 2.10 provides two main findings:

- The gauge factor k is *strain-dependent* if the number of charge carriers or their mobility *changes* by a mechanical stress. In this case, the material specific component dominates and is called *piezoresistive effect*. Here, the gauge factor k is not equal to 2. This effect dominates mainly in semiconducting or polymeric materials, which feature a high piezoresistive contribution to the change in resistance with gauge factors up to 200.

- The gauge factor k is *strain-independent* if the number of charge carriers or their mobility does *not change* by a mechanical stress. In this case, the change in resistance is dominated by the change in shape, and, thus, the geometry, which is called *resistive effect*. Here, the gauge factor k is equal to 2. The independence of the gauge factor from the strain results in a perfectly linear behavior. For metals, the influence of the piezoresistive component is negligible. Thus, the resulting change in resistance is mainly based on the resistive component.

The derivation of the sensitivity shows that the change in resistance of a mechanically loaded conductor depends on both the resistive and piezoresistive effect. However, the choice of material determines which of both effects dominates. In order to realize strain gauges based on these two effects, different technologies have been developed throughout the years, which will be presented in the following.

2.2 Technologies of strain gauges

Strain gauges are used both in transducer design as well as in stress analysis applications [89]. For this purpose, several technologies have been established to manufacture strain gauges that utilize either the resistive or piezoresistive principle. The most established technologies include metal foil strain gauges, thin-film strain gauges, thick-film strain gauges and semiconductor strain gauges [82]. Especially for stress analysis, strain gauges are required as discrete components that can be applied to the surface of various loaded structures, and, thus, are suitable for structural integration. This is provided by metal foil strain gauges, which, however, are also well suited for transducer design. Therefore, metal foil strain gauges are the most widely used among the aforementioned technologies and will be used in this work. The remaining three strain gauge technologies are predominantly used in transducer design. Furthermore, another possibility for the fabrication of strain gauges based on conductive filament is presented, which was elaborated within the scope of this work.

2.2.1 Metal foil strain gauges

Metal foil strain gauges are the predominant type of strain gauges and are therefore usually referred to when the term strain gauge is used. They are used both in experimental stress analysis as well as in transducer design. In general, these strain gauges consist of a carrier foil with a thickness between $30\,\mu\text{m}$ and $50\,\mu\text{m}$ on which a metal foil with a thickness of about $5\,\mu\text{m}$ is laminated [Fig. 2.4(a)] [89], [97]. Then, the metal foil is patterned into a meander-shaped measuring grid by means of lithography to increase the length of the resistive path [89], [97]. Finally, a protective foil with a thickness of about $30\,\mu\text{m}$ is laminated onto the metal foil to protect it from environmental influences [89]. The carrier foil as well as the protective foil is typically made of polyimide or polyetheretherketone (PEEK) [89]. In most cases, the metal foil is made of a copper-nickel alloy, which due to the very low temperature characteristic of the electrical resistance of the material is called constantan [89]. This characteristic is provided by an alloy composition of $55\,\%$ copper and $45\,\%$ nickel [89]. Additionally, the temperature coefficient of the resistivity can be adjusted by adding small amounts of manganese as well as by the rolling process and the subsequent heat treatment [97]. Further advantages of constantan as a measuring grid material are a very linear and a rather low hysteresis behavior, resulting in an almost strain-independent change in resistance [89]. This results in a gauge factor k of about 2, which in turn implies that constantan has a very low amount of piezoresistivity that was first found by KUCZYNSKI in 1953 [106].

Meanwhile, metal foil strain gauges are being manufactured in a great variety of designs as well as sizes, which have been optimized according to the respective application of measurement [Fig. 2.4(b)]. Manufacturers of such metal foil strain gauges are, for example, HBK (Darmstadt, DE), Vishay Micro-Measurements

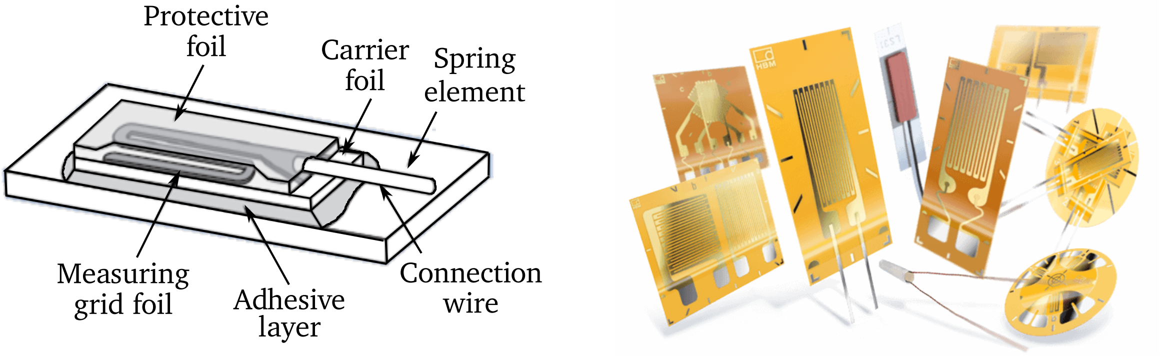

(a) (b)

Figure 2.4: Layer structure of a metal foil strain gauge bonded to a springt element [image source: www.dms-technik.de] (a); Various commercially available designs of metal foil strain gauges [image source: www.hbkworld.com] (b).

(Wendell, North Carolina, US) or Kyowa (Tokyo, JPN). The most basic design is the linear strain gauge, which features one measuring grid on a carrier in the longitudinal direction. Common base resistance values R_0 are $120\,\Omega$, $350\,\Omega$, $700\,\Omega$ and $1000\,\Omega$. Although higher base resistance values are advantageous in terms of power consumption and manufacturing tolerances, they also entail a poorer Signal-to-noise ratio (SNR). In order to use these metal foil strain gauges, they need to be bonded to a spring element by means of special adhesives that have been optimized for a nearly loss-free strain transfer [89]. These adhesives are mostly based on epoxy and phenolic resins, providing a thickness of the adhesive layer ranging from $5\,\mu\mathrm{m}$ to $30\,\mu\mathrm{m}$ [98], which, however, also depends on the manual application.

There are different spring element designs available depending on the measurement range and accuracy of the force sensor being designed, which can be categorized according to the type of stress (bending, tension/compression, shear) that the spring element is subjected to (Fig. 2.5). Spring elements based on the bending principle are particularly suitable for small and medium forces of approximately $1\,\mathrm{N}$ to about $50\,\mathrm{kN}$ and provide the highest accuracy [82]. For larger forces from $20\,\mathrm{kN}$ up to several MN, spring elements based on the shear or compression principle are used [82]. Steel or aluminum are frequently used as materials for the spring element [89]. In general, it is beneficial to consider that the spring element material features a homogeneous microstructure, high elastic deformability, good creep behavior, low hysteresis as well as a low temperature coefficient of Young's modulus [113]. The spring element needs to be designed such that deformation occurs primarily when the force is applied in the specified loading direction. In this context, the aim is to realize areas within the spring element that allow positive and negative surface strains, i.e., areas with elongation and compression, of about $\pm\,1000\,\mu\mathrm{m\,m^{-1}}$ when the nominal load is applied [82]. This allows two strain gauges to be bonded into each of the elongated and compressed areas, thus obtaining a full-bridge configuration, which will be discussed in more detail in Sec. 2.4. In the following, further key properties and disturbance variables of metal foil strain gauges are discussed, which influence the accuracy of force sensors built with them.

Sensitivity

The sensitivity of a sensor describes the ratio of the change in the output of the sensor and the input that causes this change. In case of metal foil strain gauges, a strain ε causes a change in resistance ΔR, thus the

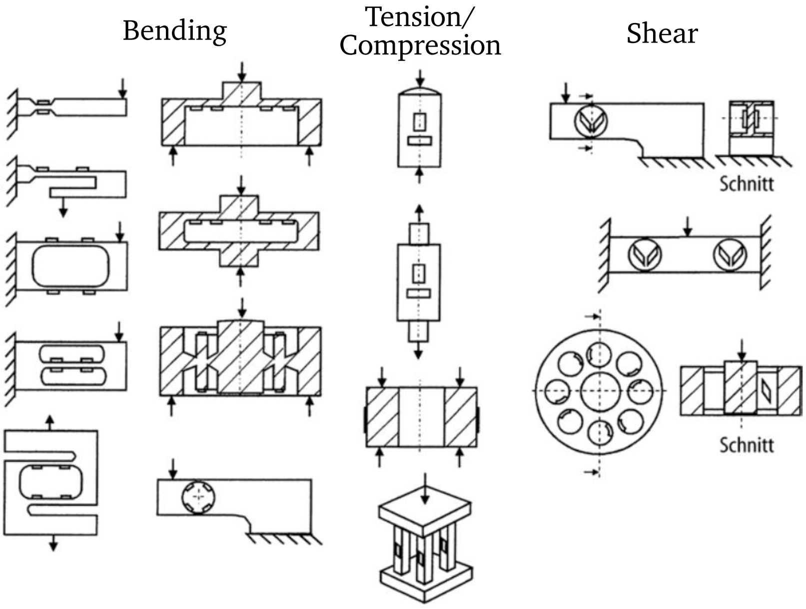

Figure 2.5: Spring element designs for strain gauge based force sensors. The graphic is taken from [82].

following relationship is valid [89]

$$\frac{\Delta R}{R_0} = k \cdot \varepsilon, \tag{2.11}$$

with R_0 as the base resistance and k as the gauge factor or sensitivity. In Sec. 2.1.2 it has been shown that for a metallic conductor the change in resistance is dominated by the change in shape, and, thus, the geometry, resulting in a gauge factor k of 2. This is valid only in approximation for metal foil strain gauges, since on one hand there is a marginal amount of piezoresistive effect even with constantan, and on the other hand a metal foil strain gauge is not made of a rectangular conductor but of a meandering shape with reverse loops. These reverse loops affect the sensitivity of the metal foil strain gauge due to transverse strain [106]. However, this effect is minimized in modern metal foil strain gauges, resulting in a cross-sensitivity of less than $1\,\%$ in most cases [89]. This results in gauge factors of metal foil strain gauges in the range of 1.8 to 2.2 [97]. The choice of the measuring grid material, which in this case is metal, limits the sensitivity. However, this is taken into account, since metals as measuring grid material are associated with a lower temperature sensitivity and high linearity [82].

Temperature behavior

The main disturbance variable for a strain gauge is temperature [114]. A change in temperature causes two effects, which influence the output signal of the strain gauge. First, a temperature-related change in resistance of the strain gauge occurs that superimposes the actual strain-based change in resistance ΔR [89]. This temperature-related change in resistance ΔR_T is based on one hand on the temperature coefficient of the resistance α_R [89], which causes a change in resistance with temperature of every electrical conductor. Although this effect is small due to the choice of a suitable material for the measuring grid such as constantan, it is still undesirable. On the other hand, the difference in the thermal expansion coefficients of the measuring grid α_M and the spring element α_S also enhance the temperature-induced change in resistance [89]. Thus, thermal expansion of the spring element forces elongation or compression of the strain gauge, depending on which thermal expansion coefficient predominates. This temperature-related change in resistance of these two sources is independent of the strain to be measured due to a force acting on the spring element and leads to a change in the zero signal of the strain gauge. Therefore, this is referred to the temperature coefficient of the zero point TK_0 [89]. The second effect that occurs due to a change in temperature is the change in sensitivity of the strain gauge, since the gauge factor k is temperature dependent [89]. In the case of constantan as the material of the measuring grid, the gauge factor increases with increasing temperature due to its positive temperature coefficient α_k. Thus, an increase of the output signal with increasing temperature can be observed at a constant strain. Therefore, this is referred to the temperature coefficient of sensitivity TK_C [89]. Additionally, the Young's modulus of the spring element material also exhibits a temperature dependency, which means that metallic spring elements deform more under constant load but increasing temperature. The result is also an increasing signal that is detected.

In order to minimize the influence of changes in temperature, compensation measures are taken by the manufacturers. In this process, the temperature coefficient of the resistance α_R is adjusted by the rolling process of the measuring grid foil such that it almost compensates for the influence of α_M, α_S and α_k while retaining only a small residual error [97]. Thus, strain gauges can be fabricated to match specific spring element materials and are therefore called self-compensating strain gauges [89]. Typical values for the TK_0 of metal foil strain gauges are $-30 \times 10^{-6}\,\mathrm{K}^{-1}$ to $30 \times 10^{-6}\,\mathrm{K}^{-1}$ [97] while the TK_C ranges from $100 \times 10^{-6}\,\mathrm{K}^{-1}$ to $200 \times 10^{-6}\,\mathrm{K}^{-1}$ [97].

Humidity

Humidity has a negative effect with regard to the performance of the metal foil strain gauges. This can lead to the formation of shunt resistors, which in turn decrease the insulation resistance [113]. Additionally, fluctuations of the humidity cause a long-term drift of the signal measured [113]. In general, the impact of humidity increases with a larger base resistance [113]. In order to minimize the influence of humidity on the strain gauge, and, thus, on the measurement, the strain gauges need to be sealed with protective coatings [89]. For this purpose, various protective coatings and silicone rubbers are commercially available.

Creep

Metal foil strain gauges exhibit creep when elongated for a long period of time. The main reason are occurring relaxation phenomena of the carrier material and adhesive layer, which cause an enlargement of the transition zones of the reverse loops of the measuring grid [89]. This causes a reduction in the restoring force of the measuring grid, thus causing it to release to some extent [89]. As a result, the output signal changes slightly over time t in the direction of relief [Fig. 2.6(b)]. This effect is more pronounced for strain gauges with a short measuring grid length than for strain gauges with longer measuring grid lengths, since in these cases the fraction of the reverse loops and the transition zones present there are more important for strain initiation [89]. Therefore, the creep of the metal foil strain gauge can be adapted by modifying the length u of these reverse loops [Fig. 2.6(c)]. In order to eliminate creep for accurate measurements, not only the possibility to adjust the creep behavior but also the elastic relaxation of the spring element is utilized [113]. In case of an applied load on the spring element, there is a progressive time-dependent and asymptotic strain due to relaxation of the material in addition to the spontaneous strain [Fig. 2.6(a)] [113]. Based on the fact that the creep of the spring element and the metal foil strain gauge are each in opposite directions, both effects can be used for compensation purposes. Thus, metal foil strain gauges are available with different lengths of the reverse loops in order to provide a specific creep adjustment. Basically, a smaller reverse loop corresponds to a higher stiffness, and, thus, leads to an increased creep of the metal foil strain gauge [113]. However, even with ideal creep matching, it should be noted that the thickness of the adhesive layer and the temperature also contribute to creep [113].

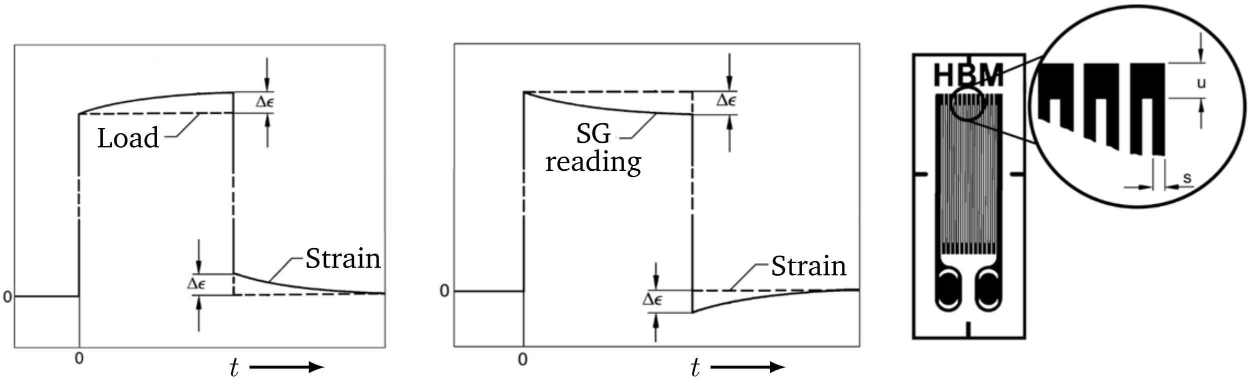

(a) (b) (c)

Figure 2.6: Creep compensation of metal foil strain gauges. The spring element features an elastic relaxation in the direction of load (a), whereas the signal of the strain gauge changes in the direction of relief due to relaxation phenomena of the carrier material and adhesive layer (b). By modifying the length of the reverse loops, the creep behavior of the strain gauge can be adapted, and, thus, provides a possibility to compensate for creep (c). The graphic is taken from [113].

2.2.2 Thin-film strain gauges

The thin-film technology enables direct deposition of layers with thicknesses below 1 µm onto metallic or ceramic spring elements using coating processes such as vapor deposition or sputtering [82]. Here, process parameters influence the homogeneity of the deposited thin-film layer. An increase of the substrate temperature, i.e. of the spring element, for example, leads to an enhancement of the diffusion processes, which results in a homogeneous structure [115]. This allows the formation of layers that either feature a crystalline structure with grain boundaries or no crystalline structure at all [115]. Thin-films with crystalline layers exhibit a very similar behavior to metal foils [97]. Thin-films without crystalline layers are known as *discontinuous* thin-films [116] enabling the fabrication of strain gauges with novel properties.

Typically, thin-film strain gauges are based on crystalline layers. In order to realize a thin-film strain gauge, first an insulating layer consisting of Al_2O_3, SiO_2 or Si_3N_4 is deposited on the spring element, which is in most cases steel [97]. Afterwards, the sensing layer is deposited, which in most cases consists of CrNi for thin-film strain gauges [97], [117]. This is followed by deposition of a conductive layer. Subsequently, both the sensing layer as well as the conductive layer are lithographically patterned to achieve a meander-shape [82], as in the case of metal foil strain gauges. Finally, the sensing layer is trimmed using laser ablation to adjust the base resistance followed by applying coating layer for protection.

Generally, thin-film strain gauges offer a high degree of miniaturizability, requiring only small areas for the deposition of the sensing layer. The thin layers and high sheet resistances result in base resistances that are typically in the range of 3 kΩ to 8 kΩ [97], and, thus, higher than those of metal foil strain gauges. The higher base resistance results in lower thermal losses and reduces energy consumption. Furthermore, the direct deposition of the strain gauge on the spring element eliminates the need for adhesive bonding as in the case of metal foil strain gauges. This reduces potential sources of error such as a systematic creep through relaxation processes in the polymeric adhesive layer [82]. Usually, the resistive effect dominates in thin-film strain gauges with crystalline layers, making their properties comparable to those of metal foil strain gauges [97], [117]. The gauge factor k of these thin-film strain gauges is in the range of about 2 to 4 [97]. In addition, thin-film strain gauges exhibit a similar temperature behavior as metal foil strain gauges with a TK_0 and TK_C of $<100 \times 10^{-6}\,\mathrm{K}^{-1}$ and $<200 \times 10^{-6}\,\mathrm{K}^{-1}$ [97], respectively. Despite the aforementioned advantages, however, the manufacturing of thin-film strain gauges is only profitable for large quantities due to the expensive production equipment. Thus, thin-film strain gauges are mainly used for manufacturing pressure sensors [Fig. 2.7(a)] by companies such as Senstech (Fehraltorf, CH), Sensor-Technik Wiedemann (Kaufbeuren, DE) or Siegert TFT (Hermsdorf, DE) for industrial and automotive applications. In addition, Siegert TFT (Hermsdorf, DE) also offers thin-film strain gauges on a stainless steel carrier that can be welded onto a spring element, thus enabling force sensing [Fig. 2.7(b)].

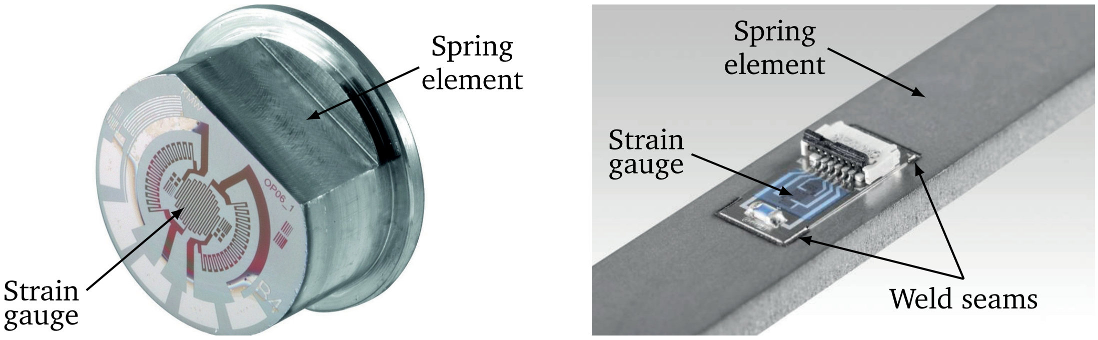

(a) (b)

Figure 2.7: Examples of thin-film strain gauges: (a) pressure sensor in thin-film technology [image source: www.stw-mobile-machines.com], (b) thin-film strain gauge on a steel carrier that is welded on a bending beam [image source: www.siegert-tft.de].

In the field of non-crystalline thin-film strain gauges, approaches exist in research with modified thin films that provide much higher sensitivities. On one hand, suspensions containing gold nanoparticles are formed into an ink in order to deposit coherent films with an average thickness of $220\,\mathrm{nm}$ on various substrates using inkjet printing [118]. The conductivity within the film arises through tunneling of electrons. By stretching the film, the spacing of the gold particles changes leading to a change in the conductivity of the film. The resulting resistance features an exponential dependence on the tunneling barrier, thus enabling a strain measurement. The exponential characteristic provides very high sensitivities with gauge factors in the range of 50 to 100 [118], although the reproducibility of the effect is poor [97]. On the other hand, composites based on amorphous carbon and nickel are deposited as a thin layer by sputtering onto a substrate, which is patterned using a laser [119]. This allows manufacturing thin-film strain gauges with a base resistance of up to $50\,\mathrm{k\Omega}$ and a gauge factor of up to 25 depending on the material composition and deposition conditions [119]. The drawbacks are a higher cross-sensitivity as well as a higher creep compared to metal foil strain gauges or crystalline thin-film strain gauges.

2.2.3 Thick-film strain gauges

The third established technology for the fabrication of strain gauges is the thick-film technology. Here, compounds are used to apply layers by screen printing that are subsequently sintered [82]. The thick-film compounds consist of an organic carrier material containing solvents and organic binders. Furthermore, depending on the intended functionality, metal powders (conductive paste), metal oxides (resistive pastes) or ceramics (insulating paste) are added [82]. In contrast to thin-film technology, the layers produced using thick-film technology feature larger thicknesses in the range of $5\,\mu m$ to $50\,\mu m$ [82], [98]. However, the strain gauge is also applied directly onto the spring element as in the thin-film technology.

First, multiple layers of an insulator paste are applied to a substrate and then sintered. A minimum of three layers is recommended to ensure a sufficient insulation resistance [120]. Second, conductive paths are printed and also sintered. Third, the resistive layer is printed. After sintering the resistive layer, the base resistance is measured and adjusted by laser ablation [97]. Finally, a protective layer is printed, which is also known as overglaze [121]. The substrates used in most cases are ceramics [82], such as aluminum oxide and glass ceramics [98], but also sometimes steel. This is mainly due to the high temperatures during the sintering process, in which temperature profiles with temperatures up to $900\,°C$ are used [82].

The metal oxides in the resistor paste significantly influence the resulting resistance as well as the other properties of the thick-film strain gauge. Palladium oxide/silver, iridium oxide/platinum, ruthenium oxides or ruthenates are frequently used as metal oxides [122]–[124]. These pastes result in sheet resistivities between $50\,\Omega/\square$ and $10^6\,\Omega/\square$ at film thicknesses of $20\,\mu m$ to $25\,\mu m$ [123]. The sheet resistance significantly influences the gauge factor of the thick-film strain gauge. For example, a sheet resistance of $1\,k\Omega/\square$ results in a gauge factor of about 2, while a sheet resistance of $10\,k\Omega/\square$ results in a gauge factor of about 10 [125]. However, this correlation is limited to a certain range [125]. In addition, an increased sheet resistance leads to increased noise, thus a higher sheet resistance also has drawbacks. Usually, the sheet resistances and layer thicknesses are chosen such that gauge factors of the thick-film strain gauges are in the range of 8 to 12 [98]. A further characteristic of the thick-film technology is that the resistance values scatter by $15\,\%$ to $20\,\%$ after production [126], [127]. This is mainly due to contamination of the resistive paste by gas infiltration, substrate composition and roughness, varying thickness of the layer and the heating profile during sintering [128]. Therefore, the resistance of the thick-film strain gauge is not designed to the nominal value but to approximately $70\,\%$ of the final value [127]. Then, laser ablation is used to remove material across the resistive layer, which increases the resistance with decreasing thickness. In this way, resistance values can be precisely adjusted with a deviation of less than $1\,\%$ with respect to the nominal value [126]. Basically, a linear and reproducible change in resistance is achieved in response to an applied strain [125]. However, this is accompanied by a high cross-sensitivity of $70\,\%$ to $80\,\%$ [126], [129]. In a temperature range of $-80\,°C$ to $120\,°C$, the temperature coefficients $\mathrm{TK_0}$ and $\mathrm{TK_C}$ are $<100 \times 10^{-6}\,K^{-1}$ [125], [129] and $<200 \times 10^{-6}\,K^{-1}$ [129], respectively. Overall, it can be concluded that thick-film strain gauges cannot match the accuracies of metal foil or thin-film strain gauges, but they certainly offer their superiority in the area of low-cost production in small and large quantities in combination with a higher sensitivity. Thick-film strain gauges are used especially in the field of pressure sensors. Manufacturers of such thick-film strain gauges (Fig. 2.8) include Metallux (Leutenbach, DE) and Primosensor (Dieburg, DE).

2.2.4 Semiconductor strain gauges

The main representative of piezoresistive strain gauges are semiconductor strain gauges, which are usually based on silicon as base material that is doped. Here, the effect is anisotropic due to the crystalline structure of silicon [82]. Therefore, depending on the direction of the current density vector J and the mechanical stress component σ_i, three effects are distinguished: longitudinal effect (current i parallel to the normal stress), transverse effect (current i perpendicular to the normal stress) and shear effect (current i parallel or perpendicular to the shear mechanical stress) [98]. The predominant piezoresistive contribution of this technology implies that the change of the resistivity is decisive. In case of semiconducting materials such as

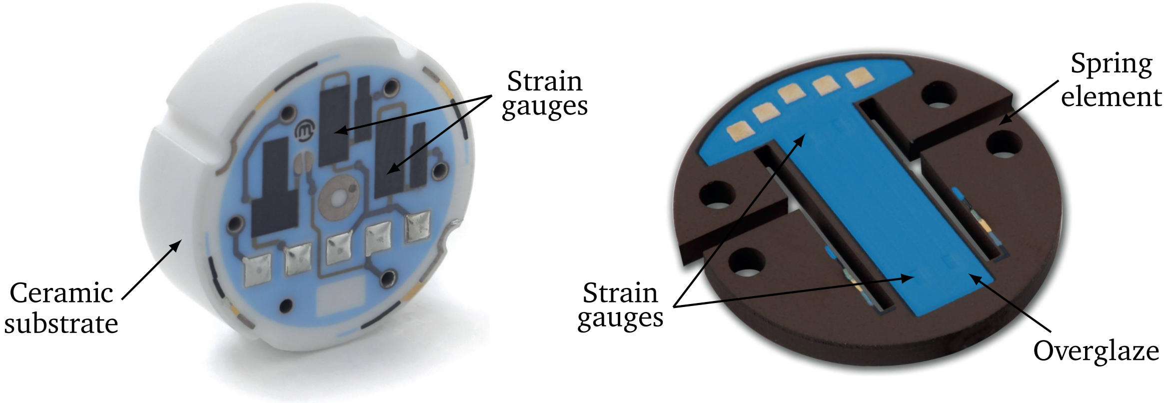

(a) (b)

Figure 2.8: Examples of thick-film strain gauges: (a) pressure sensor in thick-film technology on a ceramic substrate [image source: www.metallux.de], (b) thick-film strain gauge on a steel substrate for force sensing applications [image source:www.primosensor.de].

silicon, this is modeled by [82]

$$\frac{\Delta R}{R} \approx \frac{\Delta \rho}{\rho} = \pi_\mathrm{l} \cdot \sigma_\mathrm{l} + \pi_\mathrm{t} \cdot \sigma_\mathrm{t}, \tag{2.12}$$

where π_l denotes the longitudinal piezoresistive coefficient, π_t denotes the transversal piezoresistive coefficient, σ_l denotes the stress in longitudinal direction and σ_t denotes the stress in transversal direction. The piezoresistive coefficients depend on the crystallographic orientation of the piezoresistive strain gauge and the concentration of the dopant.

Piezoresistive sensors are categorized into two groups: homogeneously doped and inhomogeneously doped strain gauges [82], [97], [98]. The homogeneously doped strain gauges, which are also called semiconductor strain gauges, are created by cutting a homogeneously doped wafer (p- or n-doped) that is thinned to thicknesses between $20\,\mu\mathrm{m}$ and $50\,\mu\mathrm{m}$ into rectangular or U-shaped pieces [97]. Here, base resistance values ranging from $120\,\Omega$ to $8\,\mathrm{k}\Omega$ are achieved [97], [98]. On one hand, these semiconductor strain gauges can be applied on a spring element by means of glass solder, while on the other hand, application onto a carrier such as polyimide is also possible [97]. The latter case is similar to metal foil strain gauges, since this allows application of these semiconductor strain gauges to a spring element using an adhesive. In general, the longitudinal effect dominates in these semiconductor strain gauges [98]. Thus, the change in resistance is given by

$$\frac{\Delta R}{R} \approx = \pi_\mathrm{l} \cdot \sigma_\mathrm{l} = \underbrace{\pi_\mathrm{l} \cdot E}_{k_\mathrm{l}} \cdot \varepsilon_\mathrm{l}, \tag{2.13}$$

where the stress in longitudinal direction σ_l is expressed as strain in longitudinal direction ε_l through the Young's modulus E. This allows the gauge factor k_l to be determined. The gauge factor k_l can be 50 to 100 times greater than that of metal foil strain gauges, depending on the doping concentration [82], [130]. This high sensitivity is a key advantage of semiconductor strain gauges. However, the high sensitivity is accompanied by a high temperature dependency with a TK_0 and TK_C of approximately $1000 \times 10^{-6}\,\mathrm{K}^{-1}$ and $-3500 \times 10^{-6}\,\mathrm{K}^{-1}$ [97], [130], respectively, and a high linearity error of up to $10\,\%$ [97], which also depend on the doping concentration. Here, a trade-off is required, as the linearity error decreases with increasing dopant concentration, while the gauge factor and the base resistance also decrease [97]. The inhomogeneously doped strain gauges are based on a p-doped or n-doped silicon substrate, in which piezoresistive areas are created by means of thermal diffusion or ion implantation with impurities [98], [130]. The pn-junction created by the additional doping serves as electrical insulation of the piezoresistive resistors from the remaining substrate [97]. Depending on the doping method chosen, different resistor thicknesses as well as different doping profiles over the resistor thickness can be achieved, which influence the behavior of the piezoresistive resistor [98], [130]. This process allows a high degree of miniaturization, and, thus, the realization of a full bridge configuration in a single rectangular unit with edge lengths of less than 1 mm [82].

Although piezoresistive strain gauges offer the advantages of high sensitivity and a high degree of miniaturization, some drawbacks need to be taken into account. These include a high temperature sensitivity, a high linearity deviation, a more difficult installation and bonding process due to their small size as well as a low mechanical stability due to silicon as stiff but brittle substrate [98], [130]. These piezoresistive strain gauges are used in the field of pressure sensors by manufacturers, such as Wika (Klingenberg, DE) or Jumo (Fulda, DE).

2.2.5 3D-printed strain gauges based on conductive filament

In addition to the well-established technologies presented so far for the realization of strain gauges, printed strain gauges have recently been investigated, providing an additional method for strain measurement. In the state of the art, several approaches have been introduced, where mostly aerosol or inkjet printing techniques are used to apply a meander-shaped structure to a 3D-printed spring element [131]–[134]. More recently, approaches based on 3D-printed strain gauges made of conductive filament that are directly printed on a 3D-printed spring element by means of fused filament fabrication (FFF) have been proven to be a promising route for sensor-integration [135], [136] while being very cost-effective. However, 3D-printed strain gauges manufactured by FFF have not been bonded to metallic spring elements as in the conventional method by using metal foil strain gauges and investigated regarding their strain response. Therefore, an approach for manufacturing 3D-printed strain gauges made of conductive filament is presented in this work, which can be bonded to a structure that is loaded. This provides a strain measurement just like conventional metal foil strain gauges, which is a typical use case in experimental stress analysis applications. The experiments were assisted by Esan Sundaralingam within his Master's thesis [137].

Strain gauge design

In order to use the 3D-printed strain gauge as a conventional strain gauge, a two-layer design based on a subtrate layer and a measuring grid layer is used (Fig. 2.9). The meander-shaped measuring grid consists of four tracks and an effective length of 6 mm. For minimizing the impact of cross-sensitivity, the end loops are designed to feature a larger width than the measuring grid line width. The outer and inner radii of the end loops are 1 mm and 0.4 mm, respectively, corresponding to a U-shape as in the case of conventional strain gauges. This design is prepared for FFF using the open source software PrusaSlicer (Prusa Research a.s., Prague, Czech Republic). Here, a filament change is provided during an interruption between the substrate and measuring grid layers. The non-conductive substrate layer is based on polylactic acid (PLA) while a conductive compound filament (type: Protopasta Conductive PLA, Protoplant Inc., Vancouver, WA, USA) is used for the measuring grid layer. The compound (PLA-C) is primarily composed of PLA and electrically conductive carbon black. Its conductivity is dominated by the percolation mechanism. Here, the mobility of dispersed particles inside the material leads to a reconfiguration of the conductive path, and, thus, to a change in resistance [138].

Fabrication of the strain gauge is done by using a 3D-printer (type: Prusa MK3s, Prusa Research a.s., Prague, Czech Republic) with a nozzle diameter of 0.4 mm and a bed temperature of 60 °C. The extruder temperatures for the substrate and measuring grid layers are 215 °C and 240 °C, respectively. The substrate layer consists of a single layer with a thickness of 0.2 mm, while the measurement grid consists of two layers with a thickness of 0.15 mm each. Two layers for the measurement grid were chosen to ensure a solid print without unwanted gaps that were present during visual inspections when printing only one layer. In order to evaluate the performance of the 3D-printed strain gauge, it needs to be applied to a spring element. Here, a steel plate consisting of stainless steel (material no.: 1.4310) is used as spring element.

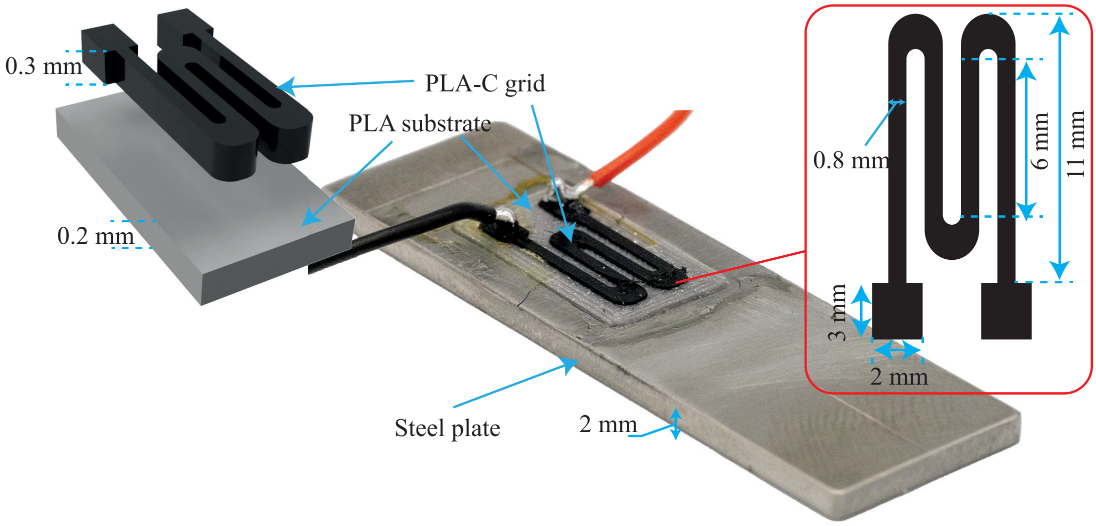

Figure 2.9: The 3D-printed strain gauge is based on a PLA substrate and a measuring grid made of conductive PLA. It is applied with a cold-curing superglue to a steel plate, which serves as spring element.

For determining a proper position for the 3D-printed strain gauge that features a high strain in the range from 500 µm m^{-1} to 1000 µm m^{-1} while not exceeding the yield strength of the steel plate, a finite element analysis (COMSOL Multiphysics 5.6, COMSOL AB, SWE) is conducted. The finite element analysis (FEA) model consists of the steel plate with attached printed strain gauge [Fig. 2.10(a)]. The Young's moduli of the steel plate, the PLA substrate and the PLA-C measuring grid are set to 186 GPa, 3.12 GPa and 3 GPa, respectively. This steel plate is clamped at one end and loaded at a distance of 40 mm from this clamping with 30 N. The simulated strain along the steel plate shows a linear behavior [Fig. 2.10(b)] with an excessive strain at the clamping edge. Thus, the 3D-printed strain gauge will be positioned at a distance of 10 mm from the clamping edge, i.e. avoiding the singularities area. This results in expected strains of the steel plate and printed strain gauge of 415.4 µm m^{-1} and 490 µm m^{-1}, respectively.

Finally, the 3D-printed strain gauge is applied to the steel plate at the predetermined location. Therefore, the application area is prepared by sanding and subsequent cleaning with acetone. The mechanical connection of the 3D-printed strain gauge is done by means of a cold curing superglue (type: Z70, HBK, Darmstadt, DE), which cures in about one minute under thumb pressure. This glue is especially used in experimental stress analysis applications. Electrical contact is established by melting copper wires into the contact pads using a soldering iron.

Analytic modeling of the static behavior under load

The force F applied to steel plate results in a deflection at the contact point in negative z-direction and forms an angle φ with the horizontal plane. In case of small deflections, the displacement of the tip of the steel plate in x-direction can be neglected as well as the transverse contraction of the steel plate. The small deflection in z-direction is given by [139]

$$z = \frac{F L_{\text{eff}}^3}{3YI} \text{ with } I = \frac{bh^3}{12}, \tag{2.14}$$

where L_{eff} is the effective length between the fixed point of the steel plate and the point of force application. Y and I are the young's modulus and moment of inertia of the steel plate, respectively. The angle φ is given as

$$\varphi = \frac{3}{2} \cdot \frac{z}{L_{\text{eff}}}. \tag{2.15}$$

Considering the difference of stiffness between the steel plate and the printed strain gauge, it is valid to assume that the mechanical property of the assembly is defined solely by the steel plate. Thus, the neutral axis of the whole structure consisting of the steel plate, PLA substrate and PLA-C grid is in the center of the thickness of the plate. Since the center of the PLA-C grid is at a distance d from the neutral axis, the resulting strain of the grid in x-direction can be calculated as

$$\Delta L = d \cdot \varphi = \frac{d\, L_{\text{eff}}^2}{2YI} \cdot F. \tag{2.16}$$

The resistance change due to an applied force can be calculated as

$$\Delta R = S \cdot F, \text{ with } S = \alpha \cdot \frac{h L_{\text{eff}}^2}{2YI}, \tag{2.17}$$

where S is the sensitivity relating the force to the resistance change and α is the proportionality factor between the strain of the PLA-C grid and change in resistance, which has to be determined experimentally.

Experimental setup for static loading

For evaluating the performance of the 3D-printed strain gauge regarding its linearity and sensitivity, a bending load of $30\,\text{N}$ is applied to the steel plate and the change in resistance of the 3D-printed strain gauge is measured [Fig. 2.10(c)]. This involves clamping $5\,\text{mm}$ from one end of the steel plate resulting in an effective beam length of $45\,\text{mm}$. The steel plate is loaded using a universal testing machine (type: inspekt table 5, Hegewald & Peschke, Nossen, DE) with a $100\,\text{N}$ reference force sensor (type: S2M/100N with $0.02\,\%$ accuracy, HBK, Darmstadt, DE) via a spherical pin at a distance of $40\,\text{mm}$ from the clamping. First, three full load cycles are performed to minimize settling. Then, the load is applied with a force-controlled slope of $0.2\,\text{N}\,\text{s}^{-1}$ followed by holding the load for $30\,\text{s}$ and subsequent unloading with the same slope. This load profile is repeated four times. A digital multimeter (type: DMM 7510, Keithley, Cleveland, OH, US) is used to measure the resistance of the 3D-printed strain gauge.

Results

The bending load results in a correlating change in resistance ΔR of the 3D-printed strain gauge upon which a creep is superimposed (Fig. 2.11). This creep results from the polymer properties of the filament as also observed in [140], which could be caused by a reorganization in conductive paths of the electrically

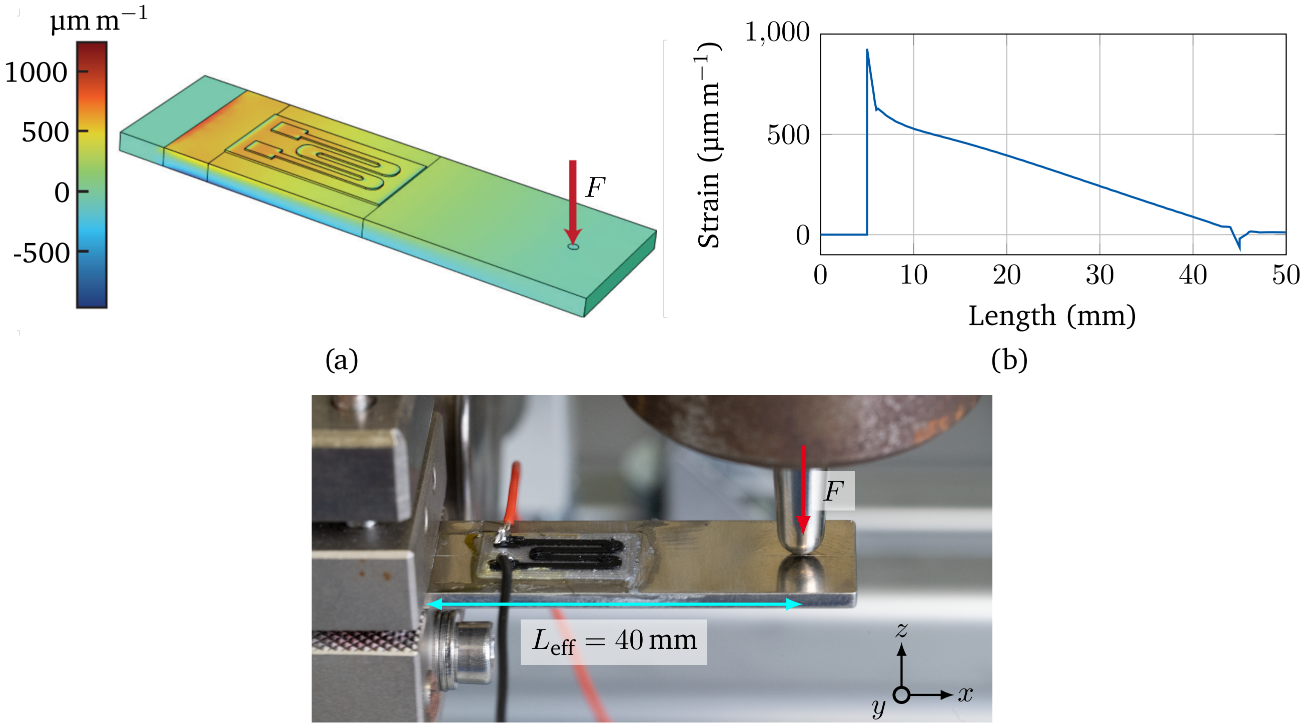

(a) (b)

(c)

Figure 2.10: Simulated strain along the steel plate for an applied load of $30\,\text{N}$, while the other end of the steel plate is clamped (a). The strain shows the expected behavior of a bending beam with a the maximum strain at the clamping area ($5\,\text{mm}$) and a linear decrease towards the loading end (b). Experimental setup for subjecting the steel plate to a bending load (c).

conductive particles [140]. However, this needs further investigations of the material used, which are beyond the scope of this work. The loading and unloading of the steel plate lead to significant changes in resistances of $64.3\,\Omega \pm 1.3\,\Omega$ and $66.7\,\Omega \pm 1.8\,\Omega$ with a confidence interval of $95\,\%$, respectively. These values are averaged over the four load cycles. Furthermore, the resistance-force characteristics for the loadings show a nearly linear behavior with correlation coefficients R^2 of 0.996 [Fig. 2.12(a)]. The linearity error of the loadings is within $\pm 4\,\%$ [Fig. 2.12(b)].

The gauge factor k of the 3D-printed strain gauge is calculated by

$$k = \frac{\frac{\Delta R}{R_0}}{\varepsilon_{\text{SG}}} \tag{2.18}$$

with R_0 as the base resistance of the 3D-printed strain gauge. With a base resistance of $18\,711.8\,\Omega$, the changes in resistance (Fig. 2.11), and a strain of nearly $419.4\,\text{µm}\,\text{m}^{-1}$, which is in good agreement with the simulated strain of $416.7\,\text{µm}\,\text{m}^{-1}$, a gauge factor k of 8.3 results.

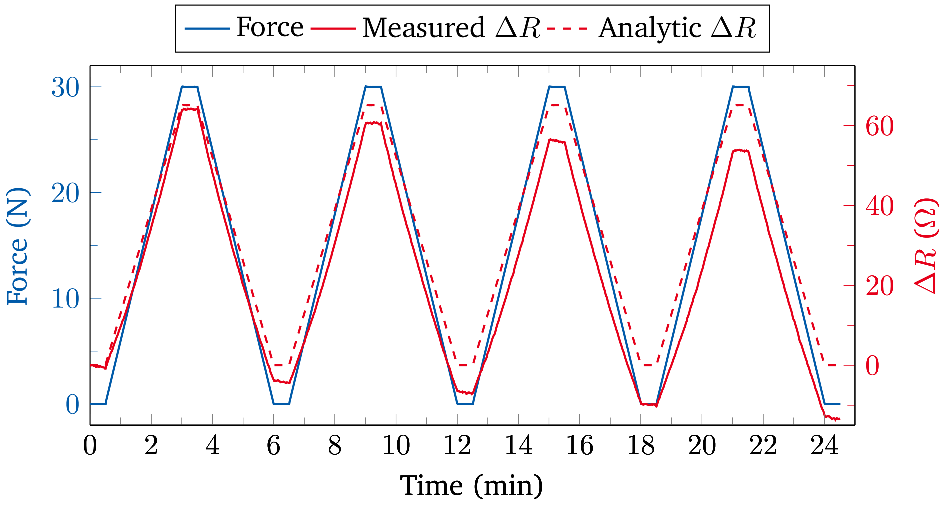

Figure 2.11: The measured and analytic change in resistance correlates directly with the applied force of $30\,\mathrm{N}$ and results in changes of $64.3\,\Omega \pm 1.3\,\Omega$ and $66.7\,\Omega \pm 1.8\,\Omega$ for the loading and unloading cycle, respectively. A nearly linear drift of the measured resistance over time is present.

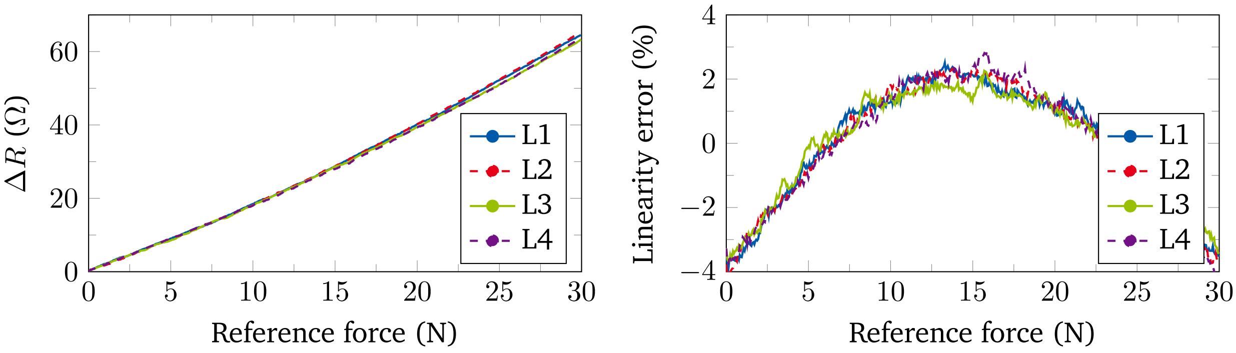

(a) (b)

Figure 2.12: The four loadings L1 - L4 of the steel plate show a nearly linear response of the change in resistance of the 3D-printed strain gauge with correlation coefficients R^2 of 0.996 (a). The linearity error of the loadings is within $\pm 4\,\%$ (b).

2.3 Installation of strain gauges

Based on their linear properties, manifold availability and simple installation and bonding technology, only metal foil strain gauges (henceforth called strain gauges) are used in this work. In order to measure accurately the strain or compression resulting from a force being applied to a spring element, a faultless and loss-free strain transmission to the strain gauge must be ensured. This is achieved by a firm and planar connection between the strain gauge and the spring element using special adhesives. In addition, other bonding methods exist such as spot welding for special use cases, which, however, require special strain gauges.

Commercial strain gauges by themselves do not allow a measurement and have to be installed on a spring element to achieve a measuring function. This installation requires special care, since its quality significantly influences the measurement accuracy. The installation of strain gauges on metallic spring elements consists of six steps (Fig. 2.13), which can be further subdivided. A description of the various steps for installing strain gauges onto the steel plates that will be integrated in LPBF-manufactured parts is given below. This procedure is introduced by the HBK Academy (HBK, Darmstadt, DE).

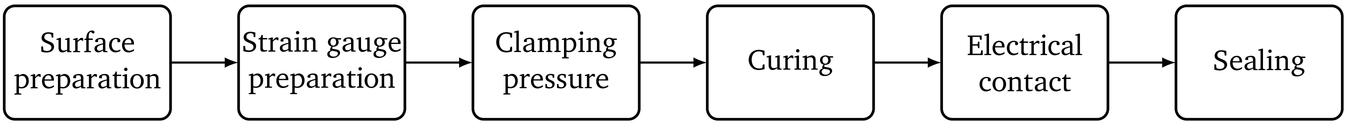

Figure 2.13: The installation of strain gauges on metallic spring elements consists of six steps.

Surface preparation

Strain gauges can be installed on a wide range of solid materials, as long as the area of application is properly prepared. In this work, only metallic spring elements are used. The first step is to prepare the area of application for the strain gauge installation to make it free of dust, pores and oxides, slightly rough and well wettable. This ensures optimum bonding with the adhesive.

Initially, the surface of the steel plate is cleaned with isopropanol using a lint-free cloth to prevent particles from being deposited on the steel plate [Fig. 2.14(a)]. This allows to remove coarse particles, dirt and grease. Afterwards, a scribe is used to create marks on the steel plate [Fig. 2.14(b)], which will be required later for precise positioning of the strain gauge. Subsequently, the area of application is roughened using a sandpaper with a grain size of 220 [Fig. 2.14(c)]. This enlarges the contact area between the adhesive and the spring element, and, thus, increases the bonding forces while minimizing running of the adhesive. The recommended surface roughness for optimum bonding at the area of application is about 2 µm [141]. The final step of the surface preparation is cleaning with acetone using a lint-free cloth. Here it should be noted that the lint-free cloth is not wiped back and forth, but always a strip is pulled over the surface followed by using a new lint-free cloth. This step is performed 3 times.

Strain gauge preparation

First, the strain gauge is placed on a clean glass plate using tweezers. Note that the bonding side of the strain gauge is not touched to prevent contamination by dirt and grease. In order to facilitate handling, a temperature resistant adhesive tape is applied to the top side of the strain gauge covering the contact pads and leaving additional 5 mm of the adhesive tape protruding [Fig. 2.15(a)]. Hence, the temperature-resistant adhesive tape serves both as a protection for the solder pads against the adhesive and as a hinge during the installation process. The strain gauge is then grasped at the adhesive tape using tweezers and aligned on the steel plate in accordance to the predefined markings [Fig. 2.15(b)]. Afterwards, the strain gauge is fixed with the attached temperature-resistant adhesive tape which ensures that its position is not changed during the following application of the adhesive. In order to apply the adhesive, the strain gauge is lifted with a flattened tweezer and bent along the edge of the temperature-resistant adhesive tape, which now acts as a hinge. This allows an even application of the adhesive to the area of application as well as to the bonding surface of the strain gauge [Fig. 2.15(c)]. A hot-curing, one-component phenolic resin adhesive (type: P250, HBK, Darmstadt, DE) is used for the strain gauge installation, which enables very thin adhesive layers of approximately 10 µm. In comparison to cold-curing adhesives, which are primarily used in experimental stress analysis, hot-curing adhesives meet higher requirements of accuracy as well as long-term stability and are therefore preferred in transducer fabrication [141]. Subsequently, the adhesive layer is dried at room temperature for 15 minutes to volatilize the solvents, and, thus, prevent blistering. The strain gauge is then

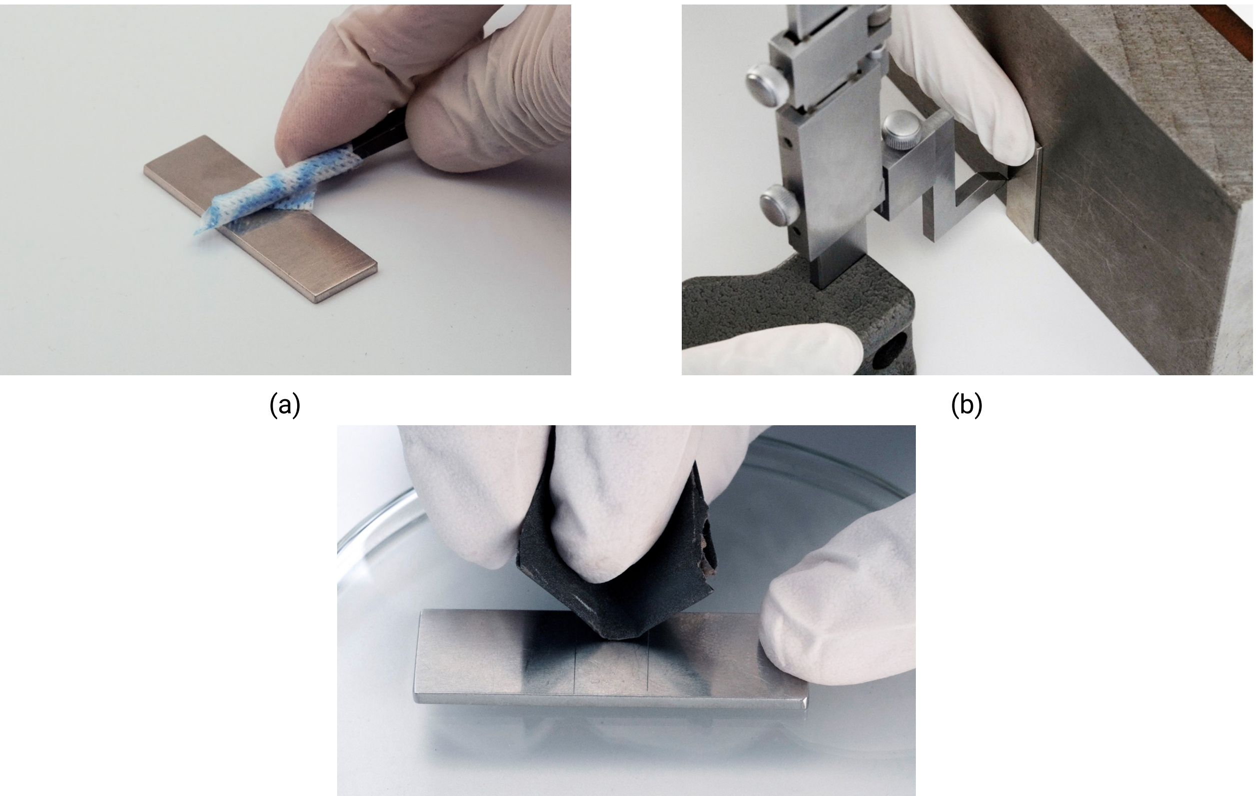

(a)

(b)

(c)

Figure 2.14: The surface preparation consists of multiple cleaning steps (a), creating marks for positioning the strain gauge (b) and roughening the surface (c).

folded back onto the adhesive surface and slightly pressed using flattened tweezers. A teflon tape is placed on the strain gauge ensuring that the adhesive will not get in contact with any other part. Finally, pressure is applied to the installation with the thumb [Fig. 2.15(d)].

Clamping pressure

A clamping pressure in the range of $10\,\mathrm{N\,cm^{-2}}$ to $50\,\mathrm{N\,cm^{-2}}$ has to be applied to the strain gauge installation when curing the adhesive. Clamps can be used for this purpose. In order to prevent the strain gauge from being damaged by the clamp, a silicone rubber pad is used. This silicone rubber pad is placed on the teflon tape that is already applied. The clamping pressure is then exerted to the strain gauge installation by two clamps via a metal plate to ensure a uniform distribution of pressure [Fig. 2.16(a)].

Curing

Curing of the adhesive takes place in an oven (type: P330, Nabertherm GmbH, Lilienthal, DE) at a temperature of $160\,^{\circ}\mathrm{C}$ over a time period of $4.5\,\mathrm{h}$. In order to heat the strain gauge installation including the steel plate evenly and minimize blistering in the adhesive layer, a heating rate of $2\,\mathrm{K\,min^{-1}}$ to $10\,\mathrm{K\,min^{-1}}$ needs to be maintained. Preliminary tests with a thermocouple applied to the steel plate have shown that a one-hour heating phase from room temperature to $160\,^{\circ}\mathrm{C}$ is sufficient. After the strain gauge installation including the steel plate has cooled down, the clamping pressure is removed. Subsequently, post-curing is performed at a

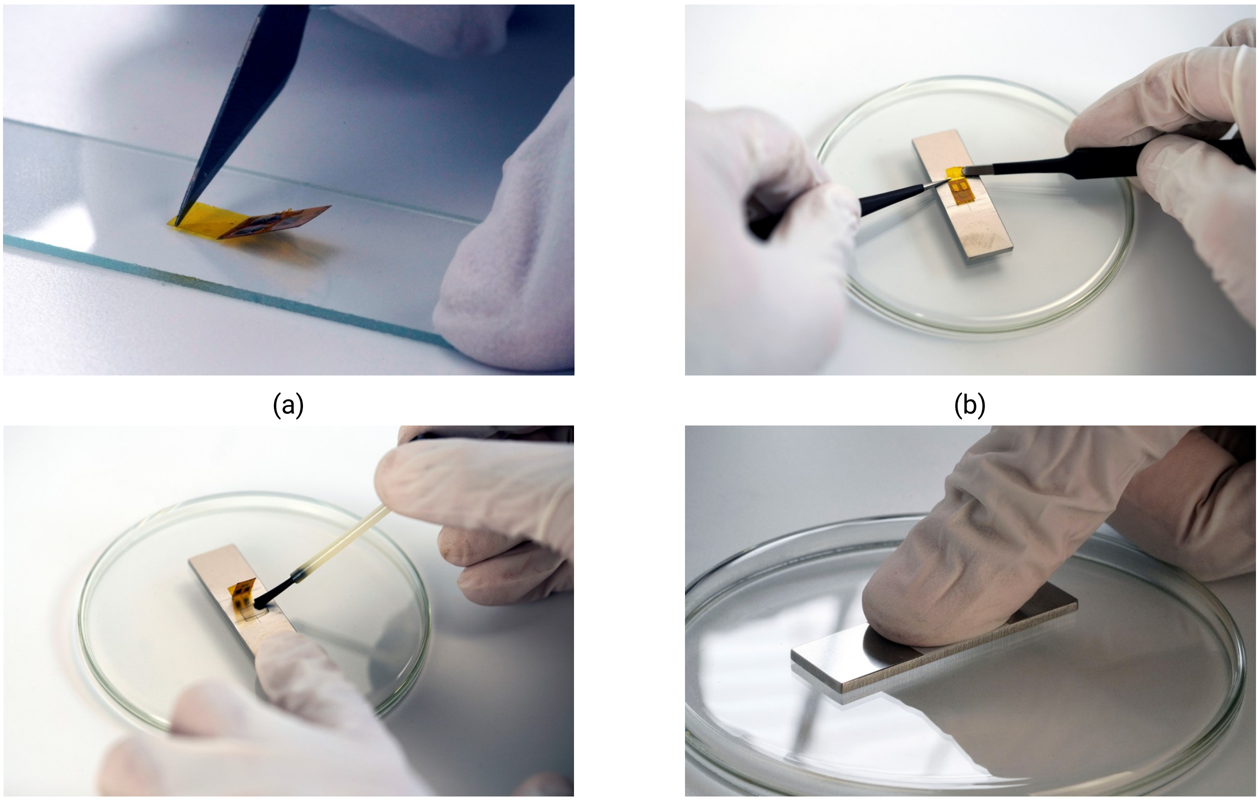

(a) (b) (c) (d)

Figure 2.15: A temperature-resistant adhesive tape is applied to the top of the strain gauge (a), which is used for fixing once the strain gauge is aligned according to the specified markings on the steel plate (b). This allows to apply the adhesive evenly to the area of application as well as to the bonding side of the strain gauge (c). Finally, a teflon tape is used as an intermediate layer and pressure is applied to the strain gauge (d).

temperature of 180 °C for 1 h without pressure. Again, a heating phase of 1 h is used and cooling down to room temperature is awaited. Then, the installation is inspected whether air bubbles are underneath the strain gauge or poorly bonded edges. Both result in a faulty installation, requiring the strain gauge to be removed as well as applying another one.

Electrical contact and sealing

The applied strain gauge requires solder terminals for establishing electrical contact [Fig. 2.16(b)]. These are also bonded to the steel plate near the strain gauge using a cold-curing adhesive (type: Z70, HBK, Darmstadt, DE), which cures within a minute. Then, a connection between the strain gauge and the solder terminal is made with enameled copper wires using a soldering iron. The temperature at the soldering iron should be maximum 300 °C and a fast soldering (roughly 2 s) is necessary to avoid damaging the strain gauge due to the thermal load. Finally, cables are connected to the solder terminals. This avoids direct contact of the cables with the strain gauge, and, thus, prevents possible cable movements from influencing the strain gauge. A measurement of the base resistance serves as an additional verification regarding the correct installation and electrical contact of the strain gauge.

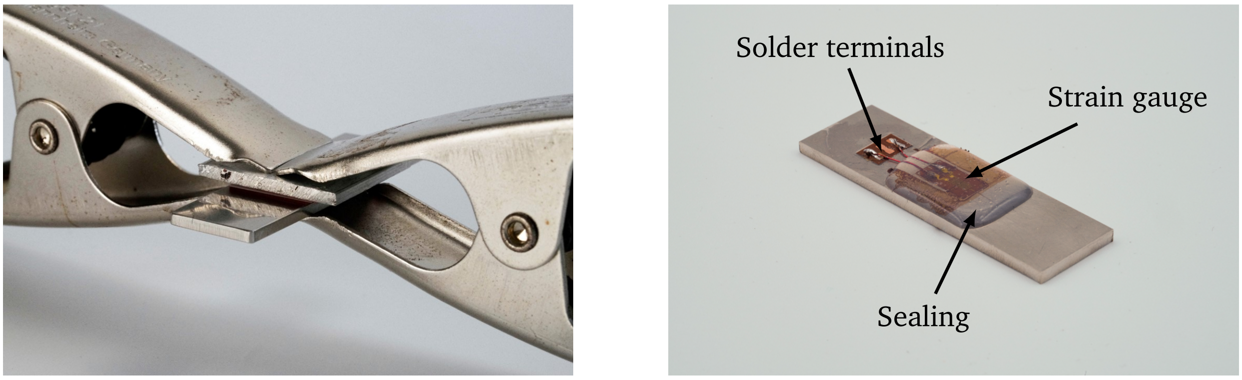

Figure 2.16: The clamping pressure is realized with two clamps via a metal plate (a). After curing of the adhesive, solder terminals are glued for establishing electrical contact to the strain gauge using enameled copper wires. A silicone rubber is used to seal the installation and protect against environmental influences (b).

Finally, the strain gauge needs to be protected against environmental influences to ensure that it remains functional over a long period of time. A significant environmental influence is humidity, which can penetrate the adhesive layer as well as the polymer layers of the strain gauge by diffusion. This results in a change of the zero point and impacts the transmission behavior. In order to protect the strain gauge installation against these influences, various covering agents are available. Here, a transparent silicone rubber (type: SG250, HBK, Darmstadt, DE) is used as covering agent, which provides very good protection against moisture and mechanical effects. This covering agent is poured over the strain gauge installation as well as the surrounding edges of about $5\,\mathrm{mm}$ and results in a layer with a thickness of about $1\,\mathrm{mm}$ to $2\,\mathrm{mm}$ [Fig. 2.16(b)]. Curing of the covering agent takes place over $48\,\mathrm{h}$ at room temperature. Consequently, the strain gauge is ready to capture strain due to a mechanical load. Therefore, the evaluation of the change in resistance of the strain gauge is described in the following.

2.4 Evaluation of a change in resistance using a bridge circuit

The operating principle of a strain gauge is based on a change in resistance due to an applied strain. The most basic method of quantifying this is to measure the resistance R by applying Ohm's law $R = U/I$. For this purpose, the strain gauge needs to be supplied with a constant current source I while the resulting voltage U is measured. However, the drawback with this method is that multimeters with very high resolutions are required to record very small changes in resistance in the promille range, as is often the case with strain gauges [97]. This drawback is overcome by subtracting the base resistance from the measurement. This was first identified by Sir Charles WHEATSTONE in 1834, who set up two voltage dividers and evaluated the difference between the center taps [106]. Thus, he was able to accurately measure small changes in resistance regardless of the stability of the voltage source [106]. This arrangement is known as the Wheatstone bridge, which is still used for evaluating resistive sensors, especially strain gauges. A Wheatstone bridge consists of four resistors ($R_1 ... R_4$), which form two voltage dividers and are supplied with a voltage source U_S (Fig. 2.17). However, current supply is also possible. Depending on the number of measuring resistors or strain gauges, whether one, two or four, a distinction is made between quarter, half and full bridge configuration. The full bridge configuration is preferred, as it is more sensitive than the quarter or half bridge configuration [89]. At the center taps of the voltage dividers, the bridge output voltage U_d is measurable.

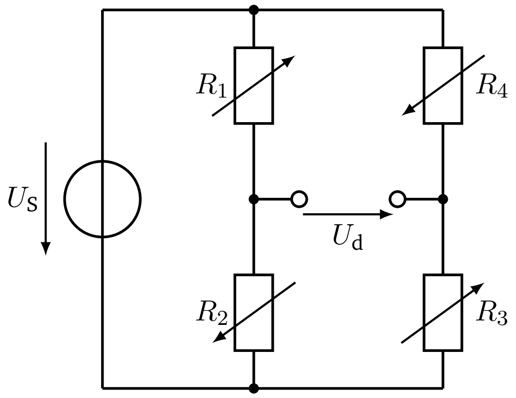

Figure 2.17: Full bridge configuration according to WHEATSTONE.

In the following, the bridge output voltage U_d is determined on the basis of a full bridge configuration, since only this configuration is used in this work. This requires four resistors (strain gauges), two of which change in opposite directions. This is the case, for example, with a bending beam as spring element, where the upper surface is elongated and the lower surface compressed, thus achieving a change in resistance on both sides in opposite directions when strain gauges are applied. The ideal case of are equal resistances ($R_1 = R_2 = R_3 = R_4 = R_0$) that results in a bridge output voltage $U_\mathrm{d} = 0$ in the unloaded state. Therefore, this state is defined as balanced bridge [82]. Otherwise, the bridge is balanced as soon as the resistance ratio of the voltage dividers meets equation 2.19.

$$\frac{R_1}{R_2} = \frac{R_4}{R_3}. \tag{2.19}$$

As soon as a mechanical load causes a change in resistance ΔR_i through the resulting strain, a change in the bridge output voltage occurs. The bridge output voltage U_d for this case is determined by [82]

$$U_\mathrm{d} = U_\mathrm{S} \cdot \frac{1}{4} \cdot \left(\frac{\Delta R_1}{R_1} - \frac{\Delta R_2}{R_2} + \frac{\Delta R_3}{R_3} - \frac{\Delta R_4}{R_4} \right). \tag{2.20}$$

Substituting equation 2.11 for the relative change in resistance $\Delta R/R$ into equation 2.20 provides the bridge output voltage U_d for metal foil strain gauges

$$U_d = U_S \cdot \frac{k}{4} \cdot \Big(\varepsilon_1 - \varepsilon_2 + \varepsilon_3 - \varepsilon_4 \Big). \tag{2.21}$$

In most cases, the ratio $U_\mathrm{d}/U_\mathrm{S}$ is considered, which is independent of the magnitude of the supply voltage, and, thus, provides better comparability [89].

Two main advantages of the bridge circuit can be identified. On one hand, the differential measurement allows the subtraction of the base resistance of the strain gauge, thus reducing the requirements on the electronics regarding the resolution. On the other hand, the bridge circuit offers the possibility of compensating disturbance variables such as temperature compensation.

2.5 Additive manufacturing processes

Additive Manufacturing (AM), popularly known as 3D-printing, refers to a group of different manufacturing processes used to create three-dimensional (3D) parts by joining material based on a computer-aided design

(CAD) model in accordance with the ISO/ASTM 52900:2015 standard [142]. This is usually done by progressively adding thin layers of materials [23], [143], [144], which is the opposite of conventional manufacturing processes such as milling or turning, where material is removed. These layers are obtained by slicing the CAD-model by means of a software in several layers with a defined thickness. The sliced layers contain the geometrical contour information of the part [33], [145]. This data is sent to an AM-machine that finally joins the layers by a defined energy input as commanded by the slicing software [23], [143], [145]. Through this approach, AM-processes enable near-net-shape manufacturing of components [27], [146] in a single production step, thus eliminating the need for additional component-specific and, in most cases, expensive tooling such as dies or punches [144]. In addition, the near-net-shape manufacturing is resource efficient, as material is only applied where it is needed [27]. Thus, a part is created according to its key functionality [29] while allowing for indivudalization of the component [147]. This is a paradigm shift that enable developers to focus solely on the performance and function of the component in their design cycle without being concerned about the constraints of traditional manufacturing processes regarding manufacturability [35]. Consequently, AM has been called a *disruptive* technology [65], [148] that will fundamentally influence many processes in production [149], supply chain design [150] and product life-cycle planning [65].

AM-processes are basically divided into single-step and multi-step processes. The single-step processes allow manufacturing a part in a single operation, in which the basic geometrical shape and the basic material parameters are achieved simultaneously [151]. Therefore, these processes are called *direct processes* [151], [152]. In contrast, multi-step processes involve manufacturing of a part in two or more steps, and, thus, are called *indirect processes* [151], [152]. Typically, the basic geometry is created in the first step while the consolidation of the part takes place in a subsequent step to achieve the intended basic material properties [151], [153]. There have been many AM-processes developed over the years, both single-step and multi-step, which are classified into seven categories according to the American Society for Testing and Materials (ASTM) F42 committee [154]. These categories are Binder Jetting (BJT), Directed Energy Deposition (DED), Material Extrusion (MEX), Material Jetting (MJT), Powder Bed Fusion (PBF), Sheet Lamination (SL), and Vat Polymerization (VT) (Tab. 2.1). Thereby, these processes differ regarding the technique for depositing layers, the method to join these layers with each other and processible materials [155].

In this thesis, the categories MJT and VT are not considered, as they do not allow the processing of metals. The focus of this work lies on the integration of sensors into additively manufactured metallic parts. Therefore, only single-step processes are an option. The post-treatment step in the multi-step processes such as sintering would lead to damage of the integrated sensor due to the high temperatures [33]. Therefore, only the categories DED and PBF with their respective technologies Electron Beam Additive Manufacturing (EBAM) and Directed Metal Deposition (DMD) as well as EBM and Laser-based Powder Bed Fusion (LPBF) are relevant for the integration of sensors into additively manufactured metallic parts. It should be noted that both terms LPBF and SLM describe the same process, and are both used in the literature. The main differences between the two categories DED and PBF are the type of feedstock and their deposition [41]. In the processes of the DED category, the feedstock is supplied directly to the point where it is melted. The feedstock is either a wire that is melted by an electron beam, as in the case of EBAM, or powder that is melted by a laser beam, as in the case of DMD [41]. In the processes of the PBF category, the feedstock is, as the name implies, a powder reservoir that is applied layer-by-layer onto a build platform (bed). This powder is selectively melted by means of an electron beam, as in the case of EBM, or a laser beam, as in the case of LPBF [41], [66].

In [33], the aforementioned four technologies (EBAM, DMD, EBM and LPBF) were evaluated in terms of their suitability for manufacturing additively manufactured metallic parts with integrated sensors. The criteria used were [33]:

Table 2.1: The ASTM classifies AM-processes in seven categories. This table is taken from [64].

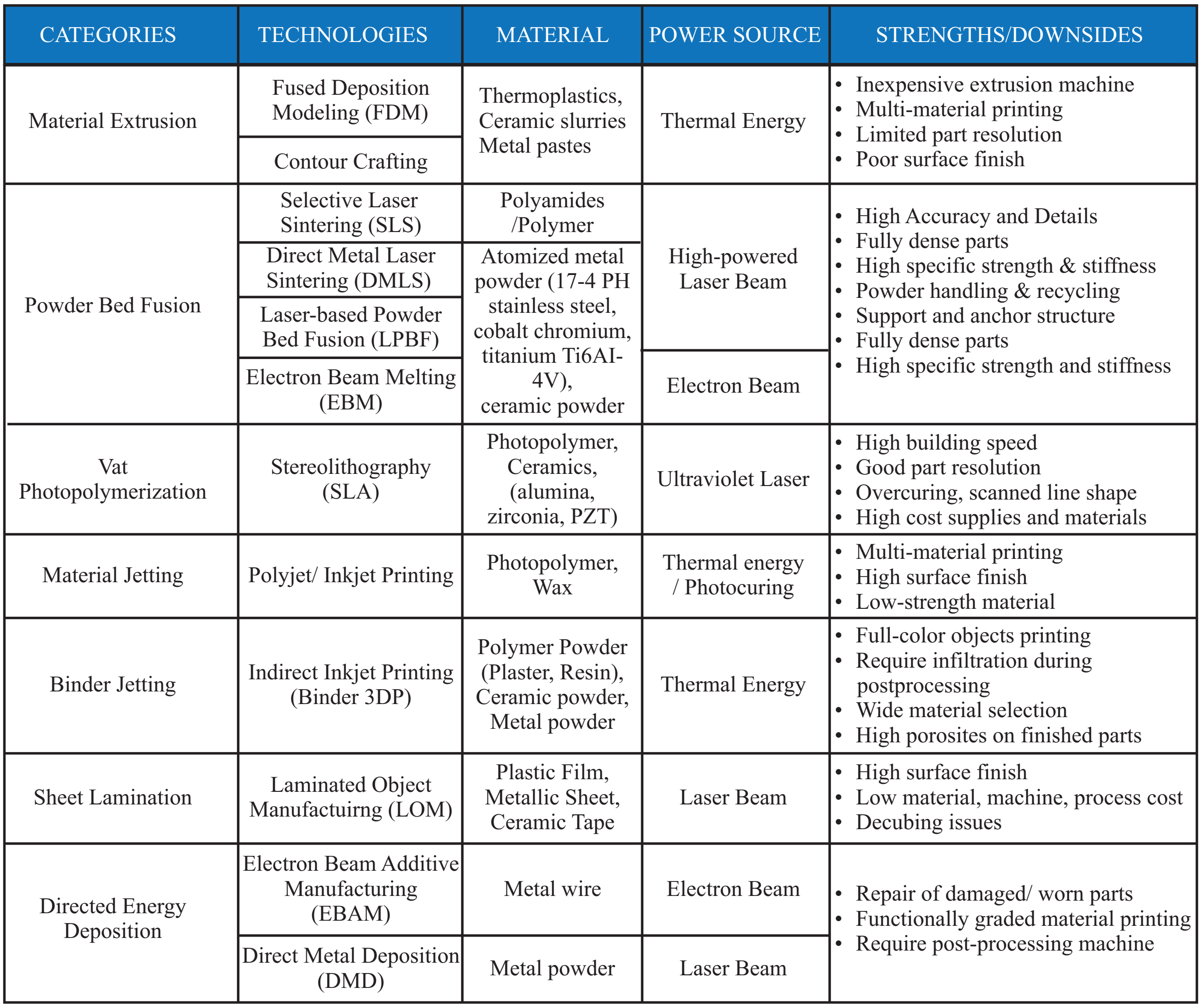

CATEGORIES	TECHNOLOGIES	MATERIAL	POWER SOURCE	STRENGTHS/DOWNSIDES
Material Extrusion	Fused Deposition Modeling (FDM)	Thermoplastics, Ceramic slurries Metal pastes	Thermal Energy	• Inexpensive extrusion machine • Multi-material printing • Limited part resolution • Poor surface finish
	Contour Crafting			
Powder Bed Fusion	Selective Laser Sintering (SLS)	Polyamides /Polymer	High-powered Laser Beam	• High Accuracy and Details • Fully dense parts • High specific strength & stiffness • Powder handling & recycling • Support and anchor structure • Fully dense parts • High specific strength and stiffness
	Direct Metal Laser Sintering (DMLS)	Atomized metal powder (17-4 PH stainless steel, cobalt chromium, titanium Ti6AI-4V), ceramic powder		
	Laser-based Powder Bed Fusion (LPBF)			
	Electron Beam Melting (EBM)		Electron Beam	
Vat Photopolymerization	Stereolithography (SLA)	Photopolymer, Ceramics, (alumina, zirconia, PZT)	Ultraviolet Laser	• High building speed • Good part resolution • Overcuring, scanned line shape • High cost supplies and materials
Material Jetting	Polyjet/ Inkjet Printing	Photopolymer, Wax	Thermal energy / Photocuring	• Multi-material printing • High surface finish • Low-strength material
Binder Jetting	Indirect Inkjet Printing (Binder 3DP)	Polymer Powder (Plaster, Resin), Ceramic powder, Metal powder	Thermal Energy	• Full-color objects printing • Require infiltration during postprocessing • Wide material selection • High porosites on finished parts
Sheet Lamination	Laminated Object Manufactuirng (LOM)	Plastic Film, Metallic Sheet, Ceramic Tape	Laser Beam	• High surface finish • Low material, machine, process cost • Decubing issues
Directed Energy Deposition	Electron Beam Additive Manufacturing (EBAM)	Metal wire	Electron Beam	• Repair of damaged/ worn parts • Functionally graded material printing • Require post-processing machine
	Direct Metal Deposition (DMD)	Metal powder	Laser Beam	

- the **temperature** that is required for processing the part,
- the **accessibility** to cavities into which the sensors will be embedded,
- the **minimum feature size** that affects the manufacturing of more filigree parts,
- the **surface quality** that affects the precise positioning of sensors and
- the **maturity** of the AM technology that is a measure for the relevance for industrial applications.

The evaluation showed that the LPBF-process is most promising for the integration of sensors into additively manufactured metallic parts [33] and is thus used as AM-process in this thesis. Therefore, the LPBF-process and its characteristics are described below in more detail.

2.6 Laser-based powder bed fusion

LPBF is currently the leading technology in the field of metal-based AM in both research and industry [66], [67] as it offers a high geometrical resolution, homogeneous process conditions and favorable mechanical properties [68]–[70]. The layer-by-layer build-up principle of the LPBF-process is shown in Fig. 2.18. First, a thin layer of metal powder is raked on a build platform by means of a coating system [41]. Then, a continuous-wave laser source is utilized to melt particles selectively onto the powder bed to build a well defined layer [41], [66]. In this process, it is necessary that the powder absorbs as much as possible of the introduced energy by the laser beam in order to achieve melting [156]. The absorption rate depends on the wavelength λ and the polarization of the laser radiation as well as the material properties of the powder [157]. In addition to absorption, a significant amount of the laser radiation passes through gaps between the powder particles into underlying powder layers [46]. After melting the powder, the heat generated by the introduced energy needs to be dissipated, thus allowing solidification of the melted material. Thereby, heat conduction and convection within the powder bed predominate, while heat radiation and convection on the surface of the manufactured part and the powder bed dominate [46], [158]. Subsequently, the build platform is lowered followed by coating the next layer of powder [41]. This way, the process is continuously repeated until the desired three-dimensional part is created. Here, the process chamber is filled with an inert gas such as argon to prevent oxidation. The layer-by-layer build-up facilitates the integration of external elements such as sensors within a fabricated part at a specific layer [25], [29] by interrupting the process.

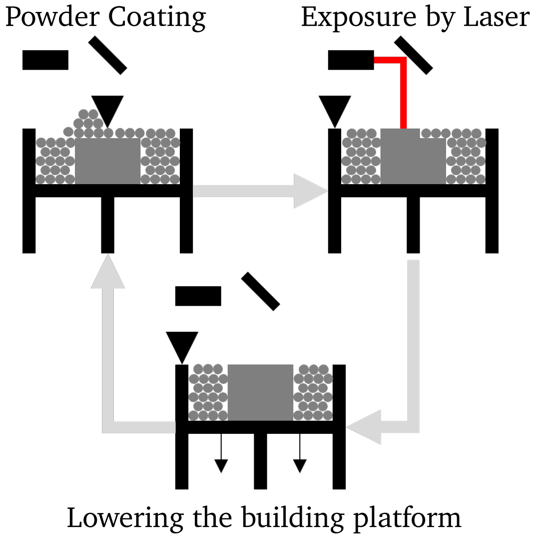

Figure 2.18: Process cycle of the LPBF-process [96]. First, steel powder is raked onto the build platform. Then, a laser source is utilized to melt and fuse particles selectively. Finally, the build platform with the powder bed is lowered. This way, the process is repeated layer by layer to create fully dense three-dimensional parts.

2.6.1 Residual stress within LPBF-manufactured parts

A typical characteristic of LPBF-manufactured parts is the presence of residual stresses [159]. Although residual stresses are generated by almost all processes when processing a material, they are particularly pronounced due to the high, rapid and localized changes in temperature that occur during the LPBF-process

[160]. These changes in temperature together with the resulting temperature gradients lead to thermally induced stresses within the LPBF-manufactured part, which ultimately remain as residual stresses [160]. The aim is to minimize these residual stresses to prevent cracking or distortion of the manufactured part [46]. In addition, the maximum resilience of the LPBF-manufactured part is reduced due to the preload caused by the residual stress. In this context, the temperature gradient mechanism (TGM) has been established to describe the residual stresses in the LPBF-process [159].

The TGM describes a two-stage effect (Fig. 2.19) [159]. Initially, a temperature gradient arises from the location of the heat input by the laser to the surrounding material. This leads to a thermal expansion $\varepsilon_{\mathrm{th}}$ of the scanned area, which is inhibited by the cooler surrounding material such that a compression occurs. If the yield point R_{e} of the material is exceeded in this process of compression, a plastic compression $\varepsilon_{\mathrm{pl}}$ occurs. In the next step, the laser beam moves away from the scanned position, which leads to returning of the thermal expansion. Due to the plastic compression of the surrounding material, a complete recovering of the thermal expansion is no longer possible. Hence, a tensile stress σ_{tens} remains in the heated area, while a compressive stress σ_{comp} is present in the area of plastic compression.

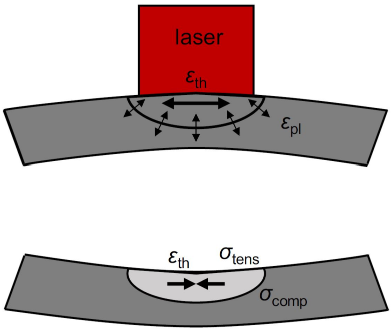

Figure 2.19: The temperature gradient mechanism describes the expansion of the material through heat input and the subsequent contraction due to cooling as well as the resulting resulting deformation. The graphic is taken from [46].

In order to reduce these residual stresses in the LPBF-manufactured part, an adaptation of the process parameters is required. This includes the exposure strategy [46], [161], the length of the scan vector [46], [159] as well as the layer thickness [160]. Therefore, the process parameters are discussed in the following.

2.6.2 Process parameters and scanning strategies

The LPBF-process offers about 130 parameters [162], which significantly influence the quality and characteristics, such as strength or porosity, of a part produced with it. The most important parameters include the laser power P_{L}, the scanning speed v_{s}, the hatch distance h_{d}, the focus diameter d_{L}, the melt pool width b_{m}, the melt pool length l_{m} and the layer thickness s (Fig. 2.20) [46].

In the following, only the parameter of the scanning strategy will be discussed, since it is essential for this work. For the other parameters, please refer to [46]. The scanning strategy describes the movement of the laser beam during melting the powder particles. One scanning process consists of two parts (Fig. 2.21): scanning of the contour of the manufactured part (contour scanning) and scanning the core area of the layer (core scanning) [163]. The scanning process starts with core exposure, in which the core area is scanned with the laser beam, depending on the scan strategy selected. However, the outer contour of the part is not

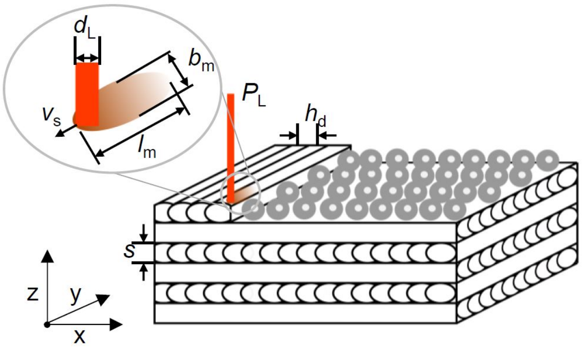

Figure 2.20: Key parameters of the LPBF-process. This graphic is taken from [46].

scanned at this time. In the simplest case (Fig. 2.21, Standard), the laser beam moves linear from one outer edge of the part to the other in alternating directions. In contrast, in the case of the scan strategies stripes and checkerboard, the area to be scanned is first divided into stripes or squares, respectively, which are scanned in the next step. Here, it is possible to specify whether the areas are scanned sequentially or randomly in order to reduce potential anisotropies [46]. The scanning strategies stripes and checkerboard are used in most cases, as they offer the possibility to reduce stresses and defects [46], [164], [165]. Especially in the case of the scanning strategy checkerboard, the lowest temperature gradients result compared to the other two scanning strategies [166], which is due to higher cooling times. In addition, residual stresses along a melt track tend to increase with longer track lengths [46]. Thus, the shorter track lengths in case of the scanning strategy checkerboard further reduce residual stresses [160], [167]. Once the core scanning is complete, the contour scanning takes place, in which the outer track of the part is scanned with the laser to improve the surface quality [168].

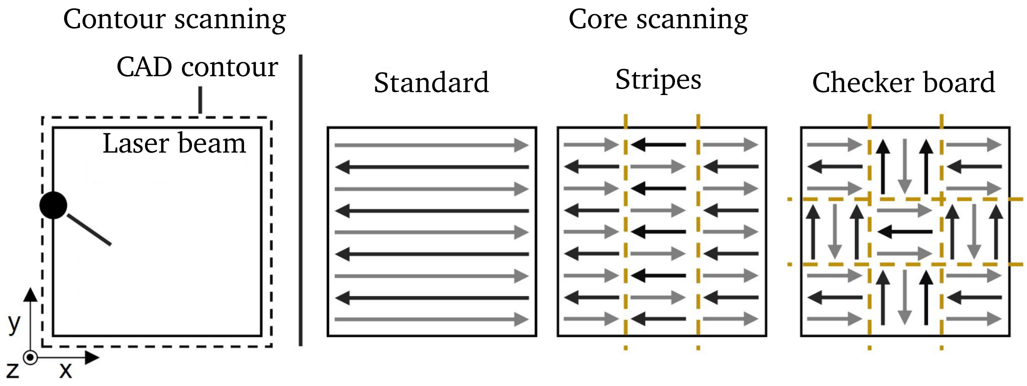

Figure 2.21: Scanning strategies used in the LPBF-process. This graphic is taken from [46].

3 Design of LPBF-manufactured spring elements

The following chapter was published in [95], [96].

In order to evaluate the suitability of the disruptive manufacturing method for fabricating force sensors based on strain gauges by means of LPBF, two aspects that significantly affect the performance of such sensors have to be investigated. On one hand, the strain transmission between the LPBF-manufactured part to the inserted measuring element carrier needs to be examined and a homogenous as well as a loss-free strain transmission ensured. On the other hand, the strain gauge behavior before and after being exposed to the LPBF-process needs to be investigated. This chapter deals with the first aspect, which is relevant to consider such LPBF-manufactured parts with an inserted measuring element carrier as suitable spring elements for force sensors. Therefore, the focus lies initially on the LPBF-manufactured spring element, which means that for all prototype force sensors presented in this chapter, the strain gauges are applied to the LPBF-manufactured spring element after its completion. This way, the strain gauges remain in their original state, avoiding potential influences of the LPBF-process on the strain gauges that could distort the evaluation of the strain transmission. In order to evaluate the strain transmission and the overall performance of the LPBF-manufactured spring element, a conventionally manufactured spring element with same geometry is prepared that serves as reference. Furthermore, spring elements with different scanning areas are manufactured by LPBF to achieve a variety of contact areas from the LPBF-manufactured base body to the inserted measuring element carrier. This enables investigating the impact of the strain transmission and the thermally induced deformation depending on the scanning area. A conventionally manufactured steel plate is used as measuring element carrier in all LPBF-manufactured spring elements.

3.1 LPBF-system

In this work, a commercially available LPBF-system (type: EOS M290, EOS GmbH, Krailing, DE) with a maximum construction volume of $250\,\mathrm{mm} \times 250\,\mathrm{mm} \times 325\,\mathrm{mm}$ is used. This system has a $400\,\mathrm{W}$ single-mode Yb-fiber continuous-wave laser with a wavelength λ_{Laser} of $1064\,\mathrm{nm}$, which is deflected via a high-speed scanner operating at a speed v_{S} up to $7\,\mathrm{m\,s^{-1}}$. The high-speed scanner consists of an F-Theta lens that focuses the laser beam to the focal point and steers it in the processing plane perpendicular to the optical axis of the lens. This lens provides a focal diameter d_{F} of the laser beam of $100\,\mathrm{\mu m}$. The layer-by-layer powder deposition is done with the coating system (Fig. 3.1), which has a coater blade made of steel. Layer thicknesses between $20\,\mathrm{\mu m}$ and $80\,\mathrm{\mu m}$ can be achieved, depending on the material used. The built-in heating allows temperatures of the build platform T_{BPF} of up to $200\,^{\circ}\mathrm{C}$. The inert gas used in this LPBF-system is argon. In order to monitor the LPBF-system and the manufacturing process, different sensors are provided. On one hand, these include sensors for monitoring the heating of the build platform, the temperature of the build chamber and the oxygen concentration. On the other hand, further camera-based systems are provided to monitor each coating process, the heat emissions from the melt pool as well as the dynamics of the melt pool. One particular feature of the LPBF system used is the fact that it is equipped with a cable harness routed from the process chamber to the outside. This allows for online measurements of sensors that are integrated into LPBF-manufactured parts.

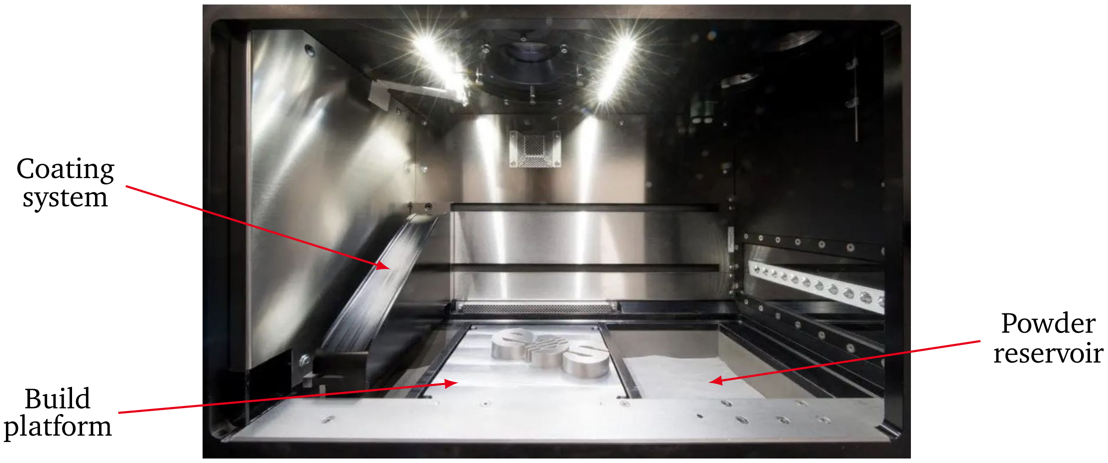

Figure 3.1: Process chamber of the LPBF-system used [image source: www.directindustry.de]. The steel powder is deposited on the build platform with the coating system.

For all experiments in this work, stainless steel 316L (material no.: 1.4404) is used. This austenitic steel exhibits a high corrosion and acid resistance as well as a high ductility and is provided as gas atomized steel powder (type: EOS 316L, EOS GmbH, Krailing, DE) with a particle diameter ranging from $7.8\,\mu m$ to $59\,\mu m$ and a characteristic D_{50} value of $25.2\,\mu m$ [158].

The preparation of a build process is done using the software supplied with the LPBF system (type: EOSPRINT V2.6, EOS GmbH, Krailing, DE). In this case, the part to be manufactured is loaded into the software in Standard Triangle Language (STL) format for setting the process parameters. The resulting build job consisting of the geometry to be manufactured with the specified process parameters is then transferred to the LPBF-system. In this work, the parameter set (316L Surface M291 1.10) qualified by the manufacturer of the LPBF-system is used together with the stripe pattern scanning. The volumetric energy of this parameter set (Tab. 3.1) is $100\,\mathrm{J\,mm^{-3}}$.

Table 3.1: Process parameters of the basic exposure.

Process parameter	**Value**
Laser power P_L	$195\,\mathrm{W}$
Scan speed v_S	$1083\,\mathrm{mm\,s^{-1}}$
Hatch distance d_H	$0.09\,\mathrm{mm}$
Layer thickness h_L	$20\,\mu m$
Stripe width s_w	$5\,\mathrm{mm}$
Overlap stripes s_o	$0.12\,\mathrm{mm}$
Rotation angle α_{rot}	$67°$
Bed temperature T_{Bed}	$80\,°\mathrm{C}$

3.2 Manufacturing of spring elements in disruptive manner

Initially, two base bodies are built up with a height of $8\,\text{mm}$ by LPBF. Here, the base bodies are scanned alternately by the laser. Each base body contains a cavity with a size of $5.1\,\text{mm}$ x $15.1\,\text{mm}$ x $2.07\,\text{mm}$ for inserting the steel plate ($50\,\text{mm}$ x $15\,\text{mm}$ x $2\,\text{mm}$), which serves as measuring element carrier. These cavities are slightly larger than the steel plate to ensure both a reproducible integration of the steel plate and a high process stability (Fig. 3.2). Smaller cavities cause a non-reproducible integration of the steel plate due to the surface roughness of the base bodies and the thermal expansion of the steel plate. The thermal expansion of the steel plate Δl_{SP} can be determined according to Eq. 3.1 [169], using l_{SP} as the length of the steel plate, $\alpha_{\text{T,SP}}$ as the coefficient of thermal expansion of the steel plate and ΔT as the change in temperature of the steel plate due to the process conditions and the impact of the laser beam.

$$\Delta l_{\text{SP}} = l_{\text{SP}} \cdot \alpha_{\text{T,SP}} \cdot \Delta T. \tag{3.1}$$

Based on an austenitic steel plate with $l_{\text{SP}} = 50\,\text{mm}$ and $\alpha_{\text{T,SP}} = 17 \cdot 10^{-6}\,\text{K}^{-1}$ [169] and an average rise in temperature of $120\,\text{K}$, which is shown in chapter 4, a thermal expansion Δl_{SP} of $0.102\,\text{mm}$ is expected. This implies that a smaller gap or even a form fit in x-direction (Fig. 3.2) would lead to a tilting as well as a significant deformation of the steel plate in z-direction during the manufacturing process. As a consequence, collisions between the coating blade and the steel plate can occur, thus reducing the process stability and leading to a faulty process or even to terminating the manufacturing process.

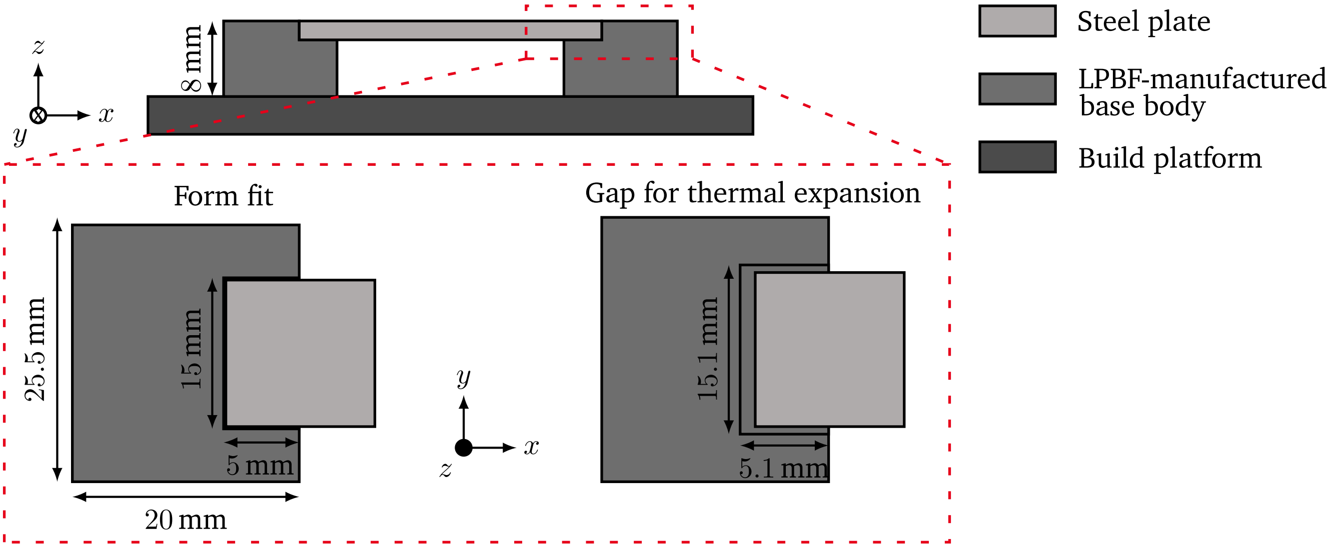

Figure 3.2: Different joining methods between the steel plate and the LPBF-manufactured base bodies in x-direction. A form fit is disadvantageous due to the thermal expansion of the steel plate, which leads to a deformation of the steel plate in z-direction. Hence, a larger cavity is designed for inserting the steel plate.

After manufacturing the base bodies, the build process is interrupted to open the process chamber and remove the powder through suction at the cavities. Next, the steel plate is inserted and protrudes $5\,\text{mm}$ into the base bodies on each side, leaving a small gap for thermal expansion (Fig. 3.2). Subsequently, a layer of powder is applied and the process is resumed to achieve a firmly bonded material connection between the LPBF-manufactured base bodies and inserted steel plate. The lateral connection and the rear connection between the inserted steel plate and the LPBF-manufactured base bodies are made at heights of 1.7 mm and 1.85 mm (Fig. 3.3), respectively.

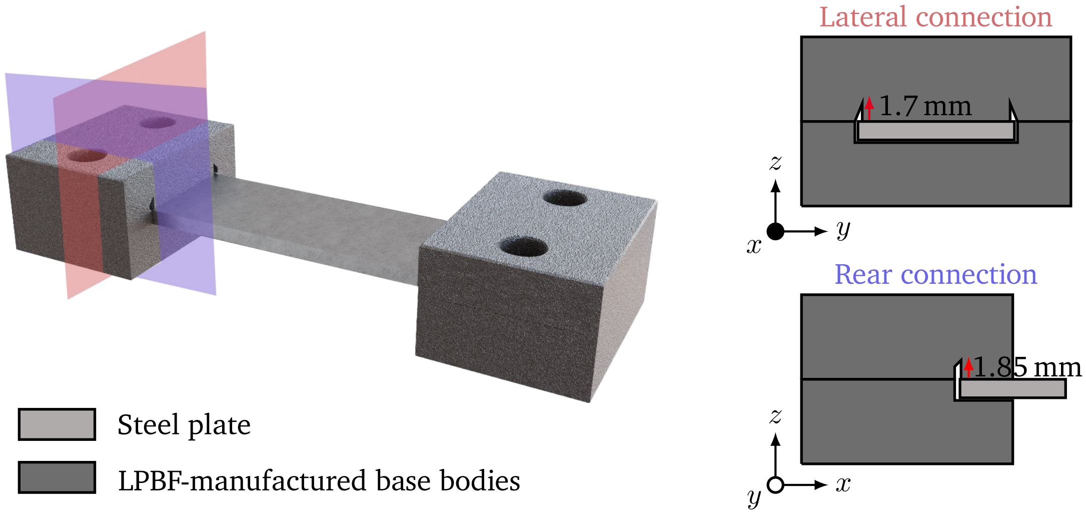

Figure 3.3: Establishing a connection between the LPBF-manufactured base bodies and the inserted steel plate is achieved through a lateral (red plane) and a rear (blue plane) material connection.

In order to investigate the influence of different steel types on the integrability in the disruptive manufacturing process presented in this work, spring elements with two different types of the steel plates are manufactured. One type of steel plates consist of stainless steel 1.4310 while the other consists of stainless steel 1.4404. Both types were cut by a CO_2 laser and deburred afterwards (Stahl Becker GmbH, Heusenstamm, DE). The steel 1.4310 is used due to its favorable mechanical and spring properties. The steel 1.4404 is used to obtain a homogeneous part with respect to the LPBF-manufactured base bodies made from the same steel type.

The scanning area is varied to achieve different contact areas from the LPBF-manufactured upper base bodies to the inserted steel plate. Here, the scanning area corresponds to the area where material is molten and built with the laser. Thus, the contact areas between the LPBF-manufactured upper base bodies and the inserted steel plate are printed either full, with stripes or checkered (Fig. 3.4). This allows the investigation of the strain transmission from the LPBF-manufactured base bodies to the inserted steel plate depending on the scanned area of the steel plate. Additionally, it is possible to investigate if the deformation of the inserted steel plate is reduced by using a smaller scanning area can be carried out. In comparison to the fully printed scanning area, the smaller scanning area, in this case the checkered scanning area, results in a reduction of the amount of energy introduced into the steel plate, and, thus, decreasing the thermally induced deformation of the steel plate. In this manner, six spring elements (P1 – P6) are manufactured with variation of steel plate material and scanning area (Tab. 3.2).

For evaluating the performance of the strain transmission of the LPBF-manufactured spring elements, a further spring element (Conv) with identical geometry is manufactured conventionally by means of milling. Stainless steel 1.4404 is used as material of this reference spring element. Note that manufacturing out of stainless steel 1.4310 is not possible, as the material is only available in thin plates. This conventionally manufactured spring element serves as reference for the LPBF-manufactured spring elements. Hence, it can be investigated if the performance of the LPBF-manufactured spring elements, which is significantly characterized by the strain transmission from the LPBF-manufactured base bodies to the inserted steel plate, is equivalent to that of the conventionally manufactured spring element.

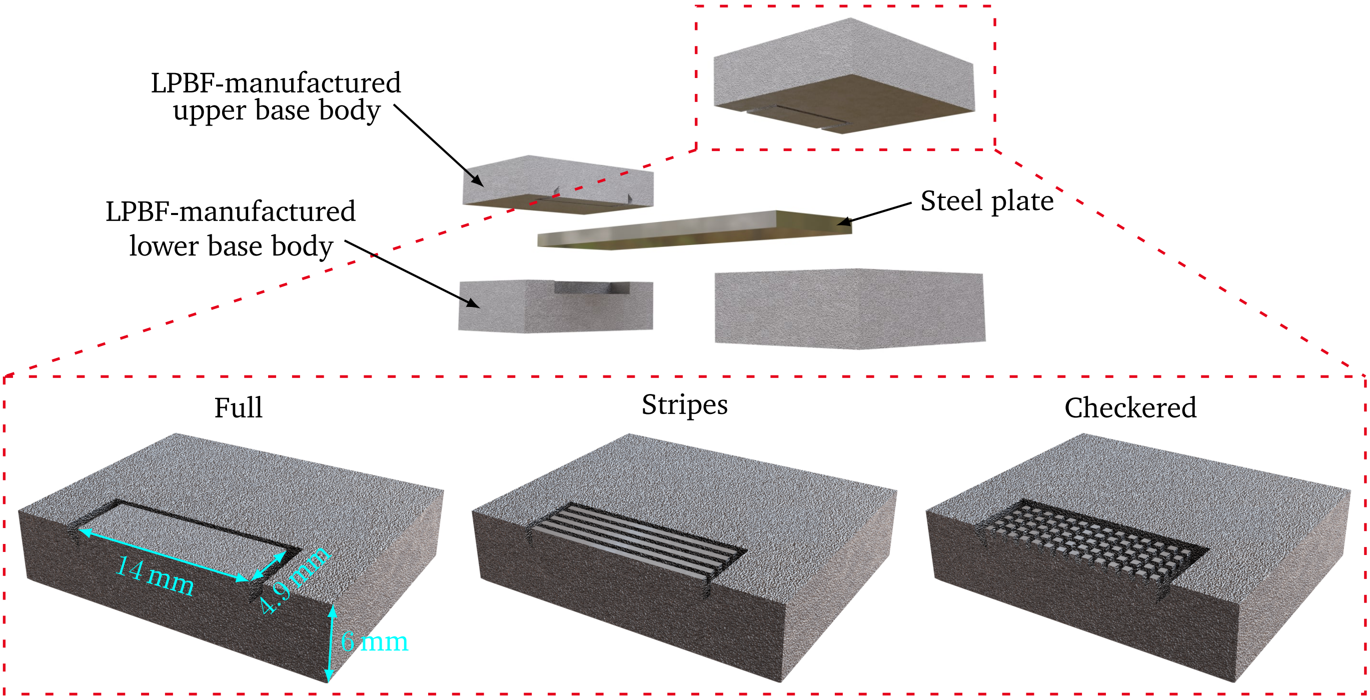

Figure 3.4: The LPBF-manufactured spring elements are built with different scanning areas. The scanning area represents the area, where material is built with LPBF. The contact areas between the LPBF-manufactured upper base bodies and the steel plate are printed either full, with stripes or checkered.

Table 3.2: List of the LPBF-manufactured spring elements with different types of steel plate and varying scanning area.

Prototype	**Steel plate material**	**Scanning area**
P1	1.4310	Full
P2	1.4310	Stripes
P3	1.4310	Checkered
P4	1.4404	Full
P5	1.4404	Stripes
P6	1.4404	Checkered

3.3 Analysis of the strain transmission

In order to investigate the mechanical behavior under load and the strain transmission from the LPBF-manufactured base bodies to the inserted steel plate, a finite element analysis (FEA) (COMSOL Multiphysics

5.6, COMSOL AB, SWE) is carried out. This allows identifying proper positions for strain gauge application, depending on a nominal load. Positions that provide high strain values in the range of $500\,\mu\mathrm{m\,m^{-1}}$ to $1000\,\mu\mathrm{m\,m^{-1}}$ at nominal load while not exceeding the yield strength of the material are preferred [90]. Therefore, a trade-off between high strain and low stress is required.

3.3.1 Determination of the Young's moduli of the steel plates

In order to model the strain transmission accurately, the Young's moduli of the steel plates E_{SP} need to be determined, since the strain gauges will be applied on them. This is a key parameter that defines the stiffness of the steel plates as well as their elastic deformation under load [169], [170]. However, this parameter varies depending on the type of stainless steel (austenitic, ferritic or duplex) and its manufacturing process (cold-formed or hot-rolled) [170]. In literature, the Young's moduli of austenitic and ferritic stainless steels are given as $195\,\mathrm{GPa}$ and $210\,\mathrm{GPa}$, respectively [170]. These values vary strongly, which is also affected to some extent by the choice of the standard for determining the Young's modulus [171]–[174]. In [170], the values for the Young's moduli of austenitic and ferritic stainless steels of several hundred specimens are compared for different product types resulting in $193.9\,\mathrm{GPa} \pm 11.1\,\mathrm{GPa}$ and $200.3\,\mathrm{GPa} \pm 15.5\,\mathrm{GPa}$, respectively. Thus, a determination of the Young's moduli of the steel plates used is necessary for an accurate modeling of the mechanical behavior of the LPBF-manufactured spring elements.

Usually, the Young's modulus E is determined in a tensile test (DIN EN ISO 6892-1), in which the specimen is stretched with a defined tensile force F by means of a testing machine while the resulting change in length of the specimen is recorded with an extensometer [Fig. 3.5(a)]. This measurement results in the stress-strain diagram [Fig. 3.5(b)] for the specimen, from which relevant parameters, can be derived [169]. These include, for example, the yield strength σ_{F}, where the material enters plastic deformation [169]. From the linear-elastic

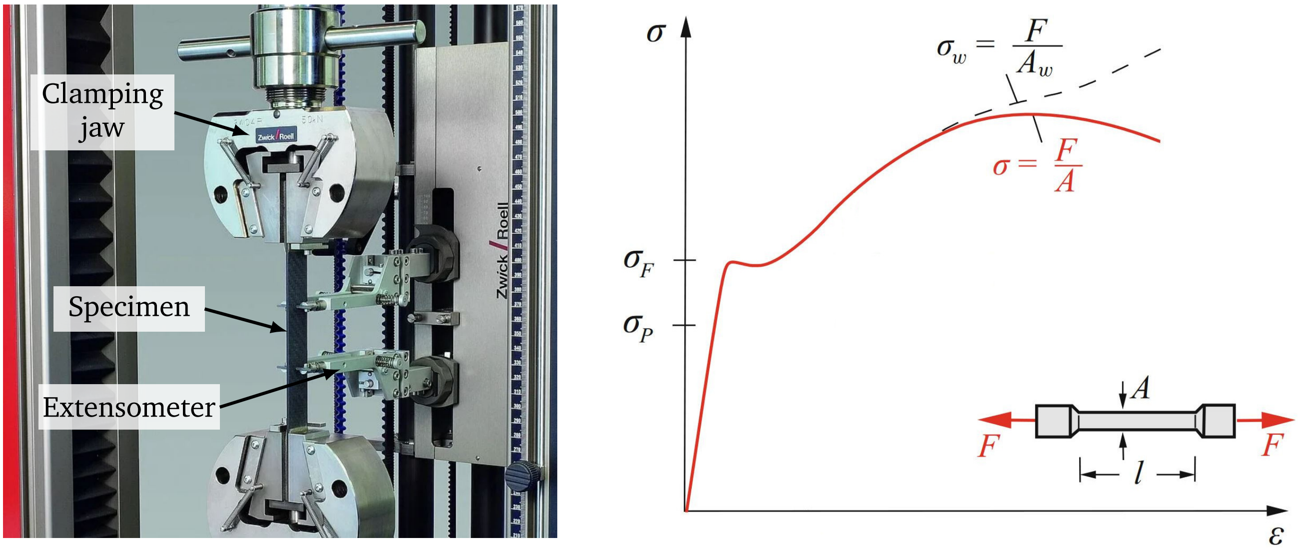

(a) (b)

Figure 3.5: The tensile test is used for material characterization: (a) a specimen is pulled with a defined velocity while measuring the required tensile force and the strain of the specimen (image source: www.zwickroell.com), (b) the resulting stress-strain diagram provides material parameters such as the Young's modulus of the specimen [169].

range up to the proportional limit σ_P of this diagram, the Young's modulus can be derived as the quotient of stress σ and strain ε according to Hooke's law (Eq. 3.2) [169].

$$\sigma = E \cdot \varepsilon \quad \Leftrightarrow \quad E = \frac{\sigma}{\varepsilon} \tag{3.2}$$

Since special clamping jaws and an extensometer are required for the tensile test, the Young's moduli of the steel plates are determined in this work in a bending test. For this purpose, five steel plates each made of stainless steel 1.4310 and 1.4404 are applied with strain gauges replacing the extensometer. One strain gauge (type: 1-LY45-1.5/350, HBK, Darmstadt, DE) with a base resistance R_0 of $350\,\Omega$ is applied to the center of each of the ten plates as described in section 2.3. These steel plates are then clamped at one end [Fig. 3.6(a)] and subjected to bending with a force F_B of $15\,\mathrm{N}$ at the other end. The load is introduced by a spherical pin using a universal testing machine (type: inspekt Table5, Hegewald & Peschke, Nossen, DE) with a $100\,\mathrm{N}$ reference force sensor (type: S2M/100N with $0.02\,\%$ accuracy, HBK, Darmstadt, DE). First, three full-load cycles are carried out using a force-controlled load with a slope of $0.5\,\mathrm{N\,s^{-1}}$ [Fig. 3.6(b)]. These three full-load cycles are not taken into consideration for determining the Young's modulus, but are necessary to exclude settling effects. Afterwards, the load is increased with a slope of $0.1\,\mathrm{N\,s^{-1}}$ until $15\,\mathrm{N}$ are reached and maintained for $30\,\mathrm{s}$. Then, the load is decreased with the same slope until the steel plate is unloaded. A digital multimeter (type: DMM7510, Tektronix, Beaverton, Oregon, US) is used to measure the resistance of the strain gauge during loading. The resistance measurement of the strain gauge is performed in four-wire configuration to eliminate the lead resistances [175], which are in the order of magnitude of the change in resistance of the strain gauge.

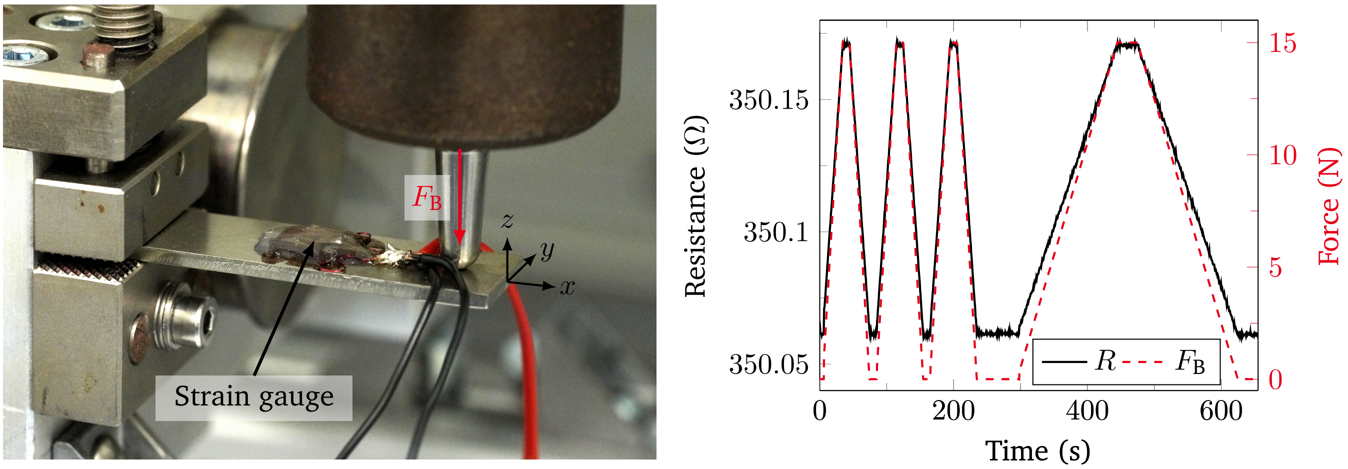

(a) (b)

Figure 3.6: The Young's moduli of the steel plates are determined in a bending test. Therefore, the steel plates with applied strain gauge are clamped at one end and subjected to bending with a force F_B at the other end (a). The measurement of the resistance R of the strain gauge shows a linear behavior during the loading (b).

In order to determine the Young's modulus according to Eq. 3.2, the stress σ_B due to the bending load in the steel plate needs to be identified. Since this experiment is based on uniaxial bending, and, thus, uniaxial stress, only a normal stress in the longitudinal direction (x-direction) of the steel plate can be approximated

[89], [169]. Hereby, it is valid to assume that $\sigma_\text{B} = \sigma$. The bending load F_B causes a bending moment M_B in the clamped steel plates [89], [176]. This bending moment rises linearly along the length of the beam and has a maximum at the clamping location [176]. The bending moment resulting at the position of the strain gauge is determined by Eq. 3.3 with x_SG as the distance between the center of the strain gauge measurement grid and the force application point [89], [176].

$$M_\text{B} = F_\text{B} \cdot x_\text{SG}. \tag{3.3}$$

The bending moment leads to a stress σ_B (Eq. 3.4) that is distributed over the cross-section of the steel plate in the z-direction [Fig. 3.6(a)]. Here, the coordinate system is chosen so that $z = 0$ is located at half the thickness of the steel plate, i.e. the neutral fiber. Thus, a tensile stress is present for $z > 0$ and a compressive stress is present for $z < 0$, resulting in elongation and compression [169], [176], respectively. This is consistent with the expected deformation behavior of a cantilever. Furthermore, the resulting stress depends on the rectangular geometry of the cross-section, which is expressed by the moment of inertia of the cross section of the steel plate I_SP as a measure of the stiffness of the geometry with the width w_SP and a height h_SP against bending [169].

$$\sigma_\text{B} = \pm\frac{M_\text{B}}{I_\text{SP}} \cdot z, \qquad \text{with} \quad I_\text{SP} = \frac{w_\text{SP} \cdot h_\text{SP}^3}{12}. \tag{3.4}$$

The maximum stress $\sigma_\text{B, max}$ arises at the largest distance z_max from the neutral fiber [169], [176]. This corresponds to the surface area of the steel plate, and, thus, half the thickness of the steel plate $h_\text{SP}/2$. In case of maximum stress, the section modulus against bending W_B can be introduced according to Eq. 3.5.

$$W_\text{B} = \frac{I_\text{SP}}{z_\text{max}} = \frac{w_\text{SP} \cdot h_\text{SP}^2}{6}. \tag{3.5}$$

Finally, Eq. 3.3 and Eq. 3.5 can be substituted into Eq. 3.4 to obtain the maximum stress

$$\sigma_\text{B,max} = \pm\frac{6 \cdot F_\text{B} \cdot x_\text{SG}}{w_\text{SP} \cdot h_\text{SP}^2}. \tag{3.6}$$

With $F_\text{B} = 15\,\text{N}$, $x_\text{SG} = 19.5\,\text{mm}$, $w_\text{SP} = 15\,\text{mm}$ and $h_\text{SP} = 2\,\text{mm}$ a maximum stress $\sigma_\text{B,max}$ of $29.25\,\text{MPa}$ occurs at the application area of the strain gauge. Plotting the calculated stress σ_B for the bending load against the strain ε_B derived from the relative change in resistance $\Delta R/R_0$ and the gauge factor k, which is $2.00 \pm 1.5\,\%$ for the strain gauges used, results in an linear behavior for both types of steel plates (Fig. 3.7). This linear behavior of the stress-strain curve is expected since the stress is far below the yield stress ($200\,\text{MPa}$) of both steel plate types, and, thus, in the linear elastic range of the material.

The slope from the stress-strain curve provides the Young's modulus of the steel plates. The stress-strain curve (Fig. 3.7) shows that at the same stress, the 1.4404 steel plate is elongated more than the 1.4310 steel plate. This implies that the 1.4310 steel plate is stiffer than the 1.4404 steel plate, and, thus, has a higher Young's modulus. Based on the stress-strain curves for all 10 steel plates (Tab. 3.3), the higher Young's modulus of the 1.4310 plates compared to the 1.4404 plates is confirmed.

In order to obtain valid measurement results for the Young's moduli of the two steel plate types from the multiple and error-prone measurements of the steel plates, an uncertainty analysis is performed according to the Guide to the Expression of Uncertainty in Measurements (GUM) [177]. The functional relationship for the determination of the Young's modulus based on equations. 3.2, 3.6 and 2.11 is set up as follows

$$E = \frac{6 \cdot F_\text{B} \cdot x_\text{SG} \cdot R_0 \cdot k}{w_\text{SP} \cdot h_\text{SP}^2 \cdot \Delta R}. \tag{3.7}$$

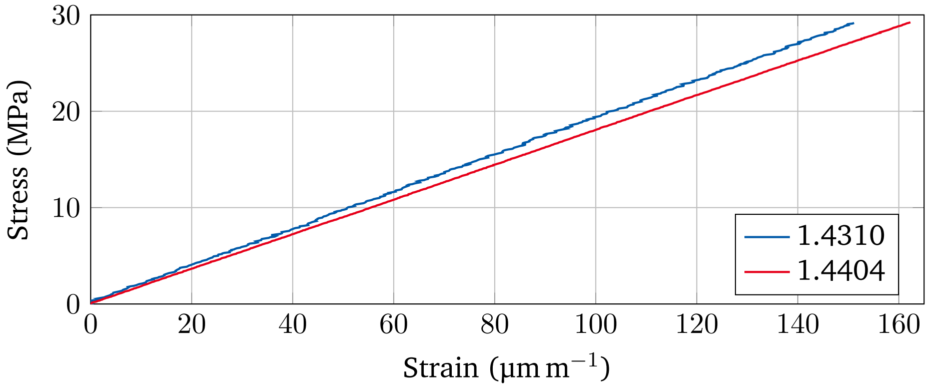

Figure 3.7: The stress-strain curves of exemplary specimens from both types of steel plates (1.4310 and 1.4404) resulting from the bending test show an expected linear behavior, since the stress is far below the yield stress, and, thus, in the linear elastic range of the material.

Table 3.3: Determined Young's moduli from the slope of the stress-strain curves for the two stainless steel plate types.

Specimen	Stainless steel 1.4310	Stainless steel 1.4404
1	188.4 GPa	181.1 GPa
2	190.1 GPa	179.9 GPa
3	185.8 GPa	179.4 GPa
4	191.8 GPa	180.2 GPa
5	189.2 GPa	178.7 GPa

Note that Eq. 3.7 considers only the tensile stress and strain regarding the sign. It is also possible to determine the Young's modulus with the compressive stress and compression. In Eq. 3.7, the parameters R_0, ΔR, x_{SG} and k are subject to uncertainty. The mean values and empirical standard deviations are determined for these parameters (Tab. 3.4). Except for the gauge factor k, which is taken from a data sheet, and, thus, assumed to have a rectangular distribution, the other three parameters are assumed to be normally distributed. The parameters F_{B}, w_{SP} and h_{SP} in Eq. 3.7 are considered as constants without uncertainty. These parameters are used to determine the mean values and uncertainties of the Young's moduli using GUM and the Gaussian error propagation. This results in Young's moduli of the two steel plate types for a confidence level of $95\,\%$ of

$$E_{1.4310} = 187.1\,\mathrm{GPa} \pm 3.4\,\mathrm{GPa} \qquad \text{and} \qquad E_{1.4404} = 179.1\,\mathrm{GPa} \pm 2.8\,\mathrm{GPa}. \tag{3.8}$$

These determined Young's moduli allow for modeling the strain transmission of the LPBF-manufactured spring elements in the next step.

3.3.2 Modeling of the structural mechanics

The FEA model of the LPBF-manufactured spring elements is based on a form assembly. It consists of the two LPBF-manufactured base bodies (lower and upper base bodies are already connected), the inserted steel plate and two steel fasteners. The steel fasteners are required for attaching the LPBF-manufactured spring

Table 3.4: Parameters for the uncertainty analysis of the Young's moduli.

Parameter	**Mean $\overline{x}$**	**Empirical standard deviation s_x**	**Distribution**
$R_{0,1.4310}$	$350.0506\,\Omega$	$0.1321\,\Omega$	normal
$\Delta R_{1.4310}$	$0.1099\,\Omega$	$0.0011\,\Omega$	normal
$x_{\mathrm{SG},1.4310}$	$19.58\,\mathrm{mm}$	$0.08\,\mathrm{mm}$	normal
$R_{0,1.4404}$	$350.0294\,\Omega$	$0.2612\,\Omega$	normal
$\Delta R_{1.4404}$	$0.1146\,\Omega$	$0.0006\,\Omega$	normal
$x_{\mathrm{SG},1.4404}$	$19.54\,\mathrm{mm}$	$0.05\,\mathrm{mm}$	normal
k	2	0.03	rectangular

elements for subsequent characterization by a testing machine as well as for a central force introduction, i.e. application of a force at equal distance to the two ends. The model takes into account that a connection between the LPBF-manufactured base bodies and the steel plate is only made by the molten powder of the LPBF-manufactured upper base bodies. Therefore, the part is modeled to be continuous across that connection boundary via the *Identity pair* boundary whereas the surfaces of the steel plate and LPBF-manufactured lower base bodies can only transfer normal contact forces an soon as a contact is made through the *Contact pair* boundary (Fig. 3.8). Note that between the surface underneath the steel plate and the LPBF-manufactured lower base bodies a small gap of $70\,\mu\mathrm{m}$ is considered. This is due to the height ($2.07\,\mathrm{mm}$) of the manufactured cavity, which is designed to be larger because of the surface roughness. All other touching boundaries such as the transition from steel fasteners to the LPBF-manufactured base bodies are also continuous. The materials used are 1.4310 stainless steel (prototypes P1 – P3) and 1.4404 stainless steel (prototypes P4 – P6) to define the steel plates and 1.4404 stainless steel to define the LPBF-manufactured base bodies. Furthermore, structural steel from the built-in material library is used for the steel fasteners.

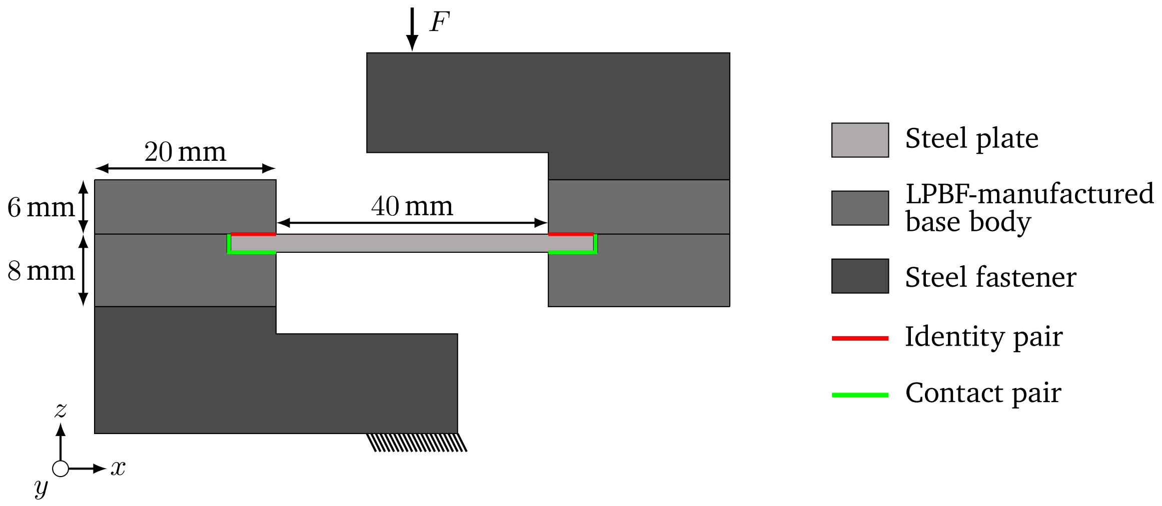

Figure 3.8: Schematic of the FEA model of the LPBF-manufactured spring element with boundary conditions. The spring element is attached to steel fasteners that are used to introduce a centric force.

The mesh of the steel plate consists of cubes with an edge length of $0.4\,\mathrm{mm}$, and the LPBF-manufactured base bodies as well as the steel fasteners are meshed with tetrahedrals (Fig. 3.9). The size of the mesh elements of the steel plate is a result from a mesh refinement study, which revealed that smaller mesh elements do not provide a measurable change in the result. In comparison to a mesh, where the steel plate is also meshed with tetrahedrals of the same size, the chosen mesh yields a reduction in the number of elements by $39.4\,\%$ and an increase in mesh quality by $9.7\,\%$. The skewness is used as a quality measure [178]. Consequently, both numerical efficiency and a more accurate result are obtained with the chosen mesh.

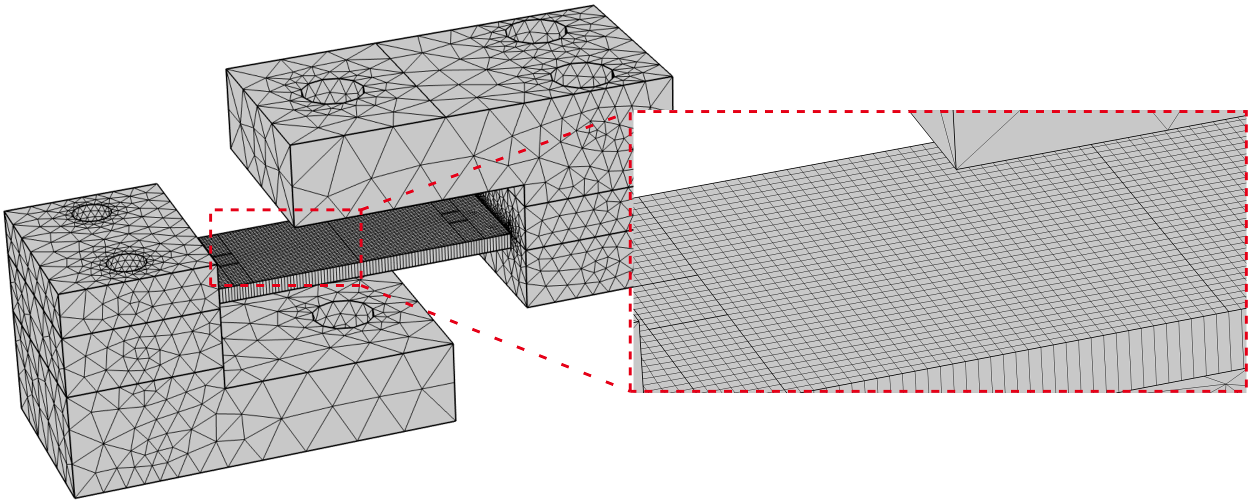

Figure 3.9: The mesh elements of the modeled LPBF-manufactured spring element consist of cubes and tetrahedrals. Since the strain of the steel plate is sought, it is meshed more finely.

The stress σ and strain ε of the LPBF-manufactured spring element caused by a force F are calculated considering three equations: the equilibrium balance, the kinematic relation relating displacement to strain, and the constitutive relation relating stress and strain [169], [179]. Note that tensors (written in bold) are considered, since the stress and strain are sought at all points of the spring element in 3D. The equilibrium balance is defined through Newton's second law of motion. In tensor form [179], the equilibrium relation is given by

$$\nabla \cdot \boldsymbol{\sigma} + F_{\mathrm{V}} = \rho \cdot \ddot{u}, \tag{3.9}$$

where $\boldsymbol{\sigma}$ is the stress tensor (second order tensor) that defines the state of stress at any point within a body [169], F_{V} is the body force per volume, ρ is the density, and $\ddot{u}$ is the acceleration. In static analyses, no movement of the body is assumed, so that there is no acceleration, and, thus, $\ddot{u} = 0$.

The stresses cause deformations and displacements of the body. Based on the kinematic relation, a relationship between the displacement tensor $\boldsymbol{u}$ and the strain tensor $\boldsymbol{\varepsilon}$ (second order tensor) of an infinitesimal cuboid within the body is described. This results in tensor form to

$$\boldsymbol{\varepsilon} = \frac{1}{2}\left[\nabla \boldsymbol{u} + (\nabla \boldsymbol{u})^{\mathrm{T}}\right], \tag{3.10}$$

where T denotes the tensor transpose [179]. If only small deformations are assumed according to the infinitesimal strain theory [169], [179], the strain tensor from Eq. 3.10 can be represented for rectangular

Cartesian coordinates in indicial notation as

$$\varepsilon_{ij} = \frac{1}{2}\left[\frac{\delta u_j}{\delta x_i} + \frac{\delta u_i}{\delta x_j}\right], \tag{3.11}$$

where i, j correspond to the coordinate directions x, y, z [169], [179].

The third equation is a constitutive equation. It describes the deformation of a body caused by stresses, and, thus, relates stress and strain. For a linear-elastic material behavior, the tensors of these two variables are related through the generalized Hooke's law as

$$\boldsymbol{\sigma} = \boldsymbol{C} : \varepsilon, \tag{3.12}$$

where $\boldsymbol{C}$ represents the fourth order elasticity tensor, which is based on the intrinsic material properties [169], [179]. The : denotes the double dot tensor product. The generalized Hooke's law from Eq. 3.12 is extended in Comsol to

$$\boldsymbol{\sigma} - \boldsymbol{\sigma}_{\text{inel}} = \boldsymbol{C} : (\varepsilon - \varepsilon_{\text{inel}}), \tag{3.13}$$

with $\boldsymbol{\sigma}_{\text{inel}}$ and $\varepsilon_{\text{inel}}$ as the inelastic stress and strain components, respectively. These inelastic components include, for example, the pre-stress and pre-strain of the body, as far as they are initially present, but also contributions that result from further external parameters such as temperature. For the calculation of the investigated spring elements, the inelastic components are not considered, and, thus, set to 0.

The elasticity tensor $\boldsymbol{C}$ consists of 81 components in 3D. However, due to symmetry reasons, this number is reduced to 36 components [180]. For an isotropic material, the elasticity tensor can then be expressed as a 6x6 elasticity matrix using the Voigt notation [181]

$$\boldsymbol{C} = \begin{bmatrix} \lambda+2\mu & \lambda & \lambda & 0 & 0 & 0 \\ \lambda & \lambda+2\mu & \lambda & 0 & 0 & 0 \\ \lambda & \lambda & \lambda+2\mu & 0 & 0 & 0 \\ 0 & 0 & 0 & \mu & 0 & 0 \\ 0 & 0 & 0 & 0 & \mu & 0 \\ 0 & 0 & 0 & 0 & 0 & \mu \end{bmatrix} \tag{3.14}$$

with λ and μ as the Lamé constanst given by

$$\lambda = \frac{\nu}{(1+\nu)(1-2\nu)} \cdot E \qquad \text{and} \qquad \mu = \frac{1}{2(1+\nu)} \cdot E, \tag{3.15}$$

where E is the Young's modulus and ν is the Poisson's ratio [180]. In 3D, both the stress tensor and the strain tensor consist of 9 components, of which only 6 are independent due to symmetry. Using the Voigt notation, Eq. 3.12 can be represented in matrix notation as

$$\begin{bmatrix} \sigma_{11} \\ \sigma_{22} \\ \sigma_{33} \\ \sigma_{23} \\ \sigma_{31} \\ \sigma_{12} \end{bmatrix} = \begin{bmatrix} \lambda+2\mu & \lambda & \lambda & 0 & 0 & 0 \\ \lambda & \lambda+2\mu & \lambda & 0 & 0 & 0 \\ \lambda & \lambda & \lambda+2\mu & 0 & 0 & 0 \\ 0 & 0 & 0 & \mu & 0 & 0 \\ 0 & 0 & 0 & 0 & \mu & 0 \\ 0 & 0 & 0 & 0 & 0 & \mu \end{bmatrix} \cdot \begin{bmatrix} \varepsilon_{11} \\ \varepsilon_{22} \\ \varepsilon_{33} \\ 2\varepsilon_{23} \\ 2\varepsilon_{31} \\ 2\varepsilon_{12} \end{bmatrix}, \tag{3.16}$$

where the indexes 1, 2 and 3 represent the coordinate directions x, y and z.

Based on Eq. 3.9, 3.11, 3.15 and 3.16, the stress and strain caused by a tensile or compressive force can be calculated for each mesh element. The Young's moduli of the LPBF-manufactured base bodies are set to $185\,\mathrm{GPa}$. For the steel fasteners, structural steel from the Comsol material library is selected, and, thus, a Young's modulus of $200\,\mathrm{GPa}$. A Poisson's ratio of 0.3 is set for all components of the model. Besides the contact boundaries, the FEA model remains the same for the conventionally manufactured spring element.

In order to identify suitable locations for the application of the strain gauges, the nominal force F_N at which the resulting stress remains below the yield strength of the material must be determined. This prevents plastic deformation. Since the maximum stress occurs at notches, such as at the transitions from the steel plate to the LPBF-manufactured base bodies, a notch stress analysis is performed. This analysis showed that for both types of steel plates, a nominal force F_N of $15\,\mathrm{N}$ leads to a maximum notch stress of $130\,\mathrm{MPa}$. Taking a safety factor of 1.5 into account regarding the yield strength ($200\,\mathrm{MPa}$), no plastic deformation is expected to occur at a load of $15\,\mathrm{N}$. In the next step, a stationary study is thus performed with this nominal force as a compressive force.

This loading case can be considered as two cantilevers with half the length of the steel plate, which are loaded at the free end with opposing forces and are thus symmetric to each other with respect to the center of the steel plate (Fig. 3.10). Thus, the spring element modeled can be considered like a bending beam that is clamped at the left end and guided vertically at the right end. This is commonly used in load cells with a double bending beam structure. The simulation shows exactly the expected strain behavior. The vertically guided end enforces a vertical lowering of the load application point. As a result, the deformation is S-shaped [Fig. 3.11(a)]. This causes elongation and compression on the top and bottom of the left end of the steel plate, respectively, which are inverted compared to the right end of the steel plate. Since the maximum strain and compression occur at the edge regions of the steel plate, these areas are suitable for application of the strain gauges [Fig. 3.11(b)].

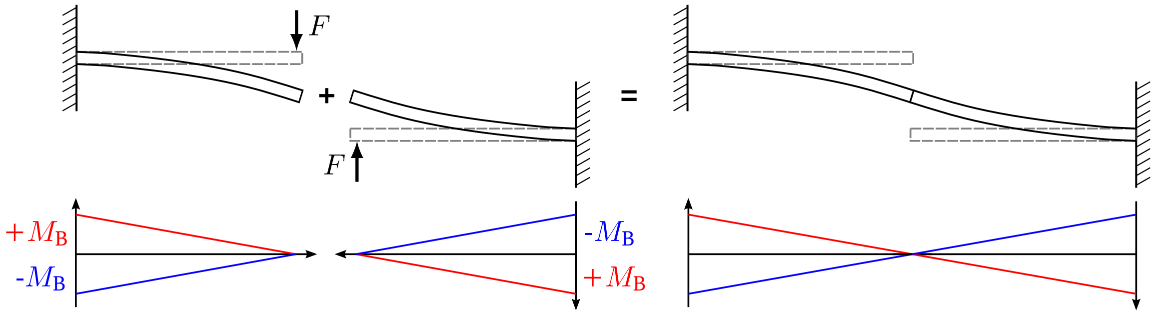

Figure 3.10: The deformation loaded with a compressive force can be modeled with two cantilevers, which are loaded at the free end with opposing forces. Thus, an S-shaped deformation occurs.

In theory, the strain profile for this load case is identical on the top and bottom surfaces along the plate for such a spring element, but inverted. However, as a firmly bonded material connection between the steel and the LPBF-manufactured base bodies is only made on the upper side of the steel plate, there are small deviations in the strain profile between the top and bottom surfaces (Fig. 3.12). Larger deviations occur at the transition from the steel plate to the LPBF-manufactured base bodies. Singularities are observed especially on the upper side at the continuous connection of the steel plate to the LPBF-manufactured base bodies, which

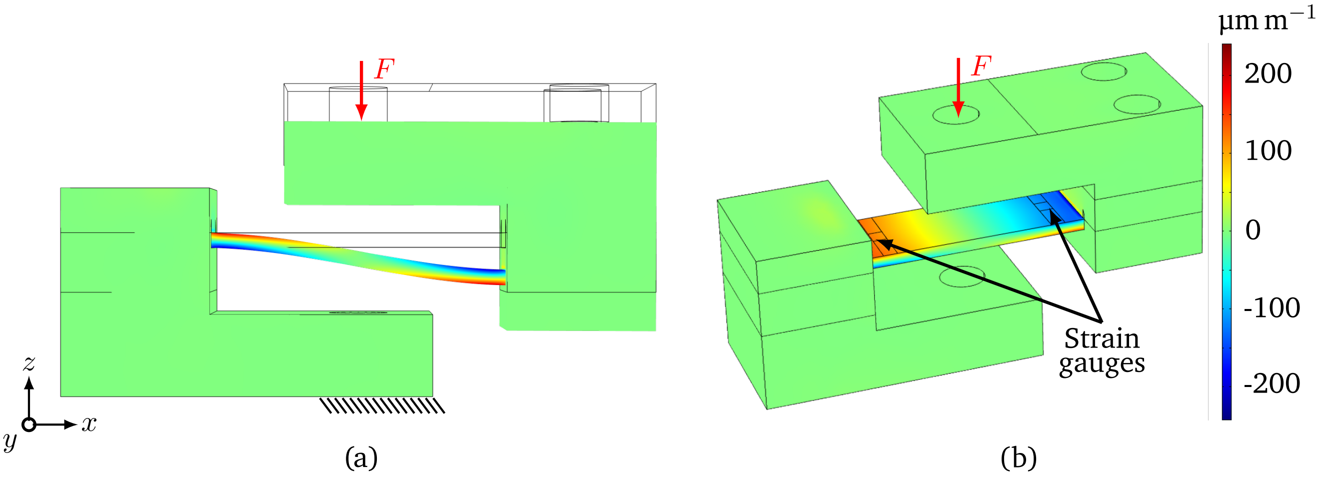

Figure 3.11: Simulated strain of the spring element with a 1.4310 steel plate and fully printed scanning area (Prototype P1) when loaded with 15 N. The expected behavior of an S-shaped deformation is present (a). The maximum strain and compression are at the edge regions of the steel plate, which makes the locations at the ends of the steel plate suitable for strain gauge application (b).

lead to excessive strain and compression values. This is caused by the formed notch, which is not present on the bottom side of the steel plate due to the lack of bonding to the LPBF-manufactured base bodies. Excluding the edge areas, the strain profile of the top and bottom surface of the steel plate is nearly equal. Therefore, positions with a distance of 2 mm from the edge are chosen for applying the strain gauges (Fig. 3.12, dashed lines), i.e. avoiding the singularities area. Since the initial focus is only on the strain transmission from the LPBF-manufactured base bodies to the inserted steel plate, the strain gauges are applied after fabrication of the spring element. Two strain gauges are applied to the top side and two to the bottom side of the steel plate. This allows implementing a full bridge configuration since two strain gauges undergo strain and the other two undergo compression.

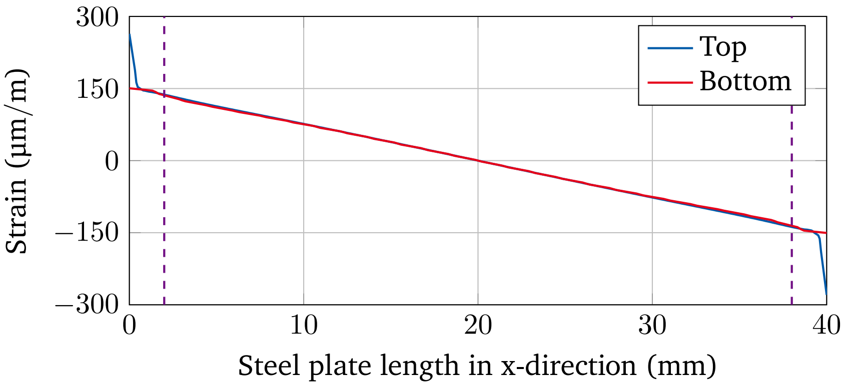

Figure 3.12: The strain and compression are nearly equal at the top and bottom surface while exhibiting the maximum values at the edges of the steel plate. Note, that the strain profile for the bottom surface is multiplied by -1 for better comparability. For the application of the strain gauges, positions with a distance of 2 mm from the edge are chosen (marked as dashed lines), i.e. avoiding the singularities area.

The strain behavior (Fig. 3.11) and strain profile along the steel plate (Fig. 3.12) exemplarily shown for prototype P1 are also valid for all other LPBF-manufactured spring elements (Tab. 3.2). For all these LPBF-manufactured spring elements, which differ in steel plate type and scanning area, the simulated strain at the strain gauge application areas is determined and averaged (Tab. 3.5). As a result, strains in the ranges of $111.9\,\mu\mathrm{m\,m^{-1}}$ to $116.2\,\mu\mathrm{m\,m^{-1}}$ and $117.2\,\mu\mathrm{m\,m^{-1}}$ to $121.1\,\mu\mathrm{m\,m^{-1}}$ will be expected for all LPBF-manufactured spring elements with 1.4310 and 1.4404 steel plates, respectively. This serves as a measure for subsequent verification and validation of the model.

Table 3.5: Simulated strains for all prototypes that are expected to be measured by the strain gauges.

Prototype	Steel plate material	Simulated strain
P1	1.4310	$114.1\,\mu\mathrm{m\,m^{-1}} \pm 2.1\,\mu\mathrm{m\,m^{-1}}$
P2	1.4310	$114.0\,\mu\mathrm{m\,m^{-1}} \pm 2.1\,\mu\mathrm{m\,m^{-1}}$
P3	1.4310	$114.1\,\mu\mathrm{m\,m^{-1}} \pm 2.1\,\mu\mathrm{m\,m^{-1}}$
P4	1.4404	$119.1\,\mu\mathrm{m\,m^{-1}} \pm 1.9\,\mu\mathrm{m\,m^{-1}}$
P5	1.4404	$119.1\,\mu\mathrm{m\,m^{-1}} \pm 1.9\,\mu\mathrm{m\,m^{-1}}$
P6	1.4404	$119.2\,\mu\mathrm{m\,m^{-1}} \pm 1.9\,\mu\mathrm{m\,m^{-1}}$

3.4 Characterization of the prototype force sensors

For investigating the performance of the LPBF-manufactured spring elements, two main properties of interest are:

- Manufacturing characteristics, and
- Behavior under static load.

Regarding the first point, the influence of the material connection as well as the bending of the spring elements due to thermally induced stresses have to be examined. In fact, the conventionally manufactured spring element is made of a single part, i.e. without any material transition. Therefore, the intrinsic stresses resulting from milling are not as severe as in the case of the LPBF-process. It should be noted that explicitly no heat treatment is performed, since in the later stage the strain gauges will be integrated before completion of the LPBF-manufactured spring element, and, thus, stress relieving at high temperatures is also not possible. This ensures better comparability. Regarding the second point, characteristic values of force sensors such as linearity error, hysteresis error, temperature behavior, creep error and behavior under cyclic loading of the prototype force sensors have to be determined and compared to the ones of the conventionally manufactured reference sensor.

Hence, the experiments are grouped into two categories. Based on these two investigations it is to be determined whether the strain transmission of the LPBF-manufactured spring elements is as good as in the case of the conventionally manufactured spring elements. This is mandatory for fabricating force sensors based on the disruptive manufacturing process presented here that act as equivalent sensors based on the conventional approach.

3.4.1 Investigation of the manufacturing characteristics

The disruptive manufacturing process of all six LPBF-manufactured spring elements (P1 – P6) resulted in a firmly bonded material connection between the LPBF-manufactured base bodies and the inserted steel plates. However, thermally induced stresses from the manufacturing process are clearly evident, which cause severe deformation of the steel plates (Fig. 3.13). Generally, such residual stresses are caused by high temperature gradients, shrinkage or non-uniform plastic deformation during the heating and cooling cycle as well as large amounts of thermal expansion [157], [159], [160], [182] and can cause distortion [160], cracking [160], [183], [184] and delamination [185] of the manufactured part. All the above-mentioned sources for the residual stresses are process-related. In the case of the spring element with inserted steel plate considered in this work, the residual stresses arise through an interaction of the process characteristics and the chosen geometry, which in turn lead to the deformation.

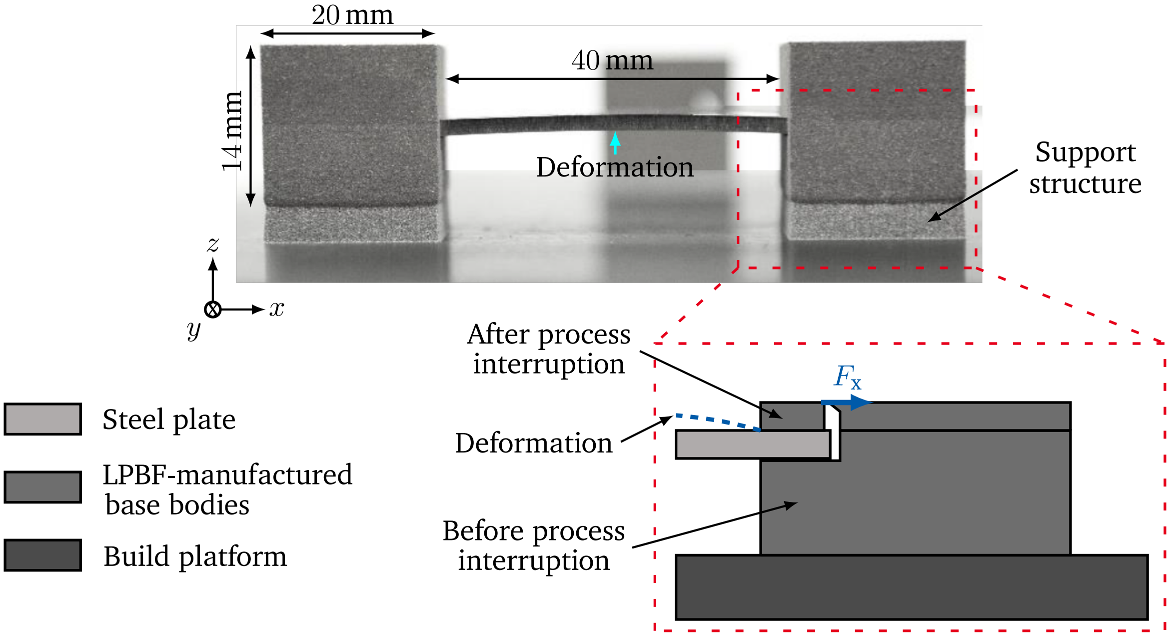

Figure 3.13: Thermally induced stresses cause a severe deformation of the inserted steel plate. The magnitude of the deformation depends on the process parameters and the different cooling rates of the material built on the steel plate and LPBF-manufactured base body at the level of the rear connection. This results in a tensile stress, and, thus, a force F_x that acts from the steel plate to the LPBF-manufactured base body. Hence, this leads to the deformation of the steel plate.

The deformation of the steel plate is caused by a tensile stress that acts in the x-direction resulting from the layer-by-layer build-up in the LPBF-process [46]. Here, powder is applied layer-by-layer and melted by means of the energy introduced by the laser. The heated and melted material becomes softer, and, thus, expands [184]. The material then cools down and contracts [184]. In the area of the rear connection (Fig. 3.3), i.e., when the connection is made between the inserted steel plate and the LPBF-manufactured base bodies, tensile stress occurs in the x-direction. The molten material cools down faster in the area of the larger LPBF-manufactured base bodies due to better heat conduction than in the area of the inserted steel plate. The heat convection via the surrounding air and the powder bed is much lower. Thus, the tensile stress acts from the inserted steel plate towards the LPBF-manufactured base bodies. Since the LPBF-manufactured base bodies are joined to the build platform, the tensile stress results in a force F_x that deforms the steel plate

(Fig. 3.13). This effect also occurs in the y-direction due to a resulting force F_y during the lateral connection, whereas the x-direction dominates. Based on the height of the rear connection, a lever arm is formed, which influences the force acting on the steel plate significantly [46].

The resulting deformation has two drawbacks. On one hand, the mechanical properties are affected [159], [182] due to a possible remaining plastic deformation within the steel plate, which impairs the linear behavior of the LPBF-manufactured spring element. Furthermore, the strength of the LPBF-manufactured spring element is reduced, since residual stresses in the LPBF-manufactured spring element must always be taken into account when loaded. On the other hand, the process stability is affected, as the deformation leads to collisions between the coating blade and the steel plate. Consequently, defects occur in the coating process [46], i.e., gaps arise when a new powder layer is applied (Fig. 3.14). These defects in the coating increase the porosity of the manufactured part leading to bonding failures in the subsequent layers, due to the insufficient amount of powder for building the layer. Based on these issues, a reduction of this deformation is required for the development of well-defined force sensors. This topic is an essential part of the work of the PTW group [46] and will be discussed in chapter 5.

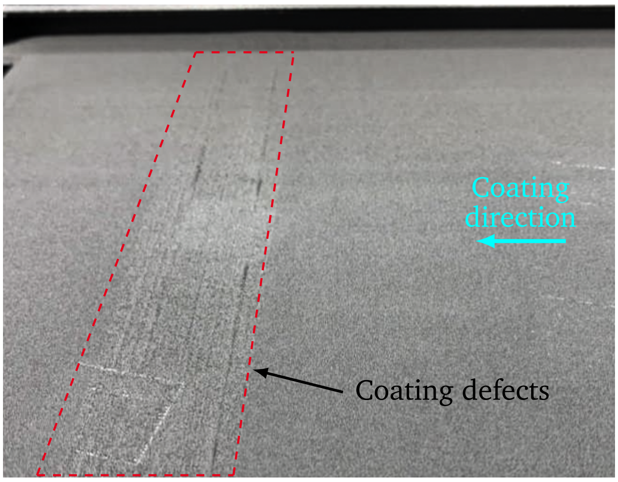

Figure 3.14: The deformation of the inserted steel plate causes collisions with the coating blade. This results in defects in the coating, so that gaps are created [46]. Note that the defects in the coating are reworked using image processing so that they are more prominent.

In order to quantify the deformation, the surface of the steel plate [Fig. 3.15(a)] is measured with a 3D surface microscope (type: InfiniteFocusG5 plus, Alicona Imaging GmbH, Graz, AUT) at a twentyfold object magnification and a vertical resolution of $d_\mathrm{A} = 80\,\mathrm{nm}$. This results in an accuracy of $0.05\,\%$. The LPBF-manufactured spring element remains on the build platform and in a cooled state at room temperature during the measurement. The measurement provides information about the height profiles along the steel plate. For better investigating the entire deformation of the steel plate, the height profiles along the x-axis are evaluated at three locations on the y-axis: $0\,\mathrm{mm}$, $7.5\,\mathrm{mm}$ and $15\,\mathrm{mm}$, which are the front, center and back of the plate when considering the y-axis [Fig. 3.15(a)]. The extracted height profiles contain some outliers [Fig. 3.15(b)], which are caused by overexposure at higher reflecting areas of the steel plate. The maximum deformation values from the height profiles are obtained by using third-order polynomial fit for each of the curves. The maximum deformation values recored in the middle of the steel plate are $0.478\,\mathrm{mm}$, $0.514\,\mathrm{mm}$ and $0.484\,\mathrm{mm}$ for the three height profiles at the front, center and back of the steel plate surface, respectively. Based on these values and the different start and end points of the three height profiles, it can be concluded that the steel plate is not only deformed but also tilted. The magnitude of the deformation, which is shown for the LPBF-manufactured spring element P1 (Fig. 3.15), is approximately the same for the remaining spring elements P2 – P6.

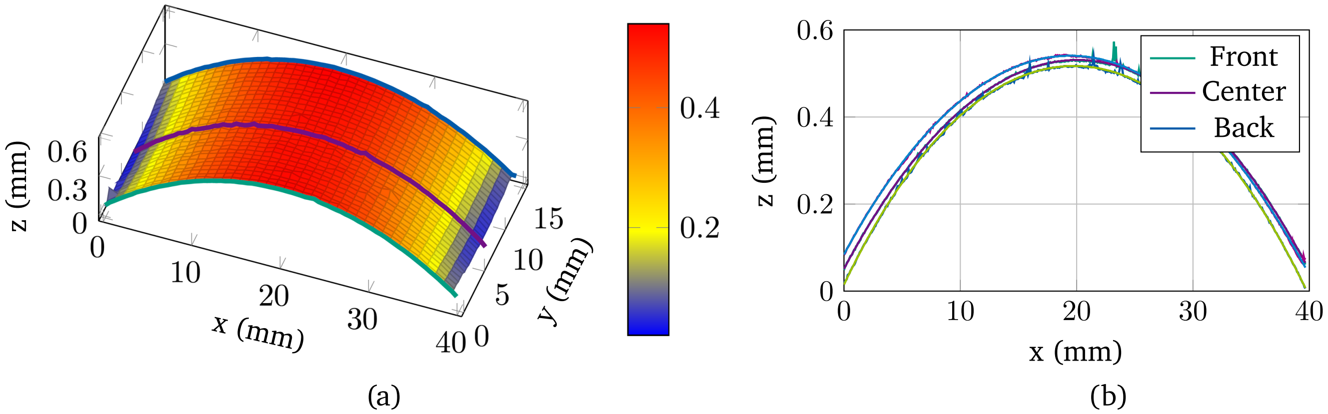

(a) (b)

Figure 3.15: The maximum deformation of the inserted steel plate of the LPBF-manufactured spring element P1 is about $0.5\,\mathrm{mm}$. Furthermore, the height profiles along the x-axis that are evaluated at three locations on the y-axis: $0\,\mathrm{mm}$ (front), $7.5\,\mathrm{mm}$ (center) and $15\,\mathrm{mm}$ (back) show that not only a deformation is present but also a tilting [186].

In the next step, the LPBF-manufactured spring elements are separated from the build platform using a band saw. The deformation of the steel plate is thereby released due to relaxation processes. However, part of the thermally induced stresses remain and are revealed in skew edges. An optical evaluation using a microscope (type: VHX-600D, Keyence, Osaka, JPN) shows that the angle between the inserted steel plate and the LPBF-manufactured base bodies is about $93°$ [Fig. 3.16(a)]. This corresponds to a distortion of $3°$, which is almost identical for all six LPBF-manufactured spring elements (P1 – P6). Hence, the deformation of the different LPBF-manufactured spring elements is nearly equal regardless of the scanning area. The expected lower deformation due to the lower introduced thermal energy in case of the LPBF-manufactured spring elements P2 and P5 with stripes as scanning area as well as for P3 and P6 with checkered scanning area is not achieved. There are two possible causes for this. On one hand, the influence of the occuring tensile stress due to the different cooling rates in combination with the lever might dominate the formation of the deformation. On the other hand, it is possible that in the case of the smaller scanning areas, the same amount of energy is introduced effectively throughout the entire build-up process as in the case of the fully printed scanning area. In the beginning of the re-start of the LPBF-process, there is definitely less energy introduced in the cases with smaller scanning area. However, after 38 layers, the both types of smaller scanning areas (stripes and checkered) merge and turn into the fully printed scanning area. Both aspects lead to the fact that the resulting deformation of the steel plate due to thermally induced stresses is independent of the scanning area for the currently selected geometry. In order to investigate the influence of the smaller scanning area independently, the pattern (stripes or checkered) is not allowed to be merged, as in the case of this work. This will be further examined in the next chapter.

For investigating the material bonding between the LPBF-manufactured base bodies and the inserted steel plate, micrographs are prepared. Therefore, a further spring element with fully printed scanning area and a 1.4310 steel plate as in the case of LPBF-manufactured spring element P1 is fabricated with the same process parameters and then sliced centrally along its longitudinal axis (x-axis). Subsequently, one of the two halves is grinded and polished followed by an examination with the microscope (type: VHX-600D, Keyence, Osaka, JPN). The cross-sectional view [Fig. 3.16(b)] shows the one-sided bonding of the inserted steel plate with the LPBF-manufactured upper base body. Here, a clear bonding zone with the material transition can be identified. In addition, a material intermixing takes place resulting in the intrusion of the molten 1.4404 steel powder into the steel plate.

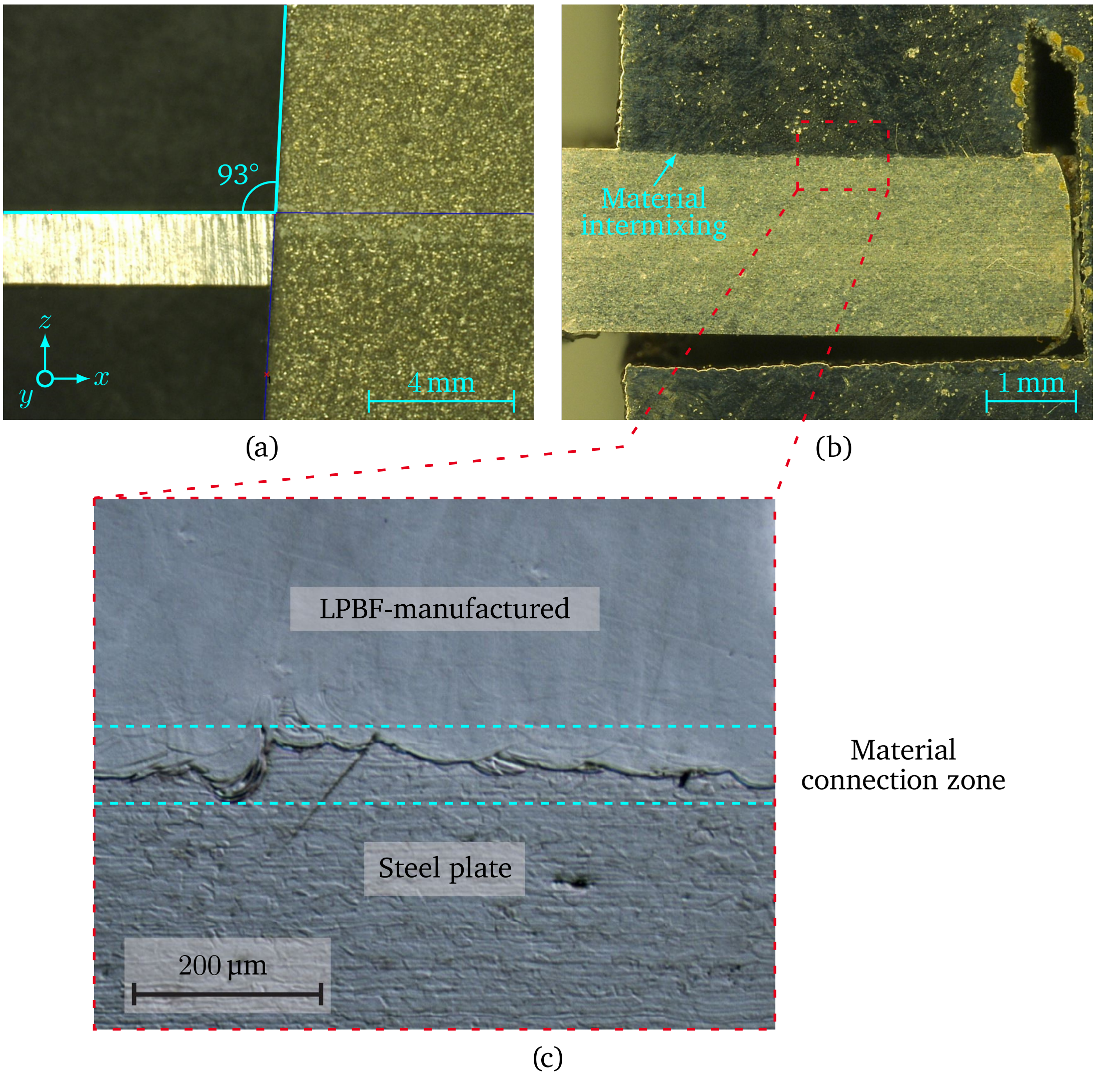

(a) (b) (c)

Figure 3.16: The thermally induced stresses in the LPBF-manufactured spring elements lead to skew edges that form an angle of $93°$ with the horizontal as illustrated (a). However, the cross-sectional view of a spring element with fully printed scanning area shows a clear bonding zone between the LPBF-manufactured upper base body and the inserted steel plate (b). The dashed lines in cyan in the micrograph show the material intermixing of the LPBF-manufactured upper base body with the inserted steel plate (c). This shows a proper material bonding.

For a more detailed investigation of the bonding zone with the material intermixing, the other half is prepared according to conventional metallographic methods. Therefore, the specimen is first cleaned with isopropanol and then embedded in an epoxy resin mixture (type: EpoFix Resin and EpoFix Hardener, Struers, Kopenhagen, DK) with a mixing ratio of 25:3 [46]. The curing time is at least 15 h. Subsequently, the specimen is grinded, polished to a surface roughness of lower than 1 µm and etched [46]. The etching solution consists of distilled water, hydrochloric acid, nitric acid and pickling inhibitor. An optical microscope (type: Smartzoom 5, Carl Zeiss Microscopy, Oberkochen, DE) is used for evaluation. The micrograph exhibits different melting depths due to the changing scan direction of the build process [Fig. 3.16(c)]. The material intermixing at the bonding zone takes place in a range of up to 100 µm into the inserted steel plate and results from the melt pool dynamics. During the LPBF-process, the laser intrudes into the underlying layers and temporarily forms a vapor capillary due to the energy distribution of the laser. The molten metal contracts after removal of the laser and forms a spherical surface due to the surface tension [187]. The depth of material intermixing of up to 100 µm is in typical order of magnitude for the LPBF-process [33], [188], [189]. In case of the LPBF-manufactured spring elements, the laser intrudes into the inserted steel plate, and, thus, ensures a proper material bonding between the LPBF-manufactured base bodies and the steel plate without detectable irregularities in form of cracks or pores. Due to the material intermixing, it is possible to achieve a proper connection that is not the weakest zone in the manufactured part [46]. This allow the LPBF-manufactured spring elements to be considered as fully dense components despite the inserted steel plate. Thus, a proper strain transmission from the LPBF-manufactured base bodies to the inserted steel plate is ensured.

3.4.2 Investigation of the force sensor performance under static load

The second part of the characterization is focused on the behavior of the LPBF-manufactured spring elements under static load. This is used to validate the validation of the FEA model as well as to compare the strain transmission between the LPBF-manufactured and the conventionally manufactured spring elements, and, thus, for establishing a performance baseline. In preparation for the measurements, the LPBF-manufactured spring elements (P1 – P6) are reworked by milling and M5 threaded holes are drilled in the end faces to allow their fastening to the measurement setup. Subsequently, strain gauges are applied to the LPBF-manufactured spring elements as well as the conventionally manufactured spring element (Conv) at the predetermined positions [Fig. 3.17(a)], as described in section 2.3. Four linear strain gauges (type: 1-LY41-1.5/350, HBK, Darmstadt, DE) with a gauge factor of $1.95 \pm 1.5\,\%$ and a base resistance of $350\,\Omega \pm 0.3\,\%$ are used per spring element to implement a full bridge configuration. The strain gauges are applied so that a distance of 2 mm is maintained between the carriers of the strain gauges and the LPBF-manufactured base bodies (section 3.3.2). Furthermore, the solder tabs are directed towards the center of the steel plate. As of now, these LPBF-manufactured spring elements are called LPBF-manufactured prototype force sensors for the rest of this work. Finally, two steel fasteners are built, which are used to attach the prototype force sensors to the measurement setup and for force introduction [Fig. 3.17(b)].

Measurement setup for static loading

The prepared LPBF-manufactured and conventionally manufactured prototype force sensors (Fig. 3.18) are characterized regarding their linearity with respect to a best-fit line and hysteresis in the next step. A universal testing machine (type: inspekt Table5, Hegewald & Peschke, Nossen, DE) with a 100 N reference force sensor (type: S2M/100N with 0.02 % accuracy, HBK, Darmstadt, DE) is used for loading the prototype force sensors (Fig. 3.19). The loading is conducted using a force-controlled step profile according to the OIML R60 guideline [190], which provides a recommendation for measuring load cells. Initially, three full-load cycles are performed to preload the prototypes and exclude settling followed by a rest of five minutes [190]. Therefore, these three cycles are not considered in the evaluation. Subsequently, the prototype force sensors are loaded with a step profile featuring a step size of 3 N and a load rate of $0.5\,\mathrm{N\,s^{-1}}$ up to a maximum load of 15 N. Each step is held for 90 s and the step profile is repeated three times. A metal sphere is used to assure a punctiform force transmission.

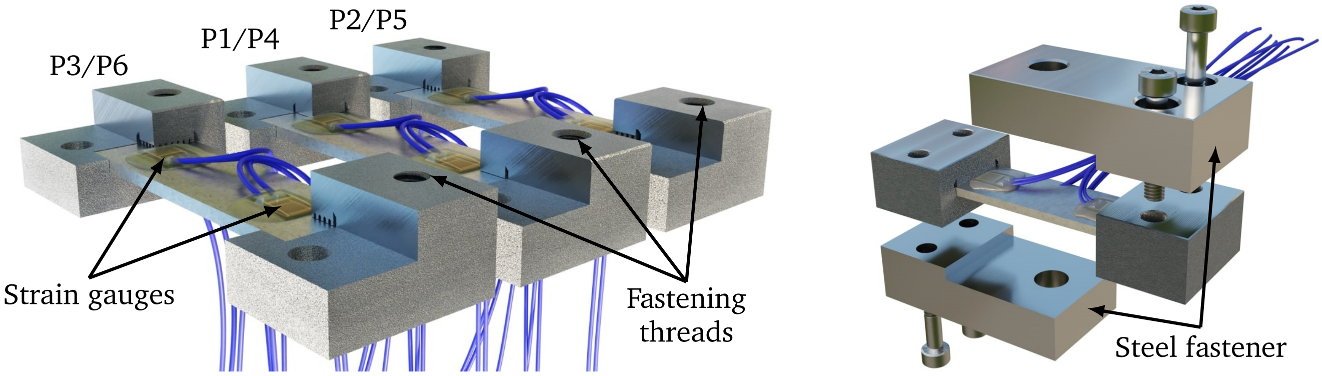

(a) (b)

Figure 3.17: The LPBF-manufactured base elements of all six prototypes (P1 – P6) are reworked by milling and M5 threaded holes are drilled (a). After applying the strain gauges, the prototype force sensors are attached to the measurement setup through steel fasteners (b).

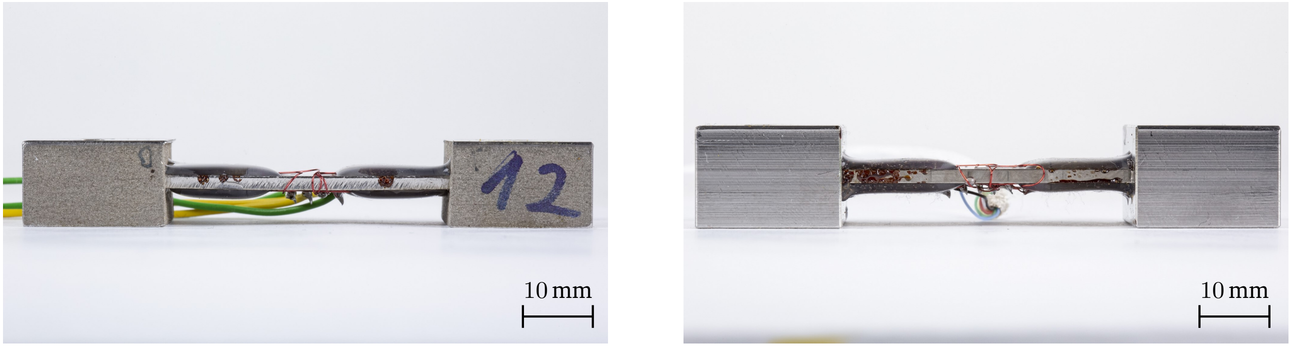

Figure 3.18: The LPBF-manufactured (left) and conventionally manufactured (right) prototype force sensors with an implemented full bridge configuration.

Since two sensors, namely the reference force sensor of the testing machine and the prototype force sensor, have to be measured simultaneously, two commercially available bridge amplifiers (type: EL3356-0010, Beckhoff Automation, Verl, DE) with an accuracy of $<0.01\,\%$ are used. Each bridge amplifier supplies one sensor with $5\,\mathrm{V}$ and measures its bridge output voltage. The measured output voltages are forwarded to a data acquisition system (DAQ) (type: cRIO-9074, National Instruments, Texas, US) and synchronized. Furthermore, the temperature is constantly recorded with a thermocouple (type: 5TC-GG-KI-30-1M, OMEGA Engineering inc., Deckenpfronn, DE) during the measurements. The thermocouple is connected to an additional analog input terminal (type: EL3314-0010, Beckhoff Automation, Verl, DE), which in turn is connected to the same data acquisition system as the bridge amplifiers. The recording of all three data streams with a time stamp is provided using LabVIEW.

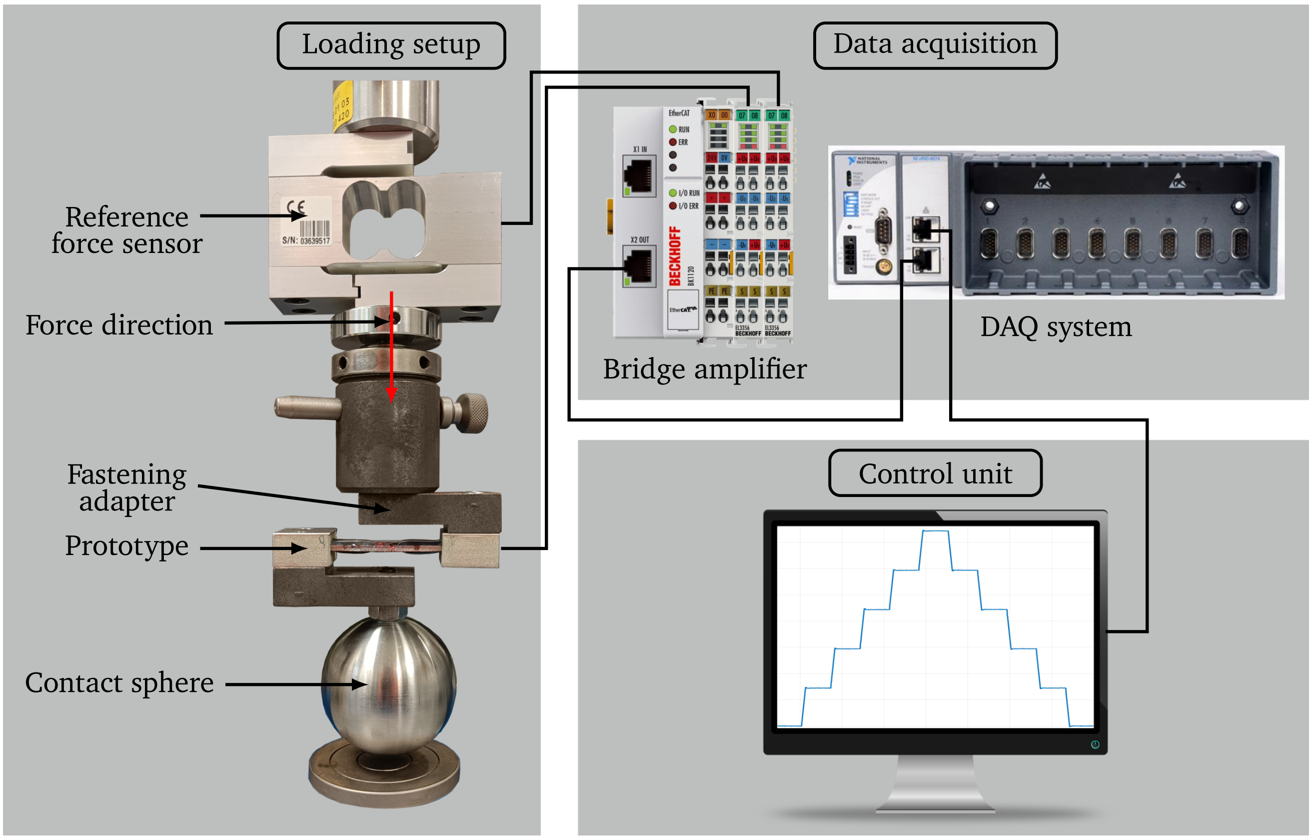

Figure 3.19: The developed LPBF-manufactured prototype force sensor is loaded by a universal testing machine with different reference forces. The output signals of the reference force sensor of the testing machine and the prototype force sensor are recorded via bridge amplifiers, which are then transmitted to a computer using a DAQ system.

Sensitivity of the prototype force sensors

The measured data show that the bridge output voltage U_D of the prototype force sensor, which is referred to the bridge excitation voltage $U_\mathrm{S} = 5\,\mathrm{V}$, clearly follows the change of the applied force F, and, thus, exhibits a high linearity [Fig. 3.20(a)]. This excellent linearity is confirmed by an R^2 value of 1 [Fig. 3.20(b)]. The exemplary behavior of prototype P1 illustrated in Fig. 3.20 is also valid for the remaining prototype force sensors. Evaluation of the sensitivities of all prototype force sensors from the data measured reveals similar sensitivities S for the prototype force sensors P1, P2 and P3 as well as for prototype force sensors P4, P5 and P6 (Tab. 3.6). These similar values prove the reproducibility of the disruptive manufacturing method of the LPBF-manufactured spring elements with an inserted steel plate. The small deviations in the sensitivities S between the prototype force sensors with the same steel plate material but different scanning area (full, stripes or checkered) are $0.18\,\%$ and $0.64\,\%$ (related to the fully printed prototype in each case) for the two different steel plate materials 1.4310 and 1.4404, respectively. This implies that the deformation of the LPBF-manufactured prototype force sensors under load, and, thus, the resulting strain and compression is nearly equal for the same steel plate material but different scanning area. Therefore, the different scanning area does not influence the strain transmission in the developed LPBF-manufactured prototype force sensors.

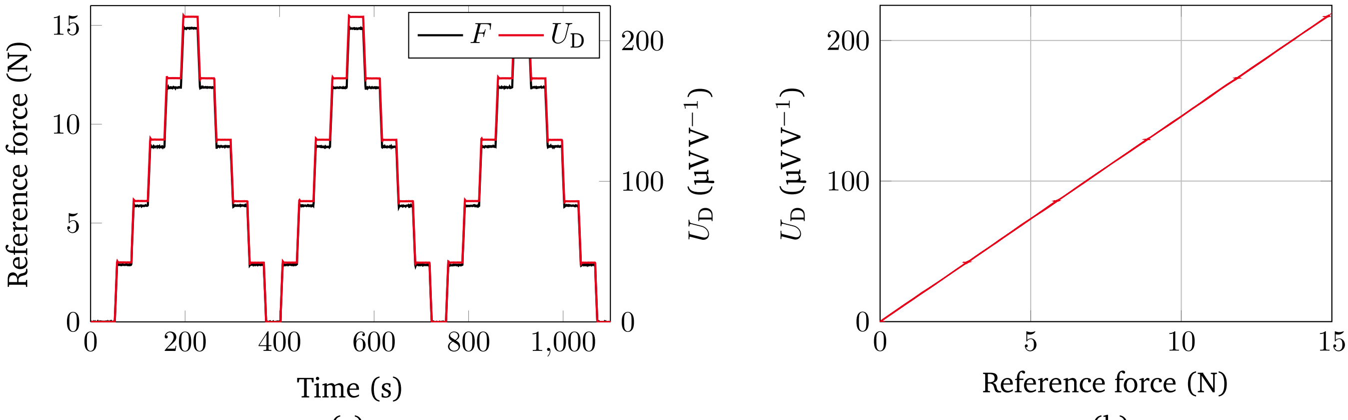

(a)

(b)

Figure 3.20: The measured bridge output voltage U_D of the prototype force sensor P1 closely follows the loading profile, which is represented by the reference force sensor of the testing machine (a). A perfectly linear behavior is evident when plotting the bridge output voltage against the specified reference force up to $15\,\mathrm{N}$ (b).

The lower Young's modulus of the 1.4404 steel plates leads to a greater deformation, and, thus, higher strain and compression in case of prototype force sensors P4, P5 and P6. Consequently, these feature larger sensitivities than the prototype force sensors P1, P2 and P3. Furthermore, excellent agreement between the measured and simulated sensitivities is achieved. The uncertainties in the simulated sensitivities are due to the tolerances of the determined Young's moduli, which affect the resulting strain of the spring element, as well as the tolerances of the gauge factor of the strain gauges. The comparison of the sensitivities of the prototype force sensors P4, P5 and P6 with the conventionally manufactured reference force sensor (Conv) out of 1.4404 steel shows a good consistency due to the same steel type. Deviations between the sensitivities of prototype force sensors P1, P2 and P3 and the conventionally manufactured reference force sensor are due to the differences in the Young's moduli resulting from different steel types.

Table 3.6: Sensitvities S of the developed prototype force sensors. The prototype force sensors P1, P2 and P3 have a 1.4310 steel plate and differ in the scanning area. The same applies to the prototype force sensors P4, P5 and P6, which possess a 1.4404 steel plate. The conventionally manufactured reference force sensor is made of stainless steel 1.4404.

Prototype	**Measured S**	**Simulated S**
P1	$(218.6 \pm 0.1)\,\mu\mathrm{V\,V^{-1}}$	$(222.3 \pm 5.0)\,\mu\mathrm{V\,V^{-1}}$
P2	$(218.4 \pm 0.1)\,\mu\mathrm{V\,V^{-1}}$	$(222.3 \pm 5.0)\,\mu\mathrm{V\,V^{-1}}$
P3	$(218.0 \pm 0.1)\,\mu\mathrm{V\,V^{-1}}$	$(222.6 \pm 5.0)\,\mu\mathrm{V\,V^{-1}}$
P4	$(234.9 \pm 0.3)\,\mu\mathrm{V\,V^{-1}}$	$(232.2 \pm 4.8)\,\mu\mathrm{V\,V^{-1}}$
P5	$(233.4 \pm 0.1)\,\mu\mathrm{V\,V^{-1}}$	$(232.2 \pm 4.8)\,\mu\mathrm{V\,V^{-1}}$
P6	$(233.8 \pm 0.2)\,\mu\mathrm{V\,V^{-1}}$	$(232.5 \pm 4.8)\,\mu\mathrm{V\,V^{-1}}$
Conv	$(236.4 \pm 0.3)\,\mu\mathrm{V\,V^{-1}}$	$(231.0 \pm 4.8)\,\mu\mathrm{V\,V^{-1}}$

Linearity and hysteresis error of the prototype force sensors

Since the R^2 value for all prototypes is 1, a comparison of the behavior of the prototype force sensors under load is limited. Therefore, only the deviations of the bridge output voltages of the prototype force sensors from a linear fit are presented hereinafter, allowing the determination of the linearity and hysteresis error. This provides more insight into the sensor performance.

The linearity and hysteresis errors of the prototype force sensors are based on the mean values of the load steps [Fig. 3.20(a)]. For the linearity error, best-fit lines are determined for all loading and unloading cycles based on the mean values. The deviations between the mean bridge output voltage of each load step and the corresponding best-fit line are referred to the nominal value (equivalent to the sensitivity) to define the linearity error. The largest linearity error of all six loading and unloading cycles is then given for each prototype force sensor. For the hysteresis error, the deviation between the mean values of the respective load steps within a loading and unloading cycle is determined and also referred to the nominal value. Similar to the linearity error, the largest hysteresis error of all three loading cycles is given for each prototype force sensor. This results in linearity and hysteresis errors for each prototype force sensor within $\pm 0.1\,\%$ full scale and $\pm 0.2\,\%$ full scale (Fig. 3.21), respectively. Predominantly, the linearity error of each prototype force sensor is within $\pm 0.05\,\%$ full scale. Hence, no significant difference in terms of linearity and hysteresis is found between the LPBF-manufactured prototype force sensors and the conventionally manufactured reference force sensor. Furthermore, these small errors confirm a well strain transmission from the LPBF-manufactured parts to the inserted steel plate.

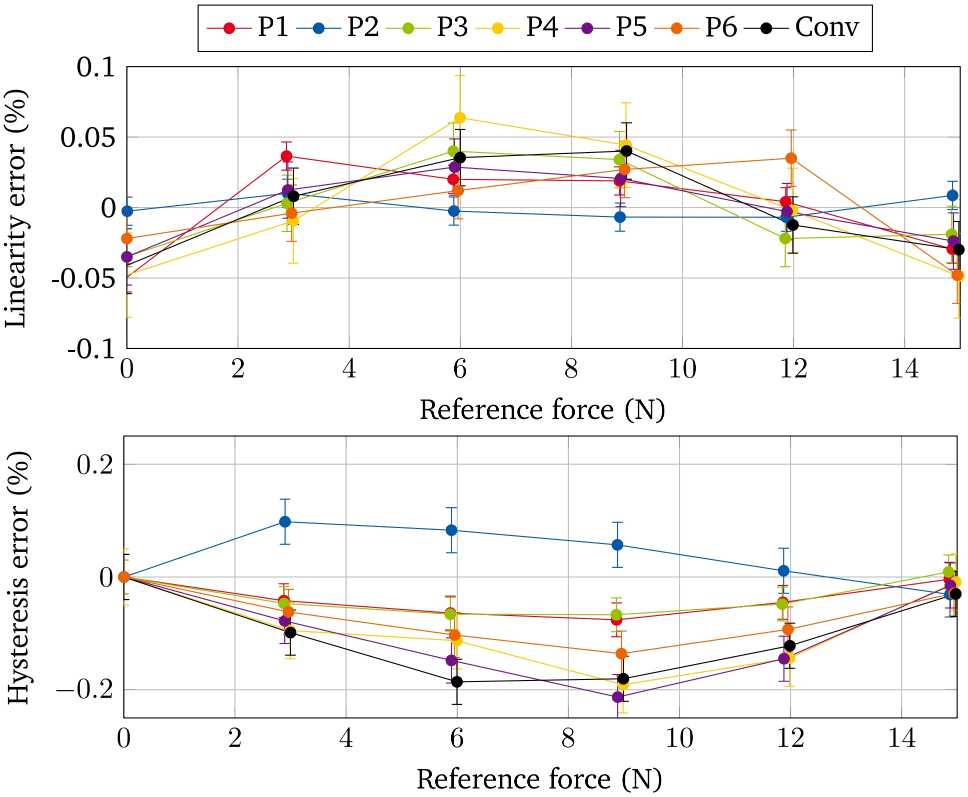

Figure 3.21: The linearity and hysteresis errors of the LPBF-manufactured prototype force sensors and the conventionally manufactured reference force sensor are nearly equal making them comparable with regarding the loading performance.

Temperature behavior of the prototype force sensors

In case of the temperature behavior the temperature coefficients of the zero point ($\mathrm{TK_0}$) and the sensitivity ($\mathrm{TK_C}$) of the prototype force sensors are investigated. The $\mathrm{TK_0}$ defines the change in signal with zero load only due to the temperature dependence of the resistance and the material expansion resulting in measuring an apparent strain. The $\mathrm{TK_C}$ defines the change in signal with load due to the temperature dependence of the gauge factor and the Young's modulus. Therefore, the prototype force sensors are loaded during the heating process. The load is applied through a weight plate of 1 kg with an accuracy of ± 10 mg. Heating is done in a temperature chamber (type: custommade temperature chamber, Fresenberger, Wipperfuerth, DE) from 20 °C up to 100 °C. The heating process consists of a three-hour heat-up to ensure a complete heating of the sensors, followed by a two-hour hold time and a cool-down to room temperature. A thermocouple is attached near the strain gauges during the entire measurement.

The measurements show that all prototype force sensors feature a mostly linear temperature behavior (Fig. 3.22) providing temperature coefficients of $<0.3\,\%/10\,\mathrm{K}$ and $<0.6\,\%/10\,\mathrm{K}$ for the $\mathrm{TK_0}$ and $\mathrm{TK_C}$, respectively (Tab. 3.7). Note the fact that the $\mathrm{TK_0}$ superimposes the $\mathrm{TK_C}$ value is taken into consideration. It is noticeable that the conventionally manufactured reference force sensor shows the lowest temperature coefficients. In particular, the LPBF-manufactured prototype force sensors with stripes as scanning area (P2 and P5) and checkered scanning area (P3 and P6) have temperature coefficients almost 1.5 to 2 times as high as the conventionally manufactured reference force sensor. It is likely that the pre-stress due to the manufacturing process is related to the higher temperature coefficients. The different scanning areas lead to

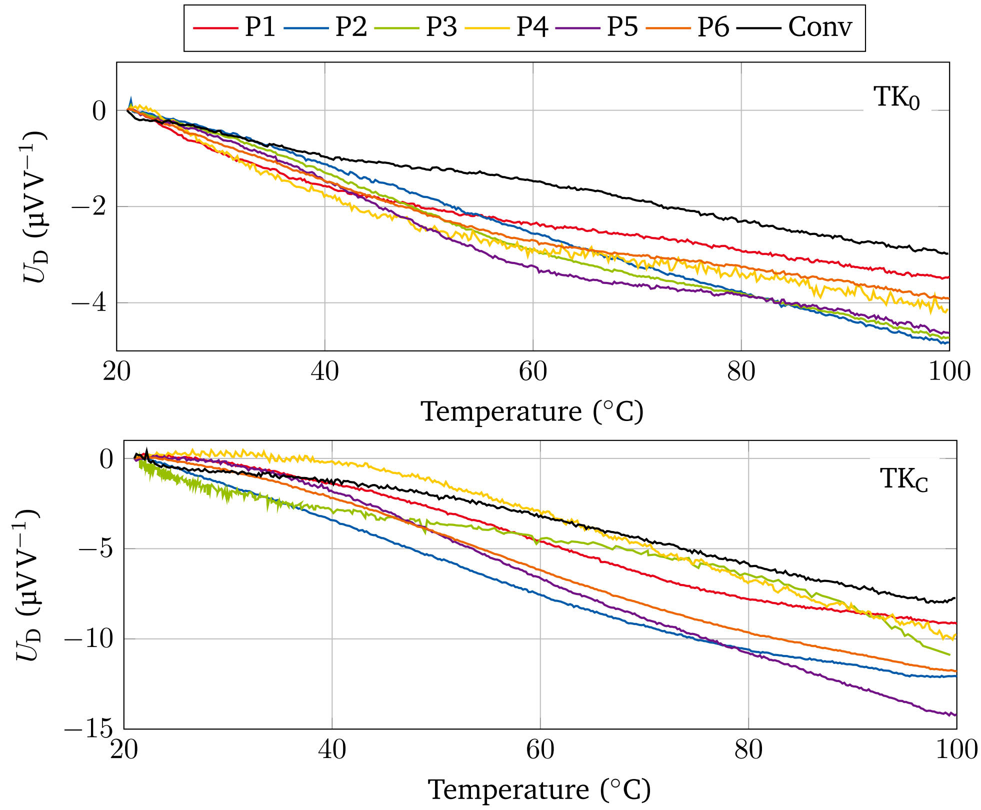

Figure 3.22: The temperature behavior ($\mathrm{TK_0}$ and $\mathrm{TK_C}$) of the prototypes show a nearly linear behavior with similar temperature coefficients of the reference sensor.

different pre-stresses, which strengthen this assumption. In combination with the temperature dependent Young's modulus, this pre-stress can lead to greater deformation, and, thus, a higher temperature coefficient. However, since the temperature behavior of the prototype force sensors is nearly linear, a simple compensation is feasible.

Table 3.7: Temperature coefficients of the prototype force sensors.

Prototype	**TK_0**	**TK_C**
P1	0.18 %/10 K	0.46 %/10 K
P2	0.30 %/10 K	0.47 %/10 K
P3	0.28 %/10 K	0.22 %/10 K
P4	0.20 %/10 K	0.41 %/10 K
P5	0.25 %/10 K	0.60 %/10 K
P6	0.20 %/10 K	0.52 %/10 K
Conv	0.15 %/10 K	0.30 %/10 K

Creep of the prototype force sensors

In the context of strain gauge based force sensing, creep is a reversible small signal deviation when a constant load is applied [191]. This change in signal is approximately expressed in the form of an e-function [191]. In order to evaluate the creep behavior, a simple setup with a weight plate is used to load the prototype force sensors. This provides a very constant load over a longer period of time. The prototype force sensors are fixed over one of the steel fasteners, while a plate is attached to the other steel fastener to support the weight plate. Loading is done through the same weight plate ($1\,\mathrm{kg}$) that was used for investigating the temperature behavior in the previous section. Regarding the gravity of $9.81\,\mathrm{m\,s^{-2}}$, this corresponds to a force of $9.81\,\mathrm{N}$. The low uncertainty ($\pm\,10\,\mathrm{mg}$) of the mass of the weight plate is neglected in this measurement.

The measurement is performed with the LPBF-manufactured prototype force sensors P1 and P4 (fully printed scanning area, but different types of steel plate) as well as the conventionally manufactured reference force sensor. All three force sensors are successively loaded with the weight plate for $40\,\mathrm{h}$. For minimizing the environmental influences, the measurement is carried out in an air-conditioned room. Two thermocouples (type: 5TC-GG-KI-30-1M, OMEGA Engineering inc., Deckenpfronn, DE) are used to record the temperature. One of them is fixed directly to the spring elements with adhesive tape. The remaining one is positioned at a distance of about $5\,\mathrm{cm}$ from the spring elements. For the measurement of the output signals of all three force sensors and the thermocouples, the same DAQ system is used as for the measurements with the universal testing machine (Fig. 3.19).

The bridge output voltages increase steeply after the load is applied and result in $143.1\,\mathrm{\mu V\,V^{-1}}$ and $153.8\,\mathrm{\mu V\,V^{-1}}$ for the two prototype force sensors P1 and P4, respectively. Subsequently, the bridge output voltages of both prototype force sensors decrease slightly according to an e-function as expected from theory. The same behavior is also found for the conventionally manufactured reference force sensor with a resulting bridge output voltage of $154.4\,\mathrm{\mu V\,V^{-1}}$. In order to determine the creep error, the signals of the bridge output voltages are subtracted with their respective maximum value and referred to it. The result shows that the maximum creep values are reached asymptotically [Fig. 3.23(a)]. Furthermore, a superimposed oscillation on the creep is clearly noticeable. This is due to the fact that the temperature was not constant over the 40 hours and fluctuated by about $2\,^{\circ}\mathrm{C}$, which is measured by both thermocouples. However, only the thermocouple, which is attached directly to the spring elements, is shown for each force sensor ($\mathrm{TC_{P1}}$, $\mathrm{TC_{P4}}$ and $\mathrm{TC_{Conv}}$) for the sake of clarity [Fig. 3.23(b)]. An increase in temperature leads to an increase in the bridge output voltages of the all three force sensors, which counteracts the creep. This is interpreted as a $\mathrm{TK_C}$ component, as an increase in temperature leads to a decrease of the Young's modulus of the spring element as well as an increase of the gauge factor of the strain gauges. Thus, an increased signal is provided.

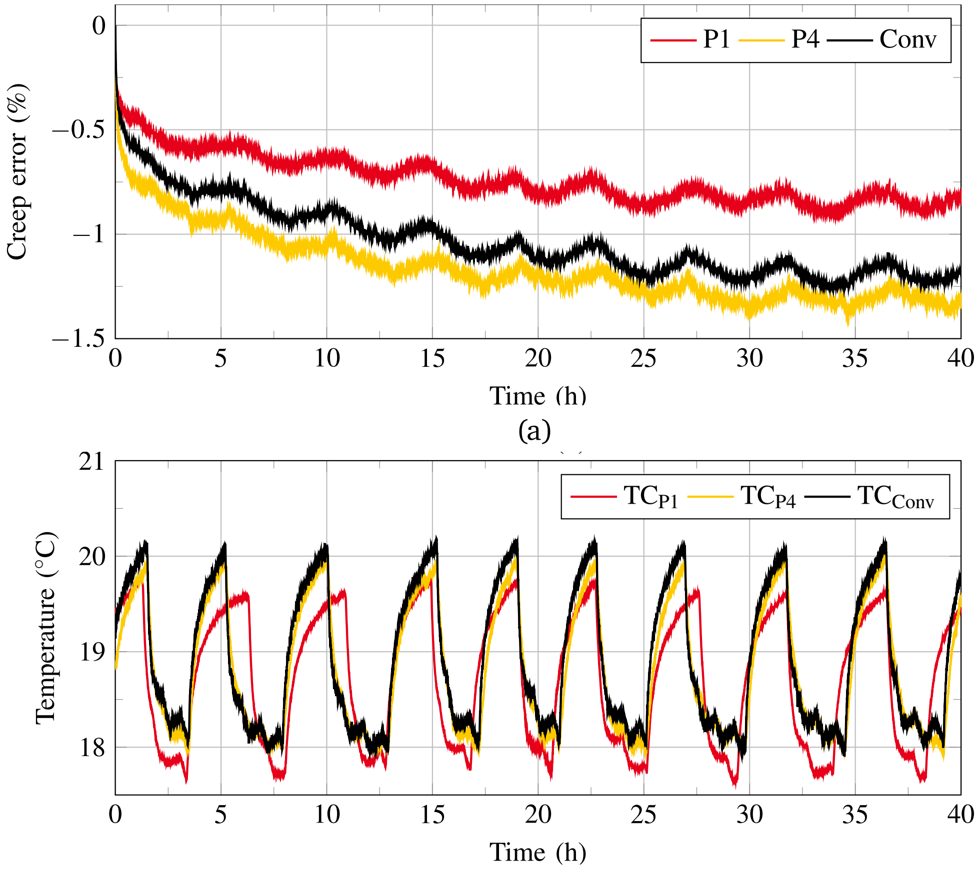

(a)

(b)

Figure 3.23: The creep of all three force sensors (P1, P4, and Conv) shows an expected deviation of the bridge output signal in the form of an e-function (a). The superimposed oscillation on the creep is due to the fact that the temperature (measured by the thermocouples $\mathrm{TC_{P1}}$, $\mathrm{TC_{P4}}$ and $\mathrm{TC_{Conv}}$) has not been constant during the measurement period of 40 hours, but fluctuated by $2\,^{\circ}\mathrm{C}$ (b).

The creep errors of the two prototype force sensors P1 and P4 over the load period of 40 hours are $-0.91\,\%$ and $-1.38\,\%$, respectively. Accordingly, the absolute creep of prototype force sensor P4 is greater than that of prototype force sensor P1. However, the creep of the conventionally manufactured reference force sensor is $-1.27\,\%$, which is comparable in magnitude to that of the prototype force sensor P4. The creep of all three force sensors is based on two components: creep of the spring element and creep of the strain gauges (Sec. 2.2.1). Since the strain gauges are the same for all three force sensors, the difference in the creep behavior is due to the material. This is further confirmed by the measured values of the creep error of prototype force sensor P4 and the conventionally manufactured reference force sensor with regard to the magnitude. Both have in common that they are made of stainless steel 1.4404. For the prototype force sensor P4, the material of the steel plate is decisive, which is stainless steel 1.4404. In contrast, prototype force sensor P1, which consists of a steel plate made of stainless steel 1.4310, features the lowest creep error. Moreover, since the creep behavior is negative for all three force sensors, the creep contribution of the strain gauges predominates the creep contribution of the spring elements. Neglecting the rapid change in bridge output voltages up to a measurement duration of one hour, which is dominated by the different material, a comparable residual drift over the remaining 39 hours of $0.50\,\%$, $0.63\,\%$ and $0.66\,\%$ results for the force sensors P1, P4 and Conv, respectively. These results confirm that the LPBF-manufactured spring elements perform equivalent to conventionally manufactured spring elements in terms of creep behavior as well. Consequently, the creep can be minimized by using strain gauges with adapted length of the reverse loops of the grid, as the behavior is the same for all three sensors.

Cyclic loading of the prototype force sensors

Finally, the LPBF-manufactured prototype force sensors are subjected to a cyclic load to obtain a first trend regarding fatigue. The focus of this experiment is to determine if multiple load cycles have an impact on the sensitivity S. In addition, this experiment also provides information about the reproducibility of the LPBF-manufactured prototype force sensors. The measurement is performed with the LPBF-manufactured prototype force sensors P1 and P4 (fully printed scanning area) as well as the conventionally manufactured reference force sensor. The three force sensors are loaded with the same setup using the universal testing machine as for the linearity and hysteresis test. Here, the nominal load of $15\,\mathrm{N}$ is applied 100 times. This loading is applied at a load rate of $1\,\mathrm{N\,s^{-1}}$ followed by a holding time of $30\,\mathrm{s}$ and unloading at the same rate.

The loading of the force sensors that lasts $2.5\,\mathrm{h}$ results in trapezoidal bridge output voltages, and, thus, proves that the force sensors have excellent compliance to the loading [Fig. 3.24(a)]. Note that only half of the load cycles of the LPBF-manufactured prototype force sensor P1 are shown exemplarily in Fig. 3.24(a) for the sake of clarity. This signal is used in the next step to determine the sensitivity for each load cycle. The sensitivities of all three force sensors over the complete 100 load cycles remain rather constant with a small deviation [Fig. 3.24(b), (c) and (d)], which lie in the measurement uncertainties of the pre-determined sensitivities (Tab. 3.6). The resulting sensitivities for the LPBF-manufactured prototype force sensors P1 and P4 as well as for the conventionally manufactured reference force sensor from the cyclic loading (Tab. 3.8) are in excellent agreement with the previously determined sensitivities (Tab. 3.6). Although 100 load cycles are insufficient to draw conclusions about fatigue of the force sensors, a high degree of stability and reproducibility is still evident. In fact, the reproducibility of the prototype force sensors is similar to that of the conventionally manufactured reference force sensor.

Table 3.8: Sensitivities S of the force sensors for the cyclic loading.

Prototype	S
P1	$218.61\,\mathrm{\mu V\,V^{-1}} \pm 0.05\,\mathrm{\mu V\,V^{-1}}$
P4	$234.85\,\mathrm{\mu V\,V^{-1}} \pm 0.07\,\mathrm{\mu V\,V^{-1}}$
Conv	$236.38\,\mathrm{\mu V\,V^{-1}} \pm 0.05\,\mathrm{\mu V\,V^{-1}}$

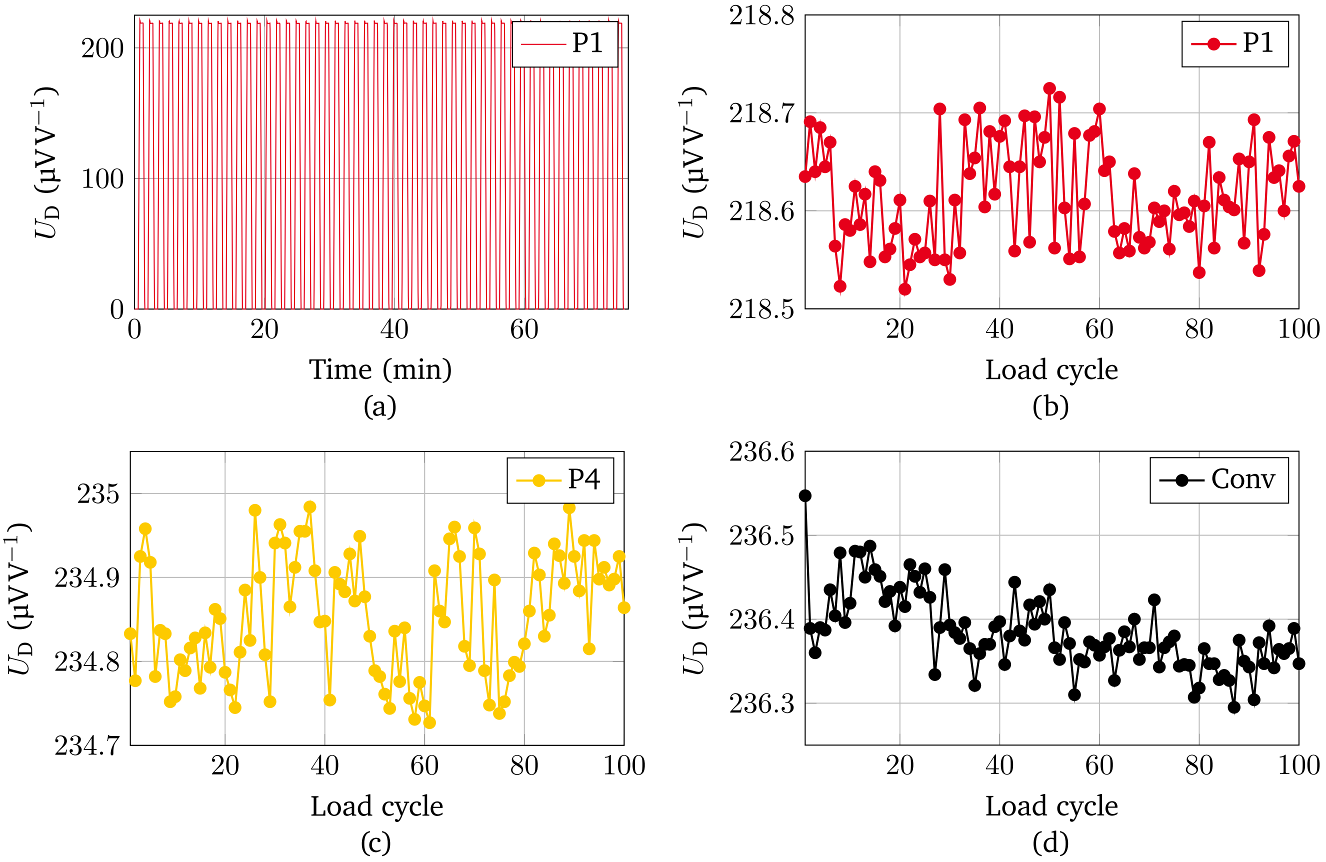

Figure 3.24: The cyclic loading (only 50 cycles shown) up to the nominal load of 15 N shows that the force sensors have excellent compliance to the loading (a). The measured sensitivities of the two LPBF-manufactured prototype force sensors P1 (b) and P4 (c) as well as of the conventionally manufactured reference force sensor (d) prove excellent reproducibility of all three force sensors without signs of fatigue.

3.5 Conclusion

In this chapter, a method for additively manufactured spring elements in disruptive manner based on LPBF for force sensing applications has been introduced. This approach allows the integration of strain gauges into LPBF-manufactured parts through the integration of a steel plate. It has been found that this disruptive manufacturing method leads to successfully fabricate spring elements while establishing a proper material bonding between the LPBF-manufactured base bodies and the inserted steel plate without detected cracks or pores. This material bonding features a material intermixing at the bonding zone in a range of up to 100 µm, and, thus, ensures a proper strain transmission the LPBF-manufactured base bodies to the inserted steel plate. The resulting deformation of the steel plate due to the thermally induced stresses during the LPBF-process has no measurable negative effect on the sensor performance. This is confirmed by the FEA model presented, which provides a reliable prediction of strain transmission despite the neglected thermally induced stresses in these spring elements. However, it is necessary to consider that after separating the LPBF-manufactured spring elements from the build platform, most of the thermally induced stresses are released, while a small amount is retained. Nevertheless, the remaining thermally induced stresses do not penalize the performance of the LPBF-manufactured prototype force sensors. This is reinforced by the low linearity and hysteresis errors, which also confirm the firmly bonded material connection between the LPBF-manufactured base bodies and inserted steel plate. The investigated different scanning areas do not provide the presumed reduction of the thermally induced deformation of the steel plate, as this results mainly through the interaction of the process parameters with the chosen geometry of the manufactured spring element regarding lateral and rear connection of the steel plate. Furthermore, no significant impact of the scanning areas is recorded on the strain transmission at room temperature. The comparison of the LPBF-manufactured prototype force sensors with a conventionally manufactured reference force sensor has proved that the LPBF-manufactured spring elements are competitive with conventionally manufactured spring elements in terms of their sensitivity, linearity, hysteresis, temperature behavior, creep and reproducibility during a cyclic loading. The characterization provides a data sheet for the LPBF-manufactured prototype force sensors (Tab. 3.9), which emphasizes that LPBF-manufactured spring elements with inserted metal components can be used analogously to conventionally manufactured spring elements. This confirms one of the two aspects introduced initially regarding the performance of LPBF-manufactured force sensors based on the disruptive approach. The impact of the LPBF-process on the strain gauges will be investigated in the next step.

Table 3.9: Derived data sheet of the LPBF-manufactured prototype force sensors and the conventionally manufactured reference force sensor with a nominal force of 15 N.

Specification	**P1**	**P4**	**Conv**
Nominal sensitivity ($\mu V V^{-1}$)	218.6	234.9	236.4
Non-linearity (%)	0.05	0.09	0.06
Hysteresis (%)	0.11	0.24	0.23
TK_0 (%/10 K)	0.18	0.20	0.15
TK_C (%/10 K)	0.46	0.41	0.30
Relative Creep (%)	−0.91	−1.38	−1.27
Reproducibility (%)	0.02	0.03	0.02

4 Investigation of the behavior of strain gauges within the LPBF-process

In the last chapter, the strain transmission between the LPBF-manufactured base bodies and the inserted steel plate was investigated. It was shown that a proper bonding and a loss-free strain transmission are ensured. For all experiments conducted so far, the strain gauges were applied after completion of the LPBF-manufactured spring elements to exclude the impact of the process on the strain gauges. Therefore, the focus of this chapter lies on investigating the impact of the LPBF-process on the strain gauges by comparing their behavior before and after being exposed to the process. Since the inserted steel plate is not only heated by the continuous energy input of the laser during the layer build-up, but is also deformed by thermally induced stresses when joined to the LPBF-manufactured base bodies, the investigation is carried out in multiple steps.

First, the impact of the laser and the build-up of material on the steel plate with an applied strain gauge is investigated. This involves manufacturing material on the steel plate only by means of LPBF without establishing a connection to the LPBF-manufactured base bodies. Second, the influence of the combination of the process and the resulting thermally induced deformation of the steel plate is investigated. Measurements of the change in resistance of the strain gauges as well as temperature measurements during the LPBF-process are made possible through the cable harness, which is routed into the process chamber. These experiments allow not only to investigate the strain gauge behavior within the process, but also to provide a more detailed insight into the process during the manufacturing of the spring elements. In particular, the reduction of the thermally induced deformation of the steel plate can be examined properly.

4.1 Impact of the LPBF-process on the strain gauges

The first step is to investigate whether the strain gauges can withstand the harsh process conditions in the LPBF machine. Therefore, a strain gauge is applied to the center of each of a 1.4310 and 1.4404 steel plate and sealed with silicone rubber (Sec. 2.3). The same steel plates as in the last chapter are used here with a size of $50\,\mathrm{mm}$ x $15\,\mathrm{mm}$ x $2\,\mathrm{mm}$. The strain gauges utilized are linear strain gauges (type: 1-LY45-1.5/350, HBK, Darmstadt, DE) with a gauge factor of $2.00 \pm 1.5\,\%$ and a base resistance R_0 of $350\,\Omega \pm 0.3\,\%$. In order to expose the strain gauges to the LPBF-process, two LPBF-manufactured base bodies are manufactured with the same geometry as for the LPBF-manufactured spring elements from the last chapter (Sec. 3.2). Since the first step is to investigate the impact of the process conditions and especially of the heat generated during scanning the steel plate by the laser on the strain gauges, two LPBF-manufactured parts of $1\,\mathrm{mm}$ height are built-up on top of the steel plate [Fig. 4.1(a)]. Note that only material is added on top of the steel plates without establishing any connection between the steel plate and the LPBF-manufactured base bodies. This corresponds to the manufacturing of 50 layers, where each layer exhibits a thickness of $20\,\mathrm{\mu m}$. These two parts are manufactured on both ends on the top side of the steel plate and exhibit the same length and width of $15\,\mathrm{mm}$ and $5\,\mathrm{mm}$, respectively. The top side of the steel plate corresponds to the opposite side on which the strain gauge is applied, otherwise a collision of the coating blade and the strain gauge would occur. The steel plates are introduced into the LPBF-process one by one.

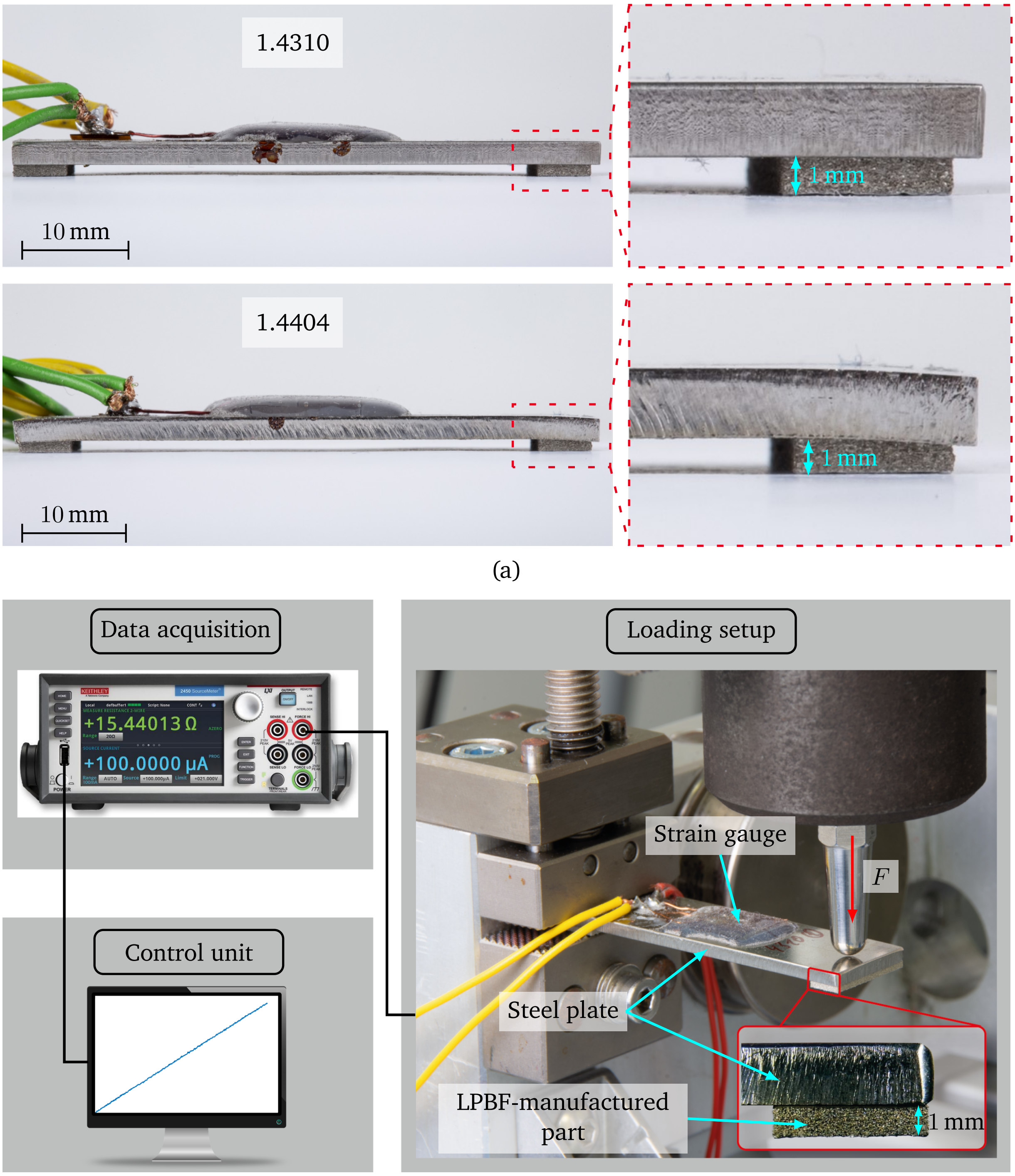

(a)

(b)

Figure 4.1: The steel plates with applied strain gauge are subjected to a bending load of $15\,\mathrm{N}$ using a universal testing machine before and after being exposed to the LPBF-process by manufacturing two parts of $1\,\mathrm{mm}$ height on top of it (a). The change in resistance of the strain gauge is measured in 4-wire configuration with a digital multimeter and then forwarded to a computer (b).

After the LPBF-process is completed, a proper material bond between the steel plates and the LPBF-manufactured parts is present. The LPBF-manufactured parts feature the expected thickness of $1\,\mathrm{mm}$, which was set in the software. However, it is noticeable that the 1.4404 steel plate has undergone a more pronounced deformation than the 1.4310 steel plate in the areas, where the layers are built up by means of LPBF [Fig. 4.1(a)]. This is due to the fact that the 1.4404 steel plates have a lower ultimate tensile strength and consequently a lower yield strength than the 1.4310 steel plates. The ultimate tensile strengths for the 1.4310 and 1.4404 steel plates are $1010\,\mathrm{N\,mm^{-2}}$ and $632\,\mathrm{N\,mm^{-2}}$, respectively. The resulting residual stresses, which arise due to high temperature gradients during the LPBF-process when material is molten and soldified (Sec. 2.6.1), exceed the yield strength. Thus, a plastic deformation occurs in the areas where material is built up in the case of the 1.4404 steel plate.

The performance of the strain gauge is evaluated by subjecting the steel plate to a bending load of $15\,\mathrm{N}$ before and after being exposed to the process. Hereby, the change in resistance of the strain gauge is measured [Fig. 4.1(b)]. The loading is applied by a spherical pin [Fig. 4.1(b)] using the universal testing machine with a $100\,\mathrm{N}$ reference force sensor (Sec. 3.4.2). The distance between the application of load and the center of the measuring grid of the strain gauge is $20.2\,\mathrm{mm}$. The load is force-controlled with a load rate of $0.1\,\mathrm{N\,s^{-1}}$. A sourcemeter (type: SMU 2450, Keithley, Cleveland, OH, US) is used to measure the resistance of the strain gauge.

The comparison of the base resistance R_0 before and after being exposed to the LPBF-process shows a slight reduction in the base resistance of $-0.017\,\% \pm 0.005\,\%$ for both strain gauges. The bending load of $15\,\mathrm{N}$ results in strains ε of up to $167.4\,\mathrm{\mu m\,m^{-1}}$ and $174.7\,\mathrm{\mu m\,m^{-1}}$ corresponding to measured change in resistances ΔR of $116.7\,\mathrm{m\Omega}$ and $123.5\,\mathrm{m\Omega}$ for the 1.4310 and 1.4404 steel plates, respectively. These strains are measured before exposing the strain gauges to the LPBF-process. Relating these changes in resistance to the base resistance of the respective strain gauge lead to excellent linear resistance-strain characteristics (Fig. 4.2). After the LPBF-process, the new base resistances of the strain gauges are considered to define the resistance-strain characteristics. The resistance-strain characteristics show an almost identical behavior of both applied strain gauges before and after being exposed to the LPBF-process, which is clearly indicated by the maximum relative error of $-0.04\,\%$ for both steel plates. The resulting gauge factor of the strain gauge applied on the 1.4310 steel plate is 1.98, which in fact remains constant even after being exposed to the LPBF-process.

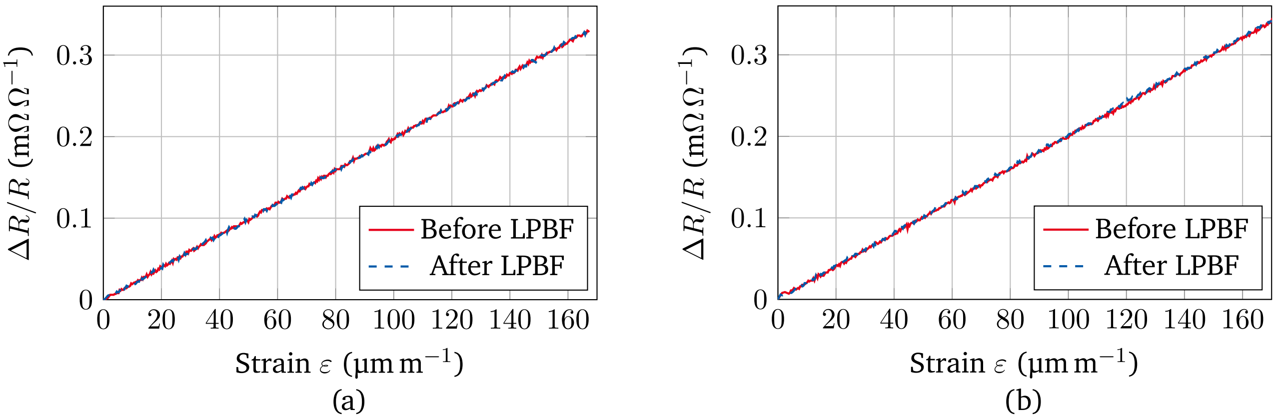

Figure 4.2: The resistance-strain characteristics are almost identical for both strain gauges before and after being exposed to the LPBF-process that are applied to the 1.4310 (a) and 1.4404 (b) steel plate, while featuring excellent linearity.

The resulting gauge factors of the strain gauge applied on the 1.4404 steel plate for before and after being exposed to the LPBF-process are 2.00 and 2.01, respectively. In conclusion, this experiment show that the LPBF-process slightly affect the strain gauge in terms of an irreversible change in the base resistance, which is most likely due to a plastic deformation of the steel plates. However, since the behavior under load as well as the sensitivity, which is represented through the gauge factor, of the strain gauges are almost not affected by the LPBF-process, it is valid to assume that the strain gauges withstand the LPBF-process. Therefore, they are suitable for integration into LPBF-manufactured parts for developing structural integrated force sensors.

4.1.1 In-situ measurements of centrally applied strain gauges

The comparison of the strain gauges properties before and after being exposed to the LPBF-process showed that strain gauges applied to the center of the steel plate maintain their linear resistance-strain behavior. A further interesting aspect is the behavior of strain gauges during the LPBF-process. For this purpose, one strain gauge is applied to the center of each of six 1.4310 steel plates (SP_1 to SP_6), as described in the previous section. In order to expose these strain gauges to the LPBF-process, two LPBF-manufactured lower base bodies are manufactured with the same geometry as for the LPBF-manufactured spring elements from the last chapter (Sec. 3.2). Then, the steel plates are inserted during the process interruption according to the disruptive manufacturing method presented in this work. The steel plates are introduced into the LPBF-process one by one. The strain gauges are connected via screw terminals to the cable harness within the process interruption to measure the response of the strain gauges during the process. This is done by measuring the resistance of the strain gauges in four-wire configuration using a sourcemeter (type: SMU 2450, Keithley, Cleveland, OH, US). Additionally, the base resistances of the strain gauges are measured before and after the process when the steel plates have cooled down to room temperature. After continuing the LPBF-process, two LPBF-manufactured parts with the same thickness of 1 mm are built-up on top of these steel plates without establishing any connection between the steel plate and the LPBF-manufactured base bodies. The LPBF-manufactured parts are fully printed on three of these plates [Fig. 4.3(a)], SP_1 to SP_3), while the other three plates are printed with a checkered surface [Fig. 4.3(b)], SP_4 to SP_6). This is done in accordance with the P1 and P3 prototypes from the last chapter. It has been shown that the smaller scanning area as in case of the checkered surface has no impact on the thermally induced deformation of the steel plate in the designed geometry of the LPBF-manufactured spring element. However, it has to be investigated if this also applies to the electrical behavior, i.e., that the smaller scanning area leads to a lower thermal load on the strain gauge, and, thus, to a smaller change in its resistance.

The changes in resistance are related to the respective resistances before the first scanning and are therefore considered as the base resistances for the in-process measurement. The base resistances of the strain gauges prior to the LPBF-process are not used, because it takes about 20 minutes between the insertion of the steel plate and the effective start of the LPBF-process to establish the process conditions. Establishing the process conditions mainly involves heating the build platform to $80\,^{\circ}\mathrm{C}$ and achieving an oxygen concentration below $0.1\,\%$. During this time, the strain gauges heat up within the enclosed build chamber and a change in resistance arises as a result. The curves of all six strain gauges of all steel plates show the typical characteristic of the layer-by-layer manufacturing process through the 50 recurring pulses corresponding to the 50 manufactured layers [Fig. 4.3(b), (d)].

The curves of the relative changes in resistance of the steel plates with fully printed scanning area show a rapid change in the first 12 layers, which then stabilizes for the remaining layers [Fig. 4.3(b)]. It is likely that in these first layers, the temperature within the steel plates increases and reaches thermal equilibrium for the remaining layers. The recurring laser beam in each new layer introduces pulse-like energy in form of heat into the steel plates and the strain gauges, which rapidly dissipates. The measurement of the relative changes in resistance of the steel plates with checkered scanning area show a significantly smaller change for more than half of the process duration compared to the steel plates with fully printed scanning area [Fig. 4.3(d)]. This is primarily due to the significantly smaller scanning area. A rapid change occurs starting from the 31st layer. As the checkered area merges progressively, the energy introduced by the laser beam per layer increases, so that the steel plate and the strain gauge heat up to the same temperature as in the case of the steel plate with fully printed scanning area. Consequently, the relative changes in resistance in both scanning areas cases are nearly equal, thus no noticeable impact on the strain gauges is to be expected with respect to a fully printed or checkered scanning area. This is also reflected in the comparison of the base resistances before and after the LPBF-process, which differ by a maximum of $-0.009\,\% \pm 0.005\,\%$. This measurement also emphasizes the reason for the same magnitude of the thermally induced deformation in prototype force sensors P2, P3 compared to the fully printed prototype force sensor P1 from the last chapter, despite the smaller scanning area.

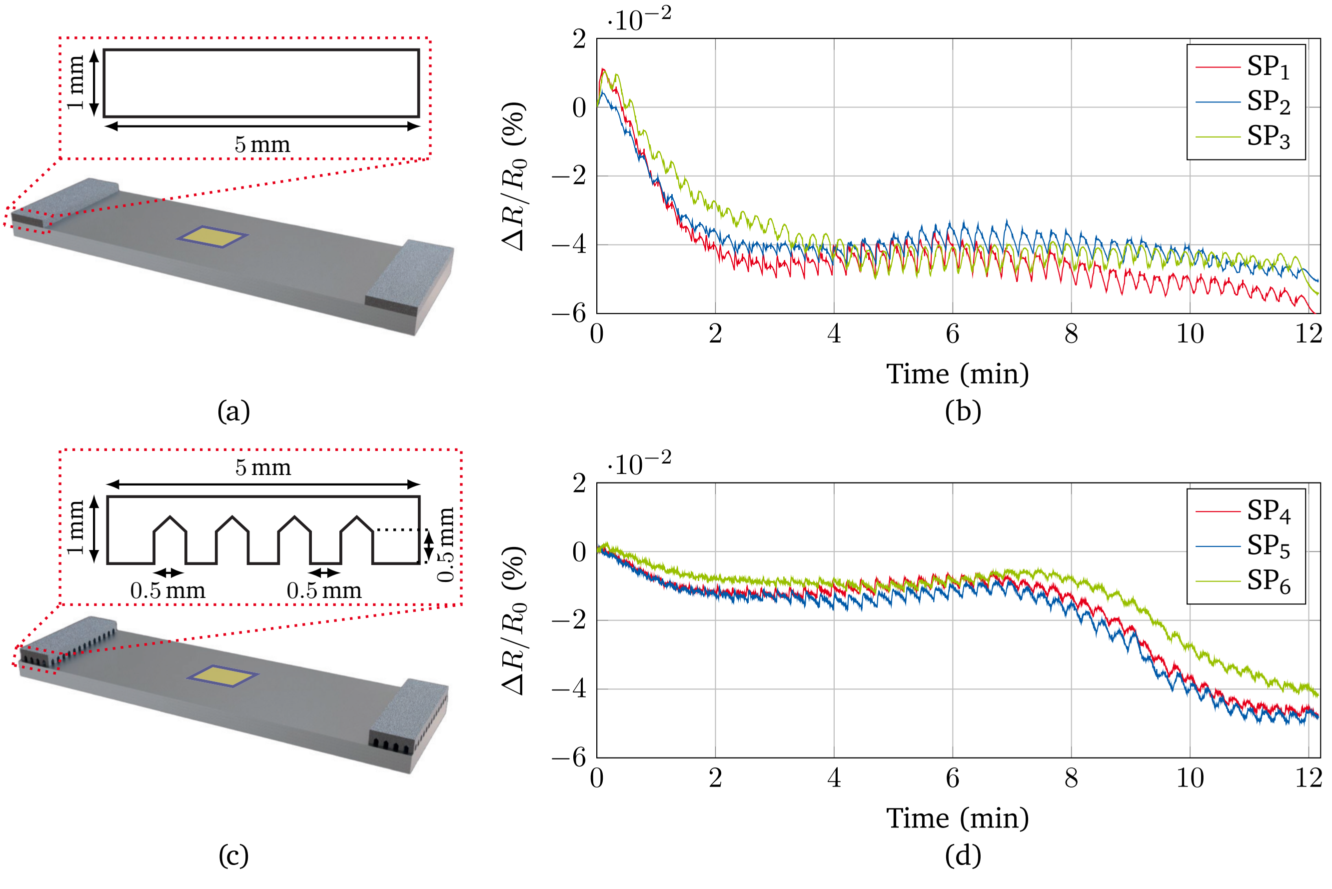

(a) (b) (c) (d)

Figure 4.3: The relative change in resistance of the strain gauges located in the center of the steel plates (yellow marked areas) with fully printed scanning area SP_1, SP_2 and SP_3 (a) and checkered scanning area SP_4, SP_5 and SP_6 (c) over the whole process is nearly the same with about $-0.06\,\%$ (b), (d). Note that the areas marked in yellow indicate the location of the strain gauge, which is actually on the other side of the steel plate. The expected lower thermal load due to the smaller scanning area for the checkered surface is present until the checkered area is merged (d).

4.1.2 In-situ measurements of laterally applied strain gauges

Up to now, only strain gauges applied in the center on the steel plate have been considered. In order to use the LPBF-manufactured spring elements with an S-shaped deformation as described in the last chapter (Chap. 3), the strain gauge needs to be shifted from the center to the edge of the steel plate (Fig. 4.4). This results in the strain gauges being closer to the scanning area, and, thus, closer to the laser beam, and are consequently subjected to a larger thermal load. Therefore, one strain gauge (type: 1-LY45-1.5/350, HBK, Darmstadt, DE) with a base resistance R_0 of $350\,\Omega \pm 0.3\,\%$ is applied at a distance of 7 mm from one end of a 1.4310 steel plate. This corresponds to the same position at which the strain gauges were applied to the LPBF-manufactured prototype force sensors from the last chapter. Again, two LPBF-manufactured lower base bodies are manufactured with the same geometry as for the LPBF-manufactured spring elements from the last chapter (Sec. 3.2) to allow insertion of the steel plate, and, thus, expose the strain gauge to the LPBF-process. After continuing the LPBF-process, two LPBF-manufactured parts of 6 mm height with fully printed scanning area are built-up on top of these steel plates without establishing any connection between the steel plate and the LPBF-manufactured base bodies. This corresponds to the height of the LPBF-manufactured upper base bodies of the spring elements considered so far. The resistance of the strain gauge is recorded during this process in four-wire configuration with a sourcemeter (type: SMU 2450, Keithley, Cleveland, OH, US). In addition, the base resistance of the strain gauge is measured before and after the process as soon as the steel plate has cooled down to room temperature.

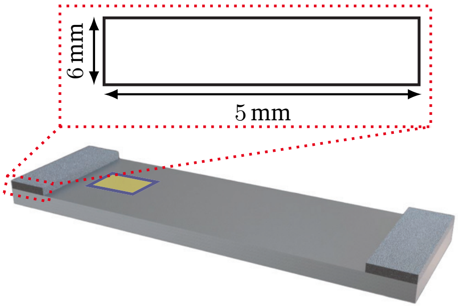

Figure 4.4: The strain is now shifted from the center of the steel plate to the edge (yellow marked area), which corresponds to the position at which the strain gauges were applied to the LPBF-manufactured prototype force sensors from the last chapter. Note that the areas marked in yellow indicate the location of the strain gauge, which is actually on the other side of the steel plate.

The measurements of the relative change in resistance in this experiment show as well a typical characteristic of the layer-by-layer manufacturing process through the 300 recurring peaks corresponding to the 300 manufactured layers [Fig. 4.5(a)]. The peaks in this case are significantly more pronounced compared with the signal of the strain gauges applied to the center of the steel plates [Fig. 4.3(b), (d)]. The time between two scannings (equivalent to two layers) is determined from this resistance signal by means of a Fast Fourier transform (FFT) using Matlab (R2019b, MathWorks, Massachusetts, US). This results in a distinctive frequency peak of $0.067\,14$ Hz, which corresponds to 14.89 s that is in excellent agreement with the time between two peaks of the measured signal.

The curve of the relative change in resistance shows again the characteristic course of a rapid change, which

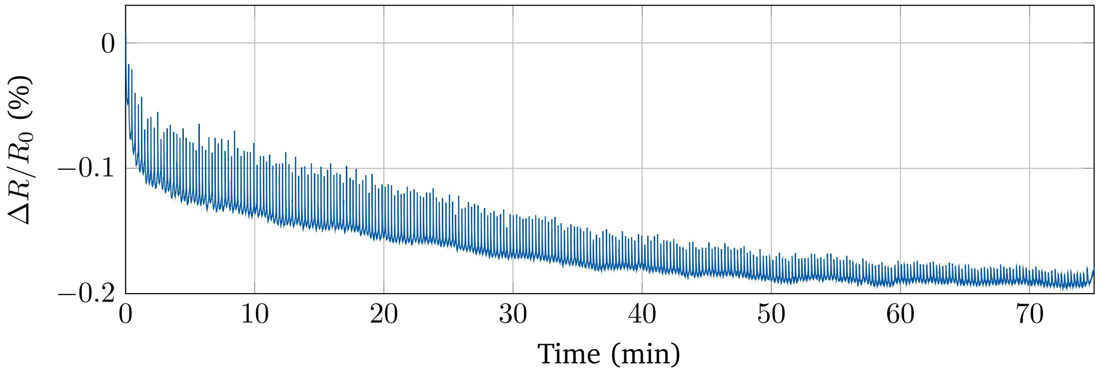

(a)

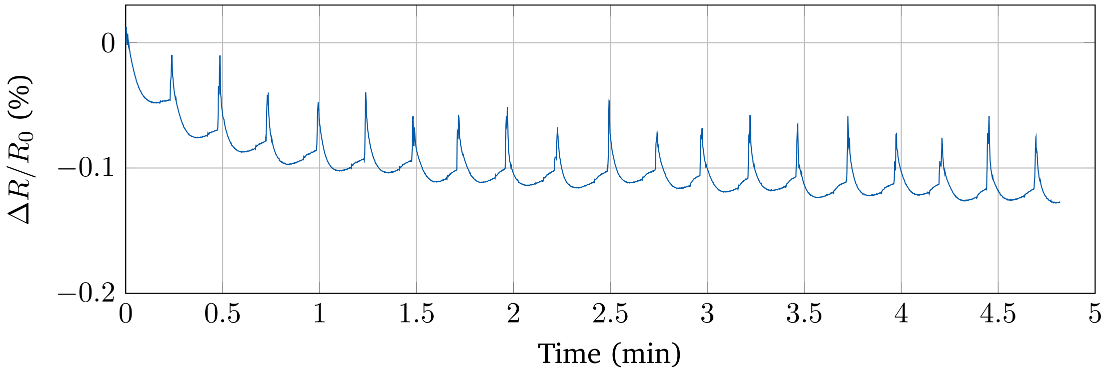

(b)

Figure 4.5: The relative change in resistance of the strain gauge located at the edge of the steel plate with fully printed scanning area shows one sharp peak for each scanning or manufactured layer. The rapid change in the signal turns into a saturation due to reaching a thermal equilibrium within the steel plate and strain gauge (a). The first 15 scannings or manufactured layers are shown in (b). They show that during the first cycles, the compression at the bottom side of the steel plate is more dominant, which is caused by the temperature gradients in the steel plate.

then slowly turns into saturation [Fig. 4.5(a)]. Several effects occur during the LPBF-process, which are more prominent in this measurement with the strain gauge positioned at the edge of the steel plate than in the measurement with strain gauges positioned in the center. These include the temperature dependency of the resistance of the strain gauge as well as the thermal expansion, which on one hand increases the length of the steel plate as well as that of the strain gauge and on the other hand bends the steel plate due to large temperature gradients. In this context, the thermal expansion has a lower dynamic than the temperature dependency of the resistance of the strain gauge. During each scanning, energy is introduced into the steel plate, causing a rapid rise in temperature that heats up the strain gauge accordingly. In this case, heating of the steel plate and strain gauge takes place because the cooling time is too short before re-scanning. Therefore, a rise in the signal due to the temperature dependency of the resistance and thermal expansion is measurable. Moreover, a bending of the steel plate is caused by temperature gradients, as the scanned upper side of the steel plate is hotter than the lower side with the strain gauge. This results in different amounts of expansion between the two sides of the steel plate. In the first six to eight scanning cycles (equivalent to six to eight layers), the rise in the peaks is smaller than their drop [Fig. 4.5(b)]. This is due to the fact that after scanning, besides the decrease of the temperature in the steel plate due to heat conduction and convection, the compression on the bottom side of the steel plate begins. Consequently, the resistance of the strain gauge continues to drop. The gradient within the steel plate decreases regarding the top and bottom as it continues to heat up during the process. Thus, the ratio between the rise and drop of the further peaks becomes more or less balanced. However, the effect of compression remains after each scanning, even in a smaller degree. Over the entire LPBF-process, a thermal equilibrium is established, where the compression is stabilized and the relative change in resistance saturates at about $-0.19\,\%$. In addition, the decreasing peaks of each layer show that less energy from the laser beam is introduced into the plate by the increasing size of the LPBF-manufactured parts. This contributes to achieving the thermal equilibrium. The relative change in resistance through the LPBF-process is thus nearly four times the relative change in resistance of the strain gauge that was applied in the center of the steel plate. The irreversible change in the base resistance of the laterally applied strain gauge after the process is $-0.139\,\% \pm 0.001\,\%$, which is significantly larger than that of the applied strain gauges in the center. This emphasizes further the increased impact of the larger thermal load due to the LPBF-process in this case.

4.2 Behavior of strain gauges during manufacturing of the spring element

Temperature and strain profile along the inserted steel plate are measured, with the goal of gaining a deeper insight into the impact of the thermally induced deformation on the strain gauges while manufacturing the spring element. These measurements were conducted as part of a bachelor thesis of Tim Engel [186].

4.2.1 In-situ measurement of the temperature of the steel plate

The temperature profile along the inserted steel plate is recorded using thermocouples (type: 5TC-GG-KI-30-1M, OMEGA Engineering inc., Deckenpfronn, DE) with an accuracy of $\pm\,1.5\,°\mathrm{C}$. For this purpose, five of these thermocouples (TC_1 to TC_5) are bonded to a 1.4310 steel plate using an epoxy adhesive (type: M-121HP, Henkel AG & Co. KGaA, Düsseldorf, DE). The thermocouples are located so that the measuring tips of the two outermost thermocouples (TC_1 and TC_5) are at a distance of $9.65\,\mathrm{mm}$ with respect to the edge of the steel plate. Thus, the measuring tips of these two thermocouples are located at the position of the measuring grid center of the strain gauges, as they were located in the prototype force sensors in the previous chapter. Consequently, temperature measurements are feasible that the strain gauges are exposed to when being integrated into the LPBF-process during the manufacturing of the spring elements. The remaining three thermocouples (TC_2, TC_3 and TC_4) are attached equidistantly between the two outer thermocouples.

For the application of the thermocouples, markings are made with a scribe at the designated locations. Then, a small amount of adhesive is applied at one of the marked locations followed by the placement of a thermocouple. In order to prevent the thermocouple from slipping while the adhesive is curing, it is fixed directly behind the measuring tip to the steel plate with a clamp. Afterwards, a hot air soldering station is used to cure the adhesive at $150\,°\mathrm{C}$. This procedure is repeated for all five thermocouples consecutively. Finally, a drop of the adhesive is placed over each of the thermocouples, since some of them had detached from the steel plate in preliminary tests [186]. This additional adhesive layer cures for $24\,\mathrm{h}$ at room temperature.

The steel plate is inserted into the LPBF-process after the adhesive has cured completely. The same geometry as for the LPBF-manufactured prototype force sensors (Chap. 3) is selected (Fig. 4.6). However, the height of the LPBF-manufactured upper base bodies will be halved in this experiment to reduce the amount of material required. The integration of the steel plate with applied thermocouples is done during a process interruption according to the disruptive manufacturing method presented in this work. At the same time, the thermocouples are connected via screw terminals to the cable harness, which is routed within the LPBF machine into the process chamber. This allows to read out the thermocouples during the process, and, thus, to measure the temperature profile along the steel plate during the manufacturing of the upper base bodies with a height of 3 mm. The data of all five thermocouples is acquired with a temperature measurement module (type: NI-9213, National Instruments, Austin, Texas, US) with an accuracy of $\leq 0.25\,°C$. The sampling rate is 20 Hz.

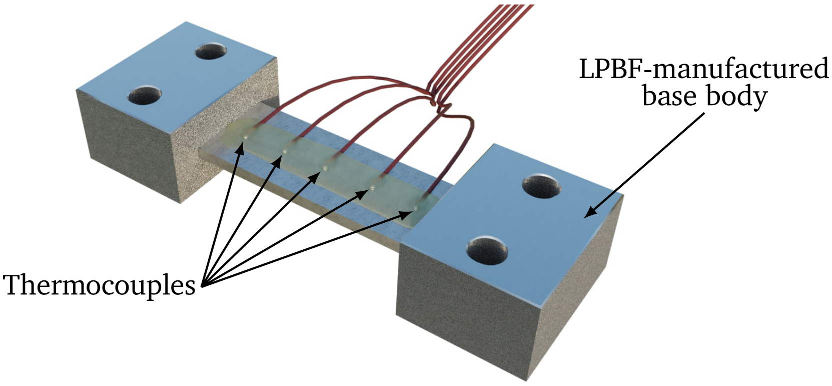

Figure 4.6: The steel plate with bonded thermocouples TC_1 to TC_5 (from left to right) is integrated within the LPBF-manufactured spring element, which allows for measuring the temperature profile during manufacturing within the LPBF-process. Here, the bottom side of the LPBF-manufactured spring element is shown to illustrate the thermocouples. It must be noted that the side of the steel plate with applied thermocouples faces the build platform when it is integrated into the LPBF-process.

The temperature measurement during the process shows that all five thermocouples start at almost 70 °C [Fig. 4.7(a)]. This corresponds to a temperature difference of about 10 K from the preset build platform temperature T_{BPF} of 80 °C. This is due to the fact that the inserted steel plate and the thermocouples, respectively, are not in direct contact with the build platform. Furthermore, the temperature set for the build platform is actually the controlling temperature for the heater that is located underneath the build platform. There is loss across the build platform in terms of heat due to heat transfer and convection, thus the temperature at the surface of the build platform may deviate from the 80 °C that are set. For steady state, i.e., over a long period of time, the temperature within the steel plate would equalize to the temperature of build platform. However, the process conditions are reached prior to this steady state leading to the process starting.

The curves of all five thermocouples show the typical characteristic of the layer-by-layer manufacturing process through the recurring peaks [Fig. 4.7(a)]. There are 150 peaks in the signal of each of the five thermocouples, which result from the LPBF-manufactured upper base bodies with a height of 3 mm and a layer height of 20 µm. The scanning time between two scannings is determined from the signal of the thermocouples by means of a FFT using Matlab (R2019b, MathWorks, Massachusetts, US). A distinctive peak at a frequency of 0.0394 Hz can be found in the FFT of the signals of all five thermocouples. This corresponds to 25.38 s, which is in very good agreement with the time between two peaks of the measured signals and is, therefore, the coating time.

The signals of the outer two thermocouples (TC1 and TC5) are almost overlapping [Fig. 4.7(a)]. This is as expected, since they are located equidistant from the laser beam. The same applies to the two thermocouples TC2 and TC4 with respect to the distance from the laser beam. However, a deviation is noticeable between the signals of these two thermocouples. This is due to the unprecise positioning of these thermocouples and slippage that occurred during the curing of the adhesive. A sharp rise in the temperature of the steel plate

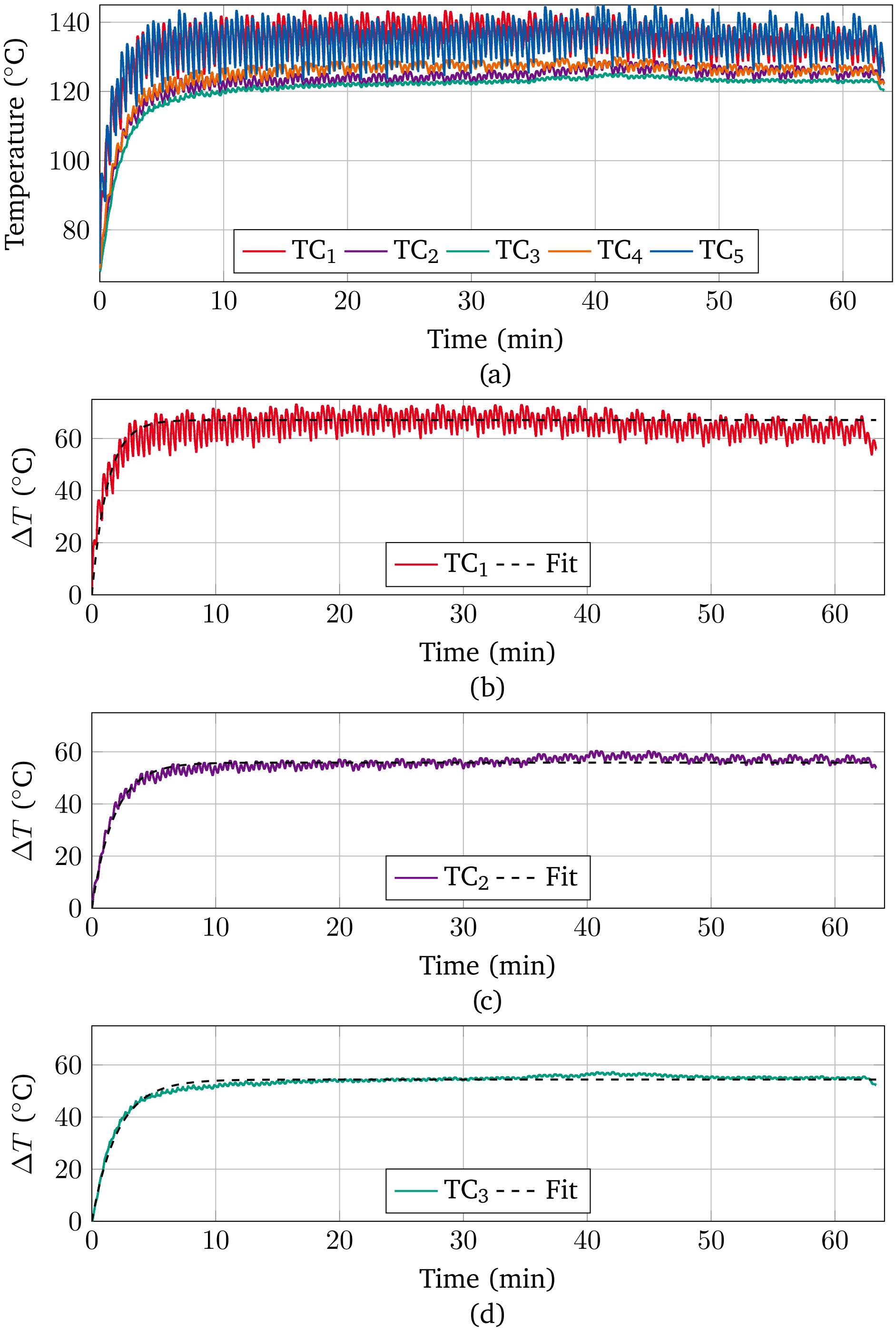

Figure 4.7: The temperature profile along the steel plate, which is measured by five thermocouples, shows a sharp increase of the temperature within the steel plate as soon as the first scanning starts as well as the layer-by-layer build-up through the LPBF-process by the prominent peaks (a). In addition, a temperature gradient with decreasing temperature from the outer edge to the center of the steel plate is present (b), (c), (d). The temperature curve is fitted with the aid of an exponential function in analogy to the charging process of a capacitor.

takes place as soon as the LPBF-process starts with the first layer [Fig. 4.7(a)]. This sharp rise in temperature decreases after 12 layers and almost turns into a plateau. It is noticeable that the peak-to-peak temperature of the outer thermocouples ($\mathrm{TC_1}$ and $\mathrm{TC_5}$) is significantly larger with around $20\,°\mathrm{C}$ than the peak-to-peak temperature of the center thermocouple ($\mathrm{TC_3}$) with almost $2\,°\mathrm{C}$. This characteristic is as expected, since the outer thermocouples are closer to the exposed surface, and, thus, closer to the laser beam. The remaining two thermocouples ($\mathrm{TC_2}$ and $\mathrm{TC_4}$), which are attached in between the outer and center thermocouples, undergo a peak-to-peak temperature of about $5\,°\mathrm{C}$. Consequently, the change in temperature during a scanning step is higher, the farther the thermocouple is attached with respect to the center of the steel plate. Considering the last 10 layers in the build process, the peak-to-peak temperatures for the outer and center thermocouples decrease to less than $12\,°\mathrm{C}$ and $1\,°\mathrm{C}$, respectively. The decrease in the changes in temperature results from the increasing build-up of material within the LPBF-process, which causes an increase in the heat capacity of the test specimen.

In addition, the change in temperature ΔT, which is defined as the difference between the measured temperature and the initial temperature, i.e., the temperature prior to the start of the first scanning, is also higher, the farther the thermocouple is attached with respect to the center of the steel plate. This is evident when comparing the changes in temperature of the steel plate from the exterior to the center of the steel plate of $\Delta T_{\mathrm{TC1}} = 67.1\,°\mathrm{C} \pm 3.4\,°\mathrm{C}$, $\Delta T_{\mathrm{TC2}} = 56.1\,°\mathrm{C} \pm 1.6\,°\mathrm{C}$ and $\Delta T_{\mathrm{TC3}} = 54.4\,°\mathrm{C} \pm 1.1\,°\mathrm{C}$ [Fig. 4.7(b), (c), (d)] by the thermocouples $\mathrm{TC_1}$, $\mathrm{TC_2}$ and $\mathrm{TC_3}$, respectively. These values are obtained by averaging the temperature readings starting from $t = 10\,\mathrm{min}$ of the respective thermocouple. Based on these values, the temperature curves, which have the characteristic shape of a charging process of a capacitor, can be modeled as a heat-up process $T_{\mathrm{Fit}}(t)$ (4.1) [192] of the steel plate using the electrical-thermal analogy [193]

$$T_{\mathrm{Fit}}(t) = T_0 \cdot \left(1 - e^{-\dfrac{t}{\tau}}\right), \tag{4.1}$$

where T_0 is the stationary temperature, t is the time and τ is the characteristic time constant. The stationary temperatures for the different locations of the steel plate are set to the determined values ΔT_{TC1}, ΔT_{TC2} and ΔT_{TC3}. Modeling of the temperature curves $T_{\mathrm{Fit,\,TC1}}(t)$, $T_{\mathrm{Fit,\,TC2}}(t)$ and $T_{\mathrm{Fit,\,TC3}}(t)$ is performed using the least-squares method by varying the characteristic time constants τ_{TC1}, τ_{TC2} and τ_{TC3}, respectively. As a result, the temperature curves during the process at the different locations of the steel plate can be modeled properly with the time constants $\tau_{\mathrm{TC1}} = 77.1\,\mathrm{s}$, $\tau_{\mathrm{TC1}} = 108.9\,\mathrm{s}$ and $\tau_{\mathrm{TC1}} = 125.1\,\mathrm{s}$ [Fig. 4.7(b), (c), (d)]. Two observations are evident from these results. On one hand, a temperature gradient is maintained along the steel plate, which means that the temperature in the whole steel plate does not reach a stable point during the more than one-hour lasting process. On the other hand, it takes about 1.5 times as long to reach the stationary temperature in the center of the steel plate as at the outer locations.

In the following, a moving average of the signals of the thermocouples after the 12th layer is considered (Fig. 4.8), since no influence of the connection points, i.e., the lateral and rear connection of the inserted steel plate and the LPBF-manufactured upper base bodies (Fig. 3.3), is visible in the raw signals considered so far. In this case, 10 layers are chosen as the window size for the moving average. Thus, the peaks caused by the layer-wise laser beam are no longer predominant with a more pronounced temperature gradient in the steel plate. Moreover, an increase in the temperature of the steel plate of up to $3\,°\mathrm{C}$ is observed with the beginning of the lateral and rear connection between the steel plate and the LPBF-manufactured upper base bodies (Fig. 4.8). The lateral and rear connections result in a larger scanning area as well as improved thermal conductivity between the steel plate and the LPBF-manufactured base bodies. Both aspects lead to the increase of temperature in the steel plate. After a few more layers, thermal equilibrium is reached again, so that the temperature in the steel plate remains constant. In conclusion, although a temperature gradient is present in the steel plate during the manufacturing of the spring element, the temperatures at the locations for the strain gauge installation remain below 145 °C, and, thus, below the permitted operating temperature of the selected strain gauges of 200 °C. Therefore, no damage of the strain gauges is expected due to the temperature during the LPBF-process.

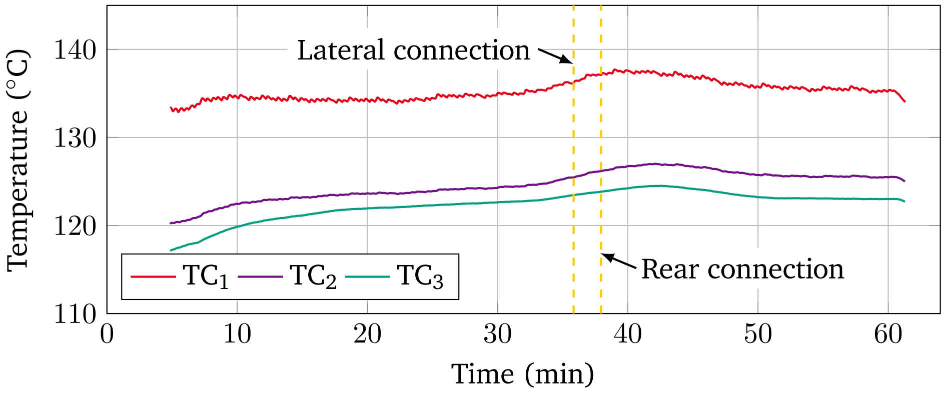

Figure 4.8: The moving average of the signals of the thermocouples shows a slight increase in the temperature of the steel plate as soon as the lateral and rear connection of the steel plate with the LPBF-manufactured upper base bodies is made. This effect is due to the subsequent improved thermal conductivity.

4.2.2 In-situ measurement of the deformation of the steel plate

Since the strain gauge withstands the temperature of the LPBF-process, the next step is to investigate the influence of the deformation of the inserted steel plate due to its bonding with the LPBF-manufactured base bodies. This deformation acts as an excessive pre-strain of the strain gauge and may exceed its maximum elongation. Therefore, the strain profile along the steel plate is measured similarily to the measurement of the temperature profile with several applied strain gauges. Both steel plate types (1.4310 and 1.4404) are considered in this experiment, as it was found that the 1.4404 steel plate deforms more at the edges due to the material applied by means of the LPBF-process (Fig. 4.1). This is intended to investigate the impact of the larger deformation on the strain gauge. For this purpose, five strain gauges (SG_1 to SG_5) are applied each to a 1.4310 and 1.4404 steel plate (Fig. 4.9). Since five of the strain gauges used so far (type: 1-LY45-1.5/350, HBK, Darmstadt, DE) cannot be applied to the steel plate due to their larger size, T-rosette strain gauges (type: 1-XY11-1.5/350, HBK, Darmstadt, DE) are used in this experiment. These have a smaller carrier and two measuring grids, which are arranged at a 90° offset from each other. However, the measuring grids as well as the base resistance of the previously used linear strain gauges and the T-rosette strain gauges are of the same size. Note that these strain gauges are matched to ferritic steel in terms of their thermal expansion, which results in a small mismatch between the thermal expansion coefficients of the strain gauges and the steel plate. The strain gauges are applied to the steel plates in such a way that the position of center of the measuring grid is identical to the position of the thermocouples from the last section (Sec. 4.2.1).

Again, the same geometry as for the LPBF-manufactured prototype force sensors (Chap. 3) is selected (Fig. 4.9). The integration of both steel plates (1.4310 and 1.4404) with applied strain gauges is done during a process interruption according to the disruptive approach presented in this work. The strain gauges are connected via screw terminals to the cable harness to measure the response of the strain gauges during the manufacturing of the upper base bodies by LPBF. Here, not all five strain gauges can be measured in four-wire

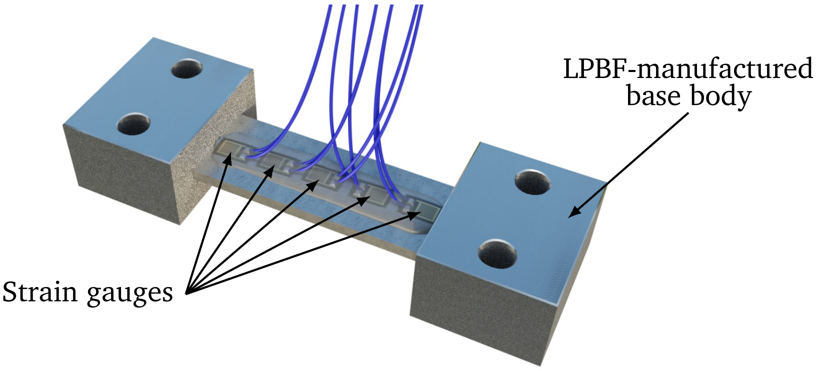

Figure 4.9: The steel plates (1.4310 and 1.4404) with applied strain gauges SG_1 to SG_5 (from left to right) are integrated within the LPBF-manufactured spring element, which allows for measuring the strain profile during manufacturing of the upper base body. Here, the bottom side of the LPBF-manufactured spring element is shown to illustrate the strain gauges. It must be noted that the side of the steel plate with applied strain gauges faces the build platform when it is integrated into the LPBF-process.

configuration, since 10 terminals are required but only 8 are available. Therefore, the two outer strain gauges (SG_1 and SG_5) and the center strain gauge (SG_3) are measured in four-wire configuration, while the other two strain gauges (SG_2 and SG_4) are measured in the common two-wire configuration. The measurement of the resistances of the strain gauges is performed with different sourcemeters, as in the case of SG_1 and SG_5 (type: SMU2450, Keithley, Cleveland, OH, US) as well as SG_2 (type: SMU2440, Keithley, Cleveland, OH, US), and digital multimeters, as in the case of SG_3 (type: DMM7510, Keithley, Cleveland, OH, US) and SG_4 (type: DMM2002, Keithley, Cleveland, OH, US) due to availability. The number of power-line-cycles (NPLC) value is set to 4.

The measurement of the change in resistance of the strain gauges during the process, i.e., during the manufacturing of the upper base bodies, provides no clear indication of the deformation of the steel plate, since various effects are superimposed. Among them, there are the thermal expansion of the steel plate, and, thus, of the strain gauge, the dynamic temperature response at the measured locations, the drift of the strain gauges due to the temperature pulses of the laser beam and the deformation of the steel plate itself. Even when using thermally matched strain gauges, a nonlinear contribution remains with respect to the thermal expansion. In addition, an uncertainty analysis based on averaging multiple measurement values is not feasible due to the high dynamic in the LPBF-process. Therefore, all these effects cause a superimposed change in the resistance of the strain gauges during the LPBF-process. Consequently, the resistance curves measured during the process can primarily be used to only identify effects that lead to the deformation of the steel in the manufacturing process of the upper base bodies. However, to evaluate the effect of the deformation of the steel plate on the strain gauges, a comparison of the change in resistance in defined steady states is carried out. For this purpose, the base resistance of each strain gauge is measured in three states. These states are:

1. Before placing the steel plate into the LPBF-process (R_0),
2. After completion of the LPBF-manufactured spring element and cooled down to room temperature, while it remains connected to the build platform (R_{BPF}),
3. After separating the LPBF-manufactured spring element from the build platform (R_{Cut}).

The resistances of the strain gauges in these three states are measured in a four-wire configuration using a sourcemeter (type: SMU2450, Keithley, Cleveland, OH, US), where 100 readings are always recorded.

The change in resistance measured for each strain gauge ΔR during the LPBF-process is related to the respective base resistance ΔR_0 before the first scanning. Similar to the measurement with the thermocouples (Fig. 4.7), the characteristic of the layer-wise build-up in the LPBF-process is also observed in the resistance measurement by the distinctive peaks (Fig. 4.10). For the sake of clarity, only the outer two (SG_1 and SG_5) as well as the center strain gauge (SG_3) are shown for both steel plate types. Each peak in the curve corresponds to a scanning for a new layer to be applied.

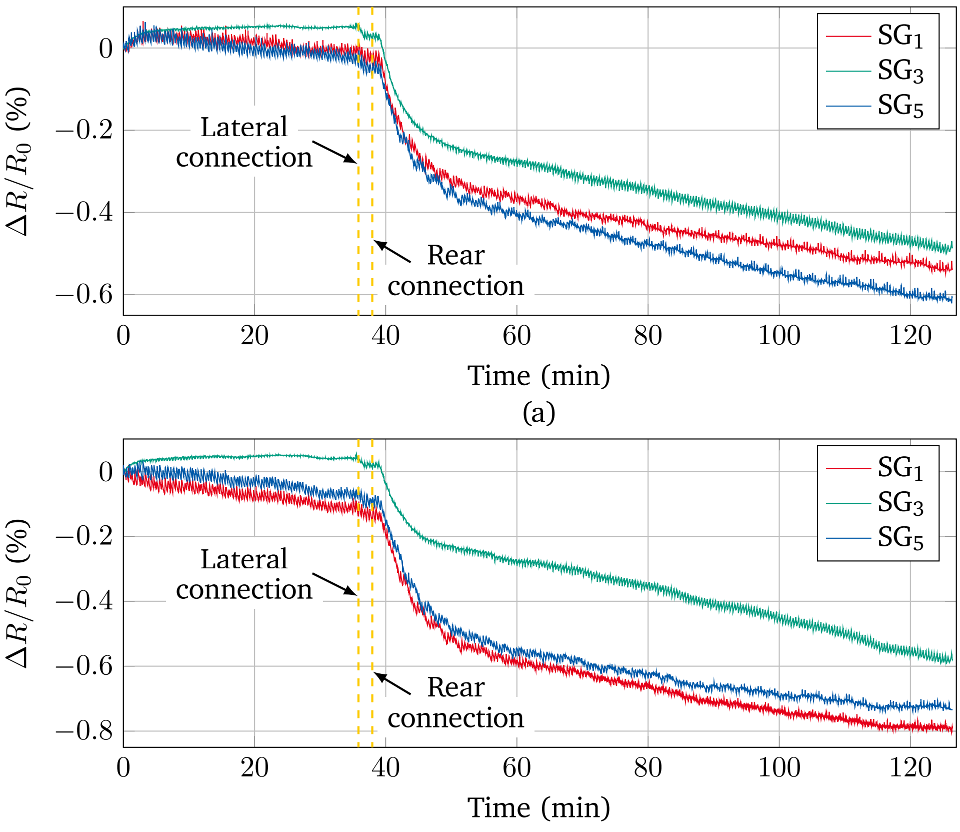

(a)

(b)

Figure 4.10: The measurement of the resistance of the outer two strain gauges(SG_1 and SG_5) as well as the center strain gauge (SG_3) of both steel plate types 1.4310 (a) and 1.4404 (b) shows the layer-wise build-up in the LPBF-process due to the predominant peaks. A significant drop in the resistance curves is noticeable shortly after completion of the rear connection, which is caused by the thermally induced deformation of the steel plate.

The course of the change in resistance is similar for both types of steel plates. The resistances of the outer two strain gauges initially decrease by up to $0.1\,\%$ until the lateral connection (Fig. 3.3) of the steel plate with the LPBF-manufactured base bodies after 85 layers is completed. This is followed by a slightly higher drop in the resistances of the strain gauges during the next seven layers, i.e., until the rear connection (Fig. 3.3) is completed. Subsequently, the most distinctive change in resistance is observed after three further layers. This is evident since in the subsequent 20 layers, which correspond to a built-up material height of $0.4\,$mm based on a layer height of $20\,\mu\mathrm{m}$, a change in resistance for the two steel plate types 1.4310 and 1.4404 of about $-0.25\,\%$ [Fig. 4.10(a)] and $-0.35\,\%$ [Fig. 4.10(b)] occurs, respectively. This significant change in resistance is an indication of the occurrence of thermally induced deformation of the steel plates (Fig. 3.13). Since the strain gauges are located on the bottom side of the steel plates where compression occurs, the negative change in resistance is plausible. The occurrence of this distinctive change in resistance moments after completion of the rear connection confirms that the occurring tensile stress due to the different cooling times of the molten material and the lever arm due to the geometry (Fig. 3.13) cause the thermally induced deformation of the steel platelets. A continuous and approximately linear decrease of the resistances is present over the remaining course of the manufacturing process, which is due to the drift of the resistances. This drift results from the combination of the strain gauges being loaded by the deformation and the dynamic temperature changes caused by the laser beam. Overall, this results in a drop in the resistances of the outer strain gauges (SG_1 and SG_5) for the 1.4310 and 1.4404 steel plates over the entire process of about $0.6\,\%$ [Fig. 4.10(a)] and $0.8\,\%$ [Fig. 4.10(b)], respectively.

In order to evaluate the impact of the thermally induced deformation of the steel plate on the strain gauges, the changes in resistance of the strain gauges from the states *on the build platform* (ΔR_{BPF}) and *separated from the build platform* (ΔR_{Cut}) are related to the initial state *before the process* (R_0). The comparison of the resistances of these defined states shows that the change in resistance of all five strain gauges applied to the 1.4404 steel plate (SG_1 to SG_5) is greater compared to those applied to the 1.4310 steel plate (Tab. 4.1). The uncertainties of all values in Tab. 4.1 are within $\pm\,0.001\,\%$ for a confidence level of $99\,\%$. Thereby, the change in resistance of the outer strain gauges (SG_1 and SG_5) is greater than the center strain gauges (SG_2, SG_3 and SG_4). Furthermore, it is shown that the thermally induced deformation of the steel plates is released after the LPBF-manufactured spring element are separated from the build platform. This is expressed by an increase in the resistances of all strain gauges compared to the state on the build platform, so that the resistance values get closer to the initial values again. After separating the LPBF-manufactured spring element from the build platform, the resistance of the strain gauges do not entirely return to their initial values measured before the process. The remaining deviation of the resistance values is larger than in the experiment from Sec. 4.1, which indicates a low remaining residual stress, and, thus, a low remaining residual deformation within the LPBF-manufactured spring element.

Table 4.1: The remaining changes in resistance are measured in two different states of the strain gauges and then referred to the respective base resistance before the strain gauges were exposed to the LPBF-process. The different states are, on the one hand, when the spring elements have cooled down to room temperature while remaining on the build platform (ΔR_{BPF}) and, on the other hand, after being separated from the build platform (ΔR_{Cut}).

State	**Steel plate 1.4310**					**Steel plate 1.4404**				
	SG_1	SG_2	SG_3	SG_4	SG_5	SG_1	SG_2	SG_3	SG_4	SG_5
$\Delta R_{\mathbf{BPF}}/R_0$ **(%)**	-0.57	-0.47	-0.41	-0.47	-0.57	-0.75	-0.57	-0.55	-0.56	-0.75
$\Delta R_{\mathbf{Cut}}/R_0$ **(%)**	-0.15	-0.08	-0.04	-0.10	-0.15	-0.55	-0.32	-0.31	-0.32	-0.55

Behavior under static load

The previous experiment has shown that an irreversible change in the base resistance of the strain gauges occurs after their embedding in the LPBF-manufactured spring element through the inserted steel plate.

Therefore, it needs to be investigated whether this has an influence on the static behavior under load as a force sensor. This is evaluated using the prototype with the 1.4310 steel plate including the five applied strain gauges from the last section. In order to establish a performance baseline regarding the linearity with respect to a best-fit line and the sensitivity, this new prototype force sensor is loaded using the setup with the universal testing machine (Fig. 3.19) as presented in previous chapter. The force is increased with a load rate of $0.2\,\mathrm{N\,s^{-1}}$ until $15\,\mathrm{N}$ are reached and then maintained for $10\,\mathrm{s}$. Afterwards the force is decreased with the same slope until the new prototype force sensor is unloaded. Here, only the outer two strain gauges (SG_1 and SG_5) are evaluated, since they are located at proper positions due to the S-shaped deformation. Note that the positions of strain gauges SG_1 and SG_5 correspond to the positions of the strain gauges of the LPBF-manufactured prototype force sensors discussed in Chap. 3, that were applied after the manufacturing process.

This new LPBF-manufactured prototype force sensor (strain gauges applied to the steel plate prior to the manufacturing process) exhibits a linear behavior under load according to the relative change in resistance (Fig. 4.11). The pre-strain of the strain gauges caused by thermally induced deformation of the steel plate results in different base resistances of both strain gauges. These values are considered as the current base resistances of the strain gauges. The load of $15\,\mathrm{N}$ corresponds to a relative change in resistance ΔR of $218.74\,\mathrm{\mu\Omega\,\Omega^{-1}}$ and $-218.86\,\mathrm{\mu\Omega\,\Omega^{-1}}$ for the elongated (SG1) and compressed (SG5) strain gauge, respectively. Furthermore, a small linearity error of $\pm 0.1\,\%$ with respect to a best-fit line is achieved for both strain gauges. In order to provide a better comparison with the previous LPBF-manufactured prototype force sensor with afterwards applied strain gauges (Chap. 3), the sensitivity of the new LPBF-manufactured prototype force sensor can be determined using a full bridge configuration. For this purpose, the signal of both strain gauges (SG_1 and SG_5) is used twice to achieve a full bridge configuration. Hereby, the compressed strain gauge signal corresponds to both decreasing resistances and the elongated strain gauge signal corresponds to both increasing resistances of the full bridge. This results in a theoretical relative bridge output signal of $218.8\,\mathrm{\mu V\,V^{-1}}$, which is in excellent agreement with the previous LPBF-manufactured protoype force sensor (Tab. 3.6, prototype P1).

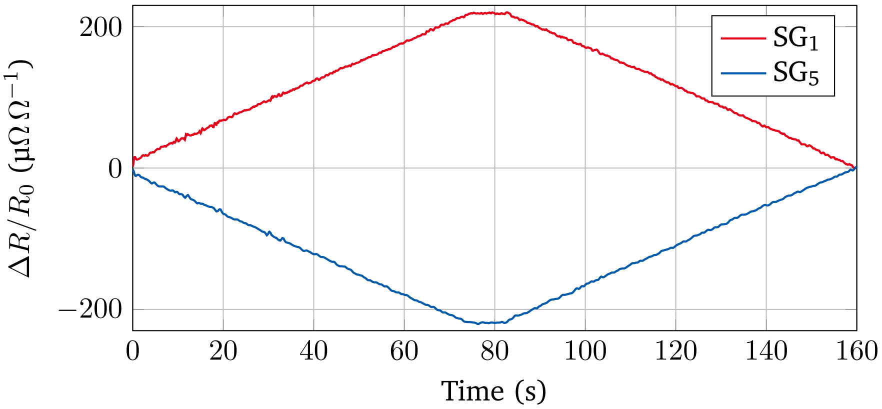

Figure 4.11: The relative change in resistance of both strain gauges is linear proportional to the applied load up to $15\,\mathrm{N}$. As expected one strain gauge undergoes an elongation (SG_1) and the other a compression (SG_5).

4.3 Behavior of a full bridge configuration during manufacturing of the spring element

In the final experiment, the behavior of a full bridge configuration is investigated during and after the LPBF-process to provide a better comparison with the previous LPBF-manufactured prototype force sensors (strain gauges applied after the process). The full bridge configuration requires four strain gauges with two being elongated under load while the other two undergo compression. All four strain gauges need to be applied to one side of the steel plate, while the other side has to remain free due to the coating blade moving over it. This is in contrast to the previous LPBF-manufactured prototype force sensors from the last chapter, which had strain gauges on both sides of the steel plate (Fig. 3.18). However, the full bridge configuration is achievable because of the S-shaped deformation of the LPBF-manufactured spring elements. This deformation provides both elongation and compression on one side of the steel plate (Fig. 3.11). Hence, two strain gauges must be applied at each of these locations. Double linear strain gauges are used for this purpose (type: 1-DY41-1.5/350, HBK, Darmstadt, DE), since the application of two linear strain gauges (type: 1-LY41-1.5/350, HBK, Darmstadt, DE) next to each other causes difficulties in terms of space. Moreover, the double linear strain gauges reduce the application effort, since two measuring grids are provided on one carrier. Two of these double linear strain gauges are applied to one side of a 1.4310 steel plate, each at a distance of $7\,\mathrm{mm}$ from the edge of the steel plate, which is the same distance as in the case of the previous LPBF-manufactured prototype force sensors from the last chapter. This steel plate is inserted during a process interruption in the same geometry with fully printed scanning area used so far.

The measurement of the bridge output voltage U_D, which is referred to the bridge excitation voltage $U_\mathrm{S} = 5\,\mathrm{V}$, during the LPBF-process shows again a typical characteristic of the layer-wise build-up in the LPBF-process by the distinctive peaks (Fig. 4.12). Note that only the recorded signal of the first 200 layers of the complete 300 layers are shown in Fig. 4.12, since the remaining part of the signal is nearly the same as in the layers before. It is noticeable that the peaks predominate the signal of the bridge output voltage during the LPBF-process. The amplitudes of the peaks are comparable to a bridge output voltage which results from

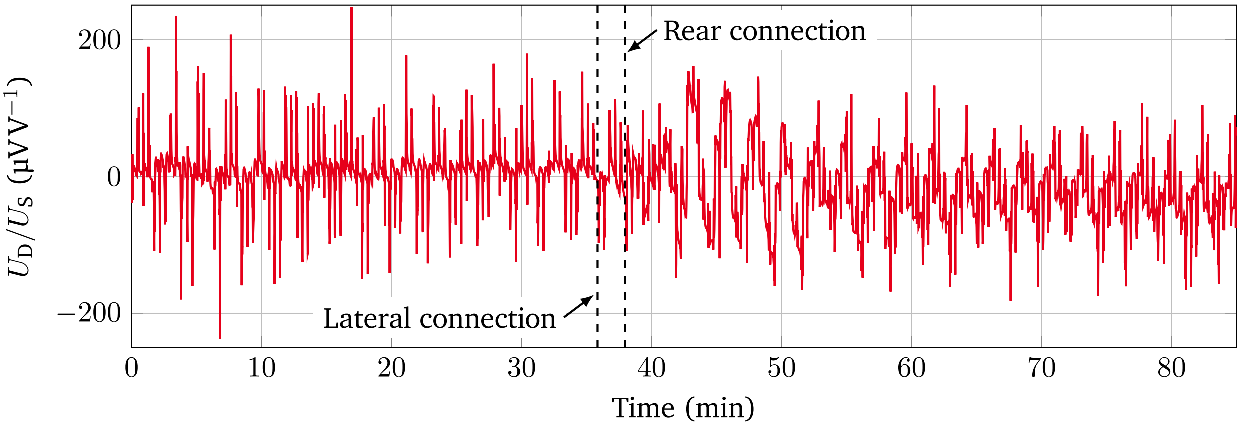

Figure 4.12: The measurement of the change in the bridge output voltage of shows the layer-wise build-up in the LPBF-process due to the predominant peaks. The amplitudes of most of the peaks are comparable with the resulting output voltage of the force sensor, which results when the sensor is loaded with about $10\,\mathrm{N}$. The shape of the curve between 40 and 50 minutes is different from the rest of the curve, which is due to the resulting thermally induced deformation of the steel plate.

a load of the force sensor with about $10\,\mathrm{N}$. Moreover, other effects such as the onset of thermally induced deformation of the steel plate are not directly apparent, as in the case of measuring resistance of the single strain gauges (Fig. 4.10). Before the steel plate is joined to the LPBF-manufactured base bodies through the lateral and rear connection, the signal returns to approximately $0\,\mu\mathrm{V}\,\mathrm{V}^{-1}$ after each scanning. This is due to the temperature compensating effect of the full bridge configuration, since all strain gauges experience nearly the same temperature. A slight change in the shape of the signal of the bridge output voltage is visible between the 40th and 52nd minute, due to the occurring thermally induced deformation of the steel plate. Subsequently, the signal is stabilized again, however, the average of the signal does not return to $0\,\mu\mathrm{V}\,\mathrm{V}^{-1}$ due to the superimposed deformation of the steel plate. In addition, the amplitude of the peaks decreases as more material is built-up progressively, and thus, the energy introduced by the laser is not directly transmitted to the steel plate.

After finishing the fabrication process, the LPBF-manufactured prototype force sensor is separated from the build platform by a band saw and reworked by milling. Hereby, M5 threaded holes are drilled for fastening the LPBF-manufactured prototype force sensor to the measurement setup (Fig. 3.19) for its characterization under load. The loading is performed using a step profile in the same way as for the previous LPBF-manufactured prototype force sensors until reaching a maximum load of 15N.

The sensitivity of this LPBF-manufactured prototype force sensor is $239.1\,\mu\mathrm{V}\,\mathrm{V}^{-1} \pm 0.1\,\mu\mathrm{V}\,\mathrm{V}^{-1}$ for a load of $15\,\mathrm{N}$. This is higher than the sensitivity of the equivalent previous LPBF-manufactured prototype force sensor P1 (Tab. 3.6). In fact, the smaller substrate of the double linear strain gauges used here causes the measuring grid to be closer to the edge of the steel plate, which in turn subjects the strain gauges to higher elongation or compression. A comparison with the FEA model (Fig. 3.12) that is evaluated at the position of the measuring grid of the double linear strain gauge leads to a sensitivity of $242.1\,\mu\mathrm{V}\,\mathrm{V}^{-1} \pm 0.1\,\mu\mathrm{V}\,\mathrm{V}^{-1}$. This confirms that there is no difference between the sensitivities.

In addition, the linearity and hysteresis errors are determined, similar to the previous LPBF-manufactured spring elements (Sec. 3.4). These are based on the deviations between the mean values of the load steps and are determined using best-fit lines for all loading and unloading cycles, which are then referred to the nominal value (equivalent to the sensitivity). The largest errors of all load cycles are given as the linearity and hysteresis error, respectively. This results in a linearity and hysteresis error within $\pm\,0.05\,\%$ full scale and $\pm\,0.13\,\%$ full scale [Fig. 3.21(b)], respectively. Thus, there is no difference found in terms of linearity and hysteresis between the new LPBF-manufactured prototype force sensor and the previous one discussed in Chap. 3. It can be concluded that the LPBF-process does not affect the behavior of the strain gauges and, consequently, the performance of LPBF-manufactured force sensors in disruptive manner.

4.4 Conclusion

This chapter addressed the influence of the LPBF-process on the strain gauge behavior, which is the second aspect besides a homogenous and loss-free strain transmission from the LPBF-manufactured base bodies to the inserted steel plate that significantly influences the performance of LPBF-manufactured force sensors. For this purpose, experiments on the resistance-strain behavior of strain gauges before and after being exposed to the LPBF-process as well as the measurement of the temperature and the strain gauges behavior during the process were performed. The experiments were performed in two stages mainly to separate the influence of the LPBF-process and the thermally induced deformation of the steel plate as much as possible.

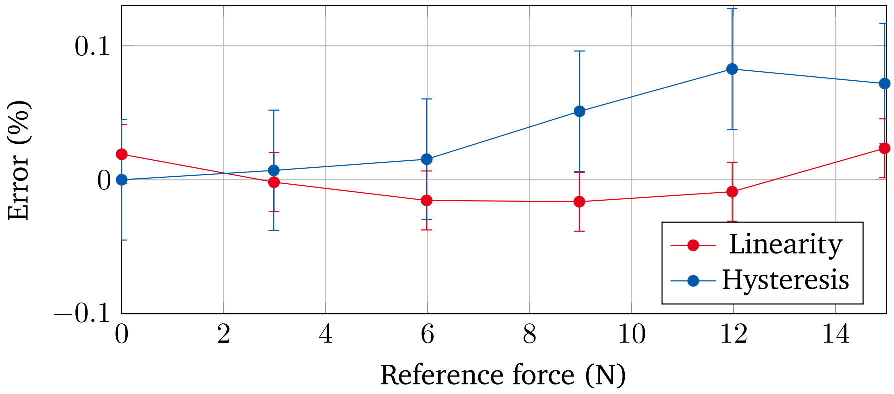

Figure 4.13: The linearity and hysteresis errors of the LPBF-manufactured prototype force sensor with prior to the LPBF-process applied double linear strain gauges in full bridge configuration show small values. These characteristic values are in excellent agreement with the ones of the LPBF-manufactured prototype force sensors with afterwards applied strain gauges.

The experiments of the first stage showed that strain gauges, which were exposed to the LPBF-process within the disruptive manufacturing method did withstand the process. Moreover, they maintained their performance regarding a linear strain sensing characteristic and sensitivity, although a slight but irreversible change in the base resistance occurred. This irreversible change in the base resistance was magnified the closer the strain gauge position to the exposed surface, and, thus, to the laser beam was. Measurements of the resistance of the strain gauges during the process of building up material without establishing a connection between the LPBF-manufactured base bodies and the steel plate showed that a smaller scanning area, as in the case of the checkered scanning area, results in a comparable change in resistance as a fully exposed area. Since the change in resistance in both cases was almost the same at the end of the process, it implied that both strain gauges experience the same thermal load and deformation of the steel plate. It could be concluded that there is no benefit in using the checkered scanning area in terms of lower thermally induced deformation of the steel plate. Moreover, this confirmed the results from the optical evaluation of the angle between the steel plate and the LPBF-manufactured base bodies (Fig. 3.16) from Chap. 3, which was almost the same in all cases, regardless of the exposed area. Thus, it provided a primary indication that a smaller scanning area does not lead to a lower thermally induced deformation of the steel plate. Furthermore, the measurements of the change in resistance of the strain gauges during the process have shown that the layer-by-layer manufacturing characteristic was prominently visible in the signal and a saturation over the process occurred as thermal equilibrium was reached.

In the experiments of the second stage the establishment of the connection between the LPBF-manufactured base bodies and the inserted steel plate was considered to investigate not only the influence of the LPBF-process but also that of the thermally induced deformation of the steel plate on the strain gauges. It was first found that the temperature in the steel plate increased rapidly and turned almost into a plateau after 10 to 12 layers due to reaching thermal equilibrium. Furthermore, a temperature gradient remained within the steel plate despite manufacturing 150 layers for a process duration of more than 1 h. This gradient was oriented from the center of the steel plate to the edges of the steel plate. This explained both the larger change in resistance of the strain gauge during the LPBF-process and the larger irreversible change in resistance after the LPBF-process of the strain gauges located at the edge of the steel plate compared to the centrally positioned strain gauges from the experiments of the first stage.

In further measurements regarding capturing the strain profile along the steel plate with five strain gauges it was shown that the occurrence of thermally induced deformation of the steel plate is reflected in a significant decrease in the resistance of the strain gauges. Before and after the occurrence of this deformation of the steel plate, the signal of the change in resistance is dominated by the thermal drift of the strain gauges. This provided a quality measure regarding the reduction of the thermally induced deformation of the steel plate. At the same time, such a signal of change in resistance of the strain gauge has the potential as a parameter for future process monitoring applications, and, thus, online tuning of process parameters. This irreversible change in the base resistance of the strain gauges in this experiment was again larger the closer position of the strain gauges to the scanned surface. The irreversible changes in resistance of the outer strain gauges in the two cases with and without establishing a connection between the LPBF-manufactured base bodies and the steel plate were $-0.15\,\%$ and $-0.14\,\%$, respectively. This implied that although the largest amount of the residual stresses was released after the LPBF-manufactured spring elements were separated from the build platform, a marginal amount remained which then caused this small difference between the changes in resistance of $-0.01\,\%$. However, the irreversible change in the base resistance of the strain gauges did not negatively affect the behavior as a force sensor under load. Rather, the linear behavior and sensitivity achieved remained in excellent agreement with LPBF-manufactured force sensors with subsequently applied strain gauges, i.e., which were not exposed to the LPBF-process. Furthermore, it was found that the thermally induced deformation of 1.4404 steel plates is larger than that of 1.4310 steel plates due to a lower yield strength. Although the thermally induced deformation of the steel plate, and, thus of the strain gauges, did not negatively affect the performance of the prototype force sensors under static load, it reduces the maximum applicable load, since the remaining residual stress acts a permanent offset stress. Therefore, only 1.4310 steel plates will be considered in the further development of the LPBF-manufactured force sensors.

The results obtained so far emphasize the suitability of the disruptive manufacturing method using LPBF for manufacturing structural integrated force sensors based on integrated strain gauges, which are competitive with force sensors manufactured using conventionally methods. The next step is to investigate and minimize the deformation of the inserted steel plate due to thermally induced stresses. This serves as a basis for a complete encapsulation of the strain gauges to realize structurally integrated force sensors featuring increased reliability based on better protection against environmental influences and capability of in-situ measurements.

5 Encapsulation of strain gauges

The results obtained so far show that a homogeneous and loss-free strain transmission between LPBF-manufactured base body and the inserted steel plate is ensured. Additionally, the strain gauges withstand the LPBF-process and maintain their linear behavior after the LPBF-process. Both aspect significantly affect the performance of the LPBF-manufactured force sensors, and, thus, build the basis for manufacturing structural integrated force sensors. However, all LPBF-manufactured spring elements discussed earlier feature a simplified geometry and do not provide a complete protection of the strain gauges yet. In contrast to the sealing of the strain gauges with silicone rubber so far, a complete encapsulation within the LPBF-manufactured part would offer a better protection of the strain gauges and thus increase their reliability. Therefore, a geometry of a spring element is presented, which allows a complete encapsulation of the strain gauges while maintaining the S-shaped deformation. In this new design, the scanning time of the laser is significantly increased, which leads to a new challenge. This challenge is the reduction of the thermally induced deformation. Since this part is the focus of the PTW group, the reduction of the thermally induced deformation is only briefly disccued. Thereby, geometrical parameters of the LPBF-manufactured spring element as well as process parameters were identified and adapted so that the thermally induced deformation of the inserted steel plate is reduced. The optimization regarding the thermally induced deformation was performed using the same geometry of the spring element that is presented and investigated in Chap. 3 and 4 of this thesis.

5.1 Reduction of the thermally induced deformation

The quantification of parameters that significantly influence the thermally induced deformation of the inserted steel plate as well as the derivation of recommendations for reducing this deformation are addressed in the PhD thesis [46], which was conducted in parallel to this work. The main drawbacks of the thermally induced deformation of the steel plate are the decrease in process stability, reproducibility regarding manufacturing as well as the limited transfer potential to other fields of application [46] explain the necessity to reduce such an effect. For this purpose, a design of experiments (DoE) was conducted to quantify various parameters that influence the thermally induced deformation. Here, the findings obtained in [46] are briefly summarized since they will be applied to the development of new geometries of spring elements throughout the remaining part of this thesis.

In order to quantify the parameters that influence the thermally induced deformation, precautions were taken first to minimize tilting of the steel plate during the LPBF-process [46]. It is shown that by modifying the cavity, in which the steel plate is inserted, tilting of the steel plate is reduced [46]. The cavity was adapted such that it featured a positioning geometry with three elevations [Fig. 5.1(a)]. These elevations reduce the displacement of the steel plate, which occurs during the coating process due to frictional forces between the solidified material, powder particles and the coating blade. Furthermore, an alignment of the LPBF-manufactured part on the build platform of $\alpha_{\text{orient}} = 75^{\circ}$ with respect to the coating direction [Fig. 5.1(b)] resulted in a lower tilting of the steel plate. This is due to the fact that in this orientation the coating blade passes more evenly over both edges of the steel plate, which reduces tilting. In subsequent investigations on the reduction of the thermally induced deformation, the LPBF-manufactured spring elements were consistently fabricated at an orientation of $75°$ with respect to the coating direction featuring a cavity with positioning geometry.

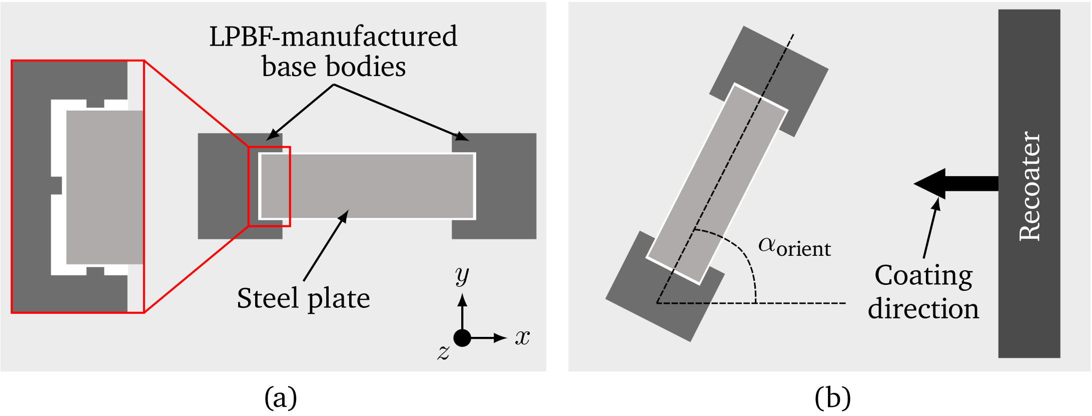

(a) (b)

Figure 5.1: The modifications to reduce tilting of the inserted steel plate consist of a positioning geometry in the cavity (a) as well as an orientation of the LPBF-manufactured part on the build platform of $75°$ with respect to the coating direction (b). The graphic is adapted from [46].

The parameters that were investigated to minimize the thermally induced deformation are [46]:

- height of the lateral and rear material connection between LPBF-manufactured base bodies and the inserted steel plate,
- scanning area on the steel plate,
- inter layer time, i.e. the time between two performed scannings,
- temperature of the build platform,
- scanning strategy and
- height of the LPBF-manufactured part after inserting the steel plate.

The experiments in [46] show that the heights of the material connections [Fig. 5.2(a)] of the inserted steel plate with the LPBF-manufactured base bodies is significant for the thermally induced deformation of the steel plate. These results confirm the theory of the formation of the thermally induced stresses due to the different cooling rates, which in turn have an amplified effect on the steel plate due to height of the rear material connection that acts as a lever arm (Sec. 3.4.1). The issue with the chosen geometry is that the lateral and rear material connections are made at a similar height. This means that the steel plate does not have sufficient support with the LPBF-manufactured base bodies, allowing the force acting over the lever arm to deform the steel plate without restriction (Fig. 3.13). However, this also means that if a lower height of the lateral material connection is selected, the steel plate will be rapidly fixated with the LPBF-manufactured base bodies. Thus, the occuring thermally induced stresses will not have such a severe impact on the steel plate. Therefore, the height of the lateral material connection $h_{\text{lateral, new}}$ in [46] was set to $0.2\,\text{mm}$ [Fig. 5.2(c)]. This corresponds to 10 layers. In contrast, the height of the lateral material connection $h_{\text{lateral, old}}$ of the previous geometry of the LPBF-manufactured spring element was $1.7\,\text{mm}$ [Fig. 5.2(b)]. The height of the rear material connection h_{rear} remains the same in both cases with $1.85\,\text{mm}$. The surface of the LPBF-manufactured spring element with lower height of the lateral connection, measured with a 3D surface microscope (type: InfiniteFocusG5 plus, Alicona Imaging GmbH, Graz, AUT), exhibits only half the deformation of the previous geometry of the LPBF-manufactured spring element. Specifically, there is a deformation of $0.25\,\mathrm{mm}$ of the inserted steel plate in the build-up direction of the LPBF-process (z-direction) in case of the LPBF-manufactured spring element with lower height of the lateral connection [46].

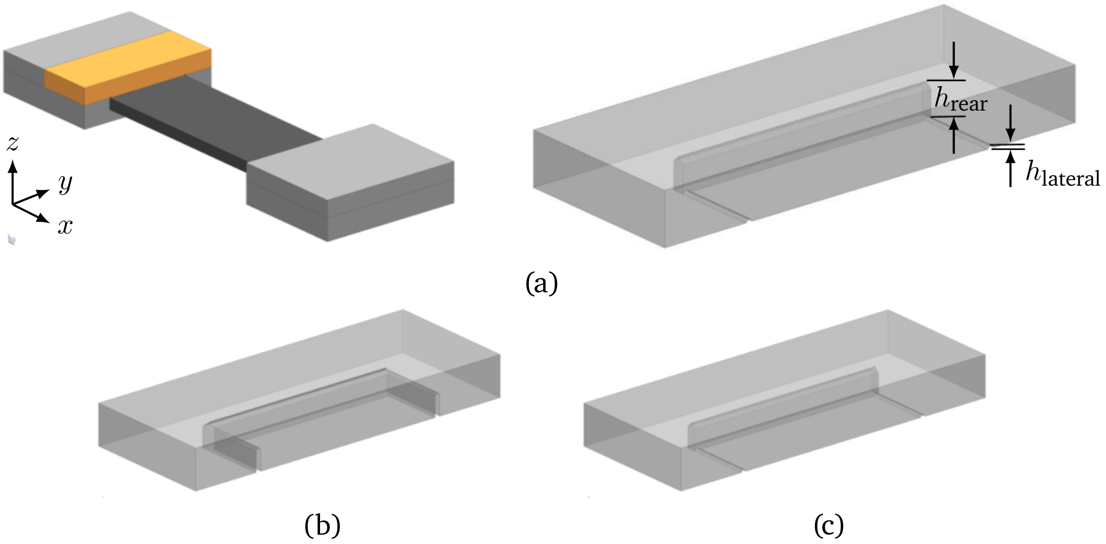

Figure 5.2: The inserted steel plate is bonded to the upper LPBF-manufactured base bodies through lateral and rear connections that lie at the heights h_{lateral} and h_{rear}, respectively (a). The lateral connection is made at a height $h_{\text{lateral, old}} = 1.7\,\mathrm{mm}$ in case of the previous geometry (b) and at a height $h_{\text{lateral, new}} = 0.2\,\mathrm{mm}$ in case of the optimized geometry (c). The rear connection remain in both cases at a height $h_{\text{rear}} = 1.85\,\mathrm{mm}$. The graphic is taken from [46].

The above-mentioned remaining five parameters have been analyzed in preliminary tests and reveal that they all influence the thermally induced deformation of the steel plate except for the parameter height of the LPBF-manufactured part after inserting the steel plate [46]. The remaining four parameters were evaluated in a full factorial experiment DoE. The following points are concluded from the result of DoE regarding the reduction of the thermally induced deformation of the steel plate [46]:

- The scanning strategy is of statistical significance. The checkerboard pattern scanning is selected as the scanning strategy in contrast to the stripe pattern scanning. This leads to an even heat distribution, and, thus, to a less distinct gradient.

- The higher inter layer time, which was quadrupled in [46] is statistically significant. This is plausible, since a longer coating time allows the LPBF-manufactured part to transmit the energy introduced by the laser to the powder bed, the build platform and the environment [194]. Thus, the LPBF-manufactured part cools down more, which means that the thermally induced stresses are lower [194].

- The increase of the temperature of the build platform from the default value of $80\,^{\circ}\mathrm{C}$ to $160\,^{\circ}\mathrm{C}$ results in a slight reduction of the thermally induced deformation of the steel plate. However, this decrease is not statistically significant. Therefore, the default processing temperature of $80\,^{\circ}\mathrm{C}$ for the used steel powder is maintained.

In summary, the adjustments to the height of the lateral material connection, the scanning strategy, and the inter layer time, in addition to modifying the cavity with a positioning geometry and a part orientation of $75°$, lead to a reduction in the thermally induced deformation of the steel plate of about $67\,\%$ [46]. These optimal parameters are therefore used in the following for the design and manufacturing of a spring element geometry with complete encapsulation of the strain gauges.

5.2 Design of a spring element with complete encapsulation of the strain gauges

In the next step, a geometry of a spring element is designed which, on one hand, allows a complete encapsulation of the strain gauges and, on the other hand, still deforms in an S-shape under a tensile or compressive load. The design as a tension rod is avoided, since such a geometry is mechanically rather stiff and therefore results in a poor measurement resolution of small forces. Consequently, the spring element for the complete encapsulation of the strain gauge is designed for bending. In this context, it is advantageous to modify the previously investigated geometry of the spring element in such a way that complete encapsulation of the strain gauges is made possible. This allows to apply the so far gained findings of the previous geometry.

5.2.1 Concept for encapsulation

In order to provide an encapsulation of the strain gauges based on the geometry of the deformation body, the two LPBF-manufactured base bodies need to be joined together. Generally, this needs to be done in a form of an enclosure of the steel plate (Fig. 5.3). However, it is important that the connecting bars joining the two LPBF-manufactured base bodies do not exhibit the same stiffness. In this case, an applied tensile or compressive force would cause compression of the whole spring element, and, thus, not lead to the desired S-shaped deformation. This S-shaped deformation of the spring element can be achieved if only the stiffnesses of the diagonal connecting bars are equal, i.e. forming two stiff and two compliant connecting bars. The relation of the stiffnesses determines the amount of force that is transmitted through the connecting arms. Hence, by realizing the stiffnesses properly, the main part of the force is transmitted in the same way as in the previous LPBF-manufactured force sensors (Fig. 5.3). Furthermore, overhang angles below $45°$ have to be avoided, otherwise additional support structures would be required.

There are several ways to realize such geometry of the spring element containing areas of different stiffness by means of LPBF:

- Utilization of different materials that allow material-specific adjustment of stiffness.
- Manufacturing of porous structures, also known as metal foam [195]–[197], by adjusting process parameters.
- Adapting the geometry in terms of using lattice structures that are bending-dominated [198] or designing thin-walled structures.

The use of different materials in the same LPBF-system is the subject of ongoing research and requires adapted powder feeding as well as coating systems [199], [200]. The use of porous structures requires the adjustment of process parameters such as the power of the laser. This in conflict with the derived optimal process parameters regarding the reduction of the thermally induced deformation of the steel plate. Therefore, both of these approaches for the realization of a geometry of the spring element with encapsulated strain gauges are not considered. A feasible option is through geometrical modification utilizing thin-walled structures that act as an enclosure for the inserted steel plate together with the strain gauges (Fig. 5.4). However, the

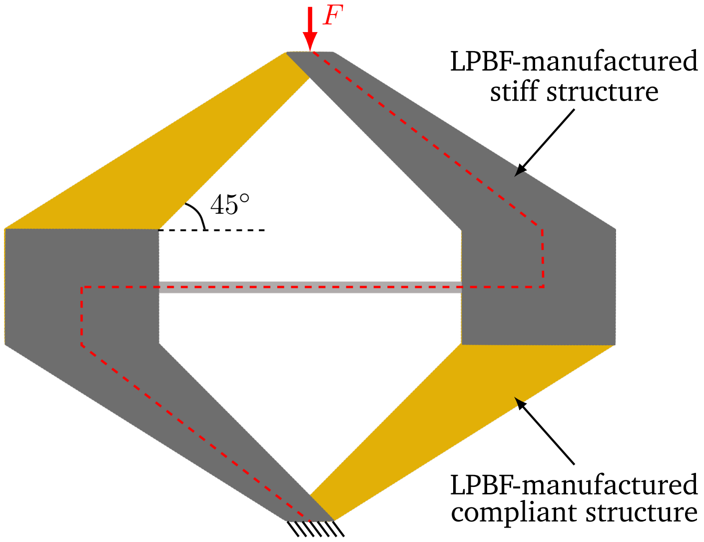

Figure 5.3: Schematic illustration of a spring element for providing an encapsulation of the strain gauges based on a LPBF-manufactured geometry with areas of different stiffnesses. The force flow can be influenced by specific adjustment of the stiffness, thus achieving the desired deformation.

schematic design (Fig. 5.4) is not manufacturable in this way using LPBF because the LPBF-manufactured base bodies require a support structure that is connected to the build platform.

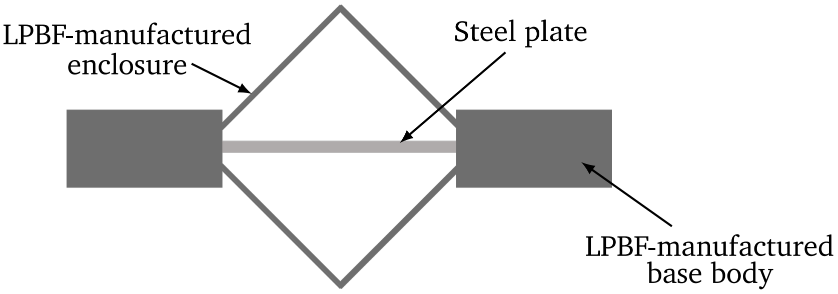

Figure 5.4: The encapsulation of the strain gauges is achieved by sheathing the steel plate with the LPBF-manufactuered enclosure.

5.2.2 Geometric adaptations towards complete encapsulations

In order to enable manufacturing by means of LPBF, the presented geometry is extended with further structures (Fig. 5.5). First, two bars are being added for force transmission, which are led from the LPBF-manufactured base bodies of the geometry of the spring element considered so far towards the center of the geometry. In these two bars a lattice structure is added, which serves to save material, and, thus, has an ecological purpose. Second, a full material support is provided underneath the right LPBF-manufactured base body so that it is manufacturable. It should be noted that this support is not the same as conventional support structures, which are used in LPBF to manufacture overhanging structures and then removed by milling after the completion of the LPBF-process. In contrast, the support designed here does not have to be removed, which simplifies the post-processing. The support as well as the enclosure of the steel plate are designed as thin-walled structures with a thickness of 1 mm. It is of particular importance that the thickness of the thin-walled structure of the enclosure is smaller than the thickness of the inserted steel plate. This ensure a major force flow through the steel plate, thus causing the desired deformation. However, a too small thickness would decrease the process stability due to thermally induced stresses that would bend this structure. There have been thin-walled structures made of steel 316L (material no.: 1.4404) manufactured with a thickness of 0.4 mm by LPBF in research [201], but these are mostly in context with lattice structures, thus the length of such a thin-walled structure is limited to a low millimeter range. Thermally induced stresses play a major role in longer lengths of thin-walled structures. Therefore, all thin-walled structures are set to 1 mm in the designed spring element, which in preliminary tests caused no difficulties during manufacturing. All overhang angles in the geometry are set to 45°, avoiding additional support structures. The desired S-shaped deformation of the spring element requires that no material connection is made between the two LPBF-manufactured base bodies through the support. However, a material connection is provided (Fig. 5.5, outlined in red), which is only relevant in terms of process stability. This ensures that the thin-walled structure of the support is fixed and does not undergo large deformations due to thermally induced stresses occurring in the manufacturing process. This connection has to be removed in post-processing by milling after completion of the LPBF-manufactured force sensor, thus creating a slot.

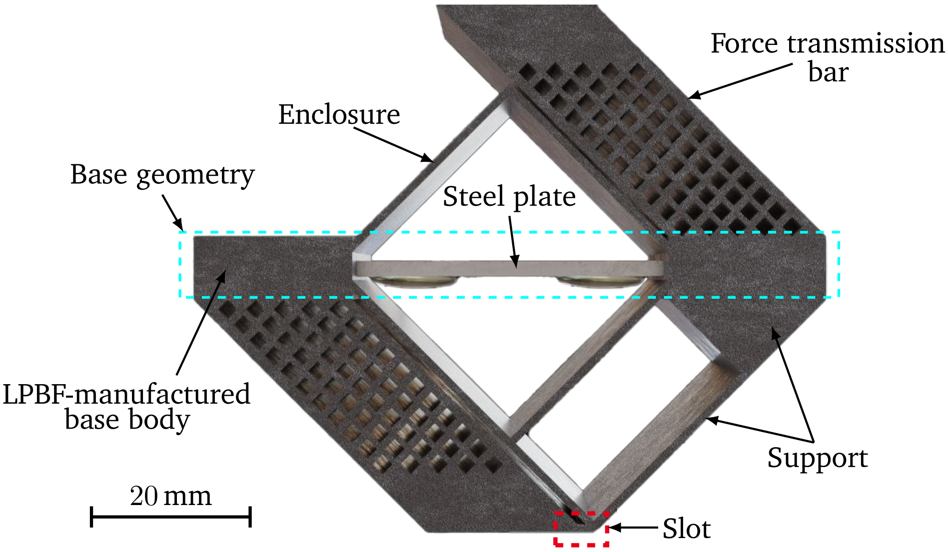

Figure 5.5: The realization of this geometry is accomplished by providing force transmission bars as well as a support structure. After completion of the spring element by LPBF, the connection between both LPBF-manufactured base bodies through the support needs to be removed in a post-processing by milling to achieve a slot.

The simulation of the force sensor under load using an FEA shows that the resulting strain behavior of the new designed spring element due to a compressive force is the same as in the case of the previous LPBF-manufactured spring elements (Fig. 5.6). There are both strain and compression areas on both surfaces of the steel plate, which are achieved through the S-shaped deformation. Here, the FEA is carried out with the same boundary conditions as described in Sec. 3.3.2 with the assumption of a 1.4310 steel plate (Fig. 3.8). Since the new geometry of the spring element is much stiffer than the previously considered geometry, only the nominal force has been increased to 50 N in the FEA. The evaluation of the simulated strain and compression at the locations of the strain gauges results in $261.4\,\mu\mathrm{m\,m}$ and $-178.6\,\mu\mathrm{m\,m^{-1}}$, respectively. This difference is due to the lack of geometrical symmetry of the new spring element. However, since in the full bridge configuration the strain is averaged over all four strain gauges, this difference does not cause an issue. This difference needs to be taken into account if the maximum allowable strain of the strain gauges would be exceeded, whereas the simulated strains and compressions are far below this limit.

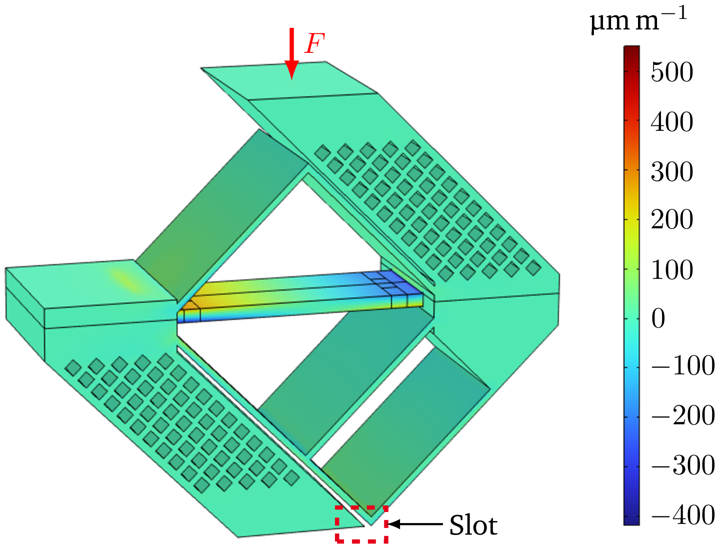

Figure 5.6: The simulation of the strain by means of an FEA demonstrates the expected behavior with areas of strain and compression of the steel plate that results from an S-shaped deformation under compressive load. This is comparable to the previously investigated LPBF-manufactured spring elements.

The fabrication of the new geometry of the spring element is made according to the disruptive manufacturing method. First, the lower half of the LPBF-manufactured part is manufactured until the cavity is completed. Then, the integration of a 1.4310 steel plate with applied strain gauges (type: 1-DY41-1.5/350, HBK, Darmstadt, DE), which are connected to a full bridge configuration, takes place. By resuming the LPBF-process with the optimized process parameters, the second half of the spring element is manufactured. After manufacturing the spring element and removing the build platform from the process chamber, it is noticed that a severe discoloration of the LPBF-manufactured material is present in the area of the right force transmission bar as well as the support structure (Fig. 5.7). This discoloration indicates an overheating of the LPBF-manufactured part due to insufficient heat dissipation. Since the discolored areas are only connected to the build platform via the thin-walled support structure, the heat arising during the manufacturing process is only poorly dissipated to the build platform, and, thus, accumulates in these areas. In contrast, the left force transmission bar is directly connected to the build platform so that the heat generated in the manufacturing process can be transferred to the build platform through higher heat conduction and no discoloration occurs.

The influence of overheating of the material is not investigated further, as a countermeasure will be presented in the design of the next spring element with complete encapsulation of the strain gauges to provide better heat dissipation. Nevertheless, this spring element is prepared for the measurement under a static load to evaluate the behavior of the strain gauges. First, the spring element is separated from the build platform using a band saw. Subsequently, the end surfaces of the force transmission bars are reworked by milling followed

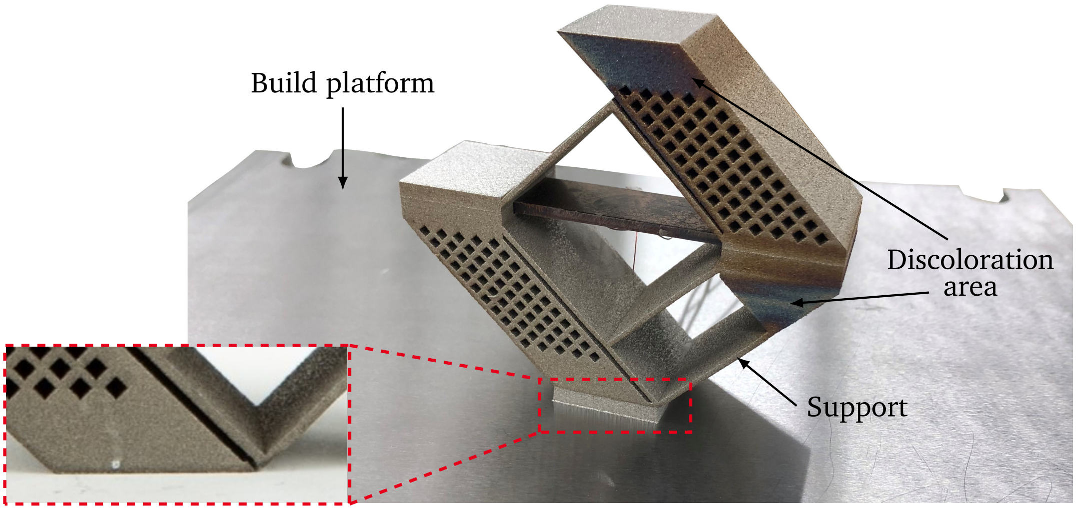

Figure 5.7: A severe discoloration of the LPBF-manufactured material in the right area occurs due to poor heat dissipation. The thin-walled support structure reduces the heat dissipation to the build platform. After separating the spring element from the build platform, a slot is created by milling to remove the material connection between the LPBF-manufactured base bodies (inset).

by drilling holes and cutting M5 threads into them. In this process, the material connection between the LPBF-manufactured base bodies through the support is cut by milling such that a slot is present (Fig. 5.6). For the loading of this LPBF-manufactured force sensor with enclosure of the strain gauges, the same setup is used as for the previous LPBF-manufactured force sensors (Fig. 3.19). The sensor shows a linear output signal at a nominal force of $50\,\mathrm{N}$ [Fig. 5.8(a)]. The output signal is the bridge output voltage U_D which is referred to the bridge excitation voltage U_S of $5\,\mathrm{V}$. The linearity and hysteresis errors are within $\pm\,0.15\,\%$. In this case, the linearity error is slightly larger than the linearity error of the previous LPBF-manufactured force sensors $(<\pm\,0.1\,\%)$. Additionally, the sensitivity of $399.1\,\mathrm{\mu V\,V^{-1}} \pm 0.2\,\mathrm{\mu V\,V^{-1}}$ has a larger deviation to the simulated sensitivity $446.6\,\mathrm{\mu V\,V^{-1}} \pm 11.8\,\mathrm{\mu V\,V^{-1}}$. The tolerance of the simulated sensitivity results from the tolerances of the Young's modulus of the steel plate and the gauge factor of the strain gauges. A possible cause for this behavior might be the overheating of the material.

In the next step, two further thin-walled structures are added to the enclosure to allow complete encapsulation of the steel plate, and, thus, the strain gauges (Fig. 5.9). These thin-walled structures also feature a thickness of $1\,\mathrm{mm}$. Additionally, a small port is provided for routing the cables of the strain gauges. Again, an FEA is conducted with this geometry applying the boundary conditions as in the case of the previous LPBF-manufactured spring elements (Fig. 3.8) and assuming a 1.4310 steel plate. Since the additional thin-walled structures for enabling complete encapsulation of the steel plate together with the strain gauges increase the stiffness of the structure, the FEA-model is evaluated with a nominal force of $100\,\mathrm{N}$. The simulated strain along the steel plate exhibits a linear characteristic, except for the edge areas (Fig. 5.10). At the edge areas, the material transition as well as the transition of the boundary conditions result in singularities. The geometry continues to undergo an S-shaped deformation under load, which is evident from the strain and compression at both ends of the steel plate. The strain gauges are positioned at a distance of $2\,\mathrm{mm}$ from the edges. This is consistent with the positioning of the strain gauges as discussed in the previous LPBF-manufactured force sensors and also avoids the singularities. As a result, a strain of $57.0\,\mathrm{\mu m\,m^{-1}} \pm 0.4\,\mathrm{\mu m\,m^{-1}}$ is expected for the

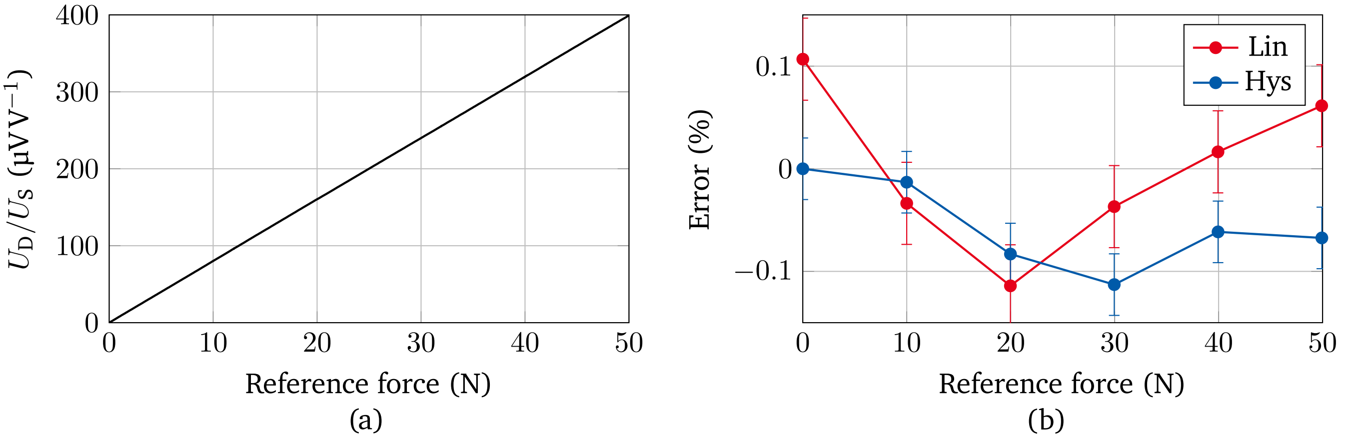

(a) (b)

Figure 5.8: The LPBF-manufactured force sensor with an enclosure shows a linear response to a force of 50 N (a) featuring small linearity and hysteresis errors (b).

full bridge configuration. The maximum stress according to the simulation is about 144 MPa, which is below the yield strength of the steel plate. Thus, no plastic deformation is expected.

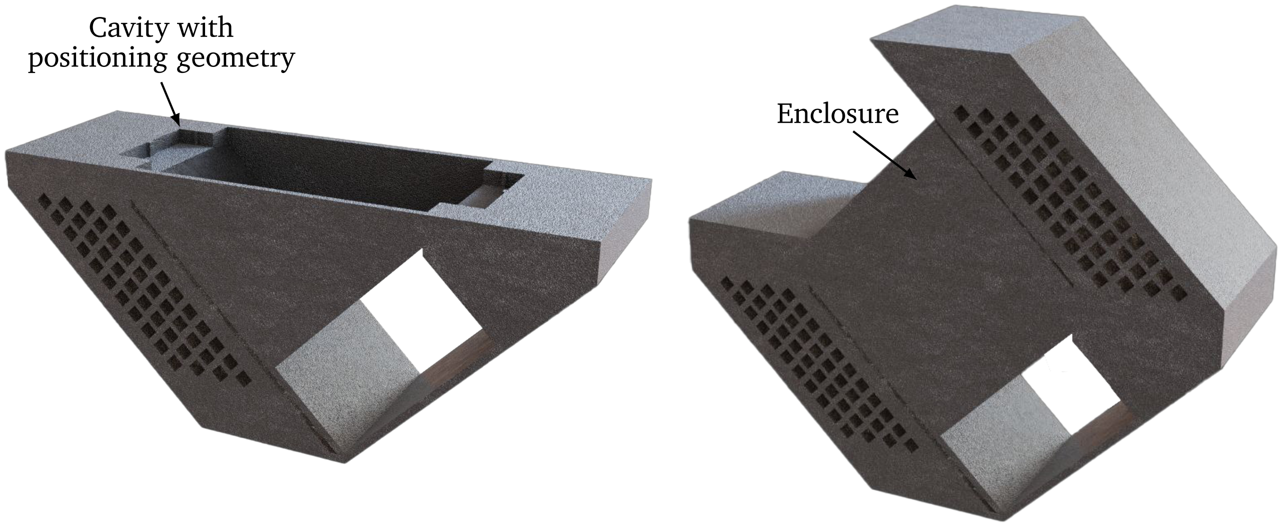

Figure 5.9: The complete encapsulation of the steel plate, and, thus, the strain gauges, is done by adding to further thin-walled structures (enclosure).

After the numerical analysis of the strain behavior, the spring element with complete encapsulation of the strain gauges is fabricated according to the disruptive manufacturing method presented. Thereby, small changes are made for the fabrication. On one hand, a small opening is provided through one of the thin-walled structures, which serves as a cable routing port at this experimental stage of the development (Fig. 5.11). On the other hand, an additional support element is provided to improve heat dissipation, and, thus, prevent overheating of the material and geometry. This support element serves as a heat conductor that transfers

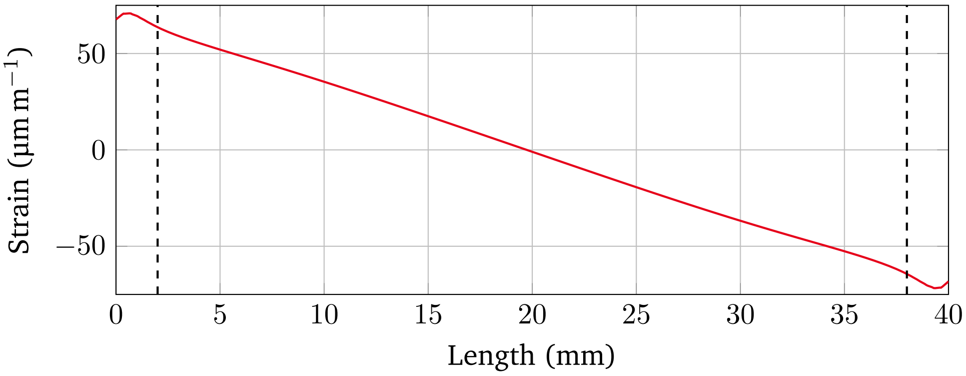

Figure 5.10: Simulated strain along the 1.4310 steel plate for the spring element with complete encapsulation of the strain gauges when loaded with $100\,\mathrm{N}$. The strain gauges will be applied at a distance of $2\,\mathrm{mm}$ from the edge (marked as dashed lines) as in the case of the previous LPBF-manufactured force sensors, i.e., avoiding the singularities area.

heat from the LPBF-manufactured part to the build platform. Initial tests have shown that the heat conductor performs well and significantly reduces discoloration due to overheating. Depending on the geometry of this heat conductor, the heat transfer can be further optimized. Additionally, the lattice structures in the force transmission bars are reduced, which were initially designed to save material. This also promotes heat conduction.

It is expected that the strain gauges will experience a higher temperature during the manufacturing process

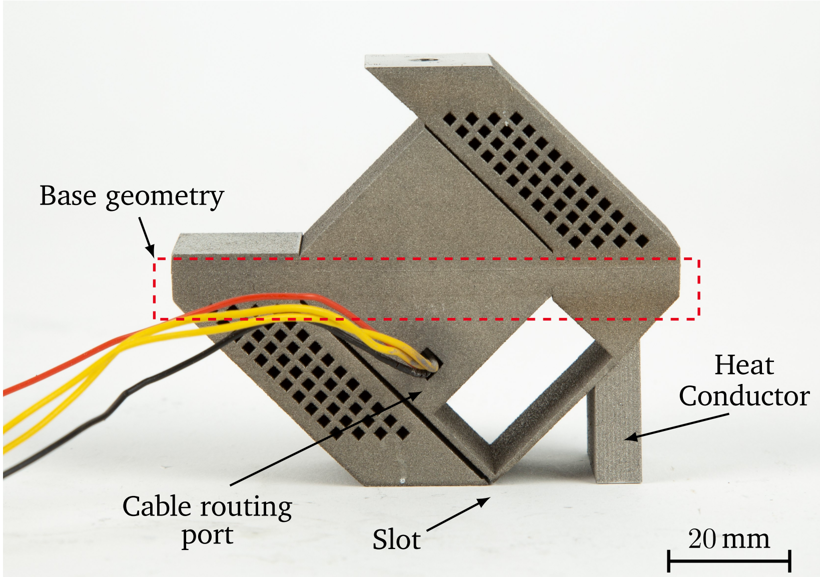

Figure 5.11: The LPBF-manufactured force sensor with complete encapsulation of the strain gauges based on the previously considered base geometry (outlined in red) is adapted in terms of of providing a small port for cable routing. Furthermore, an additional support structures is implemented that acts as a heat conductor and transfers the heat arising from the LPBF-manufactured part during the fabrication process to the build platform.

in this geometry with complete encapsulation than in the previously considered base geometry of the spring element. This is due to the fact that not only the base bodies are scanned as in the case of the previously considered base geometry, but the laser beam moves closer to the strain gauges due to the geometry of the enclosure. In order to determine the arising temperature of the steel plate with the strain gauges on its bottom, a 1.4310 steel plate with two thermocouples (TC_1 and TC_2) applied at the positions of the strain gauges is integrated into such a spring element with complete encapsulation according to the disruptive manufacturing method. This allows recording the temperature that arises within the steel plate during the manufacturing process. The application of the thermocouples (type: 5TC-GG-KI-30-1M, OMEGA Engineering inc., Deckenpfronn, DE) is done utilizing the same method discussed in Sec. 4.2.1.

The thermocouple TC_2 is located on the side of the force transmission bar that is built after resuming the LPBF-process, whereas Thermocouple TC_1 is located on the other end of the steel plate (Fig. 5.12). It should be noted that the illustration of the positioning of the thermocouples is done using the spring element without complete encapsulation, as it provides a better overview. However, the experiment is conducted with the spring element with complete encapsulation. The recorded temperature profiles of the thermocouples TC_1 and TC_2 (Fig. 5.12) show maximum temperatures of $228\,°C$ and $200\,°C$, respectively. This confirms the concerns of the temperature arising in the steel plate in case of the spring element with complete encapsulation, which is significantly higher than the previously recorded temperatures in case of the spring elements discussed in chapter 4. These are were about $145\,°C$ (Fig. 4.7). The characteristic pattern of the layer-by-layer build-up within the LPBF process is recognizable in the periodic signal shape from the thermocouples (Fig. 5.12 inset).

The temperature profiles of both thermocouples can be divided into three parts that depend on the geometry of the spring element with complete encapsulation. These three parts are from $0\,h$ to $2.2\,h$, $2.2\,h$ to $12.4\,h$ and $12.4\,h$ to $15.3\,h$ (Fig. 5.12). In the first part, both thermocouples show a similar course, in which the temperature initially rises and then reaches a saturation. Until this point, the base geometry as well as the corresponding part of the enclosure are built up. Thereby, the temperature at the position of thermocouple TC_2 is higher than the temperature at the position of thermocouple TC_1. This is due to lower heat dissipation on the side of thermocouple TC_2. While on the side of thermocouple TC_1 a connection to the build platform is available through the large force transmission bar, the heat on the side of thermocouple TC_2 is dissipated only through the small support structures to the build platform. In the second part, the temperature at the thermocouple TC_1 drops to about $120\,°C$ and stabilizes there (Fig. 5.12). This is plausible since no more material is built up on the side of thermocouple TC_1 (left-hand side of the geometry) after the base geometry is completed. Thermocouple TC_1 experiences mainly the heat generated by the build-up of the enclosure as well as the force transmission bar on the right-hand side. The profile of thermocouple TC_2 after completion of the base geometry differs from the profile of thermocouple TC_1. After manufacturing the base geometry, the temperature also initially drops at the location of thermocouple TC_2. The reasons for the drop in temperature are, on one hand, the start of building up the lattice structure in the force transmission bar and, on the other hand, a smaller area is scanned overall after completion of the base geometry. The build-up of the lattice structure significantly influences the temperature arising within the steel plate. As soon as the build-up of one row of the lattice structure begins, the temperature within the steel plate decreases, since less area is scanned. The temperature increases again when half of a row of the lattice structure is exceeded, since starting from this point the scanned area increases. Therefore, in the second part of the temperature profile of thermocouple TC_2 11 oscillations that correspond to the 11 rows of the lattice structure are recorded. This effect is also observed in the temperature profile of thermocouple TC_1, since 11 oscillations are also found here. However, these are clearly less prominent due to the larger distance of thermocouple TC_1. In the third part, an increase in temperature is observed at both thermocouples (Fig. 5.12). This is due to the increased scanning area of the remaining force transmission bar that is built after completion of the lattice structure.

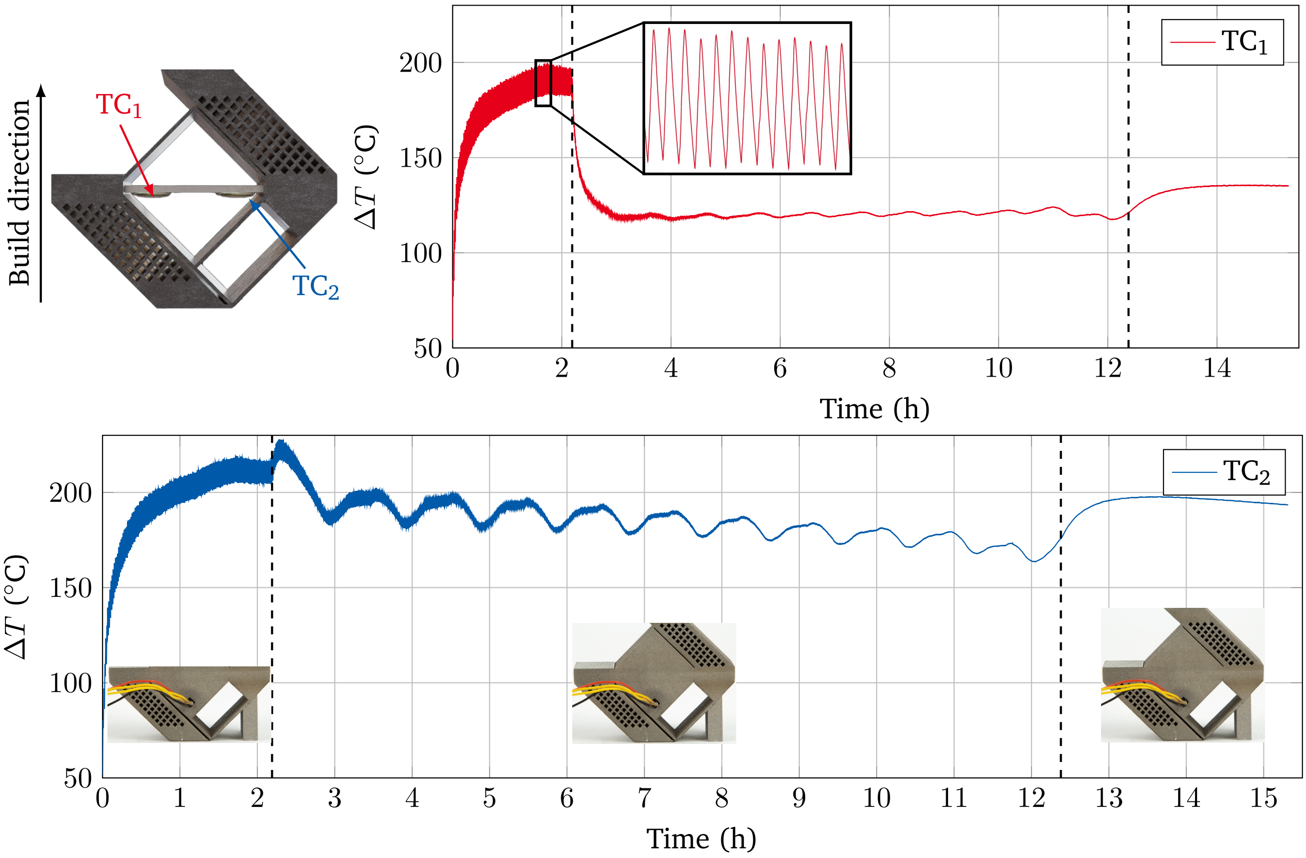

Figure 5.12: The temperature arising within the steel plate in case ot the spring element with complete encapsulation is measured with two thermocouples (TC$_1$ and TC$_2$). First, an increase of the temperature at both thermocouples is recorded. Then, the temperature drops from $2.2\,\mathrm{h}$ onwards, since the base geometry is completed at this point and a smaller area is scanned afterwards. Furthermore, the design of the lattice structure influences the resulting temperature within the steel plate due to the increasing and decreasing scanning area.

The measurements of temperature during the manufacturing process show that at least two of the four strain gauges would be exposed to a maximum temperature of $230\,°\mathrm{C}$ for a short period of time. According to the data sheet of the double-linear strain gages used (type: 1-DY41-1.5/350, HBK, Darmstadt, DE), an operating temperature range of $-70\,°\mathrm{C}$ to $200\,°\mathrm{C}$ is specified for static measurements. There is no further information on whether the $200\,°\mathrm{C}$ also represent a maximum temperature for the strain gauges, which when exceeded would cause damage to the strain gauges. However, since the adhesive of the strain gauges as well as the silicone rubber for sealing are rated up to a temperature of $250\,°\mathrm{C}$, these strain gauges are maintained and their ability to withstand the manufacturing process in combination with the geometry of the spring element with complete encapsulation is examined.

5.2.3 Characterization and results

Three of these LPBF-manufactured force sensors (S_1, S_2 and S_3) with encapsulated strain gauges are fabricated to characterize them under static loads and to draw conclusion about the reproducibility of the manufacturing process in combination with the developed geometry. Here, steel plates equipped with two double-linear strain gauges each to realize a full bridge configuration are used. The strain gauges are applied at a distance of 7 mm from each end of the steel plate. These steel plates are integrated into the LPBF-manufactured spring elements with complete encapsulation according to the disruptive manufacturing method.

After completing of the manufacturing process, the LPBF-manufactured force sensors are separated from the build platform and reworked, as in the case of the previous sensors. An initial measurement of the bridge output voltages of all three LPBF-manufactured force sensors confirms that all strain gauges basically withstand the manufacturing process despite experiencing temperatures of up to $230\,^{\circ}\mathrm{C}$. In the next step, these sensors are loaded with the presented setup (Fig. 3.19) using the universal testing machine in $20\,\mathrm{N}$ steps up to the nominal force of $100\,\mathrm{N}$. This stepwise loading is performed three time for each of the LPBF-manufactured force sensors in accordance with the OIML R60 guideline [190]. The evaluated sensitivities from the measurement of the three sensors are very similar (Tab. 5.1), thus a good reproducibility of the manufacturing process in combination with the developed geometry of the LPBF-manufactured spring element with complete encapsulation of the strain gauges is confirmed. It is found that the measured sensitivities are always slightly higher than the simulated sensitivities, which result from the calculated strains of the analytical model and the gauge factor of the strain gauges according to Eq. 2.21. Note that the deviations in the values of the simulated sensitivities are based on the tolerances of the Young's modulus of the steel plate and the gauge factor of the strain gauges. The deviation between the measured sensitivities of all three LPBF-manufactured force sensors and the simulated sensitivities is $4.5\,\% \pm 1.9\,\%$. However, a good agreement with the FEA-model is generally given. A potential source of the deviation might be an incorrect positioning of the strain gauges. Even a deviation of $0.3\,\mathrm{mm}$ in the positioning of the strain gauges brings the measured sensitivity within the range of the simulated sensitivity.

Table 5.1: Sensitivities of the force sensors for a load of $100\,\mathrm{N}$.

Prototype	Measured sensitivity	Simulated sensitivity
S_1	$121.0\,\mu\mathrm{V}\,\mathrm{V}^{-1} \pm 0.1\,\mu\mathrm{V}\,\mathrm{V}^{-1}$	$115.6\,\mu\mathrm{V}\,\mathrm{V}^{-1} \pm 2.1\,\mu\mathrm{V}\,\mathrm{V}^{-1}$
S_2	$120.7\,\mu\mathrm{V}\,\mathrm{V}^{-1} \pm 0.1\,\mu\mathrm{V}\,\mathrm{V}^{-1}$	$115.6\,\mu\mathrm{V}\,\mathrm{V}^{-1} \pm 2.1\,\mu\mathrm{V}\,\mathrm{V}^{-1}$
S_3	$120.9\,\mu\mathrm{V}\,\mathrm{V}^{-1} \pm 0.1\,\mu\mathrm{V}\,\mathrm{V}^{-1}$	$115.6\,\mu\mathrm{V}\,\mathrm{V}^{-1} \pm 2.1\,\mu\mathrm{V}\,\mathrm{V}^{-1}$

Additionally, the measurement of the bridge output voltages of all three LPBF-manufactured force sensors at this load shows a very linear behavior. This is expressed in low linearity and hysteresis errors of $\pm 0.1\,\%$ full scale [Fig. 5.13(a)] and $\pm 0.2\,\%$ full scale [Fig. 5.13(b)], respectively. Predominantly, the linearity error of each LPBF-manufactured force sensor is within $\pm 0.05\,\%$ full scale. A comparison of the linearity and hysteresis errors of these LPBF-manufactured force sensors with complete encapsulation of the strain gauges with the previously investigated LPBF-manufactured force sensors (Fig. 3.21) shows an excellent agreement. Consequently, these results confirm that the strain gauges not only withstand the temperatures of up to $230\,^{\circ}\mathrm{C}$ during manufacturing of the spring element with complete encapsulation, but are also comparable in terms of their performance to strain gauges that have not been subjected to the LPBF-process.

Therefore, the presented disruptive manufacturing method for integrating strain gauges into LPBF-manufactured

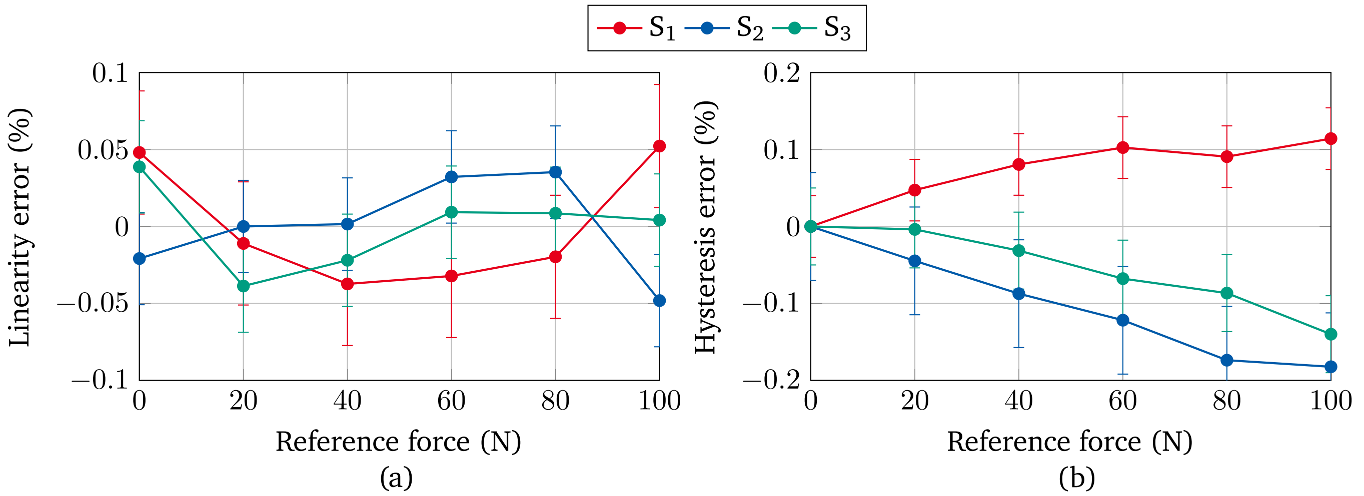

Figure 5.13: The small linearity and hysteresis errors of the LPBF-manufactured force sensors (S_1, S_2, S_3) with complete encapsulation emphasize their linear behavior.

parts by using a measuring element carrier turns out to be a promising possibility for the development of structural integrated force sensors with complete encapsulated strain gauges. In this context, the presented geometry of the spring element with complete encapsulation of the strain gauges can be used as a basic geometry around which the force transmission bars can be designed to fit the given application.

6 Manufacturing of threads by LPBF

The presented disruptive manufacturing method for the integration of strain gauges into LPBF-manufactured parts by using a measuring element carrier allows only a single-sided connection of this measuring element carrier within the processing plane [Fig. 6.1(a)]. Since the previously investigated LPBF-manufactured force sensors with the chosen geometry of the spring element only allow a uniaxial force measurement, the single-sided connection does not limit the manufacturing and performance of the force sensors. In order to apply the disruptive manufacturing method to LPBF-manufactured parts that allow for multi-axial force sensing, an integration of a more complex measuring element carrier in terms of geometry, e.g. a cylindrical shape, is required. However, such measuring element carriers for multi-axial force sensing require multi-axial integration to the force flow within the LPBF-manufactured part. Hence, a single-sided connection is not sufficient, making additional connections necessary. A promising approach for realizing the mechanical connection is based on bolted joints. Hereby, the cavity for integrating the measuring element carrier needs to be manufactured with an internal thread by means of LPBF [Fig. 6.1(b)]. This allows an easy integration of a cylindrical measuring element carrier by hand during a process interruption according to the disruptive manufacturing method. Thus, one end of the measuring element carrier is connected via the LPBF-manufactured thread while the other end is connected via a material joint when the LPBF-process is resumed. Furthermore, LPBF-manufactured threads can also be used for fastening the manufactured part, thus eliminating the need for subsequent machining operations as normally done for the force sensors discussed earlier. This significantly reduces the production time and increases the cost-effectiveness.

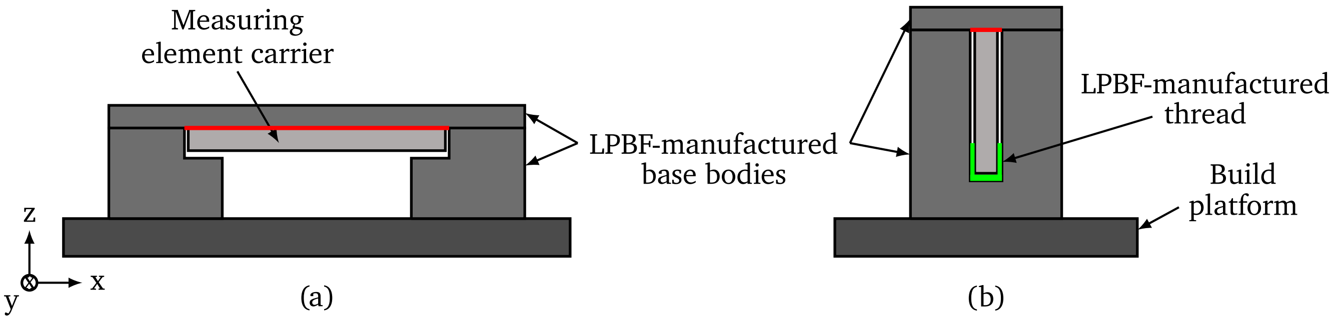

Figure 6.1: The presented disruptive manufacturing method allows only a single-sided connection (outlined in red) of the inserted measuring element carrier by means of LPBF (a). Applying this method for integrating more complex measuring element carriers, which require a two-sided connection, can be accomplished by using a screw connection with an LPBF-manufactured thread (b).

6.1 Geometric adaptation of the threads

Despite the aforementioned advantages, LPBF-manufactured threads are rarely used so far. This is mainly due to the resulting high surface roughness caused by the LPBF-process, which prevents direct use of such threads without any post-processing. Until present date, to the best of the author's knowledge, there is only one research publication of *Abele et al.* [202] concerning LPBF-manufactured threads. This deals with the comparison of directly manufactured threads by LPBF with tapped threads in LPBF-manufactured holes. Here, threads were manufactured according to the ISO standard with different sizes (M1.8, M2.5 and M4) in different orientations by LPBF. It was found that using directly manufactured threads by LPBF is not possible [202], since the surface roughness prevents fastening screws. Therefore, re-cutting the LPBF-manufactured threads was mandatory [202]. This result has been confirmed in own preliminary tests. In this context, more research effort has to be conducted to provide LPBF-manufactured threads without any post-processing that can be directly used for integrating a measuring element carrier. Note that an excessive force effort for fasting the measuring element carrier would damage it. Therefore, parameters of LPBF-manufactured internal threads are adapted in the following to facilitate fastening without any post-processing.

The main issue that limits the usability of additively manufactured threads in general is the surface quality in combination with overhang structures [203]. In context of the LPBF-process, overhang structures result in distortion and dross defects that cause dimensional inaccuracy [204], [205]. Threads according to the ISO standard have a flank angle of $60°$, which means that an overhang of $60°$ has to be produced when manufacturing such a thread by LPBF. This is basically feasible, since according to the guidelines of DfAM overhangs with an angle $\geq 45°$ are manufacturable by means of LPBF. However, the mentioned effects lead to dimensional inaccuracy that hamper fastening screws in such threads. According to [206], there are two relevant parameters of the thread that need to be changed to countermeasure the dimensional inaccuracy of LPBF-manufactured threads. The changes involve increasing the flank angle and adding an additional clearence to x_{min}, which is the point of minimal distance between the internal and external thread (Fig. 6.2) [206].

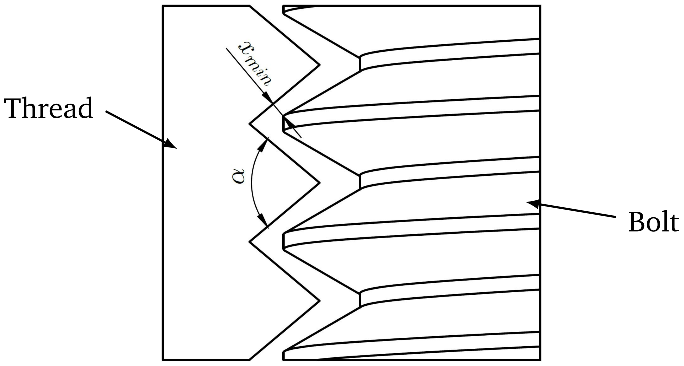

Figure 6.2: The geometry of the internal thread is modified by varying the flank angle α and adding an additional clearence to x_{min}. The graphic is taken from [206].

In order to evaluate the LPBF-manufactured threads with modified parameters, metric threads of the sizes M3, M4, M5, M6 and M8 are manufactured with three different flank angles ($80°$, $90°$ and $100°$) and five different clearences ($20\,\mu\text{m}$, $40\,\mu\text{m}$, $60\,\mu\text{m}$, $80\,\mu\text{m}$ and $100\,\mu\text{m}$). In this process, five threads with different clearences that exhibit the same flank angle are manufactured by LPBF in one specimen ($50\,\text{mm}\times 14\,\text{mm}\times 6\,\text{mm}$) (Fig. 6.3). In total, this results in 15 different configurations for each thread size, yielding 15 specimens with 75 threads combined. These specimens are manufactured with an orientation of $90°$ of the thread center axis to the build platform. The default parameter set '316L Surface M291 1.10' together with the stripe scan strategy is used for manufacturing.

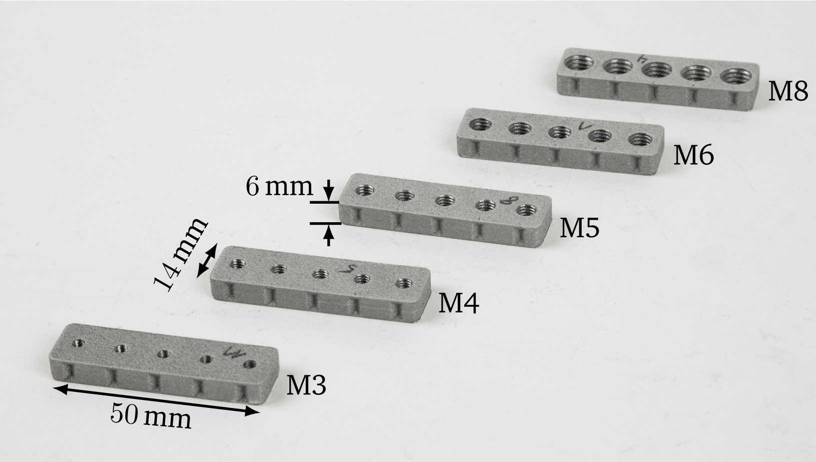

Figure 6.3: Specimen of the LPBF-manufactured threads of five different sizes (M3, M4, M5, M6 and M8) with variation of the flank angle and the clearances. Each specimen consists of one thread size featuring one of the three varied flank angles ($80°$, $90°$ and $100°$). The five threads in such a specimen differ in their clearances ($20\,\mu m$, $40\,\mu m$, $60\,\mu m$, $80\,\mu m$ and $100\,\mu m$), which increase from left to right.

6.2 Measurement setup for determining the tightening torque

For evaluating these threads, the required torque is measured, which occurs during fastening a screw into them using a torque test bench (Fig. 6.4) [206]. The test bench consists of a stepper motor (type: Nema 17 with gear ratio 20:1, OMC Corporation Limited, Jiangning, CHN) that drives the shaft of a torque sensor (type: T21WN, accuracy class 0.2, HBK, Darmstadt, DE) via a pulley and a timing belt. The torque sensor has a nominal range of $\pm\,100\,\mathrm{N\,m}$ and provides additionally the angular position through an integrated quadrature encoder. The output shaft of the torque sensor is joined to an adapter, in which bits of different size can be inserted. This setup including the stepper motor, the torque sensor and the bit adapter is mounted to a linear rail to restrict wedging. A fixture made of PLA is located underneath the adapter into which the specimens can be inserted. This fixture has a spring pin that allows to shift the specimens by one thread ensuring always the same alignment between the bit adapter and the thread to be tested.

The torque signal is provided as an analog voltage in the range of $\pm\,10\,\mathrm{V}$. This signal is forwarded to a DAQ (type: USB-6343, National Instruments, Austin, US), which is controlled by a graphical user interface in MATLAB (The MathWorks, Natick, Massachusetts, US). Additionally, the interface allows setting a torque threshold that terminates the measurement when exceeded. The motor velocity is set to a constant value of 8 revolutions per minute during the measurements. This setup is used to measure the required torque and angular position when fastening a screw into each of the LPBF-manufactured thread. Note that a new screw is used for each of the LPBF-manufactured threads. Based on these two parameters, the required torque as a function of the depth in the thread is determined. The positioning of the screw is done manually to the bit. This leads to the fact that a direct gripping of the screw into the LPBF-manufactured thread is not ensured when starting the motor. Thus, it would corrupt the measurement of the angular position. Therefore, the screw is first turned backwards until the axial step occurs at which the screw grips the thread. This serves as starting point of the measurement, allowing the measurements of the different threads to be comparable.

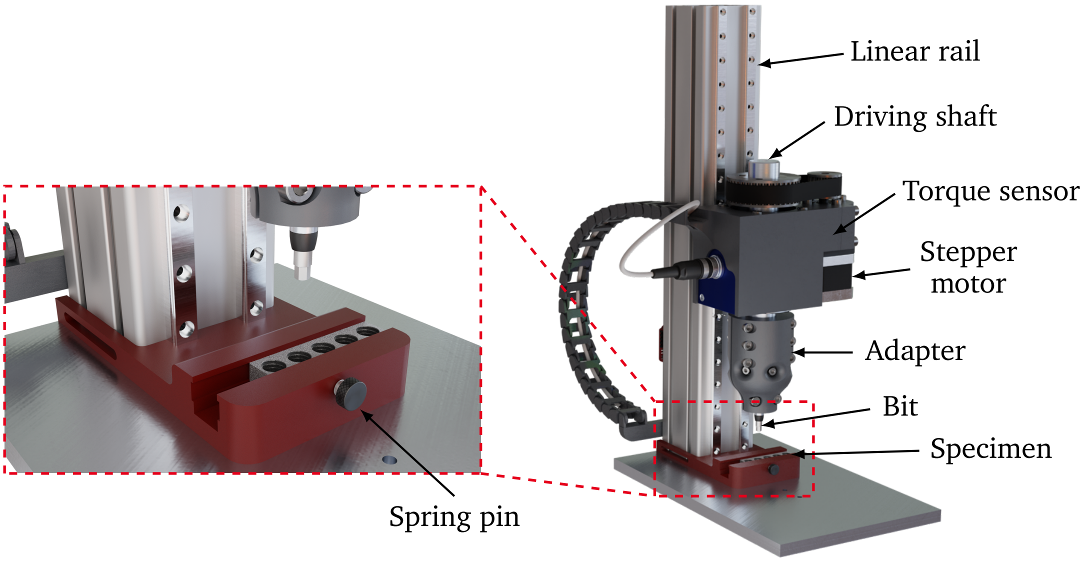

Figure 6.4: Test bench for determining torques that occur during fastening a screw into the LPBF-manufactured threads. The graphic is taken from [206].

6.3 Evaluation of the LPBF-manufactured threads

Upon manufacturing, the specimens undergo an optical examination by means of an optical microscope (type: VHX-600D, Keyence, Osaka, JPN). The surface roughness is very prominent, making it difficult to identify the thread [Fig. 6.5(a), (b)]. In the overhangs, material is present in solidified spherical form with diameters between $30\,\mu m$ and $50\,\mu m$ [Fig. 6.5(c)], which affect the performance of the LPBF-manufactured threads that are investigated in the next step.

For evaluating the torques of the different thread variants, a designation with two indices is used, where the first represents the flank angle and the second the clearence. Thus, $M3_{80,20}$ denotes a thread of size M3 with a flank angle of $80°$ and a clearence of $20\,\mu m$. Furthermore, the uncertainty of all torque measurements is within $\pm\,0.2\,Nm$. The test of the first thread ($M3_{80,20}$) leads to a break of the screw due to the high surface roughness after approximately seven revolutions (Fig. 6.6). In this case, a torque of almost $1.7\,Nm$ is reached until the screw breaks [Fig. 6.7(a)]. In order to prevent the screws from breaking within the remaining threads, a maximum torque is defined. For the M3 threads, the maximum torque is set to $1.3\,Nm$, which corresponds to the maximum fastening torque of an M3 screw of strength class 8.8. The results of the other threads of size M3 with a flank angle of $80°$ show that in all threads except for the $M3_{80,40}$ thread, fastening is possible without applying a significant force. The torque in case of the $M3_{80,40}$ thread exceeds the predefined maximum torque at almost nine revolutions, causing the test to be aborted. This characteristic is also found in the remaining threads of size M3 with the flank angles $90°$ and $100°$. Significant torques occur only in threads with clearances of $20\,\mu m$ and $40\,\mu m$ during fastening the screws [Fig. 6.7(b)]. Consequently, all the M3 threads with clearances larger than $60\,\mu m$ allow tightening of screws without any effort as in conventionally manufactured threads. Furthermore, it is evident that with an increasing flank angle for the same clearance, the torque required for fastening the screws decreases. For a flank angle of $100°$, fastening is already possible from clearances greater than $40\,\mu m$ without any effort [Fig. 6.7(b)]. Both results are as expected, since both an increased clearance as well as an increased flank angle counteract the dimensional inaccuracy caused by the overhangs within the thread geometry.

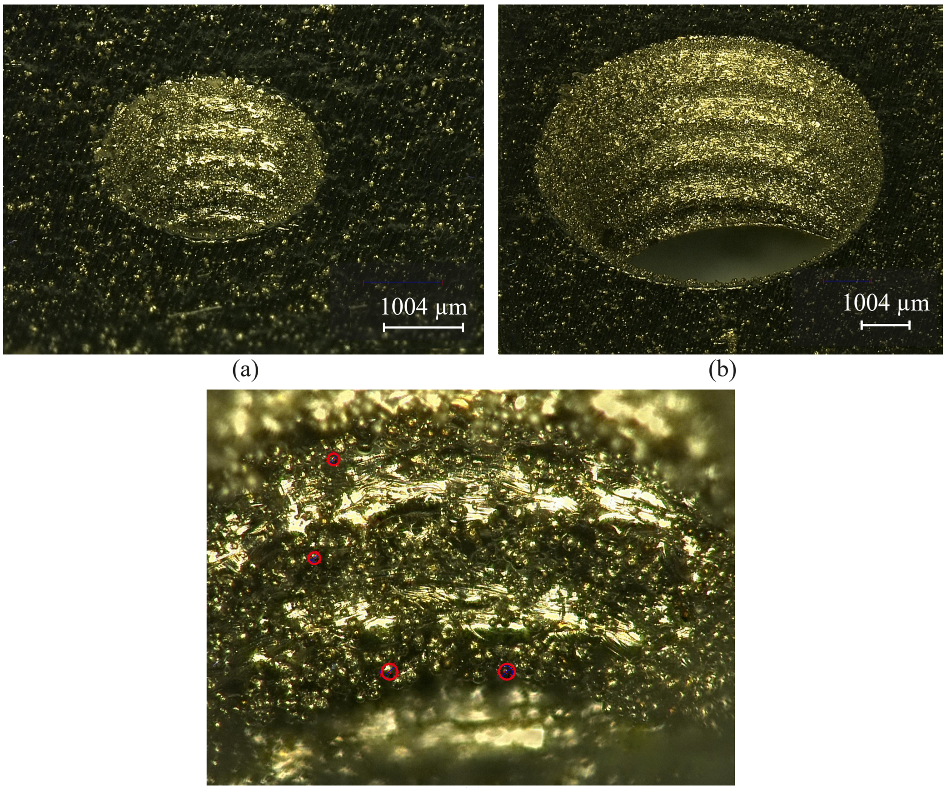

(a) (b)

(c)

Figure 6.5: The LPBF-manufactured threads feature high surface roughnesses as shown in case of the M3 (a) and M8 (b) thread with a flank angle of 80° and a clearence of $20\,\mu\mathrm{m}$. The soldified material in the overhangs forms spheres with diameters from $30\,\mu\mathrm{m}$ to $50\,\mu\mathrm{m}$ (c), which is shown red circled exemplarily for the M3 thread.

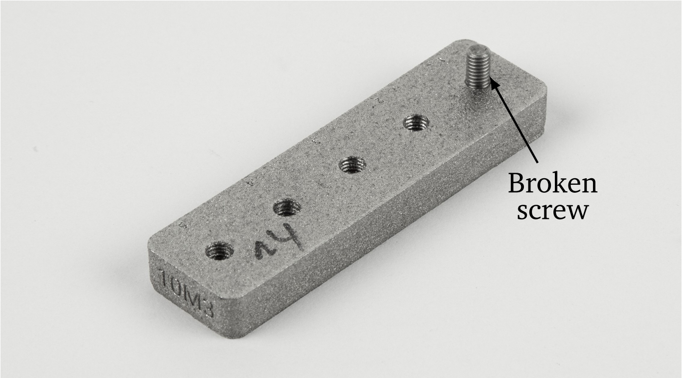

Figure 6.6: The surface roughness of the M3$_{80,20}$ thread leads to a break of the screw after seven revolutions.

This behavior is generally valid for the threads of the remaining sizes M4, M5, M6 and M8 as well (Fig. 6.8). Note that the specimens with the different thread sizes provide a varying number of revolutions, since all specimens have the same thickness, while the threads have different pitches. Thereby, for the threads of size

M4 with flank angles 80° and 90° together with a clearance of $20\,\mu m$, torques of almost $1.9\,Nm$ are recorded during fastening the screws [Fig. 6.8(a)]. In case of the flank angle of 80°, the screw also breaks as in the case of the thread of size M3. Considering the measurements of the smallest clearances ($20\,\mu m$) in combination with the smallest flank angle (80°) of all thread sizes, it is noticeable that the resulting torque during fastening the screw is consistently larger than $1.6\,Nm$ [Fig. 6.7(c)]. In these cases, the measurements are aborted, since such high torques indicate the unsuitability of these threads for integrating measuring element carriers. It can be concluded that by modifying the flank angle and the clearance, LPBF-manufactured threads can be achieved, which are directly usable without post-processing. It is found that clearances larger than $40\,\mu m$ should be chosen for fastening without any effort for all examined flank angles. However, the needed effort to fastening the screw does not provide any information about the quality of the connection in terms of backlash. A method to investigate this property is to measure the shear strength of the threads to determine their tear strength. Even though preliminary experiments have been conducted, this study is beyond the scope of this work and will be investigated in further research separately.

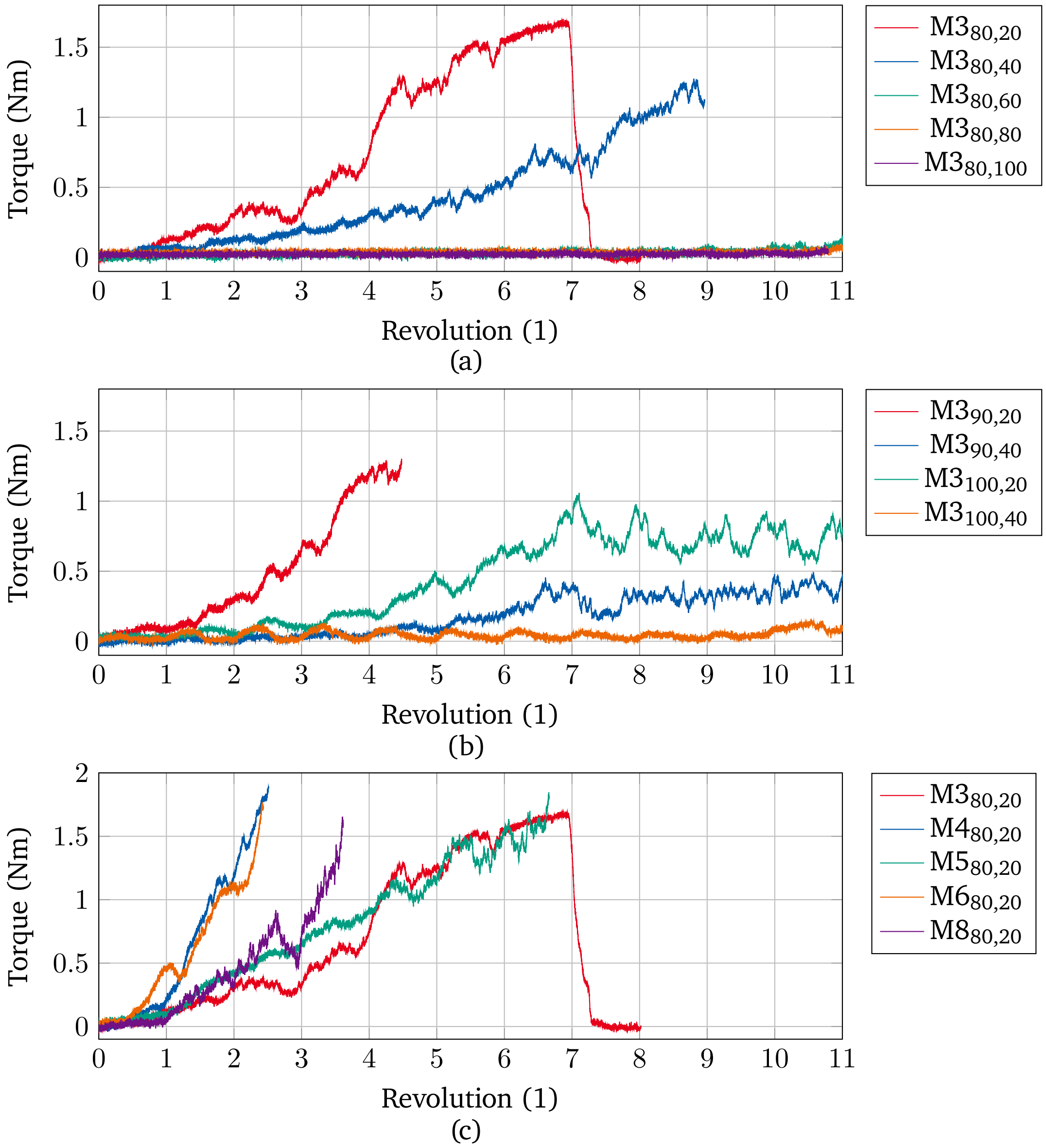

Figure 6.7: The torque measurements of the threads of size M8 with a flank angle of 80° show that from a clearance of $60\,\mu\mathrm{m}$ fastening of screws is possible without any effort. In contrast, the surface roughness of the $\mathrm{M3}_{80,20}$ (red) and $\mathrm{M3}_{80,40}$ (blue) threads is so severe that the maximum tightening torque of an M3 screw of 1.3 Nm is exceeded (a). This behavior is comparable for the remaining M3 threads with larger flank angles, which means that fastening is possible without any effort with clearances greater than $40\,\mu\mathrm{m}$. At the same time, the maximum torque decreases with increasing flank angle (b). The required torque in case of the smallest clearance together with the smallest flank angle is consistently larger than 1.6 Nm, regardless of the size of the thread (c). The measurement uncertainty of all torque measurements is within $\pm\,0.2$ Nm.

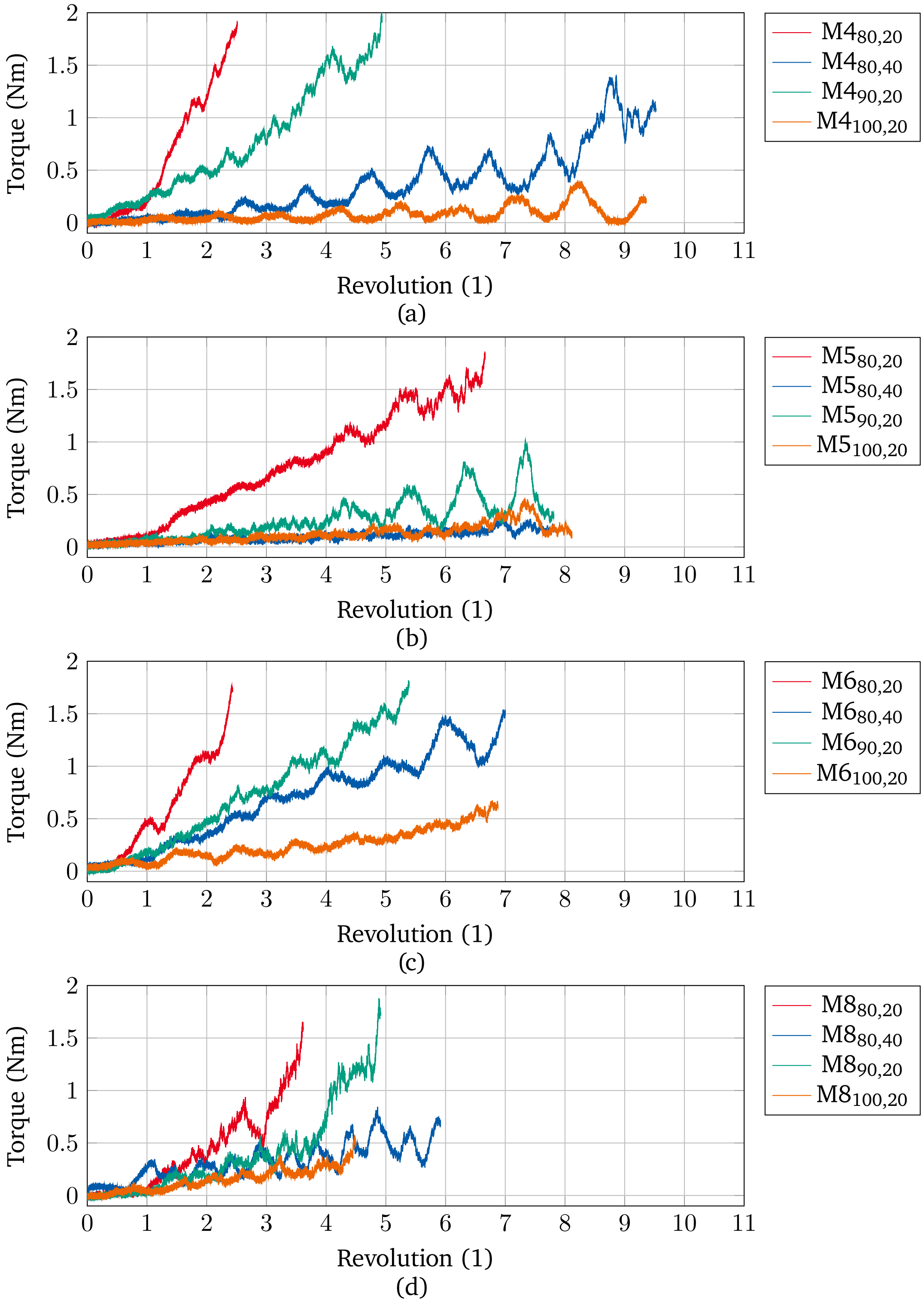

Figure 6.8: Measurement of the torque during fastening a screw in the LPBF-manufactured threads with different flank angles and clearances of $20\,\mu m$ and $40\,\mu m$ of the size M4 (a), M5 (b), M6 (c) and M8 (d). The measurements of the threads with larger clearances are not shown as they allow fastening screws without a significant force, thus providing no further information.

7 Conclusion and Future Work

In this work, a disruptive manufacturing method was introduced and investigated that allows the integration of strain gauges into additively manufactured parts based on LPBF for force sensing applications. This method breaks and re-arranges the well-known state of the art assembly sequence of conventionally manufactured force sensors by integrating the sensing elements prior to achieving the final shape of the force sensor. Thereby, a measuring element carrier, which is equipped with strain gauges, is integrated into an LPBF-manufactured part during a process interruption. By continuing the manufacturing process a material connection from the LPBF-manufactured base body to the inserted measuring element carrier is made, thus realizing a force flow between them.

It was found that this disruptive manufacturing method leads to a successful fabrication of LPBF-manufactured spring elements with an integrated steel plate that served as the measuring element carrier. This result was examined in several steps. The first property that has to be tested was the strain transmission between the LPBF-manufactured spring element and the measuring element carrier. For this end, a basic geometry of a spring element was manufactured with strain gauges applied after manufacturing, which undergoes an S-shaped deformation under tensile and compressive forces. A proper material bonding was achieved between the LPBF-manufactured base bodies and the inserted steel plate without detected cracks or pores within this geometry. This material bonding, where a material intermixing of the molten steel powder into the steel plate was present in a range of up to $100\,\mu m$, ensured a proper force transmission from the LPBF-manufactured base bodies to the inserted steel plate. Consequently, the strain transmission to the strain gauges is ensured as well. In order to evaluate the performance of the LPBF-manufactured spring elements, they were compared to a conventionally manufactured spring element with identical geometry. It has been shown that there is no measurable difference between the LPBF-manufactured spring elements and the conventionally manufactured spring element in terms of their sensitivity, linearity, hysteresis, temperature behavior, creep as well as behavior under cyclic loading. Furthermore, the low linearity and hysteresis errors of $\pm 0.05\,\%$ and $\pm 0.2\,\%$, respectively, confirmed the firm material bonding and loss-free force transmission from the LPBF-manufactured base bodies to the inserted steel plate. Thus, an excellent strain transmission to the strain gauges is confirmed, which determines significantly the quality of the force sensor. Therefore, spring elements manufactured in disruptive manner by LPBF are competitive with conventionally manufactured spring elements, although they are subjected to severe thermally induced stresses during fabrication. This led to examine the influence of the thermally induced stresses on the sensors

The thermally induced stresses occurring in the manufacturing process result in a significant deformation of the steel plate with a deflection of approximately $0.5\,mm$ in the build direction (z-direction). It is found that the thermally induced deformation of the steel plate is formed by a combination of the process parameters and the chosen geometry. Hereby, a tensile stress occurs during establishing the rear connection of the inserted steel plate with the LPBF-manufactured base bodies due to different cooling rates, which is the main contributor to the thermally induced deformation. Although the thermally induced stresses are mainly released once the LPBF-manufactured spring element is separated from the build platform, their impact remains in the form of skew edges while a small amount of them remains. However, the remaining thermally induced stresses did not penalize the performance of the LPBF-manufactured prototype force sensors. Furthermore, the presented FEA model provides a reliable prediction of the strain transmission despite the neglected remaining thermally induced stresses in these spring elements. An adaptation of the geometry of the spring element such as lowering the height of the material connection and the process parameters allows the reduction of the thermally induced deformation by 67 %.

Besides the aspect of ensuring a loss-free force transmission, and, thus, strain transmission to the strain gauge, the second aspect regarding the influence of the LPBF-process on the strain gauge behavior was investigated. In this case, the same spring elements was built as the previous ones, except that the steel plates were applied in advance with strain gauges. It is found that the strain gauges withstand not only the manufacturing process but also maintain their linear strain sensing characteristics and sensitivity. This is primarily made possible by using the steel plate as the measuring element carrier. Since the material connection is made via the steel plate, only the edges of the steel plate are scanned, thus protecting the strain gauges from direct interaction with the laser. The resulting temperatures at the positions of the strain gauges during manufacturing the base geometry are approximately 145 °C, which is below the specified operating temperature of 200 °C for the strain gauges used. Therefore, the arising temperatures are not critical for the strain gauges. Furthermore, the in-situ measurements of the strain gauges during the manufacturing process show the occurrence of thermally induced deformation of the steel plate, which is reflected in a significant decrease in the resistance of the strain gauges. On one hand, this result is used as a quality measure regarding the reduction of the thermally induced deformation of the steel plate. On the other hand, this feature of measuring the change in resistance of the strain gauge has the potential as a parameter for process monitoring applications in future, and, thus, online tuning of process parameters that countermeasure thermally induced stresses in general. Additionally, it is found that a irreversible change in the base resistance occurs after the manufacturing process, which is higher the closer the strain gauge are positioned to the scanned surface, and, thus, to the laser beam. However, this irreversible change in the base resistance did not influence the behavior of the strain gauges, since the linear behavior and sensitivity remained in excellent agreement with that of strain gauges that were not exposed to the LPBF-process.

The findings were used to develop a geometry that builds upon the basic geometry investigated while allowing for complete encapsulation of the strain gauges. Hereby, an increased energy input into the steel plate results from building the encapsulation, which leads to the rise of the temperature at the strain gauge positions up to 230 °C. Nevertheless, the strain also withstand these conditions while being comparable in terms of their performance to strain gauges that have not been subjected to the LPBF-process. Therefore, the presented disruptive manufacturing method for integrating strain gauges into LPBF-manufactured parts by using a measuring element carrier turns out to be a promising possibility for the development of structural integrated force sensors with complete encapsulated strain gauges that are competitive with conventionally manufactured force sensors. In this context, the presented geometry of the spring element with complete encapsulation of the strain gauges can be used as a basic geometry around which the force transmission bars can be designed to fit the given application. This allows developers of structural integrated force sensors based on the presented geometry to focus entirely on the required design, without being concerned about a proper and damage-free integration of strain gauges.

Future work is aimed at implementing such structural integrated force sensors in real applications. This requires solutions for a proper cable routing, avoiding cut-outs for cable routing as in the current state. This promotes the complete encapsulation of the strain gauges, and, thus, protects them against harsh environmental conditions. A further aspect regarding complete encapsulation of the strain gauges is the development of approaches to remove or minimize the unmolten powder within the housing of the strain gauges. Currently, the powder has been removed from the cut-out for the cables. A possible approach is to interrupt the process again and remove the powder before the housing is completed. Then, a further smaller steel plate could be used as a cover, on which the process is continued. Furthermore, features such as an overload protection can be realized without additional parts or effort. The presented geometry with complete encapsulation features a slot that can be designed such that contact occurs between the enclosure and the force transmission bars when the nominal deflection is exceeded. Thus, the force is bypassed and a overload protection realized.

A direct application for the disruptive manufacturing method emerges in context of the priority program 2305 of the DFG. Here, sensor-integrated machine elements are investigated and developed that are intended to replace conventional machine elements for realizing a sensing capability within condition monitoring applications. In this context, screws are a crucial machine element, and they are available in almost all machines. Thereby, screws with multi-axial force measurement are aimed at, since the load on a screw is usually multi-axial [2]. During the conventional assembly of screws, transverse forces act on the screw due to torsional loading. Additionally, safety-relevant bending and shear stresses occur in the head area of the screw during use [4], which act on the screw apart from the axial pretensioning force. Therefore, a multi-axial force measurement is required. A possible approach is to integrate a force sensor into a cavity of a conventional screw, which is produced by drilling (Fig. 7.1). This approach has the drawback that a hermetic sealing of the sensor is difficult to implement. However, this can be accomplished with the disruptive manufacturing method presented in this work.

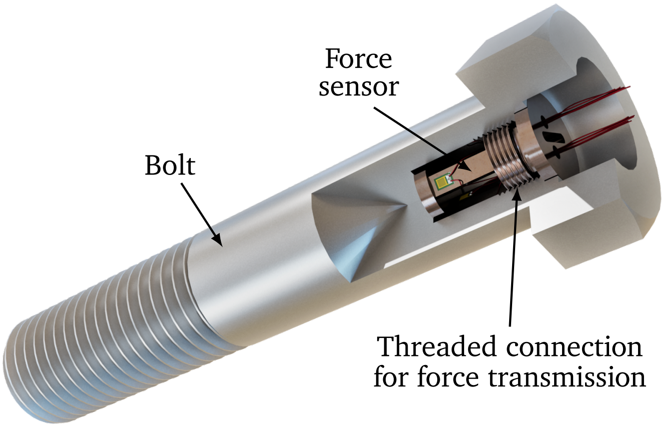

Figure 7.1: Rendering of an sensor-integrating bolt of the size M20. The graphic is taken from [206].

The process for fabricating a sensor-integrated screw according to the disruptive manufacturing method using LPBF is as follows. First, a part of the screw is manufactured that features a cavity [Fig. 7.1(a)]. This cavity serves for integrating a measuring element carrier as well as a electronic into the LPBF-manufactured screw. Second, the LPBF-process is interrupted and the measuring element carrier integrated [Fig. 7.1(b)]. In context of a multi-axial force measurement, the measuring element carrier requires a double-sided connection. This is achieved by designing a thread into the cavity, which is also manufactured by LPBF [Fig. 7.1(b)]. Thereby, the LPBF-manufactured needs to be adapted in term of its flank angle and clearence, as shown in this work, to enable a direct fastening of the measuring element carrier. Finally, the manufacturing process is resumed to establish a material connection with die upper end of the measuring element carrier [Fig. 7.1(c)] and to finalize the LPBF-manufactured screw [Fig. 7.1(d)].

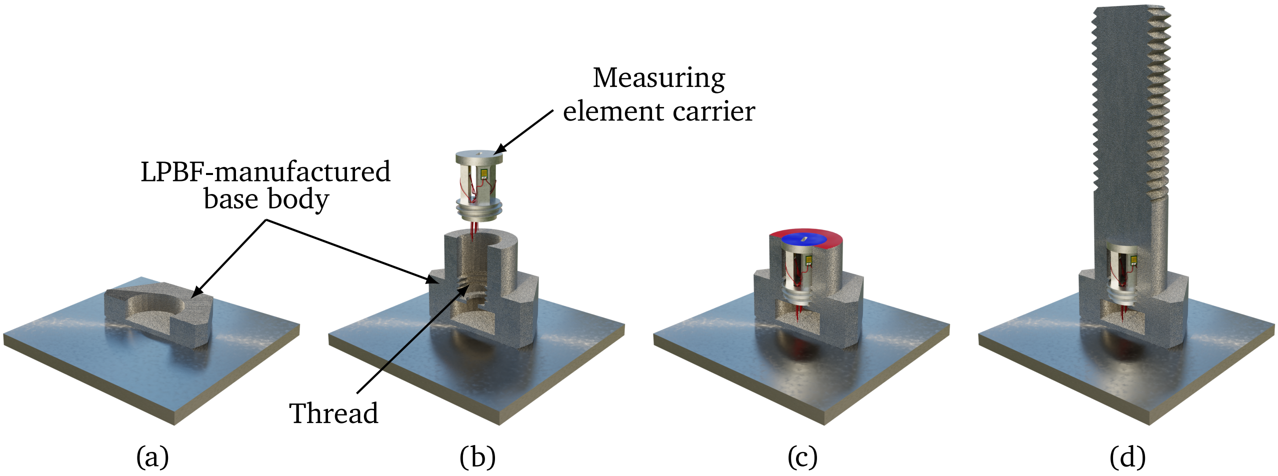

Figure 7.2: The disruptive manufacturing method is adapted to fabricate an LPBF-manufactured screw that enables a multi-axial force measurement. The required double-sided connection is achieved by an LPBF-manufactured thread on one side and a material connection created by LPBF on the other side. The graphic is taken from [206].

Bibliography

[1] H. Lasi, P. Fettke, T. Feld, and M. Hoffmann, “Industry 4.0”, *Business & Information Systems Engineering*, vol. 6, no. 4, pp. 239–242, May 2014. DOI: `10.1007/s12599-014-0334-4`.

[2] T. Kalsoom, N. Ramzan, S. Ahmed, and M. Ur-Rehman, “Advances in Sensor Technologies in the Era of Smart Factory and Industry 4.0”, *Sensors*, vol. 20, no. 23, Nov. 2020. DOI: `10.3390/s20236783`.

[3] I. Castelo-Branco, F. Cruz-Jesus, and T. Oliveira, “Assessing Industry 4.0 readiness in manufacturing: Evidence for the European Union”, *Computers in Industry*, vol. 107, pp. 22–32, May 2019. DOI: `10.1016/j.compind.2019.01.007`.

[4] B. Afzal, M. Umair, G. Asadullah Shah, and E. Ahmed, “Enabling IoT platforms for social IoT applications: Vision, feature mapping, and challenges”, *Future Generation Computer Systems*, vol. 92, pp. 718–731, Mar. 2019. DOI: `10.1016/j.future.2017.12.002`.

[5] K. Zhou, T. Liu, and L. Zhou, “Industry 4.0: Towards future industrial opportunities and challenges”, in *International Conference on Fuzzy Systems and Knowledge Discovery*, Aug. 2015, pp. 2147–2152. DOI: `10.1109/FSKD.2015.7382284`.

[6] D. Mishra, R. B. Roy, S. Dutta, S. K. Pal, and D. Chakravarty, “A review on sensor based monitoring and control of friction stir welding process and a roadmap to Industry 4.0”, *Journal of Manufacturing Processes*, vol. 36, pp. 373–397, Dec. 2018. DOI: `10.1016/j.jmapro.2018.10.016`.

[7] R. B. Randall, *Vibration-based Condition Monitoring: Industrial, Aerospace and Automotive Applications*. John Wiley & Sons, Dec. 2010, ISBN: 978-0-470-74785-8. DOI: `10.1002/9780470977668`.

[8] S. Nandi, H. Toliyat, and X. Li, “Condition Monitoring and Fault Diagnosis of Electrical Motors - A Review”, *IEEE Transactions on Energy Conversion*, vol. 20, no. 4, pp. 719–729, Dec. 2005. DOI: `10.1109/TEC.2005.847955`.

[9] M. L. Wymore, J. E. Van Dam, H. Ceylan, and D. Qiao, “A survey of health monitoring systems for wind turbines”, *Renewable and Sustainable Energy Reviews*, vol. 52, pp. 976–990, Dec. 2015. DOI: `10.1016/j.rser.2015.07.110`.

[10] P. Stoll, E. Gasparin, E. Spierings, and K. Wegener, “Embedding eddy current sensors into LPBF components for structural health monitoring”, *Progress in Additive Manufacturing*, vol. 6, pp. 445–453, Jul. 2021. DOI: `10.1007/s40964-021-00204-3`.

[11] R. Moeini, M. Entezami, M. Ratkovac, *et al.*, “Perspectives on condition monitoring techniques of wind turbines”, *Wind Engineering*, vol. 43, no. 5, pp. 539–555, Oct. 2019. DOI: `10.1177/0309524X18807028`.

[12] F. Ryll and C. Freund, *Grundlagen der Instandhaltung*. Springer Berlin Heidelberg, 2010, pp. 23–101, ISBN: 978-3-642-03949-2. DOI: `10.1007/978-3-642-03949-2_2`.

[13] J. Mathew, C. Hauser, P. Stoll, *et al.*, “Integrating Fiber Fabry-Perot Cavity Sensor Into 3-D Printed Metal Components for Extreme High-Temperature Monitoring Applications”, *IEEE Sensors Journal*, vol. 17, no. 13, pp. 4107–4114, Jul. 2017. DOI: `10.1109/JSEN.2017.2703085`.

[14] H. Li, G. Xu, X. Gui, L. Liang, and Z. Li, "An FBG Displacement Sensor in Deformation Monitoring of Subway Floating Slab", *IEEE Sensors Journal*, vol. 21, no. 3, pp. 2963–2971, Feb. 2021. DOI: `10.1109/JSEN.2020.3022466`.

[15] P. D. Palma, A. Iadicicco, and S. Campopiano, "Curvature Sensor Based on FBGs Embedded in 3D Printed Patches", *IEEE Sensors Journal*, vol. 21, no. 16, pp. 17 868–17 874, Aug. 2021. DOI: `10.1109/JSEN.2021.3083961`.

[16] R. R. J. Maier, W. N. MacPherson, J. S. Barton, *et al.*, "Embedded Fiber Optic Sensors Within Additive Layer Manufactured Components", *IEEE Sensors Journal*, vol. 13, no. 3, pp. 969–979, Mar. 2013. DOI: `10.1109/JSEN.2012.2226574`.

[17] M. Hinderdael, M. Moonens, J. Ertveldt, D. De Baere, and P. Guillaume, "Analytical Modeling of Embedded Load Sensing Using Liquid-Filled Capillaries Integrated by Metal Additive Manufacturing", *IEEE Sensors Journal*, vol. 19, no. 20, pp. 9447–9455, Oct. 2019. DOI: `10.1109/JSEN.2019.2925206`.

[18] M. Hessinger, M. Kniepkamp, J. Lotichius, *et al.*, "Strain Transmission Characteristics of Steel Substrates for Additive Sensor Manufacturing with Selective Laser Melting", in *Sensor*, May 2017, pp. 2147–2152. DOI: `10.5162/sensor2017/D2.2`.

[19] L. Wang and R. X. Gao, *Condition Monitoring and Control for Intelligent Manufacturing*. Springer London, May 2006, ISBN: 978-1-84628-269-0. DOI: `10.1007/1-84628-269-1`.

[20] X. Li and F. Prinz, "Metal Embedded Fiber Bragg Grating Sensors in Layered Manufacturing", *Journal of Manufacturing Science and Engineering*, vol. 125, no. 3, pp. 577–585, Jul. 2003. DOI: `10.1115/1.1581889`.

[21] E. Kirchner, G. Martin, and S. Vogel, "Sensor Integrating Machine Elements – Key to In-Situ Measurements in Mechanical Engineering", in *International Seminar on High Technology*, Oct. 2018.

[22] G. Vorwerk-Handing, T. Gwosch, S. Schork, E. Kirchner, and S. Matthiesen, "Classification and examples of next generation machine elements", *Forschung im Ingenieurwesen*, vol. 84, no. 3, pp. 21–32, Mar. 2020. DOI: `10.1007/s10010-019-00382-1`.

[23] W. E. Frazier, "Metal Additive Manufacturing: A Review", *Journal of Materials Engineering and Performance*, vol. 23, pp. 1917–1928, Jun. 2014. DOI: `10.1007/s11665-014-0958-z`.

[24] Q. Bian, C. Bauer, A. Stadler, *et al.*, "In-Situ High Temperature and Large Strain Monitoring During a Copper Casting Process Based on Regenerated Fiber Bragg Grating Sensors", *Journal of Lightwave Technology*, vol. 39, no. 20, pp. 6660–6669, Oct. 2021. DOI: `10.1109/JLT.2021.3101524`.

[25] D. Lehmhus, C. Aumund-Kopp, F. Petzoldt, *et al.*, "Customized Smartness: A Survey on Links between Additive Manufacturing and Sensor Integration", *Procedia Technology*, vol. 26, pp. 284–301, 2016. DOI: `10.1016/j.protcy.2016.08.038`.

[26] N. Hendrich, F. Wasserfall, and J. Zhang, "3D Printed Low-Cost Force-Torque Sensors", *IEEE Access*, vol. 8, pp. 140 569–140 585, Jul. 2020. DOI: `10.1109/ACCESS.2020.3007565`.

[27] Y. Zhai, D. A. Lados, and J. L. LaGoy, "Additive Manufacturing: Making Imagination the Major Limitation", *The Journal of The Minerals, Metals & Materials Society*, vol. 66, pp. 808–816, Mar. 2014. DOI: `10.1007/s11837-014-0886-2`.

[28] I. Dani, "Smart components by additive technologies", in *IOP Conference Series: Materials Science and Engineering*, Mar. 2019. DOI: `10.1088/1757-899X/480/1/012016`.

[29] P. Stoll, A. Spierings, and K. Wegener, “Impact of a process interruption on tensile properties of SS 316L parts and hybrid parts produced with selective laser melting”, *The International Journal of Advanced Manufacturing Technology*, vol. 103, pp. 367–376, Mar. 2019. DOI: `10.1007/s00170-019-03560-1`.

[30] A. K. Bose, X. Zhang, D. Maddipatla, *et al.*, “Screen-Printed Strain Gauge for Micro-Strain Detection Applications”, *IEEE Sensors Journal*, vol. 20, no. 21, pp. 12 652–12 660, Nov. 2020. DOI: `10.1109/JSEN.2020.3002388`.

[31] T. Duda and L. V. Raghavan, “3D metal printing technology: the need to re-invent design practice”, *AI & Society*, vol. 33, pp. 241–252, Feb. 2018. DOI: `10.1007/s00146-018-0809-9`.

[32] M. Möhrle and C. Emmelmann, “Fabrikstrukturen für die additive Fertigung”, *Zeitschrift für wirtschaftlichen Fabrikbetrieb*, vol. 111, no. 9, pp. 505–509, Mar. 2016. DOI: `10.3139/104.111587`.

[33] P. Stoll, “Functionality integration in powder bed based additive manufacturing processes”, Ph.D. dissertation, ETH Zürich, Nov. 2020.

[34] A. Busachi, J. Erkoyuncu, P. Colegrove, F. Martina, C. Watts, and R. Drake, “A review of Additive Manufacturing technology and Cost Estimation techniques for the defence sector”, *CIRP Journal of Manufacturing Science and Technology*, vol. 19, pp. 117–128, Nov. 2017. DOI: `10.1016/j.cirpj.2017.07.001`.

[35] A. Iliaifar. “Frontiers in Additive Manufacturing: Overcoming Common DfAM Compromises”. (Aug. 2022), [Online]. Available: `http://velo3d.com/frontiers-in-additive-manufacturing-overcoming-common-dfam-compromises/` (visited on 01/15/2023).

[36] M. Fera, R. Macchiaroli, F. Fruggiero, and A. Lambiase, “A new perspective for production process analysis using additive manufacturing—complexity vs production volume”, *The International Journal of Advanced Manufacturing Technology*, vol. 95, pp. 673–685, Mar. 2018. DOI: `10.1007/s00170-017-1221-1`.

[37] P. Pradel, Z. Zhu, R. Bibb, and J. Moultrie, “Complexity is not for free: the impact of component complexity on additive manufacturing build time”, in *Proceedings of the Rapid Design, Prototyping and Manufacturing Conference*, Mar. 2017.

[38] C. Klahn, B. Leutenecker, and M. Meboldt, “Design Strategies for the Process of Additive Manufacturing”, *Procedia CIRP*, vol. 36, pp. 230–235, 2015. DOI: `10.1016/j.procir.2015.01.082`.

[39] Z. Doubrovski, J. C. Verlinden, and J. M. P. Geraedts, “Optimal Design for Additive Manufacturing: Opportunities and Challenges”, in *Proceedings of the ASME 2011 International Design Engineering Technical Conferences and Computers and Information in Engineering Conferenc*, Jun. 2011.

[40] S. Hällgren, L. Pejryd, and J. Ekengren, “(Re)Design for Additive Manufacturing”, *Procedia CIRP*, vol. 50, pp. 246–251, 2016. DOI: `10.1016/j.procir.2016.04.150`.

[41] I. Gibson, D. Rosen, and B. Stucker, *Additive Manufacturing Technologies*. Springer New York, 2014, ISBN: 978-1-4939-2113-3.

[42] E. Abele, H. A. Stoffregen, K. Klimkeit, H. Hoche, and M. Oechsner, “Optimisation of process parameters for lattice structures”, *Rapid Prototyping Journal*, vol. 21, no. 1, pp. 117–127, Jan. 2015. DOI: `10.1108/RPJ-10-2012-0096`.

[43] J. Kranz, D. Herzog, and C. Emmelmann, “Design guidelines for laser additive manufacturing of lightweight structures in TiAl6V4”, *Journal of Laser Applications*, vol. 27, Feb. 2015. DOI: `10.2351/1.4885235`.

[44] C. Klahn, B. Leutenecker, and M. Meboldt, “Design for Additive Manufacturing – Supporting the Substitution of Components in Series Products”, *Procedia CIRP*, vol. 21, pp. 138–143, 2014. DOI: `10.1016/j.procir.2014.03.145`.

[45] C. Emmelmann and C. Klahn, “Funktionsintegration im Werkzeugbau durch laseradditive Fertigung”, *RTe Journal*, vol. 9, 2012.

[46] M. Link, “Komponentenintegration von Dehnungsmessstreifen mittels pulverbettbasiertem Laserstrahlschmelzen”, Ph.D. dissertation, Technische Universität Darmstadt, Jun. 2022.

[47] H. A. Stoffregen, “Strukturintegration piezoelektrischer Vielschichtaktoren mittels selektiven Laserschmelzens”, Ph.D. dissertation, Technische Universität Darmstadt, Dezember 2015.

[48] H. A. Stoffregen, “Funktionsintegration mittels selektiven Laserschmelzens am Beispiel strukturintegrierter piezoelektrischer Aktoren”, in *Proceedings of Rapid.Tech 2015*, Jun. 2015.

[49] C. Tan, D. Wang, W. Ma, *et al.*, “Design and additive manufacturing of novel conformal cooling molds”, *Materials & Design*, vol. 196, Nov. 2020. DOI: `10.1016/j.matdes.2020.109147`.

[50] A. Armillotta, R. Baraggi, and S. Fasoli, “SLM tooling for die casting with conformal cooling channels”, *The International Journal of Advanced Manufacturing Technology*, vol. 71, pp. 573–583, Mar. 2014. DOI: `10.1007/s00170-013-5523-7`.

[51] M. S. Shinde and K. M. Ashtankar, “Additive manufacturing–assisted conformal cooling channels in mold manufacturing processes”, *Advances in Mechanical Engineering*, vol. 9, no. 5, pp. 1–14, May 2017. DOI: `10.1177/1687814017699764`.

[52] M. K. Thompson, G. Moroni, T. Vaneker, *et al.*, “Design for Additive Manufacturing: Trends, opportunities, considerations, and constraints”, *CIRP Annals*, vol. 65, no. 2, pp. 737–760, 2016. DOI: `10.1016/j.cirp.2016.05.004`.

[53] A. Tartar and A. Qui. “The New Rockets Racing to Make Space Affordable”. Bloomberg. (Jul. 2018), [Online]. Available: `https://www.bloomberg.com/graphics/2018-rocket-cost/` (visited on 01/16/2023).

[54] L. Mullen, W. K. Stamp Robin C.and Brooks, E. Jones, and C. J. Sutcliffe, “Selective Laser Melting: a regular unit cell approach for the manufacture of porous, titanium, bone in-growth constructs, suitable for orthopedic applications”, *Journal of Biomedical Materials Research Part B: Applied Biomaterials*, vol. 89, no. 2, pp. 325–334, May 2009. DOI: `10.1002/jbm.b.31219`.

[55] C. Zhang, F. Chen, Z. Huang, *et al.*, “Additive manufacturing of functionally graded materials: A review”, *Materials Science and Engineering: A*, vol. 764, pp. 138–209, Sep. 2019. DOI: `10.1016/j.msea.2019.138209`.

[56] M. T. Andani, N. S. Moghaddam, C. Haberland, D. Dean, M. J. Miller, and M. Elahinia, “Metals for bone implants. Part 1. Powder metallurgy and implant rendering”, *Acta Biomaterialia*, vol. 10, no. 10, pp. 4058–4070, Oct. 2014. DOI: `10.1016/j.actbio.2014.06.025`.

[57] K. O. Buehler, E. Venn-Watson, and C. W. D’Lima D. D. and Colwell, “The press-fit condylar total knee system: 8- to 10-year results with a posterior cruciate-retaining design”, *The Journal of Arthroplasty*, vol. 15, no. 6, pp. 698–701, Sep. 2000. DOI: `10.1054/arth.2000.8189`.

[58] H. A. Stoffregen, J. Fischer, C. Siedelhofer, and E. Abele, “Selective laser melting of porous structures”, in *International Solid Freeform Fabrication Symposium*, Aug. 2011.

[59] M. Gebauer, P. Stoll, B. Müller, *et al.*, “High performance sheet metal forming tooling by additive manufacturing”, in *Proceedings of 6th International Conference on additive Technologies iCAT*, Nov. 2016, pp. 354–361. DOI: `10.3929/ethz-a-010802370`.

[60] M. C. Bermudez Agudelo, M. Hampe, T. Reiber, and E. Abele, "Investigation of Porous Metal-Based 3D-Printed Anode GDLs for Tubular High Temperature Proton Exchange Membrane Fuel Cells", *Materials*, vol. 13, no. 9, May 2020. DOI: `10.3390/ma13092096`.

[61] J. G. Cham, B. L. Pruitt, M. R. Cutkosky, M. Binnard, L. E. Weiss, and G. Neplotnik, "Layered Manufacturing With Embedded Components: Process Planning Considerations", in *International Design Engineering Technical Conferences and Computers and Information in Engineering Conference*, Sep. 1999, pp. 93–101. DOI: `10.1115/DETC99/DFM-8910`.

[62] *Procedure for Rapid Fabrication of Non-Assembly Mechanisms With Embedded Components*, Sep. 2002, pp. 1239–1245. DOI: `10.1115/DETC2002/MECH-34350`.

[63] D. Mayer, H. A. Stoffregen, O. Heuss, J. Thiel, E. Abele, and T. Melz, "Additive manufacturing of active struts for piezoelectric shunt damping", *Journal of Intelligent Material Systems and Structures*, vol. 27, no. 6, pp. 743–754, Apr. 2016. DOI: `10.1177/1045389X15575090`.

[64] W. Gao, Y. Zhang, D. Ramanujan, *et al.*, "The status, challenges, and future of additive manufacturing in engineering", *Computer-Aided Design*, vol. 69, pp. 65–89, Dec. 2015. DOI: `10.1016/j.cad.2015.04.001`.

[65] R. Jiang, R. Kleer, and F. T. Piller, "Predicting the future of additive manufacturing: A Delphi study on economic and societal implications of 3D printing for 2030", *Technological Forecasting and Social Change*, vol. 117, pp. 84–97, Apr. 2017. DOI: `10.1016/j.techfore.2017.01.006`.

[66] A. Jiménez, H. Bidare Prveen snd Hassanin, F. Tarlochan, S. Dimov, and K. Essa, "Powder-based laser hybrid additive manufacturing of metals: A review", *The International Journal of Advanced Manufacturing Technology*, vol. 114, pp. 63–96, Mar. 2021. DOI: `10.1007/s00170-021-06855-4`.

[67] T. Wohlers, I. Campbell, O. Diegel, R. Huff, J. Kowen, and N. Mostow, *Wohlers report 2021: 3D printing and additive manufacturing*. Wohlers Associates, 2021, ISBN: 978-0-9913332-7-1.

[68] C. Knaak, L. Masseling, E. Duong, P. Abels, and A. Gillner, "Improving Build Quality in Laser Powder Bed Fusion Using High Dynamic Range Imaging and Model-Based Reinforcement Learning", *IEEE Access*, vol. 9, pp. 55 214–55 231, Mar. 2021. DOI: `10.1109/ACCESS.2021.3067302`.

[69] T. Töppel, H. Lausch, M. Brand, E. Hensel, M. Arnold, and C. Rotsch, "Structural Integration of Sensors/Actuators by Laser Beam Melting for Tailored Smart Components", *The Journal of The Minerals, Metals & Materials Society*, vol. 70, pp. 321–327, Jan. 2018. DOI: `10.1007/s11837-017-2725-8`.

[70] P. Stoll, B. Leutenecker-Twelsiek, A. Spierings, C. Klahn, and K. Wegener, "Temperature Monitoring of an SLM Part with Embedded Sensor", in *Proceedings of Additive Manufacturing in Products and Applications*, 2018, pp. 273–284. DOI: `10.1007/978-3-319-66866-6_26`.

[71] D. Havermann, J. Mathew, W. N. MacPherson, R. R. J. Maier, and D. P. Hand, "Temperature and Strain Measurements With Fiber Bragg Gratings Embedded in Stainless Steel 316", *Journal of Lightwave Technology*, vol. 33, no. 12, pp. 2474–2479, Jun. 2015. DOI: `10.1109/JLT.2014.2366835`.

[72] D. Havermann, J. Mathew, W. N. MacPherson, R. R. J. Maier, and D. P. Hand, "In-situ strain sensing with fiber optic sensors embedded into stainless steel 316", in *Sensors and Smart Structures Technologies for Civil, Mechanical, and Aerospace Systems*, vol. 9435, SPIE, Apr. 2015. DOI: `10.1117/12.2083843`.

[73] R. R. J. Maier, D. Havermann, W. N. MacPherson, and D. P. Hand, "Embedding metallic jacketed fused silica fibres into stainless steel using additive layer manufacturing technology", in *Fifth European Workshop on Optical Fibre Sensors*, vol. 8794, SPIE, May 2013, 87942U. DOI: `10.1117/12.2026076`.

[74] R. R. J. Maier, D. Havermann, O. Schneller, *et al.*, "Optical fibre sensing in metals by embedment in 3D printed metallic structures", in *23rd International Conference on Optical Fibre Sensors*, vol. 9157, SPIE, Jun. 2014. DOI: `10.1117/12.2064886`.

[75] J. Mathew, D. Havermann, D. Polyzos, W. N. MacPherson, D. P. Hand, and R. R. J. Maier, "SS316 structure fabricated by selective laser melting and integrated with strain isolated optical fiber high temperature sensor", in *24th International Conference on Optical Fibre Sensors*, vol. 9634, SPIE, Sep. 2015, 96340Q. DOI: `10.1117/12.2194451`.

[76] J. F. I. Paz, J. Wilbig, C. Aumund-Kopp, and F. Petzoldt, "RFID transponder integration in metal surgical instruments produced by additive manufacturing", *Powder Metallurgy*, vol. 57, no. 5, pp. 365–372, Nov. 2014. DOI: `10.1179/1743290114Y.0000000112`.

[77] J. Sehrt and G. Witt, "Additive Manufacturing of Smart Parts and Medical Instruments", in *Proceedings of AEPR*, 2012.

[78] X. Li, "Embedded Sensors in Layered Manufacturing", Ph.D. dissertation, Standford University, 2001.

[79] X. Li, A. Golnas, and F. B. Prinz, "Shape deposition manufacturing of smart metallic structures with embedded sensors", in *Smart Structures and Materials 2000: Sensory Phenomena and Measurement Instrumentation for Smart Structures and Materials*, vol. 3986, SPIE, Jun. 2000, pp. 160–171. DOI: `10.1117/12.388103`.

[80] M. Elsherif, A. E. Salih, M. G. Muñoz, *et al.*, "Optical Fiber Sensors: Working Principle, Applications, and Limitations", *Advanced Photonics Research*, vol. 3, no. 11, Jul. 2022. DOI: `10.1002/adpr.202100371`.

[81] D. Havermann, W. N. MacPherson, R. R. Maier, and D. P. Hand, "Embedding optical fibers into stainless steel using laser additive manufacturing", in *International Congress on Applications of Lasers & Electro-Optics*, 2013, pp. 381–385.

[82] H.-R. Tränkler and L. Reindl, *Sensortechnik – Handbuch für Praxis und Wissenschaft*. Springer Vieweg Berlin Heidelberg, 2014, ISBN: 978-3-642-29942-1.

[83] M. Binder, L. Kirchbichler, C. Seidel, C. Anstaett, G. Schlick, and G. Reinhart, "Design Concepts for the Integration of Electronic Components into Metal Laser-based Powder Bed Fusion Parts", *Procedia CIRP*, vol. 81, pp. 992–997, 2019. DOI: `10.1016/j.procir.2019.03.240`.

[84] A. N. Nambiar, "RFID technology: A review of its applications", in *Proceedings of the world congress on engineering and computer science*, Oct. 2009, pp. 20–22.

[85] R. Want, "An introduction to RFID technology", *IEEE Pervasive Computing*, vol. 5, no. 1, pp. 25–33, Feb. 2006. DOI: `10.1109/MPRV.2006.2`.

[86] M. Binder, F. Schönfeld, C. Anstätt, G. Schlick, C. Seidel, and G. Reinhart, "Radio-Frequency Identification of Metal AM Parts", *PhotonicsViews*, vol. 16, no. 5, pp. 59–63, Oct. 2019.

[87] H.-P. Kim, W.-S. Kang, C.-H. Hong, *et al.*, "Piezoelectrics", in *Advanced Ceramics for Energy Conversion and Storage*, Elsevier, 2020, pp. 157–206, ISBN: 978-0-08-102726-4. DOI: `10.1016/B978-0-08-102726-4.00005-3`.

[88] M. S. Hossain, J. A. Gonzalez, R. M. Hernandez, *et al.*, "Fabrication of smart parts using powder bed fusion additive manufacturing technology", *Additive Manufacturing*, vol. 10, pp. 58–66, Apr. 2016. DOI: `10.1016/j.addma.2016.01.001`.

[89] S. Keil, *Dehnungsmessstreifen*. Wiesbaden: Springer Fachmedien Wiesbaden, 2017, ISBN: 978-3-658-13611-6. DOI: `10.1007/978-3-658-13612-3`.

[90] J. Rausch, C. Hatzfeld, R. Karsten, R. Kraus, J. Millitzer, and R. Werthschützky, “Strain measurement on stiff structures: experimental evaluation of three integrated measurement principles”, *Smart materials and structures*, vol. 21, no. 6, May 2012.

[91] M. Binder, M. Fischer, S. Dietrich, C. Seidel, and G. Reinhart, “Integration of Strain Gauges in Components Manufactured by Laser-Based Powder Bed Fusion”, in *Proceedings of the Machining Innovations Conference*, Nov. 2020. DOI: `10.2139/ssrn.3724097`.

[92] V. Hammond, M. Schuch, and M. Bleckmann, “The influence of a process interruption on tensile properties of AlSi10Mg samples produced by selective laser melting”, *Rapid Prototyping Journal*, vol. 25, no. 8, pp. 1442–1452, Sep. 2019. DOI: `10.1108/RPJ-04-2018-0105`.

[93] R. Lezama-Nicolas, M. Rodriguez-Salvador, R. Rio-Belver, and I. Bildosola, “A bibliometric method for assessing technological maturity: the case of additive manufacturing”, *Scientometrics*, vol. 117, pp. 1425–1452, Dec. 2018. DOI: `10.1007/s11192-018-2941-1`.

[94] P. Stoll, J. Mathew, A. Spierings, T. Bauer, R. R. Maier, and K. Wegener, “Embedding fibre optical sensors into SLM parts”, in *2016 International Solid Freeform Fabrication Symposium*, 2016.

[95] R. Chadda, J. Probst, C. Hartmann, *et al.*, “Disruptive Force Sensor Based on Laser-based Powder-Bed-Fusion”, in *2020 IEEE SENSORS*, Oct. 2020, pp. 1–4. DOI: `10.1109/SENSORS47125.2020.9278934`.

[96] R. Chadda, M. Link, T. Engel, *et al.*, “Evaluation of additively manufactured parts in disruptive manner as deformation elements for structural integrated force sensors”, *IEEE Sensors Journal*, vol. 22, no. 20, pp. 19 249–19 258, Oct. 2022. DOI: `10.1109/JSEN.2022.3205172`.

[97] J. Lotichius, “Modellbildung der Messunsicherheit resistiver Sensorsysteme”, Ph.D. dissertation, Technische Universität Darmstadt, Oktober 2017.

[98] J. Rausch, “Entwicklung und Anwendung miniaturisierter piezoresistiver Dehnungsmesselemente”, Ph.D. dissertation, Technische Universität Darmstadt, Jul. 2012.

[99] Q. Liang, K. Zou, J. Long, *et al.*, “Multi-Component FBG-Based Force Sensing Systems by Comparison With Other Sensing Technologies: A Review”, *IEEE Sensors Journal*, vol. 18, no. 18, pp. 7345–7357, Sep. 2018. DOI: `10.1109/JSEN.2018.2861014`.

[100] R. Werthschützky, “Sensor Technologien 2022”, AMA Verband für Sensorik und Messtechnik, Tech. Rep., 2022.

[101] Y. Wei and Q. Xu, “An overview of micro-force sensing techniques”, *Sensors and Actuators A: Physical*, vol. 234, pp. 359–374, Oct. 2015. DOI: `10.1016/j.sna.2015.09.028`.

[102] W. Thomson, “On the electro-dynamic qualities of metals: Effects of magnetization on the electric conductivity of nickel and of iron”, *Proceedings of the Royal Society of London*, no. 8, pp. 546–550, 1857. DOI: `10.1098/rspl.1856.0144`.

[103] P. W. Bridgman, “The Electrical Resistance of Metals”, *Physical Review*, vol. 17, pp. 161–194, 2 Feb. 1921. DOI: `10.1103/PhysRev.17.161`.

[104] P. W. Bridgman, “The Compressibility and Pressure Coefficient of Resistance of Ten Elements”, *Proceedings of the American Academy of Arts and Sciences*, vol. 62, no. 8, pp. 207–226, 1927.

[105] D. M. Newitt, “Percy Williams Bridgman, 1882-1961”, *Biographical Memoirs of Fellows of the Royal Society*, vol. 8, pp. 26–40, 1962. DOI: `10.1098/rsbm.1962.0003`.

[106] M. Stockmann, “Mikromechanische Analyse der Wirkungsmechanismen elektrischer Dehnungsmessstreifen”, Habilitation, Technische Universität Chemnitz, 2000.

[107] J. W. Cookson, “Theory of the piezo-resistive effect”, *Physical review*, vol. 47, no. 2, 1935.

[108] W.-T. Park, “Piezoresistivity”, in *Encyclopedia of Nanotechnology*, B. Bhushan, Ed. Springer Netherlands, 2016, pp. 3246–3252, ISBN: 978-94-017-9780-1. DOI: `10.1007/978-94-017-9780-1_222`.

[109] A. C. Ruge, *Strain gauge*, US patent US2350972A, 1939. [Online]. Available: `https://patents.google.com/patent/US2350972`.

[110] E. E. Simmons, *Material testing apparatus*, US patent US2292549A, 1940. [Online]. Available: `https://patents.google.com/patent/US2292549A/en`.

[111] M. Deegan. “Birth of the foil strain gauge”. (Sep. 2016), [Online]. Available: `https://strainblog.micro-measurements.com/content/birth-foil-strain-gauge` (visited on 02/20/2023).

[112] G. Arlt, “The sensitivity of strain gauges”, *Journal of Applied Physics*, vol. 49, no. 7, pp. 4273–4274, 1978. DOI: `10.1063/1.325344`.

[113] “Der Weg zum Messgrößenaufnehmer”, Hottinger Baldwin Messtechnik GmbH, Tech. Rep., 2008.

[114] C. Rohrbach, *Handbuch für experimentelle Spannungsanalyse*. Springer Berlin, Heidelberg, 1989, ISBN: 978-3-642-48660-9. DOI: `10.1007/978-3-642-48659-3`.

[115] J. A. Thornton, “Structure-Zone Models Of Thin Films”, in *Modeling of Optical Thin Films*, vol. 821, SPIE, Feb. 1988, pp. 95–105. DOI: `10.1117/12.941846`.

[116] G. R. Witt, “The electromechanical properties of thin films and the thin film strain gauge”, *Thin Solid Films*, vol. 22, no. 2, pp. 133–156, Jun. 1974. DOI: `10.1016/0040-6090(74)90001-7`.

[117] K. Bethe and D. Schon, “Thin-film strain-gage transducers”, *Philips Technical Review*, vol. 39, pp. 94–101, 1980.

[118] J. Herrmann, K.-H. Müller, T. Reda, *et al.*, “Nanoparticle films as sensitive strain gauges”, *Applied Physics Letters*, vol. 91, no. 18, p. 183 105, Oct. 2007. DOI: `10.1063/1.2805026`.

[119] D. Vollberg, A.-C. Probst, M. Langosch, *et al.*, “Hochempfindliche Folien-Dehnungsmessstreifen auf dem Weg zur technologischen Reife”, *tm - Technisches Messen*, vol. 82, no. 10, pp. 506–516, Oct. 2015. DOI: `10.1515/teme-2015-0066`.

[120] Z. Zhang, M. Jin, and S. Liu, “Thick film resistors on stainless steel as sensing elements for strain sensor applications”, *Sensors and Actuators A: Physical*, vol. 179, pp. 50–55, Jun. 2012. DOI: `10.1016/j.sna.2012.03.012`.

[121] J. Shah and L. Berrin, “Mechanism and control of post-trim drift of laser-trimmed thick-film resistors”, *IEEE Transactions on Components, Hybrids, and Manufacturing Technology*, vol. 1, no. 2, pp. 130–136, Jun. 1978. DOI: `10.1109/TCHMT.1978.1135262`.

[122] T. Baiatu, U. Böttger, R. Bormann, *et al.*, *Keramik*. Springer-Verlag, 2013.

[123] F. Zandman, P.-R. Simon, J. Szwarc, and F. Zandman, “Resistor theory and technology”, Vishay Intertechnology, Tech. Rep., 2001.

[124] W. Menz, J. Mohr, and O. Paul, *Mikrosystemtechnik für Ingenieure*, 2005.

[125] C. Canali, D. Malvasi, B. Morten, M. Prudenziati, and A. Taroni, “Strain sensitivity in thick-film resistors”, *IEEE Transactions on Components, Hybrids, and Manufacturing Technology*, vol. 3, no. 3, pp. 421–423, Sep. 1980. DOI: `10.1109/TCHMT.1980.1135638`.

[126] N. White and J. Turner, “Thick-film sensors: past, present and future”, *Measurement Science and Technology*, vol. 8, no. 1, p. 1, 1997. DOI: `10.1088/0957-0233/8/1/002`.

[127] O. Zinke and H. Seither, *Widerstände, Kondensatoren, Spulen und ihre Werkstoffe*. Springer-Verlag, 1982, ISBN: 978-3-642-50981-0. DOI: `10.1007/978-3-642-50981-0`.

[128] R. A. Rikoski, *Hybrid Microelectronic Circuits: The Thick Film*. John Wiley & Sons, 1973, ISBN: 978-0471722007.

[129] M. Hrovat, D. Belavič, Z. Samardžija, and J. Holc, "A characterisation of thick film resistors for strain gauge applications", *Journal of materials science*, vol. 36, pp. 2679–2689, Jun. 2001. DOI: `10.1023/A:1017908728642`.

[130] A. A. Barlian, W.-T. Park, J. R. Mallon, A. J. Rastegar, and B. L. Pruitt, "Review: Semiconductor Piezoresistance for Microsystems", *Proceedings of the IEEE*, vol. 97, no. 3, pp. 513–552, 2009. DOI: `10.1109/JPROC.2009.2013612`.

[131] M. Borghetti, M. Serpelloni, and E. Sardini, "Printed Strain Gauge on 3D and Low-Melting Point Plastic Surface by Aerosol Jet Printing and Photonic Curing", *Sensors*, vol. 19, no. 19, Sep. 2019. DOI: `10.3390/s19194220`.

[132] M. Liu, Q. Zhang, Y. Shao, C. Liu, and Y. Zhao, "Research of a Novel 3D Printed Strain Gauge Type Force Sensor", *Micromachines*, vol. 10, no. 1, 2019. DOI: `10.3390/mi10010020`.

[133] H.-L. Kao, C.-L. Cho, L.-C. Chang, C.-B. Chen, W.-H. Chung, and Y.-C. Tsai, "A Fully Inkjet-Printed Strain Sensor Based on Carbon Nanotubes", *Coatings*, vol. 10, no. 8, Aug. 2020. DOI: `10.3390/coatings10080792`.

[134] H. Kang, S. Kim, J. Shin, and S. Ko, "Inkjet-Printed Flexible Strain-Gauge Sensor on Polymer Substrate: Topographical Analysis of Sensitivity", *Applied Sciences*, vol. 12, no. 6, Mar. 2022. DOI: `10.3390/app12063193`.

[135] N. Munasinghe, M. Woods, L. Miles, and G. Paul, "3-D Printed Strain Sensor for Structural Health Monitoring", in *2019 IEEE International Conference on Cybernetics and Intelligent Systems (CIS) and IEEE Conference on Robotics, Automation and Mechatronics (RAM)*, 2019, pp. 275–280. DOI: `10.1109/CIS-RAM47153.2019.9095826`.

[136] I. Mileti, L. Cortese, Z. Del Prete, and E. Palermo, "Reproducibility and Embedding Effects on Static Performace of 3D Printed Strain Gauges", in *2021 IEEE International Workshop on Metrology for Industry 4.0 & IoT*, 2021, pp. 499–504. DOI: `10.1109/MetroInd4.0IoT51437.2021.9488430`.

[137] E. Sundaralingam, "Additive Fertigung resistiver Sensoren für Applikationen in der Kraftmesstechnik", M.S. thesis, Technische Universität Darmstadt, 2023.

[138] S. Kirkpatrick, "Percolation and Conduction", *Reviews of Modern Physics*, vol. 45, pp. 574–588, 4 Oct. 1973. DOI: `10.1103/RevModPhys.45.574`.

[139] T. Beléndez, C. Neipp, and A. Beléndez, "Large and small deflections of a cantilever beam", *European journal of physics*, vol. 23, no. 3, 2002.

[140] S. Dul, A. Pegoretti, and L. Fambri, "Fused Filament Fabrication of Piezoresistive Carbon Nanotubes Nanocomposites for Strain Monitoring", *Frontiers in Materials*, vol. 7, Feb. 2020. DOI: `10.3389/fmats.2020.00012`.

[141] K. Hoffmann, "Practical Hints for the Installation of Strain Gages", Hottinger Baldwin Messtechnik, Tech. Rep., 1979.

[142] ISO/ASTM 52900:2015, "Additive manufacturing – general principles – terminology", International Organization for Standardization, Standard, 2015.

[143] S. Chowdhury, N. Yadaiah, C. Prakash, *et al.*, “Laser powder bed fusion: A state-of-the-art review of the technology, materials, properties & defects, and numerical modelling”, *Journal of Materials Research and Technology*, vol. 20, pp. 2109–2172, Sep. 2022. DOI: `10.1016/j.jmrt.2022.07.121`.

[144] A. Gebhardt, *Generative Fertigungsverfahren*. Carl Hanser Verlag, 2013, ISBN: 978-3-446-43652-7.

[145] A. Gebhardt, *Understanding Additive Manufacturing*. Carl Hanser Verlag, 2012, ISBN: 978-3-446-42552-1.

[146] R. Liu, Y. Chen, Y. Liu, Z. Yan, and Y.-X. Wang, “Topological Design of a Trabecular Bone Structure With Morphology and Mechanics Control for Additive Manufacturing”, *IEEE Access*, vol. 9, pp. 11 123–11 133, Jan. 2021. DOI: `10.1109/ACCESS.2021.3050745`.

[147] A. Gebhardt, J. Kessler, and A. Schwarz, *Produktgestaltung für die Additive Fertigung*. Carl Hanser Verlag, 2019, ISBN: 978-3-446-46133-8.

[148] I. J. Petrick and T. W. Simpson, “3D Printing Disrupts Manufacturing: How Economies of One Create New Rules of Competition”, *Research-Technology Management*, vol. 56, no. 6, pp. 12–16, 2013. DOI: `10.5437/08956308X5606193`.

[149] S. Mellor, L. Hao, and D. Zhang, “Additive manufacturing: A framework for implementation”, *International Journal of Production Economics*, vol. 149, pp. 194–201, Mar. 2014. DOI: `10.1016/j.ijpe.2013.07.008`.

[150] M. Bogers, R. Hadar, and A. Bilberg, “Additive manufacturing for consumer-centric business models: Implications for supply chains in consumer goods manufacturing”, *Technological Forecasting and Social Change*, vol. 102, pp. 225–239, Jan. 2016. DOI: `10.1016/j.techfore.2015.07.024`.

[151] J. Deckers, J. Vleugels, and J.-P. Kruth, “Additive manufacturing of ceramics: A review”, *Journal of Ceramic Science and Technology*, vol. 5, no. 4, pp. 245–260, 2014.

[152] F. I. Azam, A. M. A. Rani, K. Altaf, T. V. V. L. N. Rao, and H. A. Zaharin, “An In-Depth Review on Direct Additive Manufacturing of Metals”, *IOP Conference Series: Materials Science and Engineering*, vol. 328, no. 1, Mar. 2018. DOI: `10.1088/1757-899X/328/1/012005`.

[153] A. Davids, L. Apfelbacher, L. Hitzler, and C. Krempaszky, “Multi-step Additive Manufacturing Technologies Utilizing the Powder Metallurgical Manufacturing Route”, in *Lectures Notes on Advanced Structured Materials*. Springer International Publishing, Dec. 2022, pp. 99–117. DOI: `10.1007/978-3-031-11589-9_6`.

[154] ASTM F2792-12, “Standard Terminology for Additive Manufacturing Technologies”, ASTM, 2012.

[155] Y. Huang, M. C. Leu, J. Mazumder, and A. Donmez, “Additive Manufacturing: Current State, Future Potential, Gaps and Needs, and Recommendations”, *Journal of Manufacturing Science and Engineering*, vol. 137, no. 1, Feb. 2015. DOI: `10.1115/1.4028725`.

[156] J. Sander, “Selektives Laserschmelzen hochfester Werkzeugstähle”, Ph.D. dissertation, Technische Universität Dresden, Apr. 2018.

[157] D. D. Gu, W. Meiners, K. Wissenbach, and R. Poprawe, “Laser additive manufacturing of metallic components: materials, processes and mechanisms”, *International Materials Reviews*, vol. 57, no. 3, pp. 133–164, Nov. 2013. DOI: `10.1179/1743280411Y.0000000014`.

[158] M. Kniepkamp, “Methode zur bauteilindividuellen Prozesssteuerung beim selektiven Laserschmelzen”, Ph.D. dissertation, Technische Universität Darmstadt, Jun. 2020.

[159] P. Mercelis and J.-P. Kruth, “Residual stresses in selective laser sintering and selective laser melting”, *Rapid Prototyping Journal*, vol. 12, no. 5, pp. 254–265, Oct. 2006. DOI: `10.1108/13552540610707013`.

[160] J.-P. Kruth, J. Deckers, E. Yasa, and R. Wauthle, “Assessing and comparing influencing factors of residual stresses in selective laser melting using a novel analysis method”, *Proceedings of the Institution of Mechanical Engineers, Part B: Journal of Engineering Manufacture*, vol. 226, no. 6, pp. 980–991, Mar. 2012. DOI: `10.1177/0954405412437085`.

[161] B. Cheng, S. Shrestha, and K. Chou, “Stress and deformation evaluations of scanning strategy effect in selective laser melting”, *Additive Manufacturing*, vol. 12, pp. 240–251, 2016. DOI: `10.1016/j.addma.2016.05.007`.

[162] O. Rehme, *Cellular design for laser freeform fabrication*. 2010, vol. 4.

[163] J. Yu, D. Kim, K. Ha, J. B. Jeon, D. J. Kim, and W. Lee, “Size effect due to contour laser scanning in 316L stainless steel produced by laser powder bed fusion”, *Journal of Materials Research and Technology*, vol. 15, pp. 5554–5568, 2021. DOI: `10.1016/j.jmrt.2021.11.034`.

[164] T. Kurzynowski, W. Stopyra, K. Gruber, G. Ziółkowski, B. Kuźnicka, and E. Chlebus, “Effect of scanning and support strategies on relative density of SLM-ed H13 steel in relation to specimen size”, *Materials*, vol. 12, no. 2, p. 239, Jan. 2019. DOI: `10.3390/ma12020239`.

[165] J. Hajnys, M. Pagáč, J. Měsíček, J. Petru, and M. Król, “Influence of scanning strategy parameters on residual stress in the SLM process according to the bridge curvature method for AISI 316L stainless steel”, *Materials*, vol. 13, no. 7, p. 1659, Apr. 2020. DOI: `10.3390/ma13071659`.

[166] J.-P. Kruth, L. Froyen, J. Van Vaerenbergh, P. Mercelis, M. Rombouts, and B. Lauwers, “Selective laser melting of iron-based powder”, *Journal of materials processing technology*, vol. 149, pp. 616–622, Jun. 2004. DOI: `10.1016/j.jmatprotec.2003.11.051`.

[167] Y. Liu, Y. Yang, and D. Wang, “A study on the residual stress during selective laser melting (SLM) of metallic powder”, *The International Journal of Advanced Manufacturing Technology*, vol. 87, pp. 647–656, Feb. 2016. DOI: `10.1007/s00170-016-8466-y`.

[168] L. Wan, Z. Xia, Y. Song, *et al.*, “Parameter optimization of selective laser melting fabricated titanium alloy using skin-core and triple contour scanning strategy”, *Journal of Laser Applications*, vol. 32, no. 4, Sep. 2020. DOI: `10.2351/7.0000180`.

[169] D. Gross, W. Hauger, J. Schröder, and W. A. Wall, *Technische Mechanik 2*. Berlin, Heidelberg: Springer Berlin Heidelberg, 2017, ISBN: 978-3-662-53678-0. DOI: `10.1007/978-3-662-53679-7`.

[170] I. Arrayago, K. J. R. Rasmussen, and E. Real, “Statistical analysis of the material, geometrical and imperfection characteristics of structural stainless steels and members”, *Journal of Constructional Steel Research*, vol. 175, Dec. 2020. DOI: `10.1016/j.jcsr.2020.106378`.

[171] European Committee for Standardization, “Eurocode 3: Design of Steel Structures - Part 1–4: General Rules, Supplementary Rules for Stainless Steels, Including Amendment A1”, EN 1993-1-4:2006+A1:2015, Brussels, Belgium, 2015.

[172] S. Afshan, I. Arrayago Luquin, L. Gardner, *et al.*, *Design manual for structural stainless steel*. Steel Construction Institute publications, 2017.

[173] Australian/New Zealand Standard (AS/NZS), “Cold-Formed Stainless Steel Structures”, AS/NZS 4673:2001, Sydney, Australia, 2001.

[174] American Society of Civil Engineers (ASCE), “Specification for the Design of Cold-Formed Stainless Steel Structural Members”, SEI/ASCE 8-0, Virginia, US, 2002.

[175] M. B. Heaney, “Electrical conductivity and resistivity”, *Electrical measurement, signal processing, and displays*, vol. 7, no. 1, 2003.

[176] A. Öchsner, *Theorie der Balkenbiegung: Einführung und Modellierung der Statischen Verformung und Beanspruchung*. Wiesbaden: Springer Fachmedien Wiesbaden GmbH, 2016, ISBN: 978-3-658-14638-2.

[177] Joint Commitee for Guide in Metrology (JCGM), *Evaluation of measurement data — Guide to the expression of uncertainty in measurement*, 2008. [Online]. Available: `http://www.bipm.org/en/publications/guides/gum.html`.

[178] S. Zandi, P. Saxena, and N. E. Gorji, "Numerical simulation of heat distribution in RGO-contacted perovskite solar cells using COMSOL", *Solar Energy*, vol. 197, pp. 105–110, Feb. 2020. DOI: `10.1016/j.solener.2019.12.050`.

[179] A. Marchidan, T. N. Sullivan, and J. L. Palladino, "Load Cell Design Using Comsol Multiphysics", in *Proceedings of the 2012 Comsol Conference*, Boston, Oct. 2012.

[180] V. Giurgiutiu, "Chapter 2 - fundamentals of aerospace composite materials", in *Structural Health Monitoring of Aerospace Composites*, Academic Press, 2016, pp. 25–65. DOI: `10.1016/B978-0-12-409605-9.00002-7`.

[181] W. Voigt, *Lehrbuch der Kristallphysik: mit Ausschluss der Kristalloptik*. Johnson Reprint Corporation, 1966.

[182] S. Sun, M. Brandt, and M. Easton, "Powder bed fusion processes: An overview", in *Laser Additive Manufacturing*, M. Brandt, Ed., Woodhead Publishing, 2017, pp. 55–77. DOI: `10.1016/B978-0-08-100433-3.00002-6`.

[183] M. Cloots, P. J. Uggowitzer, and K. Wegener, "Investigations on the microstructure and crack formation of IN738LC samples processed by selective laser melting using Gaussian and doughnut profiles", *Materials and Design*, vol. 89, pp. 770–784, Jan. 2016. DOI: `10.1016/j.matdes.2015.10.027`.

[184] W. L. Smith, J. D. Roehling, M. Strantza, *et al.*, "Residual stress analysis of in situ surface layer heating effects on laser powder bed fusion of 316L stainless steel", *Additive Manufacturing*, vol. 47, Nov. 2021. DOI: `10.1016/j.addma.2021.102252`.

[185] I. Yadroitsev and I. Yadroitsava, "Evaluation of residual stress in stainless steel 316L and Ti6Al4V samples produced by selective laser melting", *Virtual and Physical Prototyping*, vol. 10, no. 2, pp. 67–76, Apr. 2015. DOI: `10.1080/17452759.2015.1026045`.

[186] T. Engel, *Temperaturverhalten und Verspannungsanalyse von disruptiv hergestellten Kraftsensoren mittels Laser-based Powder-Bed-Fusion*, Bachelor's Thesis, Technische Universität Darmstadt, 2021.

[187] Y.-C. Wu, C.-H. San, C.-H. Chang, *et al.*, "Numerical modeling of melt-pool behavior in selective laser melting with random powder distribution and experimental validation", *Journal of Materials Processing Technology*, vol. 254, pp. 72–78, Apr. 2018. DOI: `10.1016/j.jmatprotec.2017.11.032`.

[188] P. I. Pradeep, V. A. Kumar, A. Sriranganath, *et al.*, "Characterization and Qualification of LPBF Additively Manufactured AISI-316L Stainless Steel Brackets for Aerospace Application", *Transactions of the Indian National Academy of Engineering volume*, vol. 5, pp. 603–616, Aug. 2020. DOI: `10.1007/s41403-020-00159-x`.

[189] S. Ziri, A. Hor, and C. Mabru, "Combined effect of powder properties and process parameters on the density of 316L stainless steel obtained by laser powder bed fusion", *The International Journal of Advanced Manufacturing Technology*, vol. 120, pp. 6187–6204, Apr. 2022. DOI: `10.1007/s00170-022-09160-w`.

[190] L. Mussio, "OIML R60: Metrological regulation for load cells - Part 2: Metrological controls and performance tests", *Bureau International de Métrologie Légale*, 2021.

[191] M. Mathis, D. Vollberg, M. Langosch, D. Göttel, A. Lellig, and G. Schultes, "Creep adjustment of strain gauges based on granular NiCr-carbon thin films", *Journal of Sensors and Sensor Systems*, vol. 10, no. 1, pp. 53–61, Mar. 2021. DOI: `10.5194/jsss-10-53-2021`.

[192] J. P. Holman, *Heat Transfer*. New York: McGraw-Hill, 2002, ISBN: 978-0071226219.

[193] R. Marek and K. Nitsche, *Praxis der Wärmeübertragung*. München: Carl Hanser Verlag, 2012, ISBN: 978-3-446-43320-5. DOI: `10.3139/9783446433205`.

[194] G. Mohr, S. J. Altenburg, and K. Hilgenberg, "Effects of inter layer time and build height on resulting properties of 316L stainless steel processed by laser powder bed fusion", *Additive Manufacturing*, vol. 32, Mar. 2020. DOI: `10.1016/j.addma.2020.101080`.

[195] A. Changdar and S. S. Chakraborty, "Laser processing of metal foam - A review", *Journal of Manufacturing Processes*, vol. 61, pp. 208–225, Jan. 2021. DOI: `10.1016/j.jmapro.2020.10.012`.

[196] Y.-J. Hwang, K.-S. Kim, B. AlMangour, D. Grzesiak, and K.-A. Lee, "A New Approach for Manufacturing Stochastic Pure Magnesium Foam by Laser Powder Bed Fusion: Fabrication, Geometrical Characteristics, and Compressive Mechanical Properties", *Advanced Engineering Materials*, vol. 23, no. 12, Dec. 2021. DOI: `10.1002/adem.202100483`.

[197] N. Contuzzi, S. L. Campanelli, F. Caiazzo, and V. Alfieri, "Design and Fabrication of Random Metal Foam Structures for Laser Powder Bed Fusion", *Materials*, vol. 12, no. 8, Apr. 2019. DOI: `10.3390/ma12081301`.

[198] T. Maconachie, M. Leary, B. Lozanovski, *et al.*, "SLM lattice structures: Properties, performance, applications and challenges", *Materials & Design*, vol. 183, Dec. 2019. DOI: `10.1016/j.matdes.2019.108137`.

[199] Z. Liu, D. Zhang, S. Sing, C. Chua, and L. Loh, "Interfacial characterization of SLM parts in multi-material processing: Metallurgical diffusion between 316L stainless steel and C18400 copper alloy", *Materials Characterization*, vol. 94, pp. 116–125, Aug. 2014. DOI: `10.1016/j.matchar.2014.05.001`.

[200] A. G. Demir and B. Previtali, "Multi-material selective laser melting of Fe/Al-12Si components", *Manufacturing Letters*, vol. 11, pp. 8–11, Jan. 2017. DOI: `10.1016/j.mfglet.2017.01.002`.

[201] T. Puttonen, S. Chekurov, J. Kuva, R. Björkstrand, J. Partanen, and M. Salmi, "Influence of feature size and shape on corrosion of 316L lattice structures fabricated by laser powder bed fusion", *Additive Manufacturing*, vol. 61, Jan. 2023. DOI: `10.1016/j.addma.2022.103288`.

[202] E. Abele, T. Scherer, F. Geßner, and M. Weigold, "Einbringen von Gewinden in SLM-Bauteile – Strategie zur prozesssicheren Gewindefertigung in additiv gefertigten Komponenten", *wt Werkstattstechnik online*, vol. 109, 2019. DOI: `10.37544/1436-4980-2019-01-02`.

[203] S. A. Tronvoll, C. W. Elverum, and T. Welo, "Dimensional accuracy of threads manufactured by fused deposition modeling", *Procedia Manufacturing*, vol. 26, pp. 763–773, 2018. DOI: `10.1016/j.promfg.2018.07.088`.

[204] Q. Han, H. Gu, S. Soe, R. Setchi, F. Lacan, and J. Hill, "Manufacturability of AlSi10Mg overhang structures fabricated by laser powder bed fusion", *Materials & Design*, vol. 160, pp. 1080–1095, Dec. 2018. DOI: `10.1016/j.matdes.2018.10.043`.

[205] A. Charles, M. Bayat, A. Elkaseer, L. Thijs, J. H. Hattel, and S. Scholz, "Elucidation of dross formation in laser powder bed fusion at down-facing surfaces: Phenomenon-oriented multiphysics simulation and experimental validation", *Additive Manufacturing*, vol. 50, Feb. 2022. DOI: `10.1016/j.addma.2021.102551`.

[206] F. Herbst, *Development of a Sensor-Integrated Screw for Multi-Axial Force Measurement Based on Strain Gauges*, Master's Thesis, Technische Universität Darmstadt, 2022.